

Quantum Coherence and Magnetism in Bosonic and Fermionic Gases of Ultracold Atoms

by

Gyu-Boong Jo

B.S., Physics and Mathematics (2003)

Seoul National University

Submitted to the Department of Physics
in partial fulfillment of the requirements for the degree of

Doctor of Philosophy

at the

MASSACHUSETTS INSTITUTE OF TECHNOLOGY

January 2010

© Massachusetts Institute of Technology 2010. All rights reserved.

Author
Department of Physics
January 29, 2010

Certified by
Wolfgang Ketterle
John D. MacArthur Professor of Physics
Thesis Supervisor

Certified by
David E. Pritchard
Cecil and Ida Green Professor of Physics
Thesis Supervisor

Accepted by
Krishna Rajagopal
Professor of Physics, Associate Department Head for Education

Quantum Coherence and Magnetism in Bosonic and Fermionic Gases of Ultracold Atoms

by

Gyu-Boong Jo

Submitted to the Department of Physics
on January 29, 2010, in partial fulfillment of the
requirements for the degree of
Doctor of Philosophy

Abstract

In this thesis, two sets of experimental studies in bosonic and fermionic gases are described. In the first part of the thesis, itinerant ferromagnetism was studied in a strongly interacting Fermi gas of ultracold atoms. The observation of nonmonotonic behavior of lifetime, kinetic energy, and size for increasing repulsive interactions provides strong evidence for a phase transition to a ferromagnetic state. Our observations imply that itinerant ferromagnetism of delocalized fermions is possible without lattice and band structure, and our data validate the most basic model for ferromagnetism introduced by Stoner.

In the second part of the thesis, the coherence properties of a Bose-Einstein condensate (BEC) was studied in a radio frequency induced double-well potential implemented on a microfabricated atom chip. We observed phase coherence between the separated condensates for times up to 200 ms after splitting, a factor of 10 longer than the phase diffusion time expected for a coherent state for our experimental conditions. The enhanced coherence time is attributed to number squeezing of the initial state by a factor of 10.

Furthermore, the effect of phase fluctuations on an atom interferometer was studied in an elongated BEC. We demonstrated that the atom interferometer using the condensates is robust against phase fluctuations; i.e., the relative phase of the split condensates is reproducible despite axial phase fluctuations.

Finally, phase-sensitive recombination of two BECs was demonstrated on an atom chip. The recombination was shown to result in heating, caused by the dissipation of dark solitons, which depends on the relative phase of the two condensates. This heating reduces the number of condensate atoms and provides a robust way to read out the phase.

Thesis Supervisor: Wolfgang Ketterle
Title: John D. MacArthur Professor of Physics

Thesis Supervisor: David E. Pritchard
Title: Cecil and Ida Green Professor of Physics

*To my parents,
Young Ki Jo and Ok Hwa Kim
and to Helen.*

Acknowledgments

There are many people who I would like to thank for making this thesis possible. This acknowledgement is a small token of my appreciation for their supports.

First of all, I owe my deepest gratitude to Wolfgang and Dave for giving me an opportunity to work in their group. In past 5 years, I could learn how to find out an interesting problem in physics, approach the problem in an efficient way, and extract meaningful interpretation out of the observation. In almost every group meeting, Wolfgang and Dave guided us to focus on the core of the problem we faced in the lab. Their keen and deep insight into physics kept us seeing a big picture hidden behind the problem we considered.

Also, I would like to thank Wolfgang and Dave for inspiring excitement about the physics in past 5 years. When I met Wolfgang during the open house in 2004, he told me as follows, “My students often spend whole night because they love to see a new phenomenon in the lab.”. During my Ph.D. course, I realized what Wolfgang meant. The moment when I observed unexpected phenomena in the lab was unforgettable experience.

When I arrived at MIT in 2004, I joined the third generation BEC machine (BEC III), sometimes called “*the science chamber*”. I had an extreme fortune because all the people in the science chamber are very nice as well as smart. Without them, this thesis would not have been possible. Here, I would like to thank the people I have worked most closely with in the BEC III lab over the past few years.

I had spent about one year with Yong-il Shin before he graduated and started his new experiments in BEC I. I could learn almost everything that I need to know in the lab from Yong-il. To me, he has been a brother and a good friend as well as an excellent mentor. His valuable advice has always helped me to be in the right track in many respects. The atom chip experiments reported in this thesis would not have been possible without his contribution. I wish all the best for his research in Korea.

I also thank Michele for his endless helps and advices in the lab. I often found treasures in the discussion with him about physics and life. Whatever problem we faced in the lab could be solved smoothly with Michele. I am grateful to Tom Pasquini as well. He had made available his support in a number of ways. In my first and second year at MIT, I could manage my research life with the help of his invaluable advices. I also benefited from an energetic diploma student, Sebastian Will. His careful assessment of the problem we faced in the lab allowed me to solve them efficiently and focus on the physics itself. Without his contribution, the “long phase coherence

time experiment” would not have been successful.

Also I had a great fortune to work with Jae. Jae was a great labmate who could compensate for the absence of Yong-il and Michele. He brought his valuable experiences into the science chamber team, and we could improve the apparatus allowing us to run a successful experiment with sufficient stability in many respects. In addition, Caleb and Ye-Ryoung have contributed to most of experiments described in this thesis. Caleb has deep insight into electronic devices as well as physics and our lab still benefits from his presence. Ye-Ryoung brought a new energy into the science chamber team. She has provided assistance in numerous ways. I wish them good luck for their coming research. Finally, I also benefited from Tony Kim and Tout Wang. Tony could make any electronic circuit with high standard. Tout has a lot of curiosity about physics leading to broad knowledge. His enthusiasm in physics would become an invaluable asset in the science chamber .

It is a pleasure to thank those who made this thesis possible outside the science chamber. I specially thank the members in BEC I for sharing the lab space and many experimental tools with endless patience and kindness. I thank Martin Zwierlein for sharing his deep understanding of the physics, Claudiu Stan for his super-stable electronic boxes, Christian Schunck for playing the harp, and Andre Schirotzek for “nice” personality. Also, I would like to thank Kaiwen Xu, Daniel Miller, Jit Kee Chin, Yingmei Liu , Christian Sanner, Aviv Keshet, Edward Su, Ralf Gommers, Peter Zarth, Luis Marcassa, Micah Boyd, Gretchen Campbell, Jongchul Mun, Patrick Medley, Hiro Miyake, David Hucul, and David Weld. Finally, I thank all members of the Fermi I lab including Peyman Ahmadi, Ariel Sommer, Cheng-Hsun Wu, Ibon Santiago, Jeewoo Park, and Mark Ku.

CUA (Center for Ultracold Atoms) is a wonderful place for me to have a frequent discussion with other people, interact with other physicists, and finally learn the cutting-edge physics. I could benefit from many other labs in CUA in many respects; I could get helpful advices from colleagues in CUA whenever I encountered a problem. I would like to thank all CUA members for their supports. Especially, I must express my gratitude to Joanna Keseberg for her support.

I am indebted to many of my colleagues to support me outside the lab. I owe my deepest gratitude to Sang-il Lee, Seung-Hyuck Hong, Lin Han, Heechul Park, Sung-Whan Oh, Yeoreum Yoon, Wonyong Lee, Jaemyung Ahn, Seungbum Hong, Jungwoo Joh, Joonsung Lee, Daniel S. Park, Eun Gook Moon, Gyuwon Hwang, Hyung-Gyu Kwon, Jichul Woo, Sang-jin Kim, Hanlim Choi, and Jerin Gu. I also would like to thank Woojong Baek, Gangsang Lee, Gangwon Lee, Yongsuk Lee, Michael Min, Chris

Bae, and Woojae Kim.

I am grateful to Prof. Wonho Jhe for giving me an opportunity to work in his group before I started graduate school. His encouragement motivated me to explore a new physics without being afraid of a failure.

Finally, and most importantly, I would like to thank my parents. Their support, encouragement, patience and endless love have kept me feeling constantly comfortable in my Ph.d. course. Without their devotion and love, this thesis would not have been accomplished. Also, I owe my deepest gratitude to Helen. Her tolerance of my occasional nervousness is a testament of her devotion and love. I really appreciate her endless support again.

This work was supported by NSF and the Office of Naval Research, through the Multidisciplinary University Research Initiative program, and under Army Research Office grant no. W911NF-07-1-0493 with funds from the Defense Advanced Research Projects Agency Optical Lattice Emulator program. I also acknowledge additional support from the Samsung Foundation.

Contents

1	General Introduction	13
1.1	The Quest for Low Temperatures	13
1.1.1	Bose-Einstein Condensation	13
1.1.2	Ultracold Dilute Atomic Gas	14
1.2	Next Challenges in the field of Ultracold Atomic Gases: Quantum Simulator	15
1.3	Identical Particles in Quantum Theory: Bosons and Fermions	17
1.4	Outline of Thesis	19
2	Apparatus and Basic Procedures	22
2.1	Versatile Apparatus: “Science Chamber”	22
2.2	F=1 ^{23}Na Bose-Einstein Condensates in the Science Chamber	22
2.2.1	Magnetic Microtraps on an Atom Chip in the Science Chamber	24
2.3	Apparatus for Producing a Degenerate gas of ^{23}Na and ^6Li Atoms	26
2.3.1	Producing a Degenerate ^6Li Fermi Gas	26
2.3.2	Li Laser System	29
2.3.3	Tools for Experiments	31
3	Ferromagnetism in a Fermi Gas	35
3.1	Quantum Magnetism	35
3.1.1	What is magnetism?	35
3.1.2	Origin of Ferromagnetism: Exchange interactions	36
3.1.3	Two Paradigms of Magnetism	38
3.2	Itinerant Ferromagnetism	39
3.2.1	Long-standing Problem in Condensed-matter Physics	39
3.2.2	Stoner Model in a Free Electron Gas with Short-range Interactions	41
3.2.3	Ferromagnetism in Hubbard Models	43
3.2.4	Similar Studies in Normal Liquid ^3He	45

3.3	Itinerant Ferromagnetism in Ultracold Atomic Gases	47
3.3.1	A Very Simple Mean-field Prediction for Stoner's Instability in an Ultracold Atomic Gas	49
3.3.2	Domain Structure of the Ferromagnetic Ground State	52
4	Itinerant Ferromagnetism in a Fermi Gas of Ultracold Atoms	55
4.1	Two-component Fermi gas with strong repulsive interactions as a Model System	55
4.2	Implementation of the Stoner model in an Ultracold Atomic System .	60
4.2.1	Experimental Technique	61
4.3	Evidences for Itinerant Ferromagnetism in a Fermi Gas of Ultracold Atoms	64
4.4	Discussion	69
4.4.1	The Critical Value of $k_F a$ Observed in the Experiment	69
4.4.2	Estimation of the Maximum Total Repulsive Energy	70
4.4.3	Comparison with Ferromagnetism in Spinor Bose-Einstein Con- densates.	71
4.4.4	Discrepancy of the Critical Value of $k_F a$	71
4.4.5	Correlation Effects	73
4.5	Outlook: New Experiments	74
5	Quantum Phase Coherence in Degenerate Bosonic Gases	77
5.1	Phase Coherence in a Bose-Einstein Condensate	77
5.2	Decoherence in Interacting Bose Gases	81
5.3	Measurement of the Relative Phase between Two Condensates	83
5.4	Tools for the Study of Coherence Properties of a Bose gas	87
6	Long Phase Coherence Time via Number Squeezing and Phase Fluc- tuations of BECs in a Double-well Potential	91
6.1	Long Phase Coherence Time and Number Squeezing	92
6.1.1	Splitting Process in a Double-well Potential: a Bosonic Joseph- son Junction	93
6.1.2	Preparation of a Number-squeezed State on an Atom Chip	98
6.1.3	Phase Diffusion and Number Squeezing	103
6.1.4	Conclusion and Remarks	105
6.2	Matter-wave Interferometry with Phase Fluctuating Bose-Einstein Con- densates	107

6.2.1	Phase Fluctuations in an Elongated Bose-Einstein Condensate	107
6.2.2	Effect of Phase Fluctuations on Atom Interferometry	109
7	Development of Atom Optics Elements	112
7.1	Phase Sensitive Recombination of Two Bose-Einstein Condensates . .	112
7.2	Trapping of Ultracold Atoms in a Hollow-core Photonic Crystal Fiber	117
8	Conclusion and Outlook	120
8.1	The future in BEC III	120
A	Properties of ^{23}Na and ^6Li.	122
B	Designs for the Apparatus	125
C	Itinerant ferromagnetism in a Fermi gas of ultracold atoms	131
D	Long Phase Coherence Time and Number Squeezing of two Bose-Einstein Condensates on an Atom Chip	143
E	Matter-Wave Interferometry with Phase Fluctuating Bose-Einstein Condensates	148
F	Phase-Sensitive Recombination of Two Bose-Einstein Condensates on an Atom Chip	153
G	Trapping of Ultracold Atoms in a Hollow-core Photonic Crystal Fiber	158
H	Interference of Bose-Einstein condensates split with an atom chip	163
	Bibliography	168

List of Figures

1-1	Concept of the quantum simulator	16
2-1	Microfabricated atom chip mask	25
2-2	A schematic of the dual-species oven	27
2-3	Dual magnetic optical trap	28
2-4	A schematic of magnetic coils in the main chamber	30
2-5	Circuit diagram for producing a large bias magnetic field	32
2-6	A schematic of a newly designed science chamber	34
3-1	Classical electron gas in a box with external magnetic field	36
3-2	Density of states of a metal in the presence of a magnetic field	42
3-3	Hartree-Fock phase diagram for the two-dimensional Hubbard model	44
3-4	Itinerant ferromagnetism in second-order perturbation calculations	48
3-5	Mean-field model at $T = 0$: Itinerant ferromagnetism	50
3-6	Mean-field predictions for ferromagnetic phase transition at $T=0$	51
3-7	Schematic illustration of the ferromagnetic transition in the two-component Fermi gas	53
3-8	Possible configurations of the ferromagnetic ground state in a two-component Fermi gas trapped in a spherical potential.	54
4-1	The many-body branches near the Feshbach resonance.	57
4-2	The energy per particle and the thermodynamic pressure of the two-component Fermi gas with repulsive interactions near Feshbach resonance.	60
4-3	The sequence of the experiment to observe itinerant ferromagnetism.	62
4-4	The effect of eddy currents on the magnetic field ramp	63
4-5	Atom loss rate as a probe for local spin polarization	65
4-6	Kinetic energy of a repulsively interacting Fermi gas determined for different interaction parameters $k_F^{\circ}a$ and temperatures	67

4-7	Maximum in volume at the phase transition	68
4-8	The entropy difference between the normal and the ferromagnetic phase.	71
4-9	Schematic illustration of the RF quench experiment	75
4-10	Schematic illustration of the single domain experiment	76
5-1	Matter-wave interference and relative phase read-out	85
5-2	Three different methods for the phase read-out of two Bose-Einstein condensates	86
5-3	Adiabatic RF-induced splitting	88
5-4	Operation of a coherent beam splitter	89
6-1	Schematic illustration of the ground and the first excited state in a double potential.	94
6-2	Three different regimes in the description of the dynamic splitting of condensates.	97
6-3	Schematic of the atom chip interferometer	98
6-4	Phase evolution of the relative phase	100
6-5	Long phase coherence of two separated condensates	101
6-6	Quantitative study of phase coherence: Rayleigh test	102
6-7	Phase diffusion and number squeezing	104
6-8	Confined atom interferometry with enclosed area	105
6-9	Phase fluctuations in an elongated condensate	107
6-10	Measurement of phase fluctuations in a single condensate.	108
6-11	Spatial phase fluctuations and the reproducibility of of the relative phase.	110
7-1	Phase-sensitive recombination	114
7-2	Oscillations of condensate atom loss after recombination reflecting the coherent phase evolution.	115
7-3	Schematic illustrations for trapping of atoms in a hollow-core fiber . .	118
7-4	Images of atoms in the optical dipole trap during the experiment . .	119
A-1	Sodium and Lithium energy levels and relevant atomic parameters. .	123
A-2	^{23}Na and ^6Li hyperfine structure in an external magnetic field. . . .	124

List of Tables

2.1	Source of the magnetic bias field	30
3.1	Density dependence in Long-range Coulomb interactions and short-range contact interactions	40
3.2	Comparison between cold atoms and solid state in the study of itinerant ferromagnetism	49
4.1	Prediction of critical interaction strength for itinerant ferromagnetism	73

Chapter 1

General Introduction

1.1 The Quest for Low Temperatures

The quest for low temperatures has a long history over 200 years. After Gaspard Monge liquefied the first gas producing liquid sulfur dioxide in 1784, major efforts had been directed toward liquefying oxygen (1877), hydrogen (1898), and helium (1908). Helium-4, first liquified by Dutch physicist Heike K. Onnes in 1908 [140], was crucial for the developments of two major concepts in modern physics, *superconductivity* and *superfluidity*. In 1911, Onnes used liquid helium-4 as a refrigerant, and discovered that the resistivity in solid mercury abruptly disappears at the temperature of 4.19 K [140]. He called this phenomenon as “superconductivity”. Later in 1937, Pyotr L. Kapitza, John F. Allen, and Don Misener discovered that below the famous λ -transition point at 2.17 K, liquid helium-4 becomes superfluid in which a liquid flows through narrow capillaries or slits without exhibiting viscosity [3, 106]. Both concepts, superconductivity and superfluidity, have been actively researched in the 20th century leading to the enhancement of our understanding of nature.

1.1.1 Bose-Einstein Condensation

The first idea of Bose-Einstein condensation (BEC) can be traced back to 1925 when Satyendra N. Bose [28] and Albert Einstein [53, 54] predicted the occurrence of phase transition in noninteracting bosonic particles such as photons. The phase transition is accompanied by the condensation of atoms in the ground state. Unfortunately, despite the novelty of this prediction, there had not been much attention paid to Bose-Einstein condensation until the discovery of superfluidity in helium-4.

In 1938, Fritz London pointed out that Bose-Einstein condensation may be the

underlying phenomenon in superfluid helium-4 [130, 129]. Superfluid helium-4 was the prototype Bose-Einstein condensate, and intense theoretical works had been developed in order to understand the relation between superfluidity and Bose-Einstein condensation. Later, a microscopic theory for interacting Bose gases was developed by Bogoliubov in 1947 [26]. In the 1950s, Penrose and Onsager introduced the concept of off-diagonal long-range order and discussed the relation to a generalized criterion of Bose-Einstein condensation [149].

In parallel to theoretical works to understand the phenomenon of Bose-Einstein condensation, the experimental efforts had been made to realize Bose-Einstein condensates in spin-polarized hydrogen without success until 1998 [61]. Recently, Bose-Einstein condensation was also observed in metastable helium-4 in 2001 [165, 171]. The first experimental realization of Bose-Einstein condensate was achieved in 1995 in ultracold dilute atomic gases at JILA by Eric A. Cornell and Carl E. Wieman [6] and at MIT by Wolfgang Ketterle [47] independently. So far, BEC phase transitions have been achieved in dilute atomic gases of ^{23}Na , ^7Li , ^{87}Rb , ^{85}Rb , ^{39}K , ^{41}K , ^{52}Cr , ^{133}Cs , ^{170}Yb , ^{174}Yb , ^1H , and $^4\text{He}^*$ (metastable helium) [152]. The success in dilute atomic gases relied on the developments of laser cooling and magnetic trapping techniques in the 1980s [12, 92]. Recently, atomic Fermi gases of ^6Li and ^{40}K atoms also could be cooled to the degenerate temperature. This allowed for Bose-Einstein condensation of molecules consisting of a pair of fermionic atoms. The field of ultracold dilute atomic gases keeps growing as we shall see in the following sections.

1.1.2 Ultracold Dilute Atomic Gas

Ultracold dilute atomic gases have several impressive features with respect to other systems such as superfluid helium. Firstly, ultracold atomic gases have typically weak interatomic interactions so that mean-field description of the system is well-suited [92]. This is one of the advantages for investigating quantum phenomena in atomic gases which is not the case in superfluid helium.

Another feature is diluteness of the systems. The atomic density in condensates of trapped atomic gases is typically $\sim 10^{13}\text{cm}^3$ which is much lower than the density of atoms in liquids or solids, $\sim 10^{22}\text{cm}^3$. The low-density of atomic gases requires the low temperature of 10^{-5} K or less for observing quantum phenomenon. Liquid helium, in contrast to atomic gases, shows quantum phenomenon such as superfluidity near 1 K.

Despite diluteness of atomic gases, the strength of interatomic interactions can

be tunable either by exploiting the Feshbach resonance [108, 38] or by introducing optical lattices [25]. Feshbach resonance occurs when a bound state is coupled to a free unbound state of colliding atoms allowing for tuning interaction strength directly in a broad range from negative to positive values. This technique opened a new way to investigate Fermi atoms in the presence of weak attractive interactions which is relevant to the famous theory of superconductivity developed by Bardeen, Cooper, and Schrieffer (BCS theory) [17]. Further experiments realized the system of molecular Bose-Einstein condensates consisting of two Fermi atoms, fermionic pair condensates in the “BCS” side, and finally an intermediate regime, so-called a BCS-BEC crossover [212, 210], where the pair size of Fermi atoms is comparable to the interparticle distance. For comprehensive discussions, I refer to the Ref. [91]

Alternatively, the effect of atom-atom interactions can be tuned in an optical lattice. An optical lattice is a periodic potential produced by a standing-wave laser beam [25]. In this artificial crystal, ultracold atoms can mimic the strongly correlated behavior of electrons in condensed matter. One of the most prominent experiments in optical lattices is the observation of superfluid-Mott transition insulator transition of bosonic gas [66]. The sufficiently strong repulsive interactions change the many-body ground state from the superfluid to the insulating phase in which the tunneling of bosonic atoms between adjacent sites is suppressed and therefore each atom is localized in one specific lattice site.

1.2 Next Challenges in the field of Ultracold Atomic Gases: Quantum Simulator

In 1982, Richard Feynmann [57] proposed a quantum device, a so-called quantum simulator, for efficient simulation of other quantum systems. The goal of quantum simulator is to simulate a target quantum system with a controllable laboratory system governed by the same Hamiltonian. The quantum simulation is expected to simulate quantum systems that cannot be efficiently simulated on a classical computer. There have been much attention paid to this idea because the understanding of many phenomena in various field including condensed-matter physics and high-energy physics would be enhanced through quantum simulations. To this end, major efforts have been made to implement this idea with real quantum systems consisting of neutral atoms, ions, photons, and electrons.

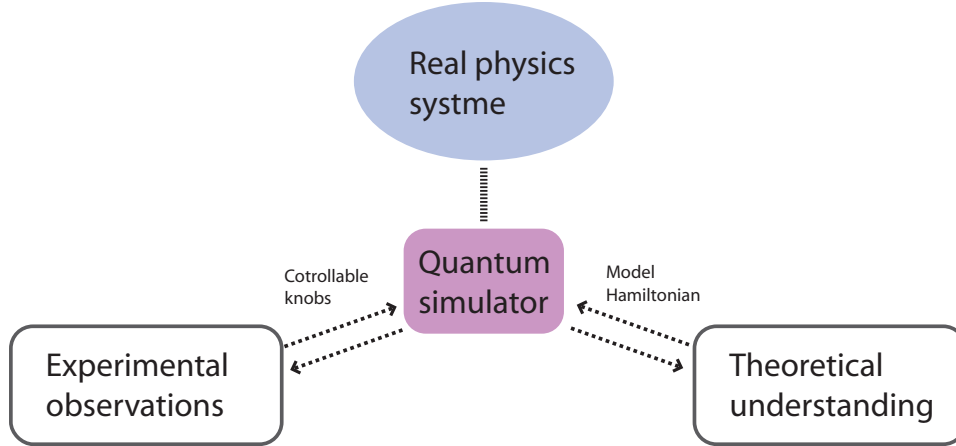


Figure 1-1: Concept of the quantum simulator. The quantum simulators are controllable quantum systems in the laboratory simulating a theoretical model Hamiltonian describing the real system.

The rapid developments in the field of dilute atomic gases over last 15 years after the first realization of Bose-Einstein condensates have featured the possibility of studying strongly correlated phenomena of condensed-matter physics in the context of quantum simulation. The seminal paper in 1998 by Jaksch [95] proposed the observation of the superfluid-Mott insulator transition in cold atoms in an optical lattice, which was experimentally observed in 2002 [66]. In the 2000s, the field of ultracold atoms entered the area of strongly correlated systems. The great successes have been achieved in the study of superfluid-Mott insulator transition of bosonic atoms in an optical lattice [25], BCS-BEC crossover in a Fermi gas with tunable interactions [91], and Anderson localizations of bosonic atoms in a disordered potential [164, 22]. Remarkably, some of experimental investigations in those systems have been validated through numerical studies.

Recently, the field of ultracold atomic gases keeps broadening the scope of research direction toward the realization of quantum magnetism in cold atomic gases which can serve as a tunable model system for understanding the physics behind real condensed matter systems. The presence or suppression of magnetic ordering is important not only for ferromagnetism and antiferromagnetism, but also for phenomena like high-temperature superconductivity, quantum magnets, and spin liquids in strongly correlated electron system [167]. In the system of ultracold atoms, the similar magnetic ordered states are expected to be realized when cold bosonic or fermionic atoms are prepared in optical lattices or in a bulk system with magnetic interactions such as exchange or superexchange interactions [123]. The magnetic interactions can

be controlled by tuning the interaction strength via Feshbach resonance and/or by quenching kinetic energy of the atom with an increase of the lattice depth. Of particular interest is the study of the repulsive Fermi-Hubbard model with two-component Fermi gases trapped in optical lattices since the high-temperature superconductivity usually occurs near the antiferromagnetic phase in complex cuprate materials. Some promising works, demonstrating the metallic and insulating behaviors in a Fermi gas, have been reported [173, 103], and major efforts are being directed toward the observation of the antiferromagnetic ordered state. In related works, the ferromagnetic ordered state in a Fermi gas is also very important because it may compete with superconductivity near quantum phase transitions [128]. Recent experimental [102] and theoretical progresses [86, 170, 4, 182, 52, 19, 206, 114] in ferromagnetism in a repulsive Fermi gas shall be discussed in the first part of this thesis.

1.3 Identical Particles in Quantum Theory: Bosons and Fermions

Two particles are identical if they are non-distinguishable under physical observations and measurements. The nondistinguishability of identical particles plays a secondary role in classical mechanics, but it becomes important in quantum mechanics characterizing the nature of the fundamental particle.

We now consider N identical particles governed by the Hamiltonian H . The wavefunction $\psi(r_1, r_2, \dots, r_N)$ represents the probability amplitude for finding N particles at the position of r_1, r_2, \dots, r_N . Under the exchange of any pair of particles, the probability density of finding N particles is invariant since all particles are identical:

$$|\psi(r_1, \dots, r_i, \dots, r_j, \dots, r_N)|^2 = |\psi(r_1, \dots, r_j, \dots, r_i, \dots, r_N)|^2 \quad (1.1)$$

This derivation implies that the wavefunction $\psi(r_1, r_2, \dots, r_N)$ has an *exchange degeneracy* under particle exchange.

$$\psi(r_1, \dots, r_i, \dots, r_j, \dots, r_N) = \pm \psi(r_1, \dots, r_j, \dots, r_i, \dots, r_N) \quad (1.2)$$

As a clear example illustrating the exchange degeneracy, let us consider two identical particles with their mass m governed by the Hamiltonian

$$H(1, 2) = \frac{P_1^2}{2m} + \frac{P_2^2}{2m} + V(|r_1 - r_2|) \quad (1.3)$$

where the potential V depends only on the distance between two particles. The energy eigenvalue equation now reads,

$$\begin{aligned} H(1,2)\psi(r_1, r_2) &= E\psi(r_1, r_2) \\ H(2,1)\psi(r_2, r_1) &= E\psi(r_2, r_1) \end{aligned} \tag{1.4}$$

where $\psi(r_1, r_2)$ and $\psi(r_2, r_1)$ are two eigenstates of the two-particle system by recognizing the invariance of the Hamiltonian $H(1,2) = H(2,1)$. Therefore, the eigenstate of the system is the superposition of $\psi(r_1, r_2)$ and $\psi(r_2, r_1)$. Without loss of generality, the eigenstate of the Hamiltonian 1.3, ψ_0 , is expressed by

$$\psi_0 = \alpha \underbrace{\left(\frac{\psi(r_1, r_2) + \psi(r_2, r_1)}{\sqrt{2}} \right)}_{\psi^{(S), \text{symmetric}}} + \beta \underbrace{\left(\frac{\psi(r_1, r_2) - \psi(r_2, r_1)}{\sqrt{2}} \right)}_{\psi^{(A), \text{antisymmetric}}} \tag{1.5}$$

$$\tag{1.6}$$

where $|\alpha|^2 + |\beta|^2 = 1$. Thus far, the eigenstate contains both symmetric ($\psi^{(S)}$) and antisymmetric ($\psi^{(A)}$) contribution. However, in contrast to above mathematical approach, only totally symmetric or antisymmetric states are observed in nature. This difficulty is removed by the famous “*symmetrization postulation*” in quantum mechanics:

“*The states of a system with N identical particles are necessarily either all symmetrical ($\alpha = 1, \beta = 0$ in the above example.) or all antisymmetrical ($\alpha = 0, \beta = 1$) with respect to particle exchanges*”

Following this postulate, particles described by the symmetric state and the antisymmetric state are called *Bosons* and *Fermions* respectively.

Systems consisting of identical particles of integral spin (0,1,2, ...) ¹ are described by symmetric wavefunctions, and such particles obey *Bose-Einstein statistics* and are called bosons. In nature, photons, π -mesons, and K-mesons are examples of bosons. On the other hand, identical particles of half-integral spin (1/2,3/2, ...) are called fermions and obey *Fermi-Dirac statistics*. Since the system consisting of fermions is described by the antisymmetric wavefunction, two identical fermions cannot occupy the same quantum state leading to the “*Pauli exclusion principle*”.

¹The connection between spin and statistics is explained by the relativistic quantum mechanics. Further discussions can be found in Ref [150].

1.4 Outline of Thesis

The experimental works in this thesis have been performed by my colleagues and me in the BEC III lab at MIT. Our team has been supervised by Professor Wolfgang Ketterle and Professor David.E. Pritchard.

In this thesis, I mainly discuss: (1) itinerant ferromagnetism in a Fermi gas of ultracold atoms [102], (2) apparatus upgrade for producing a Bose-Fermi mixture, (3) studies of quantum coherence in a Bose gas [101, 99], and (4) development of atom optics elements [100, 39]. I was also involved in the other projects including “quantum reflection of BECs” [145], “optical weak link between two BECs” [176], and “interference of BECs split on an atom chip” [179] which are described in the Ph.D. theses of former members of BEC III [89, 147].

Outline

Chapter 2 describes the experimental procedures for producing a degenerate Bose-Fermi mixture. Preliminary efforts for this apparatus upgrade are discussed in the Ph.d. thesis by Thomas A. Pasquini [147]. Here, I briefly summarize the basic procedures and tools which are used in the current experiment.

Chapter 3 and chapter 4 discuss quantum magnetism in a two-component Fermi gas of ultracold ^{23}Li atoms. In particular, the long-standing question of “*itinerant ferromagnetism*” in condensed matter physics is addressed. The concept of *quantum simulation* using cold atoms may apply to our work reported in this thesis. In chapter 3, I introduce some theoretical tools necessary to understand magnetic properties of a repulsive Fermi gas with short-range interactions. Chapter 4 mainly discusses our experimental efforts and relevant theoretical understandings to observe itinerant ferromagnetism in a Fermi gas. At the end of this chapter, I propose some future experiments which may overcome technical limitations and enhance our understanding of itinerant ferromagnetism in a Fermi gas.

In chapter 5, I deal with the basic concepts of Bose-Einstein condensates and demonstrate experimental tools necessary to study the coherence properties of a Bose gas. A coherent splitter using adiabatic RF-induced potential and phase read-out methods shall be described.

Chapter 6 discusses the quantum phase coherence of a Bose gas in a double-well system implemented on an atom chip. The observation of number squeezing in condensates shall be described. Also, I provide a theoretical model describing the dynamic splitting of the condensate. At the end of this chapter, I discuss the effect

of phase fluctuations on the coherence properties.

Finally, chapter 7 deals with newly developed techniques in the field of atom-optics. First, I demonstrate the phase-sensitive recombination of two BECs which is a new method of measuring the relative phase. Secondly, I briefly describe a proof-of-principle experiment for trapping of ultracold atoms in a hollow-core photonic crystal fiber.

• **Publications of the Ph.D. work**

- *Itinerant Ferromagnetism in a Fermi Gas of Ultracold Atoms*
Gyu-Boong Jo, Ye-Ryuoung Lee, Jae-Hoon Choi, Caleb A. Christensen, Tony H. Kim, Joseph H. Thywissen, David E. Pritchard and Wolfgang Ketterle
Science **325** , 1521-1524 (2009)
- *Trapping of Ultracold atoms in a hollow-core photonic crystal fiber*
Caleb A. Christensen, Sebastian Will, Michele Saba, Gyu-Boong Jo, Yong-Il Shin, Wolfgang Ketterle, and David Pritchard
Phys. Rev. A **78**, 033429 (2008)
- *Matter-wave Interferometry with Phase Fluctuating Bose-Einstein Condensates*
G.-B. Jo, J.-H. Choi, C.A. Christensen, Y.-R. Lee, T.A. Pasquini, W. Ketterle, and D.E. Pritchard
Phys. Rev. Lett. **99**, 240406 (2007)
- *Phase Sensitive Recombination of Two Bose-Einstein condensates on an atom chip*
G.-B. Jo, J.-H. Choi, C.A. Christensen, T.A. Pasquini, Y.-R. Lee, W. Ketterle, and D.E. Pritchard
Phys. Rev. Lett. **98**, 180401 (2007)
- *Long phase coherence time and number squeezing of two Bose-Einstein condensates on an atom chip*
G.-B. Jo, Y. Shin, S. Will, T. A. Pasquini, M. Saba, W. Ketterle, D. E. Pritchard, M. Vengalattore, and M. Prentiss
Phys. Rev. Lett. **98**, 030407 (2007)
- *Low Velocity Quantum Reflection of Bose-Einstein Condensates*
T. A. Pasquini, M. Saba, G.-B. Jo, Y. Shin, W. Ketterle, D. E. Pritchard, T.

A. Savas, and N. Mulders

Phys. Rev. Lett. **97**, 093201 (2006)

- *Optical Weak Link between Two Spatially Separated Bose-Einstein Condensates*
Y. Shin, G.-B. Jo, M. Saba, T. A. Pasquini, W. Ketterle, and D. E. Pritchard,
Phys. Rev. Lett. **95**, 170402 (2005)
- *Interference of Bose-Einstein condensates split with an atom chip*
Y. Shin, C. Sanner, G.-B. Jo, T. A. Pasquini, M. Saba, W. Ketterle, D. E.
Pritchard, M. Vengalattore, and M. Prentiss
Phys. Rev. A **72**, 021604(R) (2005)

Chapter 2

Apparatus and Basic Procedures

2.1 Versatile Apparatus: “Science Chamber”

The third generation machine at MIT, which is called the *science chamber* (or BEC III), is very unique in that one produces a Bose-Einstein condensate (BEC) in the main chamber and then manipulates and diagnoses the BEC in the auxiliary chamber. This is implemented by transporting a BEC trapped in an optical dipole trap [37, 74]. The two-step experiment - first producing the BEC and then transporting it into the auxiliary chamber - makes it possible to study the properties of the BEC in various systems such as a double-well potential on an atom chip [112, 178, 101, 99], a double-well optical potential [177, 166, 101, 99], or an atom-surface system [146, 145]. In contrast to a conventional BEC machine in which optical and physical access to cold atoms are restricted due to the presence of magnetic coils and optics near the chamber, the science chamber machine has allowed us to change the experimental system without perturbing the production of a BEC.

2.2 F=1 ^{23}Na Bose-Einstein Condensates in the Science Chamber

In this section, we demonstrate the basic operation procedure for producing a bosonic ^{23}Na F=1 BEC. The condensate consists of the sodium atoms in the hyperfine state of $|F = 1, m_F = -1\rangle$. Before the apparatus was upgraded to have a Bose-Fermi mixture (bosonic ^{23}Na and fermionic ^6Li) in 2007, most of the experiments had been performed with a F=1 condensate. Typical procedure for the production of the F=1 BEC includes:

- Pre-cooling atoms in magneto-optical trap (MOT) (~ 3 s) : A thermal atomic beam slowed by a Zeeman slower is continuously loaded into a dark-SPOT type magnetic-optical trap (MOT). The atomic flux into the MOT is $\sim 10^{11}$ atoms/s with a mean velocity of ~ 30 m/s. In the dark-spot MOT, most of atoms lie in the $F=1$ manifold.
- Forced rf-evaporation in the magnetic trap (~ 30 s) : Atoms in the $|F = 1, m_F = -1\rangle$ state are transferred from the dark-spot MOT into a Ioffe-Pritchard magnetic trap. Subsequently, forced evaporative cooling is applied using a radio frequency (rf) transition from the $|F = 1, m_F = -1\rangle$ to the $|F = 1, m_F = 0, +1\rangle$ states. We routinely produce a $F=1$ condensate of 10^7 atoms after 30 s evaporation in the main chamber. The lifetime of the $F=1$ condensate in the magnetic trap is longer than 60 s which is longer than the one for a $F=2$ condensate ¹.
- Trapping a BEC in an optical dipole trap (ODT): For the transport of the condensate into the science chamber, we load the condensate into an optical dipole trap (ODT). The loading process starts with the decompression of the magnetic trap containing the atoms for the mode-matching between the magnetic trap and the ODT. Then, the atoms are transferred from the nearly spherical magnetic trap into the ODT adiabatically. The ODT typically contains $2 \sim 4 \times 10^6$ atoms. The decompression and loading processes take 2 s and 0.5 s respectively.
- Transport into the science chamber (~ 2 s): To transport the condensate trapped in the optical dipole trap into the science chamber, the focal spot of the laser beam is spatially moved [74]. For more detailed information for the design of the transportation system, I refer to the Ph.D. thesis of the former member of the Ketterle/Pritchard group [37].
- Bose-Einstein condensates in the science chamber : Once the condensate is located in the science chamber, we initialized the condensate for a designed experiment in the ODT. Additional cooling of the condensate in this stage causes loss in the atom number. Finally, the atom number of the condensate is typically $1 \sim 2 \times 10^6$ in the science chamber.

For more detailed description of $F=1$ BEC production, I refer to previous theses [89, 147].

¹A $F=2$ condensate consists of atoms in the hyperfine state of $|F = 2, m_F = 2\rangle$.

2.2.1 Magnetic Microtraps on an Atom Chip in the Science Chamber

Atom optics on an atom chip The development of atom chips [60, 45] has led to unprecedented control of a Bose-Einstein condensate with sub-micron precision. In contrast to a conventional magnetic or optical trapping potential, the chip wires on an atom chip are very close to the atoms (e.g. $10 \sim 1000\mu m$ from the chip surface) providing much tighter and complex traps. Encouraged by this, an atom chip has evolved into a platform integrated with atom-optics elements. Following the experimental demonstration of magnetic microtraps and beam splitters with thermal atoms, atom-optics elements using Bose-Einstein condensates have been successfully integrated with an atom chip. For example, an atom Michelson interferometer [196], coherent dynamic splitting [174, 101], phase read-out through in-trap recombination [100], and diffraction from magnetic lattices [71] were experimentally demonstrated.

In parallel to these efforts, an atom chip has been also used to study quantum coherence in a double-well system [101], the non-equilibrium properties and phase fluctuations in one-dimensional Bose gases [83, 99, 85], and vortex dynamics in a condensate [112, 178]. More recently, atom chip technology has been combined with high finesse optical resonators [161].

Atom chip in BEC III Trapping neutral atoms in a magnetic potential is a well-known technique, but it usually needs several coils generating magnetic fields. In a conventional experiment, changing magnetic trap geometry requires to redesign the coils, which sometimes makes it difficult to study various system with a Bose condensate. Combining the idea of the science chamber with an atom chip, we have routinely redesigned the magnetic microtraps generated by wires on an atom chip². This has allowed for the studies of double-well atom interferometry [177, 166, 101], the quantum reflection of the atoms from a solid surface [146, 145], vortex in a Bose condensate [112, 178], integrated atom optics on an atom chip [179, 100, 101], and phase fluctuations in an elongated condensate [99]. The atom chip setup installed to the science chamber in BEC III³ is shown in figure 2-1.

²Typically, a newly designed atom chip is installed in the place of the old one every 6 - 12 months.

³This is the 5th generation atom chip in BEC III built in 2005. The previous chip designs can be found in Ref. [89].

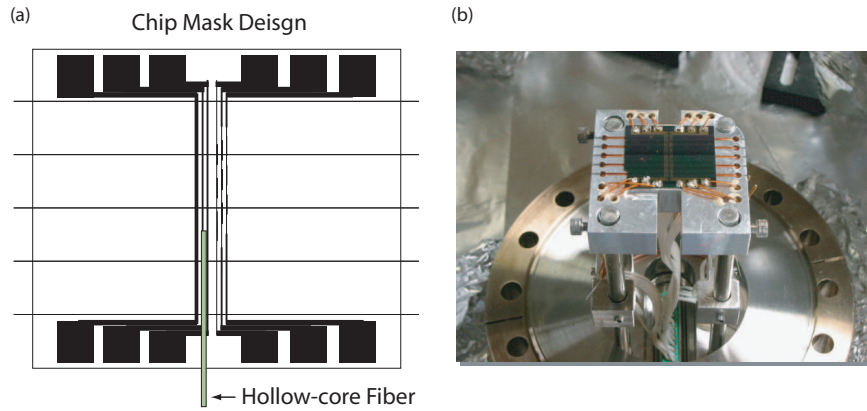


Figure 2-1: Microfabricated atom chip mask and the atom chip mounted on the holder. (a) The mask design for lithography technique is shown. The black lines describe the pattern of current-carrying wires on the substrate. The width of the wire is $100 \sim 200 \mu m$. The green line describes a hollow-core fiber mounted on separate supporting material. The conducting wires are established on the substrate through evaporation or electroplating deposition after lithography, subsequently followed by final chemical process. More details can be found in Ref. [120, 31] (b) An atom chip setup consisting of an atom chip, aluminium mounting structure ($2'' \times 2'' \times 0.5''$), and electric connections, is shown. In contrast to previous chip designs [89], electric wires are soldered directly onto the conducting wires on an atom chip. In order to prevent solder from melting during the baking stage, silver solder with a high melting point was used (purchased from “Amtech solder products, Inc.”). All chip-based experiments in this thesis have been performed with the atom chip shown here.

2.3 Apparatus for Producing a Degenerate gas of ^{23}Na and ^6Li Atoms

In 2007, our apparatus was upgraded to produce a degenerate Bose-Fermi mixture. Based on the successful experiences by other labs of the Ketterle group at MIT (BEC I and II), we naturally chose ^6Li atoms as fermions. In our lab, a degenerate Fermi gas was firstly produced in October 2007. When I was preparing for this thesis, major efforts in BEC III had been directed toward two projects including (1) the study of itinerant ferromagnetism in a Fermi gas and (2) the production of heteronuclear ground-state molecules consisting of ^{23}Na and ^6Li atoms. Both experiments have been performed in the main chamber, but the idea of the *science chamber* (i.e. the two-chamber system) is still attractive and we are planning to transport ^{23}Na and/or ^6Li atoms into the science chamber for the future experiments.

2.3.1 Producing a Degenerate ^6Li Fermi Gas

Cooling fermions appears to be standard now. Especially, three different machines (BEC I, II, and III) at MIT have a degenerate Fermi gas with a Bose-Einstein condensate as a coolant. In this section, a series of different techniques, implemented in BEC III, for the reliable production of a degenerate Fermi gas will be summarized. For more detailed descriptions of the procedure, I refer to the previous Ph.d. thesis of former members of the Ketterle group [77, 183, 213].

New features of the dual-species apparatus in BEC III

Dual-species oven The dual-species oven in BEC III adopted the same oven design implemented in BEC I and BEC II [183] as described in Figure 2-2. The only difference is an additional 45° elbow between the oven nozzle and the half-nipple lithium cup to prevent lithium and sodium from spilling-over. This is necessary because the Zeeman slower has an angle (about 45°) relative to the plane perpendicular to gravity. Except for the half-nipples for sodium and lithium, all parts including mixing/oven nozzle and mixing chamber is constantly kept at a temperature of 450°C . The typical operation temperature of the half-nipple cup is 370°C and 320°C for lithium and sodium respectively. Due to the small vapor pressure of lithium, the lithium source lasts more than a few years with only 25 g. For sodium, however, the operation lifetime with 25 g sodium is rather short, less than 1000 hours. The single-species oven with sodium allowed for ~ 2000 hours in BEC III.

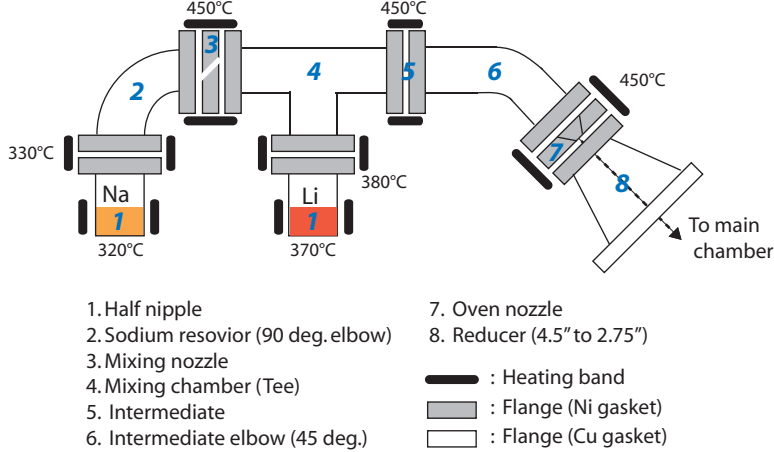


Figure 2-2: A schematic of the dual-species oven. The dual-species oven is built from 2.75 inch ConFlat fittings, made from 316SS. Customized nickel gaskets are used to seal the flanges because normal copper gaskets are likely to bond to the knife edge at the operating temperature of 450°C. The nickel gasket allows us to disassemble the oven and reuse the flange. For more technical details, please see Ref. [183].

Dual-species magneto-optical trap (MOT) To implement a new Li MOT in the main chamber, each sodium beam in the MOT optics was combined with a new lithium beam delivered through PM optical fibers⁴. To this end, one mirror in each path of sodium MOT light was replaced by a dichroic beam splitter, which are transparent for the wavelength of 589 nm and reflective for 671 nm. After lithium and sodium lights are overlapped, all the half and quarter waveplates are replaced by zeroth-order waveplates designed for the wavelength of 633 nm. This makes it possible to manipulate the polarization for both wavelengths identically. The wrong polarization effect due to non-ideal wavelength is typically less than a few percent [77]. In contrast to the dark-spot MOT for sodium, the lithium MOT is bright; each MOT beam for lithium contains both MOT and repumping lights. The typical dual-species MOT is shown in figure 2-3.

New skimmer on the cold plate An old skimmer on the cold plate was built for the single species oven (with sodium). After replacing the old single-species oven by a new dual-species one, the unexpected deposition of sodium on the skimmer led to the shorter lifetime (less than 500 hours) of the sodium in the oven. To avoid the deposition, we decided to redesign a skimmer as described in appendix B. At the

⁴PM means “polarization-maintaining”

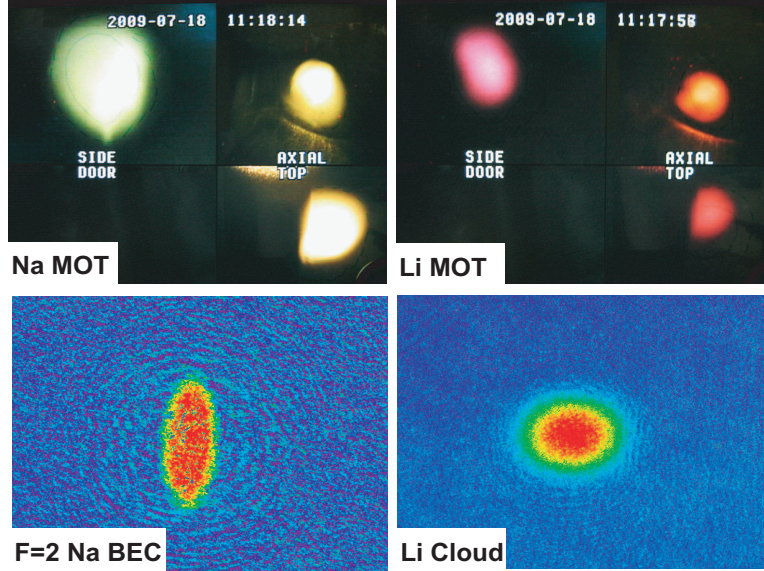


Figure 2-3: Dual-species magneto-optical traps (MOT) are shown for ^{23}Na and ^6Li respectively. A CCD camera with color filters monitors the dual-species MOT from three different angles. Typical absorption images of the ^{23}Na and the ^6Li cloud released from the magnetic trap are shown with the time-of-flight of 45 ms and 6 ms respectively.

moment when I wrote this thesis, a similar deposition of sodium on the new skimmer was observed after ~ 800 hours running and the problem is still being assessed.

Sympathetic cooling with a $F=2$ sodium Bose-Einstein condensate The rule of thumb in sympathetic cooling in a magnetic trap is that both ^{23}Na and ^6Li must lie in the low-field seeking state. This allows us to simply add fermionic ^6Li atoms in the process of evaporation cooling for ^{23}Na . To this end, two possible combination of hyperfine state are:

- (a) $|F = 1, m_F = -1\rangle_{\text{Na}} + |F = 1/2, m_F = -1/2\rangle_{\text{Li}}$
- (b) $|F = 2, m_F = 2\rangle_{\text{Na}} + |F = 3/2, m_F = 3/2\rangle_{\text{Li}}$

The other combinations suffer from spin-exchange collisions causing unwanted heating. In BEC III, we decided to choose the combination of (b) based on the experiences of BEC I and II. In this case (stretched state), ^6Li atoms in the state of $|F = 3/2, m_F = 3/2\rangle$ can be stably trapped in a magnetic potential allowing efficient sympathetic cooling of hot thermal ^6Li atoms ⁵.

⁵Here, ^6Li atoms in the state of $|F = 1/2, m_F = -1/2\rangle$ are low-field seeking only below 28 G.

First, a spin-polarized sodium cloud in the state of $|F = 2, m_F = 2\rangle$ (F=2 condensate hereafter) is achieved by optical pumping from the $F = 1$ manifold to the excited manifold (F pumping). The hyperfine pumping light with σ^+ polarization illuminates the atom cloud for 2 ms right after switching off the MOT light. For ^6Li , two pumping beams resonant with the $F=1/2$ and $F=3/2$ states are used for 400 μs to provide both F (hyperfine) and m_F (Zeeman) pumping. During the pumping stage, the polarization gradient cooling was omitted to improve the efficiency of lithium loading into the magnetic trap.

Before the Ioffe-Pritchard trap is turned on, the ^{23}Na atoms in the other hyperfine states are optically pumped into the stretched state. For the purification, the ^{23}Na atoms are illuminated by F pumping light for 2.5 s in the presence of a 1.77 MHz microwave sweep at the bias field of 80 G. Subsequently, the second purification is done only with a microwave wave sweep for 0.5 s. Finally, $\sim 30\%$ ^{23}Na atoms in the MOT are transferred into the magnetic trap. For ^6Li atoms, without the purification stage, the transfer efficiency from the MOT into the $|F = 3/2, m_F = 3/2\rangle$ is about $\sim 40\%$.

Preparation of a repulsive two-component Fermi gas of ^6Li atoms After sympathetic cooling, we routinely produce a spin-polarized Fermi gas of $\sim 5 \times 10^6$ atoms in the stretched state of $|F = 3/2, m_F = 3/2\rangle$ (hereafter $|6\rangle$ state, also see appendix A) in a magnetic trap. The typical temperature of the ^6Li cloud is $T \sim 0.5T_F$ where T_F is the Fermi temperature. Then ^6Li cloud is transferred into an optical dipole trap, followed by an RF transfer into the lowest hyperfine state $|F = 1/2, m_F = 1/2\rangle$. Finally, a Landau-Zener RF sweep is applied in order to prepare an equal mixture of $|F = 1/2, m_F = 1/2\rangle$ ($|1\rangle$ state) and $|F = -1/2, m_F = 1/2\rangle$ ($|2\rangle$ state) spin states. Additional evaporation cooling in the mixture of $|1\rangle$ and $|2\rangle$ atoms has been implemented at 300 G after decoherence for 1 s.

2.3.2 Li Laser System

The new ^6Li laser system consists of a master laser and four slave lasers. The master laser is a commercial grating stabilized diode laser purchased from TOPTICA (model: TOPTICA DL100). The master laser gives us an output of ~ 30 mW, and the linewidth is reduced to a typical value of 1 MHz (measured in a millisecond) which is reasonably smaller than the lithium natural linewidth of $\Gamma = (2\pi) \times 6$ MHz. The master laser locked to the ^6Li D_2 -resonance is amplified by injection locking of four slave lasers. The slave laser diode placed in the TEC cooled mount (Thorlabs: model

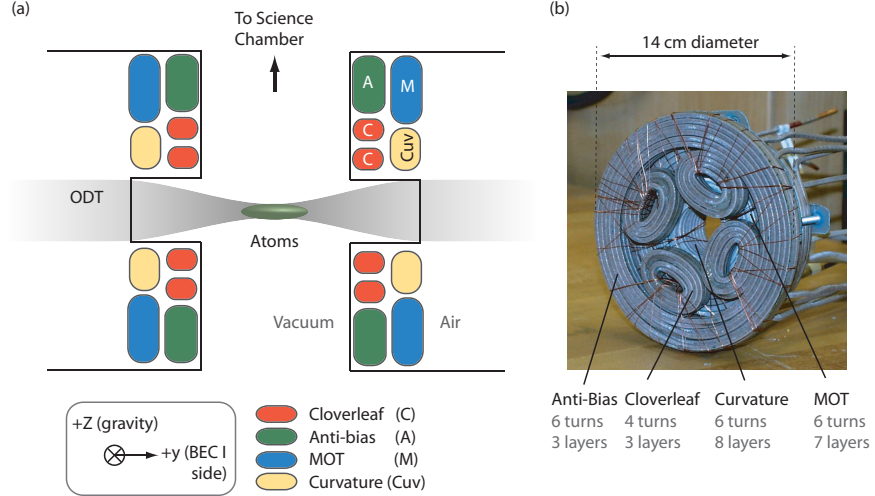


Figure 2-4: A schematic of magnetic coils in the main chamber is shown. (a) Geometry of the magnetic coils is described. The coils are implemented into the re-entrant bucket port. A photo of one of coil sets is shown in (b). A large magnetic field for the Feshbach resonance is produced by the current carried through the anti-bias coil.

TCLDM9) produces an output of ~ 150 mW at desired wavelength of 670.977 nm while retaining the narrow spectral characteristics of the master laser. The slave diode⁶ operates at a temperature of $\sim 70^\circ\text{C}$ and at a current of 370~390 mA depending on injection locking.

Power supply unit	Connected coils	Magnetic field direction
curvature	curvature and antibias	(+)
bias	only curvature	(+)
y-comp	compensation	(+)
y-trap bias	compensation	(-)
spin-flip	compensation	(+)
Feshbach	antibias	(-)

Table 2.1: The direction of the magnetic bias field is described with the information of the coil and the power supply generating the field. The (+)-direction points in the same direction as +y in figure 2-4

2.3.3 Tools for Experiments

(1) Generating a large bias field for the Feshbach resonance

One of the main tools in our dual-species apparatus is a Feshbach resonance with which one can tune the atom-atom interaction strength by changing a bias magnetic field. A Feshbach resonance occurs when the scattering state in the open channel approaches the bound molecular state in the closed channel energetically [108] leading to strong mixing between two channels. By changing a magnetic field, the energy difference associated with difference in magnetic moments can be controlled, which is called a “magnetically tuned Feshbach resonance”.

A simple form describing a magnetically tuned Feshbach resonance was introduced in Ref. [132] as follows:

$$a(B) = a_{bg} \left(1 - \frac{\Delta}{B - B_0} \right) \quad (2.1)$$

where B is a magnetic field, a denotes the s-wave scattering length, a_{bg} is the background scattering length which is associated with the open channel potential, Δ is the resonant width, and B_0 is the resonant magnetic field where a diverges. In BEC III, we are interested in two homonuclear and heteronuclear s-wave resonances: 834 G for ${}^6\text{Li}$ atoms ⁷ and 795.6 G for ${}^6\text{Li}$ - ${}^{23}\text{Na}$ atoms.

A large bias field for the Feshbach field is generated by the currents carried through the antibias coil (see figure 2-4 and table 2.1). The Feshbach field can be ramped up to 1500 G with the maximum current of 500 A. The geometry of magnetic coils in the main chamber is described in figure 2-4, and the field direction generated from the coils are summarized in table 2.1. A stabilization scheme for Feshbach fields is illustrated in figure 2-5.

(2) Optical dipole trap

In ${}^6\text{Li}$ experiments, Li atoms in states $|1\rangle$ and $|2\rangle$ are both high-field seeking at high magnetic field where the two states are strongly interacting with each other. Unfortunately, it was shown by Wing [200] that the magnitude of static electric or magnetic field in free space cannot have local maxima; therefore, they cannot trap strong-field seeking atoms. Thus, the strongly interacting mixture can be stored only in an optical dipole trap (ODT) as described in figure 2-4. The ODT is produced by a commercial fiber-amplified Nd:YAG laser from IPG (model:YLR-30-1064-LP-SF).

⁶The slave diode (model:ML101J27, Mitsubishi Laser Diodes) has a typical lifetime of a few months,

⁷This Feshbach resonance occurs between $|1\rangle$ and $|2\rangle$ state.

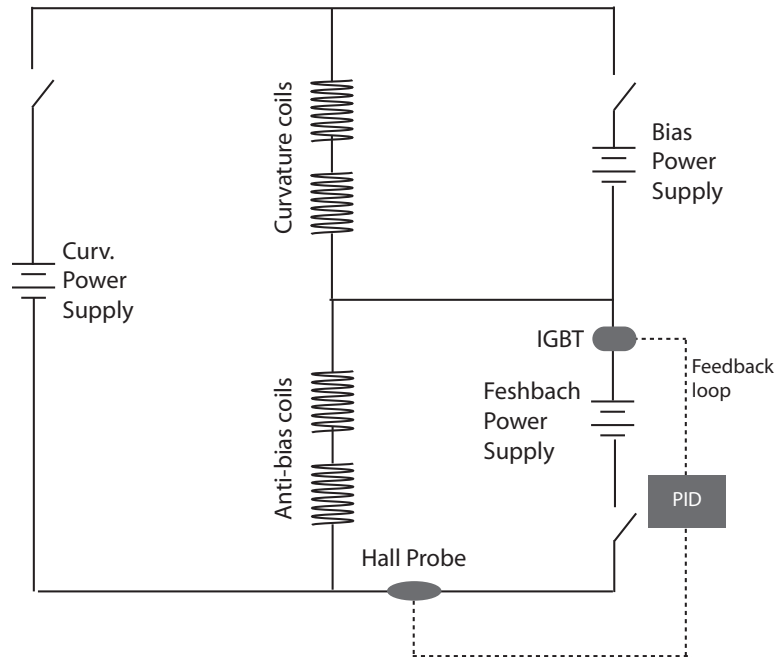


Figure 2-5: Circuit diagram for producing a large bias magnetic field (called the Feshbach field). A Feshbach power supply is connected to anti-bias coils to generate a large bias field. The Feshbach power supply run in voltage control mode providing an arbitrary current depending on the resistance. The current is PID-controlled via an IGBT operating in the linear resistance regime. The direction of the Feshbach field is opposite to one of curvature/bias as described in table 2.1. In this diagram, the “de-bounce” circuit is omitted.

The laser light has single frequency at 1064nm and fixed polarization out of the laser. The maximum output power of 30 W will be sufficient for future experiments in both the main and science chamber.

(3) Science chamber designed for optical lattice experiments

Until summer 2007, the science chamber had been replaced several times when the experiments required special features as described in other theses [89, 147]. For example, it was required to have a rather spacious science chamber with 6" OD windows in order to facilitate various atom optics experiment including atom interferometry and quantum reflection. The spacious science chamber allowed us to assemble two different experiments at the same time without any conflict. Two experiments - coherent splitting of the condensate and trapping of cold atoms in a hollow-core fiber covered in this thesis - were performed in the same setup built in the science chamber with 6" OD windows.

Despite flexibility of the spacious science chamber, it was difficult to image atoms with high resolution since the closest lens for imaging cannot be close enough to the atoms due to the 6" OD window of the chamber. This would be a potential problem in future experiments which may require single-site imaging in the optical lattice. Markus Greiner group at Harvard solved this problem by preparing an atomic cloud right below the window surface using a combination of evanescent wave, standing wave, and magnetic potential [64, 16].

To solve this imaging problem in BEC III, we adopted an idea similar to the one used in the main chamber as described in figure. 2-6 and appendix B. We installed a re-entrant "bucket" ports so that the closest lens of the imaging systems can be close enough to the atoms. The distance between the first lens and the center of the chamber (or the position of atoms) is about 1.5" which will allow us to improve imaging resolution. The bucket ports were built by UKAEA who welded the 1.33" OD viewport window onto the bucket ports supplied to them by Sharon vacuum. The viewport window was polished to $\lambda/4$. A detailed description of the science chamber is available in appendix B.

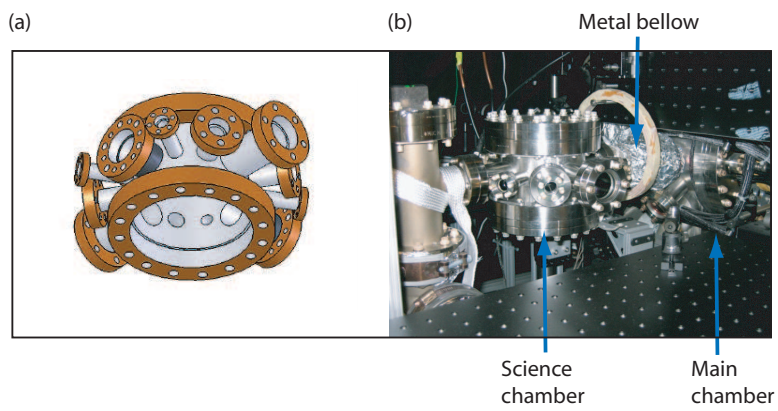


Figure 2-6: (a) The science chamber is newly designed solely for flexible optical access. The chamber is connected to the main chamber through a metal bellow as shown in (b). The bellow mechanically isolates the main chamber from the science chamber.

Chapter 3

Ferromagnetism in a Fermi Gas

Can a gas of spin-up and spin-down fermions become ferromagnetic due to repulsive interactions?

This question exhibits a long-standing problem which has not found a definitive theoretical answer. In the following two chapters, we shall discuss the theoretical and experimental efforts to find a rigorous answer in the system of a two-component Fermi gas. To begin with, we review some basic aspect of quantum magnetism in a Fermi gas.

3.1 Quantum Magnetism

3.1.1 What is magnetism?

Magnetism is a macroscopic phenomenon with its origin deeply rooted in quantum mechanics. In the early 1910's [27], Bohr pointed out that a collection of classical electrons in a box can never be sensitive to the external magnetic field; therefore any solid consisting of electrons should be non-magnetic in the classical sense. This is clearly illustrated by calculating the classical partition function Z of N electrons:

$$Z \propto \int d^{3N}x d^{3N}p \exp\left(-\frac{\beta(\vec{p} - \vec{A})^2}{2m} - \beta V(\vec{x})\right) \quad (3.1)$$

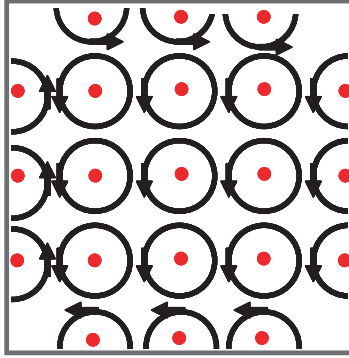


Figure 3-1: Classical electron gas in a box with external magnetic field is shown. The red dot describes the classical electron and the black circle denotes the electron's orbit. In the presence of magnetic field, the electrons move in a circle generating magnetic moments. The total magnetic moment of the electron gas in the box, however, is always zero.

As the vector potential $\vec{A} = \vec{A}(x)$ is independent of \vec{p} classically ¹, the partition function splits into two parts:

$$Z_{classical} \propto \int d^{3N}x \exp(-\beta V(\vec{x})) \underbrace{\int d^{3N}p \exp\left(-\frac{\beta(\vec{p} - \vec{A})^2}{2m}\right)}_{constant} \quad (3.2)$$

The second integral containing \vec{A} is constant leading to a conclusion that the partition function $Z_{classical}$ is insensitive to the vector potential A : $Z(\vec{A}) \equiv Z(\vec{A} = 0)$. Therefore, classical description is insufficient to explain the magnetic properties in a solid. A collection of classical electrons in a box is a good example to emphasize this as described in figure 3-1.

3.1.2 Origin of Ferromagnetism: Exchange interactions

The phenomenon of “spontaneous magnetization” or ferromagnetism, is the consequence of magnetic interactions between the discrete sources of magnetic moment. Now, we have a question: “Where do the magnetic interactions come from?”. Our first naive expectation is that the dominant magnetic interactions arise from dipole-

¹In quantum mechanics, the vector potential is not independent of \vec{p} due to $[x, p] \neq 0$.

dipole interactions between discrete magnetic moments. These interactions between dipole moments, however, are too weak to induce the magnetic structure. The magnitude of dipole-dipole interaction energy, U_{dipole} can be estimated by considering an atomic magnetic dipole moments m_1 and m_2 separated by r . For a typical solid,

$$U = \frac{1}{r^3}[m_1 \cdot m_2 - 3(m_1 \cdot r)(m_2 \cdot r)] \sim \frac{(g\mu_B)^2}{r^3} \sim 10^{-4} eV \quad (3.3)$$

The value of 10^{-4} eV is equivalent to 1K in thermal energy. Therefore the dipolar interaction is typically too weak to induce spontaneously magnetization or ferromagnetism in a solid whose ferromagnetic transition temperature is larger than 10K, even 1000K for iron.

What is the origin of spontaneous magnetization in a solid? Interestingly, magnetic fields are irrelevant to magnetic ordering of adjacent magnetic moments. Instead, Coulomb repulsion between electrons plays the important role. This seems to be unreasonable because the Coulomb interactions are spin-independent (or non-magnetic interactions). The problem is, however, reconciled by the Pauli exclusion principle imposing a strict correlation between (spin-independent) Coulomb interactions and the total spin of the system. The emergence of magnetic interactions between electrons from Coulomb repulsion becomes more clear in the calculations of the energy of a two-electron system ². Since the total wavefunction of the two-electron system must be antisymmetric under particle exchanges, a spin singlet and a spin triplet states have different symmetries of the spatial wavefunction. For example, a spin triplet state, ϕ_T , has a antisymmetric spatial wavefunction and the energy of the triplet state, ε_T , can be calculated by $\varepsilon_T = \langle \phi_T | \hat{H} | \phi_T \rangle$ where \hat{H} is the spin-independent Hamiltonian of the system including Coulomb interactions. The Hamiltonian acts only on spatial degree of freedom. Similarly, a spin singlet energy becomes $\varepsilon_S = \langle \phi_S | \hat{H} | \phi_S \rangle$. Now, the difference between triplet and singlet energies determines the tendency toward ferromagnetism.

$$\varepsilon_T - \varepsilon_S = -J \quad (3.4)$$

When J is positive, the ground state of the two-electron system becomes ferromagnetic. Here, we call J the *exchange energy* leading to magnetism from electrostatic Coulomb repulsion. The exchange interactions are nothing but the interplay of electrostatic Coulomb interactions and the Pauli exclusion principle. The exchange energy denotes

²This calculation was done by Heitler and London in 1927. For more details, I refer to Ref. [49, 134, 109, 198]

the contribution to the Coulomb interaction energy of electrons associated with the use of symmetric and antisymmetric wavefunctions.

Heisenberg model So far, we have seen that the Pauli exclusion principle correlates the symmetric and the antisymmetric spatial wavefunction with the spin wavefunctions leading to the difference of Coulomb repulsion energy for the spin singlet and the triplet states. Now, the idea of two-electron system gives us construction blocks for many-electron system. The exchange interaction can be expressed as an effective spin Hamiltonian acting only on the spin degree of freedom. Since the spin-spin interaction depends only the relative direction between two spins, the effective spin Hamiltonian, \hat{H}_{eff} , which is identical to the original Hamiltonian acting only on the spatial degree of freedom becomes

$$\hat{H}_{eff} = -J\hat{S}_1 \cdot \hat{S}_2 \quad (3.5)$$

where J is exchange energy. For a many-electron system in a lattice, the effective Hamiltonian takes the form

$$\hat{H}_{eff} = - \sum_{n,n'} J_{n,n'} \hat{S}_n \cdot \hat{S}_{n'} \quad (3.6)$$

where n denotes the n^{th} lattice site. This model, so-called *Heisenberg model*, is the starting point for further investigation of ferromagnetism and antiferromagnetism in insulators.

3.1.3 Two Paradigms of Magnetism

In condensed matter physics, there are two paradigms for magnetism: localized spins interacting via tunnelling, and delocalized spins interacting via an exchange energy. For localized spins, the magnetic phenomenon arises from the interplay of localized electrons. In this case, the exchange interactions we have just seen above come from either the *direct* Coulomb interaction among electrons from different ions or *indirect* coupling between magnetic ions mediated by nonmagnetic ions. The latter type of magnetic interaction is called *superexchange*. Major open questions for localized spins include the interplay of magnetism with d-wave superfluidity and frustrated spin materials [115].

The delocalized spins gives rise to itinerant ferromagnetism which is responsible for the properties of transition metals like cobalt, iron and nickel. Among the conduction

electrons in metals, the electrons are no longer localized but rather itinerant. The exchange interaction among the free electrons is called *itinerant exchange*, and this is the main ingredient for itinerant ferromagnetism in a free electron gas as we will see later.

Note that both kinds of magnetism involve strong correlations and/or strong interactions and are not yet completely understood. For example, phase transition theories are still qualitative for itinerant ferromagnetism [24, 187, 124, 32, 194, 190, 188]. The experimental and theoretical works for itinerant ferromagnetism shall be discussed in this chapter and the next chapter 4.

3.2 Itinerant Ferromagnetism

3.2.1 Long-standing Problem in Condensed-matter Physics

Magnetism in a free electron gas

Itinerant ferromagnetism in a free electron gas has been a long-standing problem in condensed-matter physics. Although the theory of magnetism in a free electron gas is inadequate to describe magnetism in a real metal (due to a over-simplified model), it is still of importance because of several reasons: (1) the model for itinerant ferromagnetism does not require band structure and spin-dependent interactions, (2) it represents itinerant aspect of exchange interactions, and (3) it may demonstrate the ferromagnetic behavior in transition metals ³.

The origin of ferromagnetism in real material has been one of the mystery for a long time [49]. Heisenberg first suggested that ferromagnetism is a quantum many-body effect solely arising from the interplay between the spin-independent Coulomb repulsion and the Pauli exclusion principle, generating “*exchange interaction*” [201]. In the early 1930’s, Stoner proposed that the magnetism may coexist with one-electron band theory [187]. He pointed out that exchange interactions between overlapping electrons favor ferromagnetism in an itinerant electron gas. A few years earlier, Bloch [24] first pointed out in the Hartree-Fock approximation that a free electron gas with long-range Coulomb interactions may become ferromagnetic when $r_s > 4$ where $r_s \propto 1/n^{(1/3)}$ is the Wigner-Seitz radius, depending only on the density(n) of the electron gas. However, it was pointed out that Bloch’s calculation may ignore the strong effect of

³Note that it is widely believed that the ferromagnetism in some transition metals arises from the interplay between itinerant ferromagnetism, orbital degeneracy associated with band structure, and Hund’s rule [49, 134, 109, 198]

	Long-range Coulomb interaction	Short-range contact interaction
Kinetic energy (E_{kin})	$\propto n^{2/3}$	$\propto n^{2/3}$
Interaction energy (E_{int})	$\propto n^{1/3}$	$\propto n$

Table 3.1: Density dependence in Long-range Coulomb interactions and short-range contact interactions is shown. For long-range Coulomb interactions, itinerant ferromagnetism is expected to occur at low density n as $E_{int}/E_{kin} > 1$ only when $n \sim 0$. The density dependence for short-range interactions is opposite; itinerant ferromagnetism is expected to occur at high density $n \gg 1$.

correlations which reduce the gain in interaction energy in a ferromagnetic state [199]. Recently, it was shown by quantum Monte Carlo (QMC) calculations [209, 141] that the ferromagnetic phase transition in a three-dimensional electron gas at zero temperature occurs only at the very low density of $r_s \sim 50$, suggesting that the effect of correlations should be taken into account for calculating the critical density.

A free electron model has often been improved by including the screening effect between electrons [49, 134, 109, 198]. For more simplicity, the screened Coulomb interactions are sometimes approximated by short-range contact interactions (or hard-sphere interactions). For such interactions, a rigorous calculation of the true ground state does not exist yet. Variational approximations [203], however, support the Hartree-Fock results. In contrast to bare Coulomb interactions, itinerant ferromagnetism may occur at high atomic density of the electron gas with short-range contact interactions (see table 3.2.1).

In parallel to these efforts, ferromagnetism in Hubbard models [98] has been actively studied [127, 136, 125, 189]. The Hubbard model allows us to describe the quantum correlations in a proper way, leading to rigorous calculations of the true ground state. For example, Elliott H. Lieb and F. Y. Wu showed that the true ground state in the one-dimensional lattice system should have antiferromagnetic configurations [127]. Some other mathematical proofs have been achieved in the Hubbard-type model under certain conditions. For more discussions, please see section 3.2.3. But, the question of “whether spin-independent Coulomb interaction can induce ferromagnetism in an itinerant electron system” has not yet been rigorously answered for the free gas.

3.2.2 Stoner Model in a Free Electron Gas with Short-range Interactions

Itinerant Ferromagnetism often occurs in a “metallic magnetic material”. Here, the metallic nature captures the itinerancy of electrons in a conduction band. In this section, we will discuss the Stoner model explaining the ferromagnetic instability in a free electron gas. The metallic state is characterized by the kinetic energy of conduction electrons, imposed by the Pauli principle.

Short-range contact interactions

The Stoner model can be derived by estimating total kinetic and interaction energy of the electron gas. Since electrons are itinerant, each single electron does not feel bare Coulomb repulsion produced by other electron. Instead, the metallic state profoundly modifies the Coulomb interactions between electrons, leading to a rapid decrease in the Coulomb repulsion beyond some characteristic distance, the Thomas-Fermi length λ_{TF} . The phenomenon, called *screening*, introduces a simple estimate of the Coulomb interaction. The bare Coulomb potential $U(r) = -\frac{e^2}{4\pi\epsilon_0}r$ between electrons is screened by other electrons, and becomes exponentially weaker beyond λ_{TF} ,

$$U_{scr}(r) = -\frac{e^2}{4\pi\epsilon_0} \frac{\exp(-q_{TF}r)}{r} \quad (3.7)$$

where $\lambda_{TF} = 2\pi/q_{TF}$. In typical transition metals such as iron, cobalt, and nickel, Thomas-Fermi length λ_{TF} is less than the mean distance between electrons; therefore, $q_{TF} \gg q$ for short-range of the potential. In the form of the screened Coulomb potential in momentum space

$$U_{scr}(q) = \frac{e^2}{\epsilon_0} \frac{1}{q^2 + q_{TF}^2} \quad (3.8)$$

, one can simply approximate the screened Coulomb potential $U_{scr}(q)$ to a constant neglecting the term q^2 . Then, the screened Coulomb potential reduces to a contact interaction

$$U(r) = I\delta(r). \quad (3.9)$$

To evaluate the response of the electron system in the presence of a magnetic field, we now calculate the magnetic susceptibility χ . The behavior of the magnetic susceptibility clearly illustrates the role of short-range repulsive interactions in the ferromagnetic phase transition.

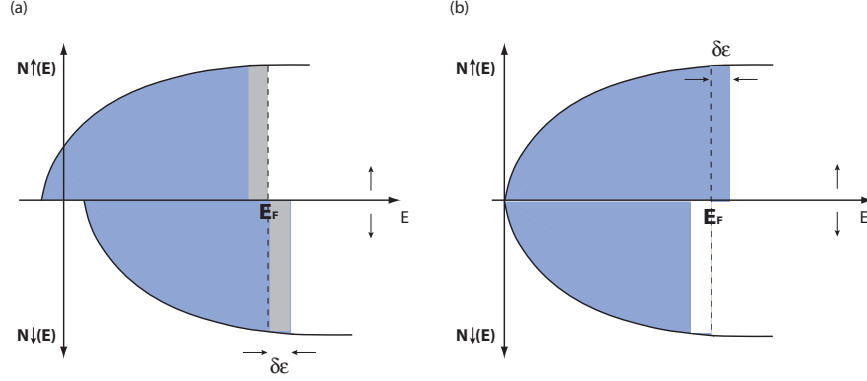


Figure 3-2: Density of states of a metal. (a) In the presence of a magnetic field, the density of states for spin-up and spin-down states shift in the opposite directions. This leads to a paramagnetic behavior. (b) With introduction of exchange interactions, the system of electrons are unstable toward a spontaneously magnetized state.

(1) Pauli paramagnetism (without Coulomb repulsion)

In the presence of the external magnetic field B , the electrons in the slice of energy thickness $\delta\varepsilon = \mu_B B$ are transferred from one spin-state to other [see figure 3-2 (a)]. The net magnetic moment in equilibrium becomes

$$M = (N(\varepsilon_F)\mu_B B \times 2\mu_B) = 2(\mu_B)^2 N(\varepsilon_F) B \quad (3.10)$$

where $N(\varepsilon_F)$ is a density of state (DOS) at the energy of ε_F . Therefore, *Pauli spin susceptibility* at $T = 0$ ⁴ becomes

$$\chi_{Pauli} = 2\mu_0(\mu_B)^2 N(\varepsilon_F) \quad (3.11)$$

clearly showing that there is no instability.

(2) Stoner model (with Coulomb repulsion)

Introducing Coulomb repulsion, we can examine the instability of the paramagnetic state towards the ferromagnetic state. Here, we assume that Coulomb interactions reduce to short-range contact interactions as describe in the relation 3.9. Thus the interaction energy can be written as $E_{int} = In_{\uparrow}n_{\downarrow}$, where n_{\uparrow} (n_{\downarrow}) is the density of electrons with the spin-up (spin-down) state and I denotes the reduction in interaction energy caused by reversing a spin. When electrons in a slice of energy thickness $\delta\varepsilon$

⁴The finite temperature effects change the density of state and displace the Fermi level. This gives: $\chi(T) = \chi(T = 0)(1 + O(T^2))$

are transferred as in figure 3-2 (b), the kinetic energy of the electron gas increases:

$$\Delta E_{kin} = N(\varepsilon_F)(\delta\varepsilon)^2 \quad (3.12)$$

The interaction energy, however, decreases:

$$\Delta E_{int} = I\left[\frac{N}{2} + N(\varepsilon_F)\delta\varepsilon\right]\left[\frac{N}{2} - N(\varepsilon_F)\delta\varepsilon\right] - I\left(\frac{N}{2}\right)^2 = -IN^2(\varepsilon_F)(\delta\varepsilon)^2 \quad (3.13)$$

Therefore, total energy changes with introduction of the perturbation,

$$\Delta E_{total} = N(\varepsilon_F)(\delta\varepsilon)^2(1 - IN(\varepsilon_F)) \quad (3.14)$$

This implies that the paramagnetic state is energetically stable only when $IN(\varepsilon_F) < 1$. When interaction strength I is strong enough satisfying the criterion of $IN(\varepsilon_F) > 1$, the electron system undergoes a ferromagnetic phase transition. The spin susceptibility becomes:

$$\chi_{Stoner} = \frac{\chi_{Pauli}}{1 - IN(\varepsilon_F)}. \quad (3.15)$$

This corresponds to the many-body correction to the Pauli susceptibility leading to the Stoner's criterion,

$$IN(\varepsilon_F) > 1 \quad (3.16)$$

where itinerant ferromagnetism occurs in a free electron gas. This Stoner's criterion involves microscopic aspects of itinerant exchange, through the term I , and the number of electrons, through the $N(\varepsilon_F)$. Stoner's model is universal in that it depends only on the two parameters. Note that two major ingredients for itinerant ferromagnetism are the Pauli principle and the Coulomb repulsion.

3.2.3 Ferromagnetism in Hubbard Models

The stoner model is generally expected to apply to systems with broad bands or partially filled bands. As the bands become narrower, atom-atom correlation effects become more important. In this case, it is much more convenient to describe the system in the Wannier basis. For this purpose, the Hubbard model [98] was proposed by British physicist, John Hubbard, in the early 1960s to describe narrow band metals in which the repulsive Coulomb interaction between two electrons at the same site is likely to suppress the hopping between adjacent sites ⁵. The model address both

⁵At about the same time, Martin Gutzwiller proposed a very similar model as well.

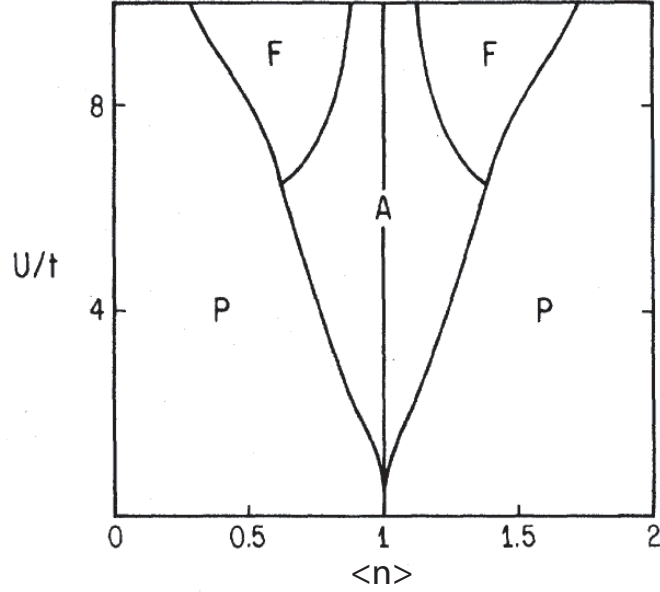


Figure 3-3: Hartree-Fock phase diagram for the two-dimensional Hubbard model. A, F, and P denote the antiferromagnetic, ferromagnetic, and paramagnetic ground state respectively. From Ref. [82]

the electronic quantum correlations and some degree of electron mobility leading to magnetism which are not fully described in the tight binding model or classical Ising model [109]. The Hubbard model has been widely believed to be the basic ingredient in order to explain two major phenomena : quantum magnetism (for example, ferromagnetism and antiferromagnetism) and electrical conductivity (for example, high-Tc superconductivity) in condensed matter.

The model has a simple Hamiltonian,

$$H = -t \sum_{\langle i,j \rangle \sigma} a_{i\sigma}^\dagger a_{j\sigma} + U \sum_i n_{i,\uparrow} n_{i,\downarrow} \quad (3.17)$$

where $a_{i\sigma}$ ($a_{i\sigma}^\dagger$) is an fermionic annihilation (creation) operator of spin σ on the site i and $n = a_{i\sigma}^\dagger a_{i\sigma}$ denotes the occupation number of the Wannier state $\phi(R_i, r)$. The Hamiltonian has two competing terms which are described by the hopping amplitude t between neighboring lattice sites and the repulsive on-site interaction U between atoms with opposite spin. For low filling factor, the Hubbard model reduces to the Stoner model when one uses the Bloch basis $\phi(k, r)$ and $2I$ in place of the Wannier basis and U .

Can the Hubbard model favor particularly ferromagnetism or antiferromagnetism? The answer is “YES in one-dimensional (1D) systems, but NOT always in other cases.”. In spite of the richness in quantum phases, an exact solution only exists in one-dimensional system [127]. Lieb and Wu proved that the ground state in the 1D system must have antiferromagnetic configuration. In the 2D system, an antiferromagnetic ground state is expected for half-filling $\langle n \rangle = 1$ in the Hartree-Fock approximation as described in figure 3-3.

On the other hand, the Hubbard model possesses a ferromagnetic ground state under certain conditions. Nagaoka rigorously proved that the very strong repulsive interactions induce ferromagnetism if the occupation number $\langle n \rangle$ is slightly short of half-filling [136]. Even with a single vacancy, the ferromagnetism occurs when $U \mapsto \infty$. Another rigorous model was discovered by Lieb [125] showing that a dispersionless flatband supports ferromagnetism. Recently, Tasaki has concluded that a ferromagnetic ground state is favored in the Hubbard model when the electron can hop farther than the nearest-neighbor sites [190].

3.2.4 Similar Studies in Normal Liquid ^3He

The seminal discovery of the exotic superfluid phases of ^3He in 1971 [143] stimulated both experimental and theoretical researches on the normal phase of ^3He as well as the superfluid phases [121, 193]. The normal liquid ^3He has served as a model system of strongly interacting fermions. Due to the high density, the interatomic interactions are approximated by short-range contact interactions neglecting an attractive Van der Waals tail.

The properties of liquid ^3He can be described by *Landau Fermi liquid theory* [157] which deals with an interacting Fermi liquid phenomenologically. The theory of Landau assumes that the ground state of an interacting Fermi liquid consists of quasiparticles (or elementary excitations) characterized by an effective mass m^* and an effective interaction parameterized by Landau parameters. Here, quasiparticles obey the same distribution function of a non-interacting Fermi liquid. In this frame work, several physical quantities such as the specific heat, the spin susceptibility, and the compressibility are given as a function of Landau parameters and m^* . For example, the spin susceptibility χ_s becomes,

$$\chi_s = \frac{\frac{m^*}{m}}{1 + F_0^a} \chi^0 \quad (3.18)$$

where χ^0 denotes the spin susceptibility for a noninteracting system and F_0^a is one of the Landau parameters.

Major efforts have been made toward an understanding of the properties of normal ^3He [121, 193]. In particular, the enhancement in the spin susceptibility, χ_s , of normal ^3He has stimulated many theoretical and experimental discussions. In the expression 3.18, F_0^a has a negative value indicating the enhancement of the spin susceptibility due to the ferromagnetic contribution arising from the Pauli exclusion principle. When $F_0^a \mapsto -1$, the diverging spin susceptibility implies a phase transition to a ferromagnetic state. The experimental measurement of χ_s [68], however, shows that the spin susceptibility is enhanced only by $F_0^a \simeq -0.75$ for all pressures ⁶.

The enhancement of the spin susceptibility can be described in the “paramagnon theory” [111, 7]. In this theory, ^3He is considered as “almost ferromagnetic” and its properties are associated with the incipient ferromagnetic phase caused by low-energy spin fluctuations. On the other hand, the same enhancement of the spin susceptibility can be understood as a result of “localization due to strong correlations” [8]. In this picture, ^3He is considered as “almost localized” (and therefore stays in the paramagnetic phase) since the effective mass m^* increases with pressure whereas the Landau parameter F_0^a is almost constant in the experiment.

⁶At a pressure of ~ 34 bars, liquid ^3He solidifies.

3.3 Itinerant Ferromagnetism in Ultracold Atomic Gases

A Fermi gas of ultracold atoms as a model system

An important recent development in cold atom science has been the realization of superfluidity and the BCS-BEC crossover in strongly interacting two-component Fermi gases near a Feshbach resonance [91]. These phenomena occur for attractive interactions for negative scattering length and for bound molecules (corresponding to a positive scattering length for two unpaired atoms). Very little attention has been given to the region for atoms with strongly repulsive interactions. One reason is that this region is an excited branch, which is unstable against near-resonant three-body recombination into weakly-bound molecules [153]. Nevertheless, many theoretical papers have proposed a two-component Fermi gas near a Feshbach resonance as a model system for itinerant ferromagnetism [86, 170, 4, 182, 52, 19, 206, 114] assuming that the decay into molecules can be sufficiently suppressed.

In contrast to the solid state system, the study of itinerant ferromagnetism in a strongly interacting Fermi gas should address the effect of trap geometry and the imposed spin polarization defined by the population imbalance for each spin state as summarized in Table 3.2. For sufficiently large clouds (therefore neglecting surface effects), trapped Fermi atoms can be simply treated as if each atoms are governed by local Fermi energy and interactions imposed by other atoms. This approximation, so-called “local density approximation (LDA)”, allows us to use the result obtained for the homogeneous Fermi gas.

Another feature of the atomic system is the pseudo-spin associated with two different hyperfine states. In an atomic Fermi gas, two lowest energy states are generally selected as pseudo-spin states; therefore spin-spin relaxation collision is prohibited energetically. In this configuration, the two-component Fermi gas is also stable against dipolar relaxation due to the Pauli exclusion principle [91].

The imposed population imbalance for each pseudo-spin state realizes a canonical ensemble with the fixed number of particles whereas solid state systems usually are represented by a grand canonical ensemble with the chemical potential. In the case of balanced Fermi mixture, the net spin polarization is zero which corresponds to zero external magnetic field in solid state systems (see Table 3.2).

One of the attractive feature in the cold atomic system is the unprecedented control of two-body interactions via the Feshbach resonance [38, 108]. There had been

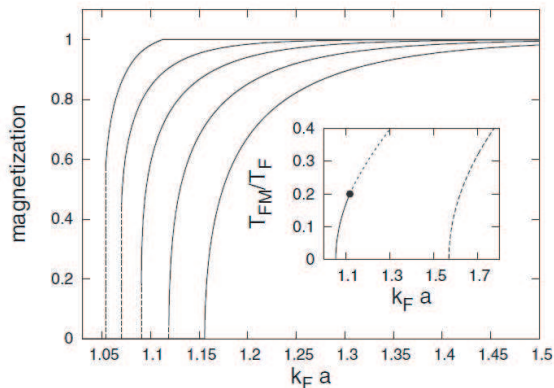


Figure 3-4: Itinerant ferromagnetism in second-order perturbation calculations. Magnetization is calculated as a function of $k_F a$, for various temperatures. From left to right $T/T_F = 0, 0.1, 0.15, 0.2$, and 0.25 . The magnetization undergoes the first-order phase transition at low temperatures (the dashed line in the graph). The critical temperature for the ferromagnetic phase transition is shown as a function of $k_F a$ in the inset. The solid line (the dotted line) denotes first-order transitions (second-order transitions). From Ref. [52]

many theoretical works studying a two-component Fermi gas with repulsive interactions as a model system of itinerant ferromagnetism. The phase separation in a two-component Fermi gas has been studied by Salasnich et al. [170] and Sogo and Yabu [182]; they treated harmonically trapped atoms in the Thomas-Fermi approximation. Duine and McDonald characterized the ferromagnetic phase transition in a homogeneous Fermi gas, showing that the transition changes from the second order to the discontinuous first order at the very low temperature [52] as summarized in figure 3-4. They indeed treated the effect of fluctuations in second-order perturbation theory, and pointed out that Hartree-Fock theory may underestimate the tendency towards ferromagnetism. Recently, the ferromagnetic phase transition and the spin structure in the ferromagnetic state have been investigated in a Fermi gas in a harmonic trap [114, 19, 44]. In addition, some aspects of nonequilibrium dynamics in a Fermi gas have been studied when a non-interacting Fermi gas undergoes a rapid quench to the repulsive side of a Feshbach resonance [14, 44]. Itinerant ferromagnetism in a Fermi gas has been also investigated in optical lattices. By engineering the band structure to have a flat band in a two-dimensional honeycomb lattice, one can realize a ferromagnetic phase in a two component Fermi gas [207, 195].

Properties	Cold atomic system	Solid state system
Thermodynamic ensemble	N_1, N_2, E fixed	μ, B, T fixed
B Field	Balanced $ 1\rangle - 2\rangle$ mixture	Electron gas with zero external magnetic field
Inter-particle interactions	s-wave scattering (short-range interaction)	Coulomb interactions (but screened)
Tunable interactions	Feshbach resonance	pressure
Charge	Neutral system	Charged system

Table 3.2: Comparison between cold atoms and solid state in the study of itinerant ferromagnetism.

3.3.1 A Very Simple Mean-field Prediction for Stoner's Instability in an Ultracold Atomic Gas

A simple mean-field model captures many qualitative features of the expected ferromagnetic phase in equilibrium. In the strongly interacting regime, however, this Hartree-Fock type approximation is not sufficient for a quantitative study since higher order terms leading to quantum fluctuations play the important role. Nevertheless, mean-field model would be a starting point to understand the properties of a two-component Fermi gas.

We consider a uniform two-component Fermi gas interacting through a short-range s-wave interactions (contact interactions). The main feature of the phase transition in a homogeneous trap is expected to be maintained in a harmonic trap within the local density approximation (LDA).

The Hamiltonian describing the system is given by

$$H = \sum_{\sigma} \int \frac{d^3k}{(2\pi)^3} E_k c_{k\sigma}^{\dagger} c_{k\sigma} + g \int d^3r c_{r,\uparrow}^{\dagger} c_{r,\downarrow}^{\dagger} c_{r,\downarrow} c_{r,\uparrow} \quad (3.19)$$

where $E_k = \frac{\hbar^2 k^2}{2m}$ is the kinetic energy of atoms with mass m and momentum $\hbar k$, and $g = \frac{4\pi\hbar^2 a}{m}$ denotes the contact interactions. Here, the interaction term represents any short-range spin-independent potential.

For a two-component Fermi gas trapped in a homogeneous trap with volume V and average atomic density n (per spin component), the total energy is given by in a mean-field model

$$E_{Total}^{normal} = \sum_{\sigma=\uparrow,\downarrow} \frac{3}{5} V (E_{F,\sigma} n_{\sigma}) + g V n_{\uparrow} n_{\downarrow} \quad (3.20)$$

with density $n_{\sigma} = N_{\sigma}/V$ of the spin σ and Fermi energy $E_{F,\sigma} = \frac{\hbar^2 k_{F,\sigma}^2}{2m}$.

Mean-field model at T=0

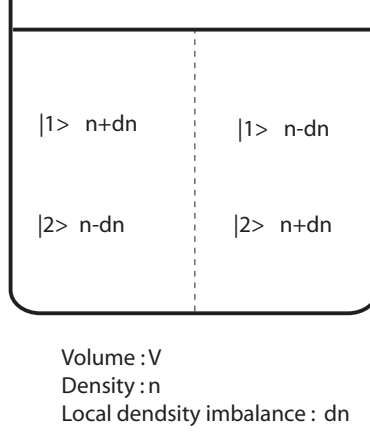


Figure 3-5: Mean-field model at $T = 0$ for itinerant ferromagnetism in a Fermi gas of ultracold atoms. With introduction of local density imbalance dn in a two-component Fermi gas, the instability toward a ferromagnetic state can be described in a mean-field model.

Now, we introduce the local magnetization of the Fermi gas, $\eta = dn/n$, as described in figure 3-5. The local magnetization of the Fermi gas is non-zero when the gas separates into two volumes although the total number of atoms in each pseudospin state is conserved. The total energy with local magnetization η becomes

$$E_{Total}^{\eta} = E_F 2Vn \left[\frac{3}{10} \{ (1 + \eta)^{5/3} + (1 - \eta)^{5/3} \} + \frac{2}{3\pi} k_F a (1 + \eta)(1 - \eta) \right] \quad (3.21)$$

For a system at constant volume, the shape of the total energy E_{Total}^{η} as a function of the magnetization η implies that the Landau-type second-order phase transition occurs at critical value of $k_F a$. Figure 3-6 (a) shows the total energy at different value of $k_F a$. It is clear that the system with minimum in energy spontaneously develops non-zero magnetization when $k_F a$ is larger than $\pi/2$. The phase transition occurs when the curvature of the energy curve becomes zero at $\eta = 0$:

$$\left. \frac{\partial^2 E_{Total}^{\eta}}{\partial \eta^2} \right|_{\eta=0} = 0 \quad (3.22)$$

giving the critical value of $k_F a = \pi/2$.

To compare this model with a cold atomic system, it is more convenient to consider the thermodynamic quantities at constant pressure because the atoms are trapped in

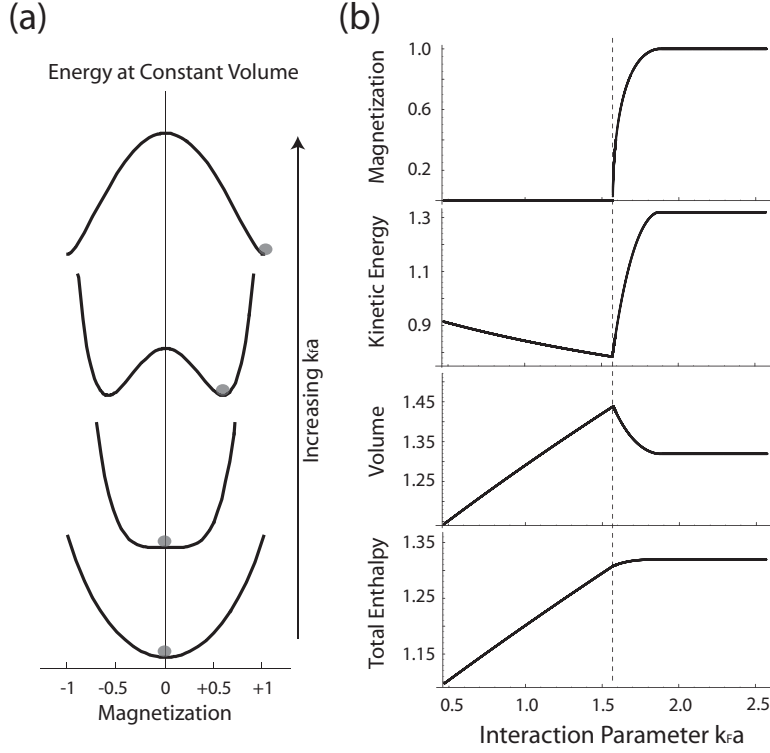


Figure 3-6: Ferromagnetic phase transition at $T=0$, according to the mean-field model described in the text. The onset of itinerant ferromagnetism occurs when the energy as a function of magnetization flips from a U-shape to a W-shape (a). Figure (b) shows the enthalpy, volume and kinetic energy (normalized to their values for the ideal Fermi gas), and magnetization as a function of the interaction parameter $k_F a$. Note that k_F is defined by the density of the gas. The dotted line marks the phase transition.

a harmonic potential ⁷. For this, we consider the enthalpy, H , of the system:

$$H^\eta = E_{Total}^\eta - PV \quad (3.23)$$

with the pressure $P = -dE_{Total}^\eta/dV$.

Similar to the constant volume case, one can calculate the magnetization η of the system at a given $k_F a$ by minimizing the enthalpy. Subsequently, kinetic energy, volume, and total enthalpy are known as a function of $k_F a$ (see figure 3-6 (b)).

- Kinetic energy: For increasing repulsive interactions, the gas expands, lowering its density and Fermi energy; kinetic energy is therefore reduced. When the

⁷In a harmonic potential, the pressure is actually not constant but this simple approach is very useful to capture qualitative features in a ferromagnetic phase transition.

gas enters the ferromagnetic phase, kinetic energy increases rapidly due to the larger local density per spin state. When the gas is fully polarized, it avoids the repulsive interaction, but increases its kinetic energy normalized by k_F^2 by a factor of $2^{2/3}$.

- Volume: The volume has a maximum value at the phase transition. This can be understood by noting that pressure in our model is given by

$$(2/3)E_{kin}/V + E_{int}/V \tag{3.24}$$

where E_{kin} is kinetic energy and E_{int} interaction energy. At the phase transition, the system increases its kinetic energy and reduces its interaction energy, thus reducing the pressure. This maximum in pressure at constant volume turns into a maximum in volume for a system held at constant pressure, or in a trapping potential.

- Magnetization: In the mean-field model, the phase transition is second-order; the magnetization, therefore, changes continuously. The phase transition, however, may become first-order at the very low temperature due to quantum fluctuations [52].

In summary, we have obtained three predictions of this mean-field model:

- (1) the onset of local magnetization
- (2) the minimum in kinetic energy
- (3) the maximum in the size of the cloud

Note that the qualitative features are generic for ferromagnetic phase transition and should be present in more advanced model.

3.3.2 Domain Structure of the Ferromagnetic Ground State

As described in figure 3-7, there are several configurations for the ground state of the ferromagnetic state in the uniform gas. When the number of atoms in each spin state is not conserved (i.e. in the grand canonical ensemble), the true ground state of the ferromagnetic phase is the homogeneous fully-polarized state with a constant magnetization \vec{M}_0 as described in figure 3-7 (b). In a trapped atomic gas, however, this is not valid since the total spin population in each state must be conserved. For the gas of equal spin populations, the total magnetization of the system is always zero: $\int dr \vec{M}(r) = 0$. Therefore, the configuration of the ferromagnetic ground state

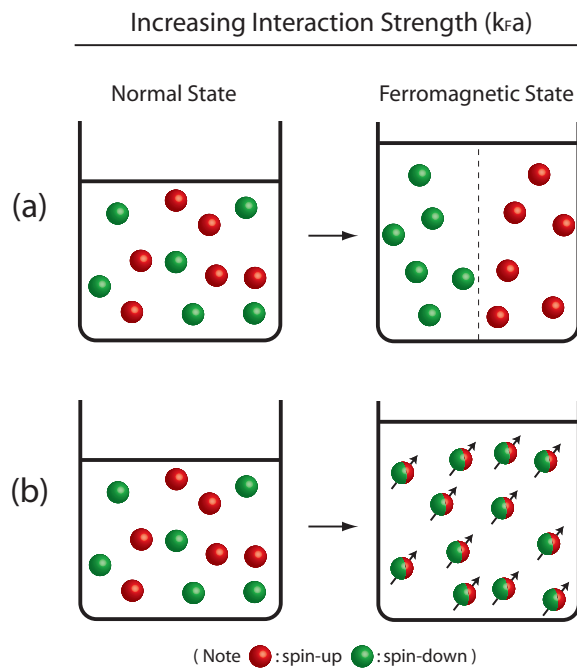


Figure 3-7: Schematic illustration of the ferromagnetic transition in the uniform two-component Fermi gas. As the repulsive interaction strength is increased, the gas of ultracold atoms becomes ferromagnetic at the critical value of $k_F a = \pi/2$ in the mean-field model. The kinetic energy of the gas increases by the factor of $2^{2/3}$ when (a) the state is phase-separated or (b) the state becomes fully coherent.

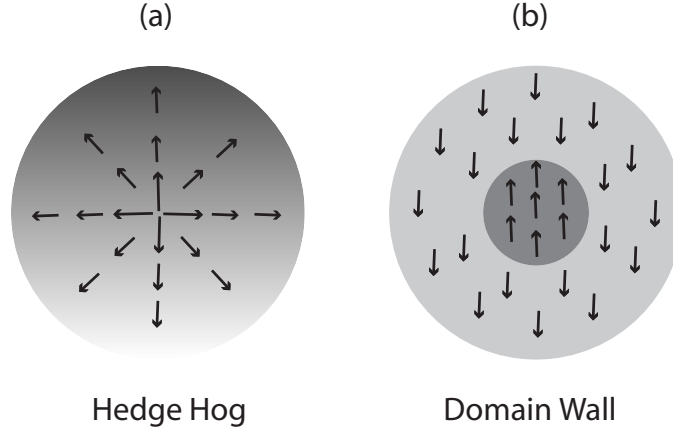


Figure 3-8: The possible configuration of the ferromagnetic ground state in a two-component Fermi gas trapped in a spherical potential. The hedgehog state and the domain wall state are shown in (a) and (b) respectively.

in the trapped gas must change to satisfy the above constraint. In a spherical three-dimensional trap, two candidates, the hedgehog and the domain wall state, for the ferromagnetic ground state are described in figure 3-8 (a) and (b) respectively. It has been shown that the hedgehog state has lower energy than the domain wall state in a three-dimensional trap [19, 114]. However, the energy difference between the two configurations turns out to be very small compared to the Fermi energy E_F or the temperature $k_B T$ of the system [114].

Chapter 4

Itinerant Ferromagnetism in a Fermi Gas of Ultracold Atoms

This chapter describes our research on itinerant ferromagnetism in a strongly interacting Fermi gas of ultracold atoms. Our experiment can be regarded as quantum simulation of a Hamiltonian for which even the existence of a phase transition was unproven. The experiment was reported in the publication:

- Gyu-Boong Jo, Ye-Ryuoung Lee, Jae-Hoon Choi, Caleb A. Christensen, Tony H. Kim, Joseph H. Thywissen, David E. Pritchard and Wolfgang Ketterle
Itinerant Ferromagnetism in a Fermi Gas of Ultracold Atoms
Science **325**, 1521-1524 (2009). Included in appendix C

4.1 Two-component Fermi gas with strong repulsive interactions as a Model System

Overview

Recent developments in the field of ultracold Fermi gases rely on the ability of tuning the scattering length a from zero to the value larger than mean interatomic distance [65, 38, 108]. This is done by simply changing the magnetic field near a Feshbach resonance. In this section, we mainly discuss the properties of the system near the Feshbach resonance. In particular, the repulsive gas is of interest since it would be a model system for the study of itinerant ferromagnetism.

As described in figure 4-1, the Feshbach resonance couples a molecular bound state (referred to as closed channel) with an unbound state describing a colliding pair

of atoms (referred to as open channel). In a two-particle picture, the energy spectrum in the system of Fermi gases near the Feshbach resonance shows that there are several energy branches for the macroscopic state of the Fermi gas (see figure 4-1). Here, the two lowest-energy branches are of importance for our purpose.

1. **The ground state branch** : The ground state branch connects two different regimes: a dilute gas of dimers (on the left-hand side of figure 4-1) and a weakly attractive gas (on the right-hand side of figure 4-1). In the dilute Fermi gas with negative scattering length ($k_F|a| \ll 1$), the many-body state can be described in the BCS picture [17] both at $T = 0$ and at finite temperature. In this regime, the *Cooper pairing instability* toward the BCS state exists even in the presence of extremely weak attraction. For the gas of dimers ($k_F a \ll 1$), the behavior can be described by the BEC picture (hereafter called BEC limit). Experimentally, the molecular Bose-Einstein condensation has been observed by several groups [211, 67, 30, 18, 144]. For both BCS and BEC limits, the gas remains stable and shows superfluidity. The many-body physics becomes much more challenging in the intermediate regime connecting the BCS and BEC limits because the scattering length is larger than mean interatomic distance $k_F|a| \gg 1$. For this regime, so-called BCS-BEC crossover, many relevant experiments and theoretical calculations have indicated that the gas exhibits superfluidity and remains stable [65, 91]. In addition, the universal behavior at the unitary regime ($k_F a \rightarrow \infty$) has been studied experimentally in good agreement with relevant numerical calculations. For more details, I refer to Ref. [65, 91].
2. **The first excited branch** : The repulsive gas of atoms is realized in the first excited branch. An attractive potential with a weakly bound state has a positive scattering length describing repulsive interactions in the continuum. In the dilute atomic gases, the true ground state in the presence of repulsive interactions is the gas of the dimers since the long-range atom-atom interactions are attractive. In the excited branch, therefore, the gas of atoms with positive scattering length a is metastable since three-body collisions between atoms tends to form a molecule [153] and populates ground state branch. The collision rate is proportional to a^6 for small scattering length, $k_F a < 1$, and the binding energy of the produced dimer is carried away by the third atom. When $k_F a \rightarrow 0$, the gas corresponds to the weakly repulsive gas.

As we have seen above, two different branches near the Feshbach resonance allow us to prepare both an attractive and a repulsive gas of atoms. Experimentally,

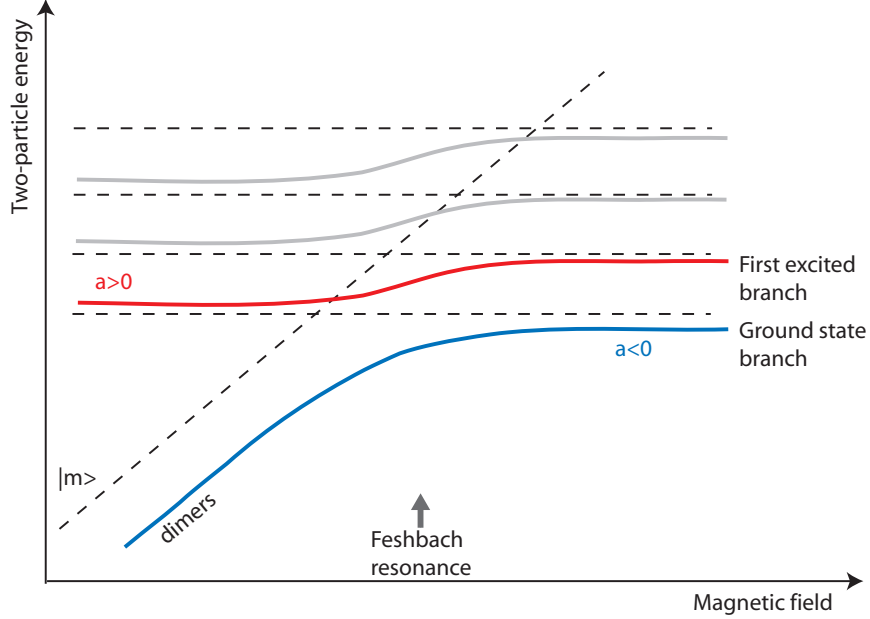


Figure 4-1: Schematic illustration of the energy spectrum of the two-particle system in a spherical harmonic potential near a Feshbach resonance.

the atomic gas in the ground state branch has been achieved by (1) producing and simultaneously cooling down a gas of dimers via three-body collisions with a fixed (positive) scattering length or (2) crossing the Feshbach resonance adiabatically starting from the negative scattering length. On the other hand, the repulsive gas can be realized by adiabatically increasing the scattering length, starting from the small value, $a = 0^+$ [29]. For the repulsive atomic gas, the strongly interacting gas suffers from molecule formation leading to a short lifetime. To minimize deleterious molecule formation in the atomic gas, one should increase the scattering length from zero to the large value as quickly as possible. This quench could be done by ramping up the magnetic field [102] or by changing the hyperfine state of the atom with an RF pulse as discussed in section 4.5.

Before we discuss the properties of the repulsive gas of atoms, it is useful to distinguish two different *universal states* in the unitary limit $|a| \rightarrow \infty$. In the ground state branch, the effective interaction in the unitary limit is attractive, whereas it is repulsive in the first excited branch. This different behavior of the gas is clearly identified in the calculation of the thermodynamic pressure in a toy model (see figure 4-2).

Strongly interacting repulsive atomic gas

For an weakly repulsive Fermi gas, the ground-state energy be exactly calculated within standard perturbation theory. The atom-atom interactions are approximated by the psedopotential with a scattering length a . At nearly zero temperature, the energy per particle is given by the following asymptotic expansion [88, 116, 126]:

$$\frac{E}{N} = E_F \left(\frac{3}{5} + \frac{2}{3\pi} k_F a + \frac{4}{35\pi} (11 - 2\ln 2) (k_F a)^2 + 0.23 (k_F a)^3 + \dots \right) \quad (4.1)$$

where $E_F = \frac{\hbar^2 k_F^2}{2m}$ is Fermi energy and k_F is the Fermi wavenumber, which should be meaningful either for weakly interacting case ($a \rightarrow 0$) or low density ($k_F \rightarrow 0$). Note that the energy in the equation 4.1 denotes the energy of the true ground state for purely repulsive potentials such as the hard-sphere model. In the dilute atomic gas, this result describes the energy of metastable repulsive gas in the first excited branch.

Each term in the expression 4.1 has a physical physical interpretation:

- The first term corresponds to the kinetic energy of the noninteracting Fermi gas.
- The second term proportional to $k_F a$ implies both direct and exchange interaction energy associated with the two-particle forward scattering. Indeed, this is related to the definition of the s-wave scattering length a for low-energy collisions in a low-density gas. Neglecting the effect of the presence of other particles in the Fermi sea, free-particle scattering amplitude $f(k, k')$ has a constant value $-a$ as $k = k' \rightarrow 0$ (low-energy limit).
- The term proportional to $(k_F a)^2$ indicates the particle-hole excitation in the presence of the Fermi sea. For example, this term includes the physical process that an incident particle excites a particle in the Fermi sea, leaving a hole behind. Subsequently, the same two particles collide with each other again, removing a hole in the Fermi sea and bringing the system back to the initial state.
- A correction of order $(k_F a)^3$ represents the three distinct collisions associated with three-particle correlations [50].

The many-body problem for a large positive scattering length, $k_F a \geq 1$, is much more challenging. To date, an exact solution of the many-body ground state in this regime is not available and one has to rely on the numerical calculations or advanced Hartree-Fock theories including the second-order fluctuations [133, 1, 52, 43].

We may now ask for the thermodynamic property of the Fermi gas when the scattering length is larger than the mean distance between particles. In particular, the ground-state energy, the compressibility, and the thermodynamic pressure of the repulsive gas near the Feshbach resonance are of interest.

For this purpose, we introduce a very simple model capturing relevant physics in the strongly repulsive Fermi gas [160]. Although the many-body effects such as correlation effects are not well taken into account in this model, it describes some properties of strongly interacting gases.

A simple model: A two-component Fermi gas with arbitrary values of the scattering length a can be simply modeled by considering a single fictitious particle in a three-dimensional spherical box interacting with a fixed scatterer at the center. The interactions between two atoms in different spin states are captured by the interaction of the fictitious particle with the scatterer. The boundary of the sphere box represents the Pauli blocking in the presence of other fermions and, indeed, the radius of the sphere, R , is determined by the density of the gas: $k_F R = \sqrt{5/3}\pi$. For $N/2$ spin $+1/2$ and $N/2$ spin $-1/2$ fermions, the total energy of the system, $E(a)$, at arbitrary scattering length a is given by [160],

$$E(k_F a) = \frac{1}{2} N \varepsilon \quad (4.2)$$

where $\varepsilon = \frac{\hbar^2 k^2}{m}$ represents the energy of fictitious particle. The wavefunction $\varphi(r)$ of the fictitious particle satisfies

$$-\frac{\hbar^2}{m} \nabla^2 \varphi = \varepsilon \varphi \quad (4.3)$$

with the contact interaction condition $\lim_{r \rightarrow 0} \frac{\partial_r(r\varphi)}{r\varphi} = -\frac{1}{a}$ [139, 154]. For low-energy limit, the only relevant partial wave is the s-wave leading to rotational symmetric solution of equation 4.3. A simple calculation gives the energy of the fictitious particle as follow; for positive (negative) energy $\frac{\hbar^2 k^2}{m}$ ($-\frac{\hbar^2 k^2}{m}$), k is determined by the solution of

$$\tan kR = ka \quad (\tanh kR = ka). \quad (4.4)$$

In figure 4-2, the total energy of the gas and the thermodynamic pressure are shown as a function of $k_F a$. Here, since we are interested in the two lowest branches, only the two smallest eigenvalues in 4.4 are considered in figure 4-2. In figure 4-2 (a), the upper branch corresponds to the first excited branch in figure 4-1 whereas

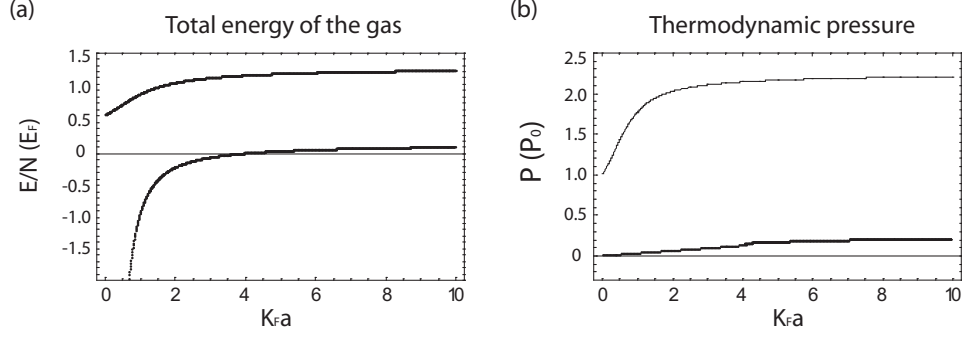


Figure 4-2: The energy per particle and the thermodynamic pressure of the repulsive interacting two-component Fermi gas in the simple model. (a) The energy per particle (in (a)) and the thermodynamic pressure (in (b)) are shown as a function of $k_F a$. They are normalized by the Fermi energy, E_F , and the pressure, P_0 , respectively for the non-interacting ideal Fermi gas.

the lower one to the ground state branch. The total energy of the repulsive gas (the upper branch) gradually increases with the interaction parameter $k_F a$ and eventually saturates near the Feshbach resonance. On the other hand, the lower branch shows the feature of dimers; the binding energy of a dimer near the resonance is given by $\sim \hbar^2/m a^2$.

The difference between the two branches becomes more prominent in the thermodynamic pressure $P(a) = -\frac{\partial E(k_F a)}{\partial V}$ where V is the volume of the system. After a simple algebra, the pressure for the first excited branch, $P_e(a)$, is given by

$$P_e(k_F a) = P_0 \times \frac{10m\varepsilon}{3\hbar^2 k_F^2} \left(\frac{1}{1 - \frac{k_F a}{\sqrt{\frac{5}{3}}\pi(1 + \frac{2ma^2\varepsilon}{\hbar^2})}} \right) \quad (4.5)$$

where $P_0 = \frac{\hbar^2 k_F^5}{15\pi^2 m}$ is the Fermi pressure of the non-interacting gas. The result in figure 4-2 (b) shows that the thermodynamic pressure at large $k_F a \gg 1$ implies the behavior of the repulsive ($P_e(k_F a) > P_0$) and attractive ($P_g(k_F a) < P_0$) gas for the first excited and the ground state branch respectively.

4.2 Implementation of the Stoner model in an Ultracold Atomic System

Motivation: So far, we have seen that the two-component Fermi gas near the Feshbach resonance may offer an opportunity to study the property of the repulsive

Fermi gas. Encouraged by this, we now implement the Stoner model [181] using a two-component gas of free fermions with short-range repulsive interactions which can capture the essence of the screened Coulomb interaction in electron gases [181]. However, there is no proof so far that this simple model for ferromagnetism is consistent when the strong interactions are treated beyond mean-field approaches. It is known that this model fails in one-dimension where the ground state is singlet for arbitrary interactions, or for two particles in any dimension [124]. Here, cold atoms are used to perform a quantum simulation of this model Hamiltonian in 3D and provide experimental evidence that it leads to a ferromagnetic phase transition [187]. A similar model is also realized in helium-3 [193], but it turns into solid and not into a ferromagnetic phase at high pressure. It has also been applied to neutrons in neutron stars [156].

4.2.1 Experimental Technique

Preparation of the ultracold ${}^6\text{Li}$ cloud

The first step is the production of a spin-polarized Fermi gas in the $|F = 3/2, m_F = 3/2\rangle$ state by sympathetic cooling with bosonic ${}^{23}\text{Na}$ atoms in a magnetic trap as described in Ref. [78]. The ${}^6\text{Li}$ cloud was then loaded into a deep optical dipole trap with a maximum power of 3W and radial trap frequency of ~ 3.0 kHz, followed by an RF transfer into the lowest hyperfine state $|F = 1/2, m_F = 1/2\rangle$. Additional axial confinement was provided by magnetic fields. An equal mixture of $|1\rangle$ and $|2\rangle$ spin states (corresponding to the $|F = 1/2, m_F = 1/2\rangle$ and $|F = 1/2, m_F = -1/2\rangle$ states at low magnetic field, see also appendix A) was prepared by a Landau-Zener RF sweep at a magnetic field of 590 G, followed by 1 s for decoherence and further evaporative cooling at 300 G. Finally, the optical trapping potential was adiabatically reduced over 600 ms, and the field increased back to 590 G. The trap had a depth of $7.1 \mu\text{K}$ and was nearly cigar shaped with frequencies $\nu_x = \nu_y \simeq 300$ Hz and $\nu_z \simeq 70$ Hz.

Magnetic field ramp

Our current coil geometry does not allow very fast magnetic field ramping. After improving the ramp rate of our power supplies to better than 1 ms, we observed that the magnetic field was still lagging 4.5 ms behind, probably due to eddy currents as described in figure 4-4. The actual magnetic field at the position of the atom cloud was determined in a spectroscopic way. In the experiment, the magnetic field was ramped up from 590 G to the field of interest within 4.5 ms.

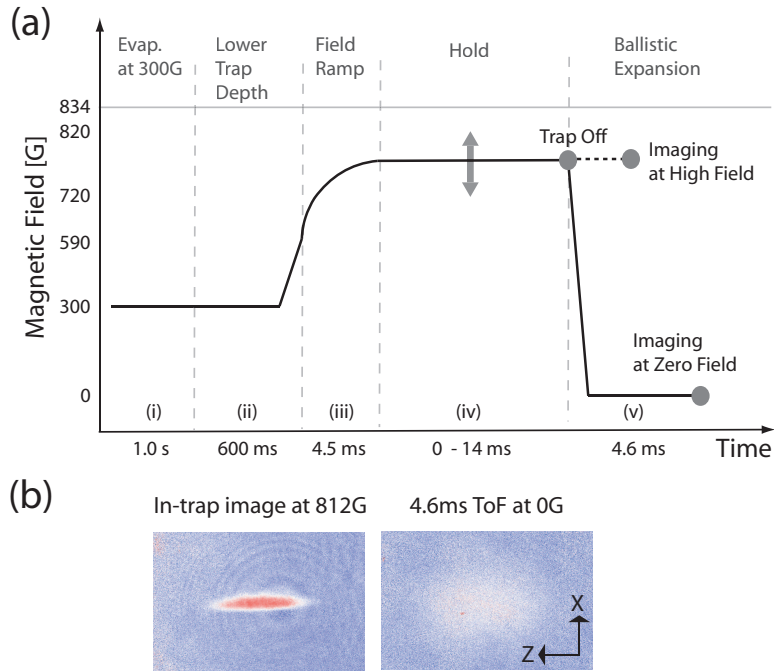


Figure 4-3: (a) The schematic shows the time sequence of the experiment. The sample was exposed to the magnetic field of interest for 0 - 14 ms and analyzed in-situ for loss measurement or after 4.6 ms time-of-flight for the measurement of kinetic energy and the axial size of the cloud. The Feshbach fields were suddenly switched off at a rate of $1\text{G}/\mu\text{s}$, preventing the conversion of interaction energy into kinetic energy during the expansion. (b) This absorption image shows the $|1\rangle$ component of the cloud trapped at 812 G (left), and after 4.6 ms ballistic expansion imaged at zero field (right). The field of view is $840\mu\text{m}\times 550\mu\text{m}$. The magnetic field ramp was limited by eddy currents to 4.5 ms. Spectroscopic measurements of the magnetic field showed that the field was trailing behind the current which was controlled with a time constant faster than 1 ms.

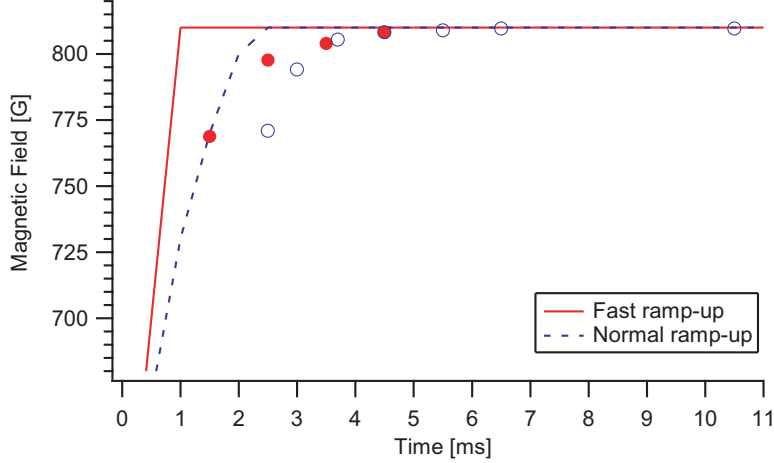


Figure 4-4: The effect of eddy currents on the magnetic field ramp was measured. Though the current from the power supply was ramped up within 1 ms (red solid curve), the magnetic field at the position of the atom cloud requires at least 4.5 ms (red solid circles). The magnetic field is also shown for the slower ramp rate (blue dotted curve and blue open circle) .

Molecule formation and the effective temperature

We start with an atom cloud consisting of an equal mixture of ${}^6\text{Li}$ atoms in the lowest two hyperfine states, $|1\rangle$ and $|2\rangle$, held at 590 G in an optical dipole trap with additional magnetic confinement. The number of atoms per spin state $\sim 6.5 \times 10^5$ corresponds to a Fermi temperature T_F of $\sim 1.4 \mu\text{K}$. The effective temperature T could be varied between $T/T_F = 0.1$ and $T/T_F = 0.6$ and was determined right after the field ramp by fitting the spatial distribution of the cloud with a finite temperature Thomas-Fermi profile. Note that k_F° is the Fermi wavevector of the non-interacting gas calculated at the trap center. Applying the procedure discussed in Ref. [107] to repulsive interactions, we estimate that the real temperature is $\sim 20\%$ larger than the effective one. The effective temperature did not depend on $k_F^\circ a$ for $k_F^\circ a < 6$. At higher temperatures, additional shot-to-shot noise was caused by large fluctuations in the atom number. From the starting point at 590 G, the magnetic field was increased towards the Feshbach resonance at 834 G, thus providing adjustable repulsive interactions. Due to the limited lifetime of the strongly interacting gas, it was necessary to apply the fastest possible field ramp, limited to 4.5 ms by eddy currents. The ramp time is approximately equal to the inverse of the axial trap frequency and therefore only marginally adiabatic. Depending on the magnetic field during observation, either atoms or atoms and molecules were detected by absorption imaging as described

in figure 4-3 [211].

4.3 Evidences for Itinerant Ferromagnetism in a Fermi Gas of Ultracold Atoms

In this section, we introduce the experimental characterization of the ferromagnetic phase transition in a Fermi gas of ultracold atoms. We have observed three different evidences for ferromagnetic phase transition. The observations are qualitatively in agreement with predictions in mean-field and more advanced models.

1. Local spin polarization

The emergence of local spin polarization can be observed by the suppression of (either elastic or inelastic) collisions, as the Pauli exclusion principle forbids collisions in a fully polarized cloud. We monitor inelastic three-body collisions which convert atoms into molecules. The rate (per atom) is proportional to $f(a, T)n_1n_2$ or $f(a, T)n^2(1-\eta^2)$ and is therefore a measure of the magnetization η . For $k_F a \ll 1$, the rate coefficient $f(a, T)$ is proportional to $a^6 \max(T, T_F)$ [48]. For $k_F a \gg 1$, the $f(a, T)$ is unknown and the rate coefficient may be suppressed at a very low temperature due to the Pauli blocking. However, the effect of the Pauli blocking has not yet been studied quantitatively. This rate can be observed by monitoring the initial drop in the number of atoms during the first 2 ms after the field ramp. We avoided longer observation times since the increasing molecule fraction could modify the properties of the sample.

Figure 4-5 shows a sharp peak in the atom loss rate around $k_F^\circ a \simeq 2.5$ at $T/T_F = 0.12$ indicating a transition in the sample to a state with local magnetization. The gradual decrease is consistent with the inhomogeneous density of the cloud where the transition occurs first in the center. The large suppression of the loss rate indicates a large local magnetization of the cloud.

2. Kinetic energy of the cloud

The kinetic energy of the cloud was determined by suddenly switching off the optical trap and the Feshbach fields right after the field ramp and then imaging state $|1\rangle$ atoms at zero field using the cycling transition after a ballistic expansion time of $\Delta_{tof} = 4.6$ ms. The kinetic energy was obtained from the Gaussian radial width σ_x as $E_{kin} = \frac{3m\sigma_x^2}{2\Delta_{tof}^2}$ where m is the mass of the ^6Li atom. Figure 4-6 demonstrates a minimum of the kinetic energy at $k_F^\circ a \simeq 2.2$ for the coldest temperature, $T/T_F = 0.12$,

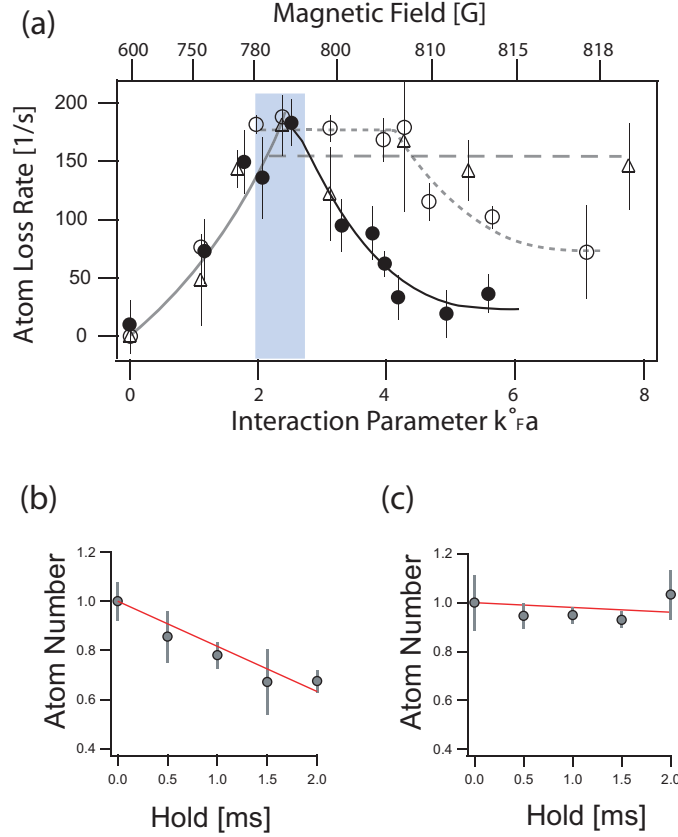


Figure 4-5: (a) Atom loss rate as a probe for local spin polarization, for different temperatures: $T/T_F = 0.55$ (dashed curve), $T/T_F = 0.22$ (dotted curve), and $T/T_F = 0.12$ (solid black curve). The curves are guides to the eye, based on the assumption of a loss rate which saturates for increasing a in the normal state. The shaded area around the phase transition at $T/T_F = 0.12$ highlights the same region as in figure 4-6 and 4-7. Atom loss rates at $k_F a = 2.5$ and $k_F a = 4.9$ are obtained by measuring the initial drop in the atom number as shown in (b) and (c) respectively.

nearly coinciding with the onset of local polarization. The peak in the atom loss rate occurs slightly later than the minimum of kinetic energy, probably because $f(a, T)$ increases with a [114]. Since the temperature did not change around $k_F^\circ a \simeq 2.2$, the increase in kinetic energy is not caused by heating, but by a sudden change in the properties of the gas, consistent with the onset of ferromagnetism. The observed increase in kinetic energy is $\sim 20\%$ at $T/T_F = 0.12$, smaller than the value $(2^{2/3} - 1) = 0.59$ predicted for a fully polarized gas. This discrepancy could be due to the absence of polarization or partial polarization in the wings of the cloud. Also, it is possible that the measured kinetic energy of the strongly interacting gas before the phase transition includes some interaction energy if the Feshbach fields are not suddenly switched off. For the current switch-off time of $\sim 100 \mu\text{s}$, this should be only a 5% effect, but the magnetic field decay may be slower due to eddy currents.

3. Cloud size

Finally figure 4-7 shows our observation of a maximum cloud size at the phase transition, in agreement with the prediction of the model. The cloud size may not have fully equilibrated since our ramp time was only marginally adiabatic, but this alone cannot explain the observed maximum.

4. Temperature dependence

The suppression of the atom loss rate, the minimum in kinetic energy, and the maximum in cloud size show a strong temperature dependence between T/T_F of 0.12 and 0.22. As the properties of a normal Fermi gas approaching the unitarity limit with $k_F^\circ a \gg 1$ should be insensitive to temperature variations in this range, this provides further evidence for a transition to a new phase.

At higher temperature (e.g. $T/T_F = 0.39$ in figure 4-6), the observed non-monotonic behavior becomes less pronounced and shifts to larger values of $k_F^\circ a$ for $3 \leq k_F^\circ a \leq 6$. For all three observed properties (figure 4-5~ 4-7), a nonmonotonic behavior is no longer observed at $T/T_F = 0.55$. The interpretation of the loss rate is complicated since $f(a, T)$ is unknown for $k_F a \geq 1$. The three body rate $f(a, T)$ is expected to be unitarity saturated for $k_F a \gg 1$ [197]. The lines in figure 4-5 indicate that the observed loss rate is consistent with unitarity saturation and a sudden drop at the phase transition, which occurs at large values of $k_F a$ at higher temperature.

One interpretation is that at this temperature and above, there is no phase transition any more. Note that in a mean-field approximation, a ferromagnetic phase

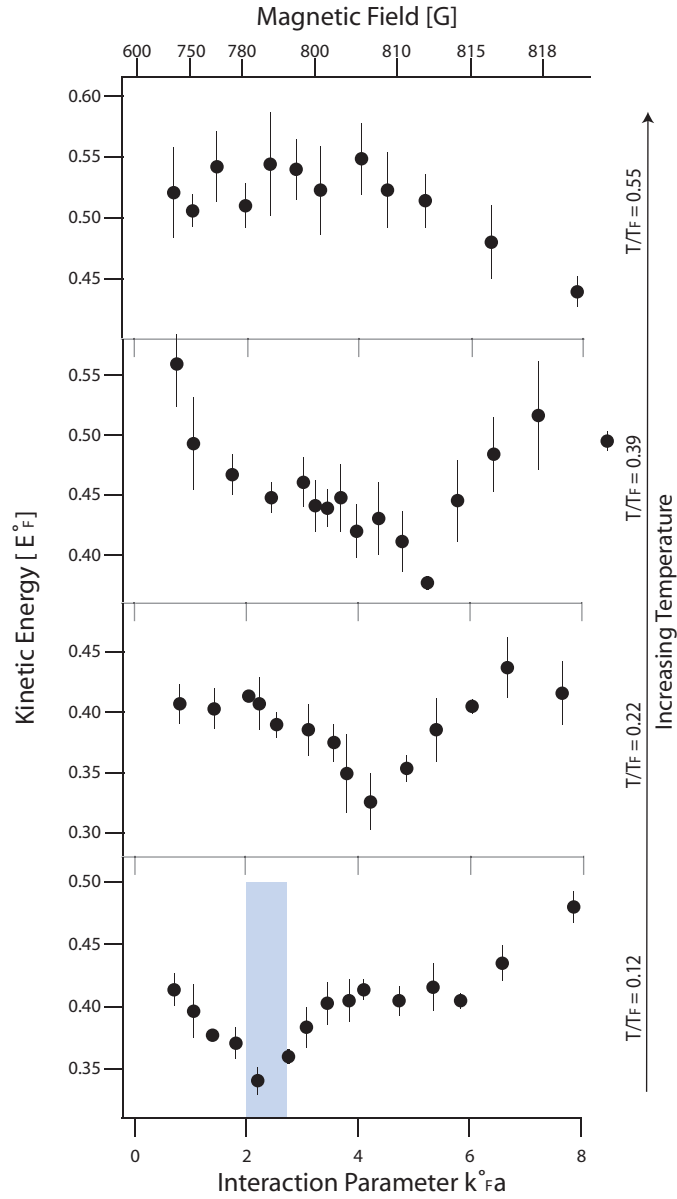


Figure 4-6: Kinetic energy of a repulsively interacting Fermi gas determined for different interaction parameters $k_F^0 a$ and temperatures. The measured kinetic energy is normalized by the Fermi energy E_F^0 of the noninteracting Fermi gas at $T=0$, calculated at the trap center with the same number of atoms per spin state. Each data point represents the average of three or four measurements.

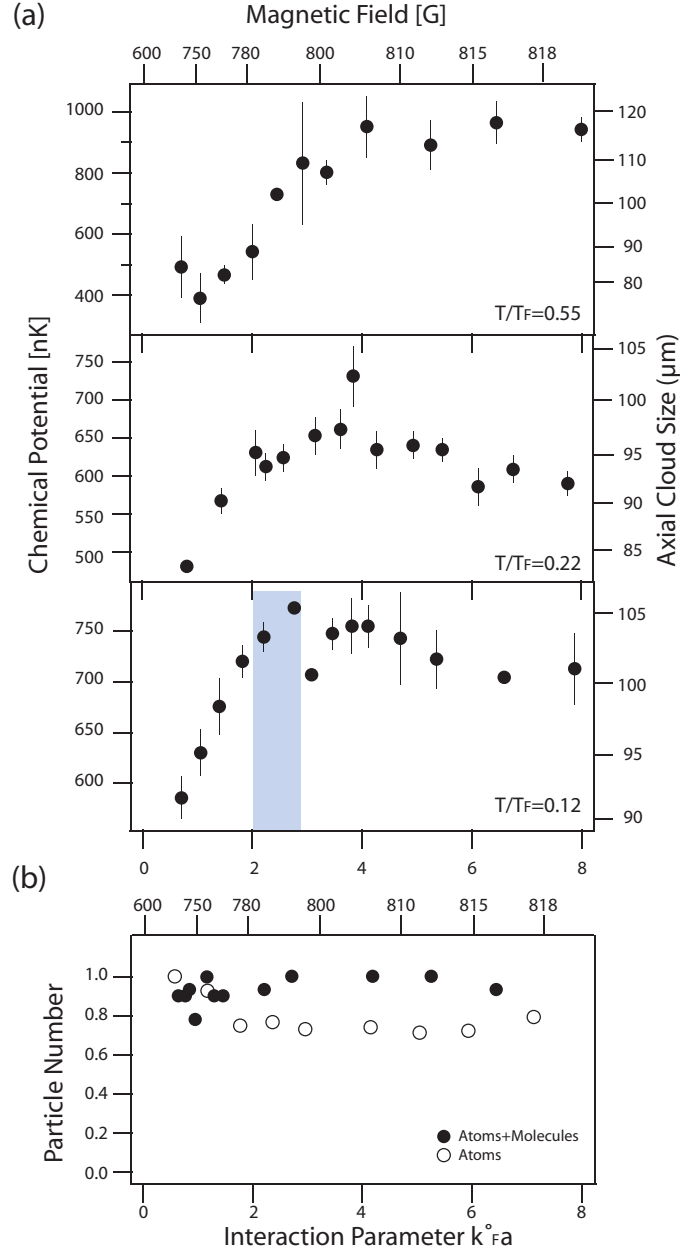


Figure 4-7: Maximum in volume at the phase transition (a) Axial size and chemical potential of the cloud for various temperatures. The chemical potential μ is determined from the measured cloud size, σ_z as $\mu = \frac{1}{2}m\omega_z^2\sigma_z^2$ (b) Number of particles including both atoms and molecules right after the field ramp. This result shows that 25 % of atoms were converted into molecules during the field ramp, and this fraction stayed constant for $k_F^0 a > 1.8$, where the phase transition was reached. This molecule fraction was independent of temperature.

would appear at all temperatures, but for increasing values of $k_F^\circ a$. Our observations may imply that the interaction energy saturates around $k_F^\circ a \approx 5$.

5. Limitations in the experiment

The spin-polarized ferromagnetic state should not suffer from inelastic collisions. However, typical lifetime were 10 - 20 ms, probably related to a small domain size (see below) and three-body recombination at domain walls.

We were unsuccessful in imaging ferromagnetic domains using differential in-situ phase-contrast imaging [180]. A noise level of $S/N \sim 10$ suggests that there were at least 100 domains in a volume given by our spatial resolution of $\sim 3 \mu\text{m}$ and the radial size of the cloud. This implies that the maximum volume of the spin domains is $\sim 5 \mu\text{m}^3$, containing ~ 50 spin-polarized atoms. We suspect that the short lifetime prevented the domains from growing to a larger size, and eventually adopting the equilibrium texture of the ground state, which has been predicted to have the spins pointing radially outward, like a hedgehog [19, 114]. All our measurements are sensitive only to local spin polarization, independent of domain structure and texture.

The only difference between our experiment and the ideal Stoner model is a molecular admixture of 25 % (see figure 4-7). The molecular fraction was constant for $k_F^\circ a > 1.8$ for all temperatures and therefore cannot be responsible for the sudden change of behavior of the gas at $k_F^\circ a \simeq 2.2$ for the coldest temperature $T/T_F = 0.12$. This was confirmed by repeating the kinetic energy measurements with a molecular admixture of 60 %. The minimum in the kinetic energy occurred at the same $k_F^\circ a$ within experimental accuracy.

4.4 Discussion

4.4.1 The Critical Value of $k_F a$ Observed in the Experiment

The observed phase transition at $k_F^\circ a \simeq 2.2$ must be rescaled in order to compare it to the theoretical predictions. For this, we have to replace the ideal gas k_F° by the value for the interacting gas, which is smaller by $\sim 15\%$ because of the expansion of the cloud (figure 4-7), and obtain a critical value for $k_F a \simeq 1.9 \pm 0.2$. At $T/T_F = 0.12$, the finite temperature correction in the critical value for $k_F a$ is predicted to be less than 5% [52]. The observed value for $k_F a$ is larger than the mean-field prediction of $\pi/2$ and the second order prediction of 1.054 at zero temperature [52]. Depending on

the theoretical approach, the phase transition has been predicted to be first or second order. This could not be discerned in our experiment due to the inhomogeneous density of the cloud.

4.4.2 Estimation of the Maximum Total Repulsive Energy

Our work demonstrates a remarkable asymmetry between positive and negative scattering length. Early work [86] predicted that for $k_F|a| = \pi/2$, both an attractive and a repulsive Fermi gas become mechanically unstable (against collapse, and phase separation, respectively). In an attractive Fermi gas, however, the mechanical instability does not occur (due to pairing [138]), in contrast to our observations in a repulsive Fermi gas. This suggests that the maximum total repulsive energy (in units of $3/5(2Vn)E_F$) is larger than the maximum attractive energy $|\beta|$ of 0.59 [34] realized for infinite a .

Full phase separation at zero temperature requires a total repulsive energy of $(2^{2/3} - 1) = 0.59$ in units of $3/5(2Vn)E_F$. At finite temperature T , one has to add TS where $S = (2Vn)k_B \ln 2$ is the entropy difference between the two phases as described in figure 4-8. We can estimate the maximum repulsive energy by considering free energy F ,

$$F = E - TS \quad (4.6)$$

where F is free energy of a two-component Fermi gas, T the temperature, and S the entropy. Across the ferromagnetic transition, the change in free energy satisfies

$$\Delta F = F_{FM} - F_{Normal} = (2^{2/3} - 1) \frac{3}{5} N E_F + k_b T N \ln 2 - \Delta E_{repulsive} < 0 \quad (4.7)$$

This gives us the maximum repulsive energy,

$$\Delta E_{repulsive} > \frac{3}{5} N E_F ((2^{2/3} - 1) + \frac{T}{T_F} \ln 2 \frac{5}{3}) \quad (4.8)$$

Our tentative observation of a ferromagnetic phase at $T = 0.39T_F$ implies a repulsive energy of ~ 1.04 assuming full phase separation, larger than the maximum attractive energy of 0.59.

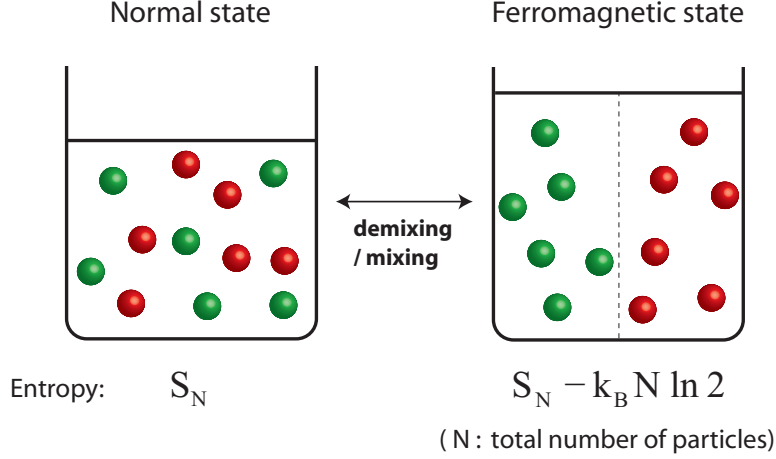


Figure 4-8: The entropy difference between the normal and the ferromagnetic phase.

4.4.3 Comparison with Ferromagnetism in Spinor Bose-Einstein Condensates.

So far, magnetism in ultracold gases has been studied only for spinor [184, 168] and dipolar [110] Bose-Einstein condensates. In these cases, magnetism is driven by weak spin-dependent interactions which nevertheless determine the structure of the condensate due to a bosonic enhancement factor. Especially in spinor condensates, the long-range dipole-dipole interactions are not negligible in contrast to a strongly interacting Fermi gas in which the short-range exchange interactions are dominant.

4.4.4 Discrepancy of the Critical Value of $k_F a$

The mean-field calculation predicts that itinerant ferromagnetism occurs at $k_F a = \pi/2$ in a homogeneous Fermi gas. The experiment reported in this thesis, however, has observed that the critical value of $k_F a$ is rather larger. More advanced models predicts even smaller critical interaction strength (see table 4.1). This discrepancy raises a question if our theoretical predictions are not precise enough or other physical mechanism plays a role. In any cases, it is very important to resolve the discrepancy in the critical $k_F a$ since it would improve our theoretical understanding of a strongly interacting many-body system. Recently, two rather opposite physical mechanisms affecting the critical $k_F a$ have been proposed: quantum fluctuations enhancing interacting energy and three-body losses damping out quantum fluctuations.

The role of quantum fluctuations

The energy density, ε , of the Stoner Hamiltonian 3.19 can be calculated up to second-order in $k_F a$ by either perturbation theory [133, 1, 52] or field-theoretical approach [43] :

$$\varepsilon = \underbrace{\frac{1}{V} \sum_{k,\sigma} \epsilon_k n_\sigma(\epsilon_k) + \frac{2k_F a}{\pi\nu} n_\uparrow n_\downarrow - \frac{2}{V^3} \left(\frac{2k_F a}{\pi\nu}\right)^2}_{\text{mean-field}} \times \sum \frac{n_\uparrow(\epsilon_{k_1}) n_\downarrow(\epsilon_{k_2}) [n_\uparrow(\epsilon_{k_3}) + n_\downarrow(\epsilon_{k_4})]}{\epsilon_{k_1} + \epsilon_{k_2} - \epsilon_{k_3} - \epsilon_{k_4}} \quad (4.9)$$

where $n_\sigma(\epsilon)$ denotes the Fermi distribution at the energy of ϵ , ν is the density of state at the Fermi surface, and a is the s-wave scattering length. The underbraced leading terms simply recovers the mean-field Stoner model. The quantum fluctuations are encoded into the term proportional to $(k_F a)^2$ leading to a first-order phase transition at low temperature. Physically, the second-order term represent particle-hole excitations which are neglected in mean-field calculations. Also, the unitarity limit close to the Feshbach resonance is taken into account by renormalizing (or regularizing) the interaction strength g [148]:

$$g \longrightarrow \frac{2k_F a}{\pi\nu} - \frac{2}{V^3} \left(\frac{2k_F a}{\pi\nu}\right)^2 \sum \frac{1}{\epsilon_{k_1} + \epsilon_{k_2} - \epsilon_{k_3} - \epsilon_{k_4}} \quad (4.10)$$

Note that this treatment regularize the unphysical divergence of the second-order terms close to the Feshbach resonance.

The presence of the quantum fluctuations enhances the interaction energy so that it decrease the critical interaction strength $k_F a^* = 1.05$. Here, the second-order contribution in 4.9 is actually *positive definite*¹ because of the renormalization of g [148].

Recently, the effect of the atom loss via the three-body collisions has been studied in Ref [42] in a Fermi gas of ultracold atoms. It was shown that the atom loss hinders the ferromagnetic phase transition by damping out the quantum fluctuations.

In summary, quantum fluctuations have an important role in a ferromagnetic transition. Recently, however, it has been pointed out that the effect of quantum fluctuations - first-order phase transition and lower critical interaction strength - may be preempted by the formation of an inhomogeneous magnetic phase [43] and three-body loss respectively [42]. In particular, the three-body loss damps quantum fluctuations and thus increases the critical interaction strength needed for a ferromagnetic

¹Therefore, the second-order term increases effective interaction strength.

Predictions	$k_F a$
MIT experiment [102]	1.9 ± 0.3
Analytic method [52] including quantum fluctuations	1.05
QMC [43]	0.85
Mean-field model [114]	1.84

Table 4.1: Prediction of critical interaction strength for itinerant ferromagnetism in a Fermi gas of ultracold atoms.

transition.

4.4.5 Correlation Effects

The interpretation of our results in terms of a phase transition to itinerant ferromagnetism is based on the agreement with the prediction of simplified models based on the Hartree-Fock approximation. In a strongly interacting regime, however, the Hartree-Fock approximation does not take into account correlation effects [56].

In the Hartree-Fock method, the parallel spins are kept apart by the Pauli exclusion principle whereas the antiparallel spins are spatially uncorrelated. Thus, the antiparallel spins possess a relatively large energy via Coulomb repulsion or other short-range interactions. In an exact treatment without any approximation, however, it is likely that the antiparallel spins are somehow correlated due to strong repulsive interactions. The correlation eventually would reduce the interaction energy, U_{int} , in the system. The difference between the exact ground state of an strongly interacting system and the approximated ground state in the Hartree-Fock method is caused by so-called “*correlation effects*” [56].

The possible importance of correlations in the Hubbard model was pointed out by Kanamori [105]. He argued that the short-range correlations reduce the effective interaction energy, U_{int} ; therefore U_{int} must be finite even with infinitely large bare interactions. Furthermore, Gutzwiller [75, 76] approximately calculated that the non-magnetic state in the presence of strong correlations can have lower energy than a ferromagnetic state at low density. For this, he constructed his famous projected wavefunction describing the reduction of on-site interaction energy in a lattice. However, both arguments by Kanamori and Gutzwiller are based on the lattice-model so that further theoretical developments are required to treat correlation effects in a interacting free Fermi gas.

Recent work [205] has shown, within a phenomenological model, that correlations

can lead to similar experimental signatures as we have observed [102]. However, the model does not quantitatively agree with our data, and has some qualitative discrepancies as well; for example the extrema of lifetime, kinetic energy and cloud size do not occur at the same value of the parameter $k_F a$ in contrast to our observations. It would be interesting to see if further development of the alternative theories could lead to quantitative agreement with experiments.

4.5 Outlook: New Experiments

RF quench experiment with $|1\rangle$ and $|3\rangle$ atoms: studying of non-equilibrium properties of the strongly interacting system.

As we have seen in the previous section, the MIT experiment shows some aspects of both equilibrium and non-equilibrium dynamics. Our theoretical understanding of Stoner’s model basically relies on equilibrium properties whereas the finite experimental time scales (for example, field ramp time of 4.5 ms) suggests that the system is marginally adiabatic after rapid ramps of the magnetic field; therefore, non-equilibrium.

In the previous experiment, we have prepared a strongly interacting mixture of $|1\rangle$ and $|2\rangle$ state atoms near the Feshbach resonance located at 834 G. For this, the magnetic field is ramped towards the resonance (834 G) within 4.5 ms. Unfortunately, our current coil geometry did not allow sufficiently fast field ramp and the timescale of the field ramp is not fast enough to study the quantum dynamics of systems in non-equilibrium state, e.g. how magnetic domains grow, how itinerant ferromagnetic phase transition occurs, and how clock shifts are suppressed.

Here, we propose a rapid switching of interaction strength using a quick RF spinflip, which transforms a weakly interacting $|1\rangle$ - $|2\rangle$ mixture of fermions into a strongly interacting $|1\rangle$ - $|3\rangle$ one (see figure 4.5). Preparing the $|1\rangle$ - $|2\rangle$ mixture near a $|1\rangle$ - $|3\rangle$ Feshbach resonance for near 670 G, and applying RF photons to transfer $|2\rangle$ atoms into the $|3\rangle$ state. The RF spinflip may take a few hundred μs which is marginally fast compared to the timescale of non-equilibrium dynamics (about $\sim (E_F/10)^{-1} \simeq 300\mu s$) [14]. Note that a $|1\rangle$ - $|3\rangle$ mixture of fermions does not suffer from “final-state effect” in the RF spectroscopy [175]. Therefore, the measurement of clock shifts in the $|1\rangle$ - $|3\rangle$ mixture offer another tool to characterize the system.

Single-domain ferromagnetic state: Ramsey-type measurement of coherence The observation of ferromagnetic domains is considered as an experimental

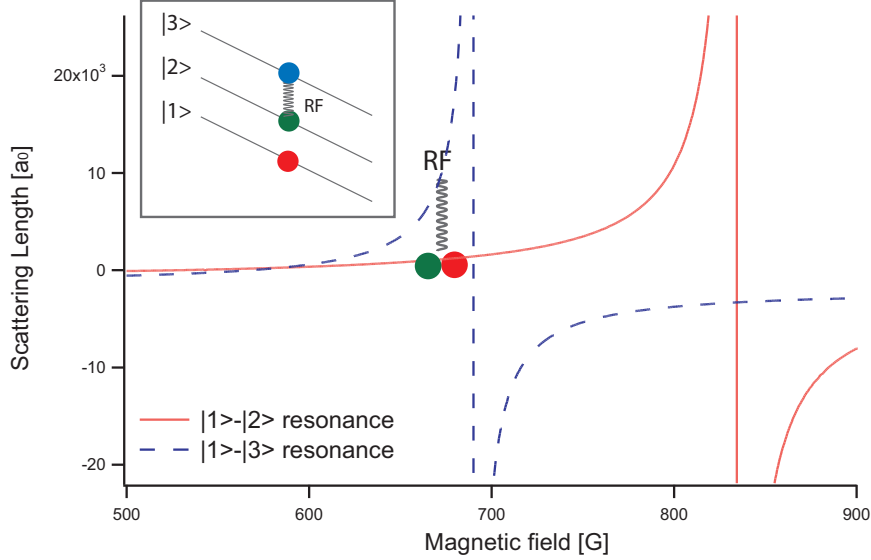


Figure 4-9: Schematic illustration of the RF quench experiment. A radio-frequency pulse is applied in order to transform a weakly interacting $|1\rangle$ - $|2\rangle$ mixture of fermions into a strongly interacting $|1\rangle$ - $|3\rangle$ one. The scattering length near the Feshbach resonance in the $|1\rangle$ - $|2\rangle$ (red solid curve) and $|1\rangle$ - $|3\rangle$ (blue dashed curve) mixture is shown.

smoking gun in itinerant ferromagnetism of cold Fermi gas since the ground state in the stable ferromagnetic state consist of a single domain. The ferromagnetic domains, however, were not observed in the previous MIT experiment [102] probably due to the short lifetime of the systems which did not allow the domains to grow to larger sizes [14]. Although non-equilibrium dynamics after quenching, such as the growth rate of the ferromagnetic domain, may offer an opportunity for experimental studies, this limits us to characterize and test the ferromagnetic equilibrium state.

Here, we propose to use an alternative approach preparing the system directly in the ground state. First, the absolute ground state can be created by preparing a coherence mixture of atoms in the $(|1\rangle+|2\rangle)/\sqrt{2}$ state as pointed out in Ref [52]. In the presence of magnetic field inhomogeneities ², the coherent mixture rapidly dephases in about ~ 10 ms for weak interactions [72]. However, in the ferromagnetic region, dephasing is suppressed since it costs energy to break up one domain into many. The suppression of dephasing in this regime may be characterized by (1) monitoring clock shifts in the sample or (2) measuring atom-atom collisions (lifetime of the sample). In the ferromagnetic ground state, we expect that clock shifts and atom-atom collisions

²In our experimental setup, magnetic field inhomogeneities are inevitable as the axial confinement in the trapping potential mainly rely on the magnetic trap

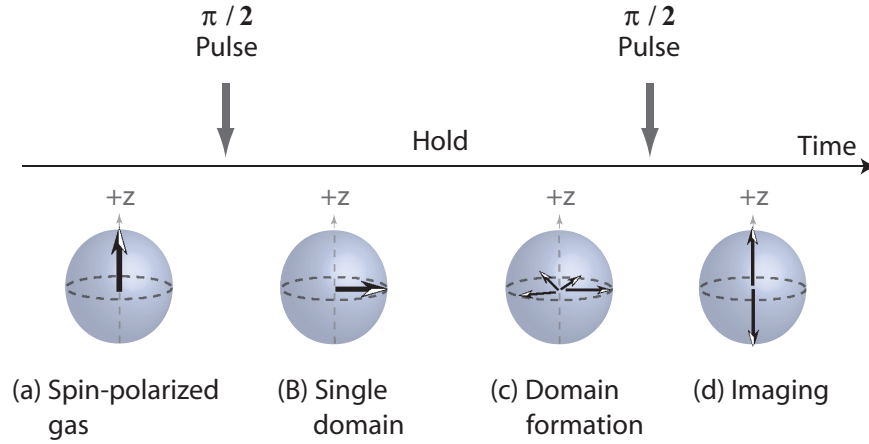


Figure 4-10: Schematics illustration of the single domain experiment

are highly suppressed.

The interplay between magnetic inhomogeneities and the ferromagnetic stabilization energy would be more prominent in the Ramsey-type measurement of coherence (see figure 4.5). Preparing a single ferromagnetic domain (in $x - y$ plane in the Bloch sphere) via the first $\pi/2$ pulse, we can resolve spatial spin structures after some dephasing by selectively imaging the atomic cloud in two spin states ($+z$ and $-z$ in the Bloch sphere) via the second $\pi/2$ pulse.

Chapter 5

Quantum Phase Coherence in Degenerate Bosonic Gases

This chapter describes phase coherence of Bose-Einstein condensates (BECs) and the decoherence dynamics. The experimental tools for a phase read-out and a phase coherent splitting of Bose-Einstein condensates shall be discussed at the end of the chapter.

5.1 Phase Coherence in a Bose-Einstein Condensate

What is the phenomenon of Bose-Einstein condensation? To understand it, one needs to formulate some of fundamental concepts such as long-range order, spontaneously broken gauge symmetry, and order parameter [9]. In this section, I summarize those concepts in the context of a weakly interacting Bose gas. From the following discussions, we shall see that a many-body ground state of weakly interacting Bose condensed atoms can be described by a condensate wavefunction (or a macroscopic wavefunction) which possesses a well-defined phase.

Criterion for Bose-Einstein Condensation

In an ideal Bose gas in three dimensional potential, Bose-Einstein condensation occurs when the particle density in the zero momentum state has a finite value. In this case, the condensation is a first-order phase transition, but this is not generally valid in a weakly interacting Bose gas [87]. The weakly interacting Bose gas requires a more general definition of Bose-Einstein condensation, and surprisingly it had taken long

time about 40 years from the first theoretical work about BEC to the generalized criterion for Bose-Einstein condensation [92]. The generalized criterion for Bose-Einstein condensation was first proposed by Penrose and Onsager [149] considering the one-particle density matrix $\rho_1(x, y) = \langle \psi^\dagger(x)\psi(y) \rangle$;

$$\langle \psi^\dagger(x)\psi(y) \rangle \longrightarrow \langle \psi(x) \rangle^* \langle \psi(y) \rangle \text{ when } |x - y| \longrightarrow \infty \quad (5.1)$$

where $\langle \rangle$ denotes ensemble average and $\psi(x)$ is a quantized boson field operator at the position of r . Here, the complex number $\langle \psi(x) \rangle$ is called as “condensate wavefunction”, and non-vanishing $\langle \psi(x) \rangle$ implies the existence of a Bose-Einstein condensate. In this case, the condensate wavefunction is characterized by a modulus $\sqrt{n_0(x)}$ and a phase $\phi(x)$

$$\langle \psi(x) \rangle = \Phi(x) = \sqrt{n_0(x)} e^{i\phi(x)} \quad (5.2)$$

This criterion is often referred to as “*off-diagonal long-range order*” [204] because it involves the off-diagonal matrix element of the one-particle density matrix.

In the above criterion, however, one immediate question is raised up as follows. Given a “global gauge invariance” of the Hamiltonian describing the system, $\langle \psi(x) \rangle$ must be always zero in the ensemble average because every value of $\psi = \sqrt{n_0} e^{i\phi}$ is canceled by a value of $\psi = \sqrt{n_0} e^{i\phi+i\pi}$ after a constant phase change of ψ . Therefore, Bose-Einstein condensation can never occur in this mathematical argument.

The resolution of this conceptual problem lies in the recognition that the symmetry of the original Hamiltonian may be spontaneously broken in nature. In this picture, the symmetry of the Hamiltonian is no longer applicable to the ground state. The concept of *spontaneously broken gauge symmetry* (SBGS) is of importance nowadays in condensed-matter physics, and generally believed to be the key to explore the exotic phenomena such as superfluidity and superconductivity [9]. The idea of SBGS is often adopted to account for a phase transition as it typically occurs between phases with different symmetry. In most cases, the phase transition brakes the symmetry during the process ¹. Following this concept of SBGS, the ensemble average of ψ , $\langle \psi(x) \rangle$, has a non-vanishing value even in the presence of the global gauge invariance.

Finally, the criterion of 5.1 reveals another major phenomenon of Bose condensates, “*phase coherence*”. Phase coherence implies that the phase of the condensate

¹This is not always true. For example, the infinite-order phase transitions are continuous but break no symmetries. One of the famous example is Kosterlitz-Thouless transition in two-dimensional XY model. In 2D, many phase transitions in electron gases belong to this class.

wavefunction, $\phi(x)$, must be spatially correlated over the length scale of the whole system. This enables us to treat Bose condensed atoms as being governed by the same wavefunction $\psi(x)$, which is actually the condensate wavefunction.

We are now ready to identify an *order parameter* describing the Bose-Einstein condensed phase. The order parameter is proposed by Landau in his theory of the second-order phase transition [9]. He pointed out that one can define the order parameter for the phase transition accompanied by symmetry breaking. The order parameter is simply any parameter which is zero in the symmetric state and has a nonzero value in the unsymmetrical state after the phase transition. In the case of Bose gases, a suitable choice of the order parameter is the condensate wavefunction 5.2. Its modulus determines the density of the condensate through $n_0^2(x) = |\psi(x)|^2$ and the phase of the condensate is well-defined through $\phi(x)$.

Mean-field description of a weakly interacting Bose gas.

So far, we have assumed that all particles stay in the zero momentum state when Bose-Einstein condensation occurs. Starting from the generalized criterion 5.1, the order parameter 5.2 characterizing the condensate wavefunction is identified for the non-interacting Bose gas. This approach still retains validity when we introduce weak interactions between atoms. To this end, the boson field operator is decomposed in the form of

$$\psi(x) = \Phi(x) + \psi'(x) \tag{5.3}$$

where $\Phi(x) = \sqrt{n_0(x)}e^{i\phi(x)}$ denotes the order parameter and $\psi'(x)$ describes the non-condensed particles which occupy non-zero momentum states which is referred to as the “quantum depletion” of the condensate. By treating $\psi'(x)$ as a small perturbation, Bogoliubov formulated a mean-field description of a dilute Bose gas with weak interactions, and developed the first-order theory for the excitations of interacting Bose gases [26]. In his approach, the boson field operator is replaced by the mean-field term $\Phi(x)$ with a small fluctuations characterized by $\psi'(x)$. For weakly interacting alkali condensates, the quantum depletion is less than 1% whereas liquid helium has large quantum depletion of 90%.

Bogoliubov’s idea separating out the condensate contribution from the boson field operator (see equation 5.3) becomes particularly useful when the quantum depletion is negligible. In this case, we can derive the equation for the condensate wavefunction $\Phi(x)$ as a result of the zeroth-order perturbation theory. To this end, we first introduce

a many-body Hamiltonian describing N interacting bosons trapped by an external potential V_{ext} in second quantization:

$$\hat{H} = \int dr \psi^\dagger(r) \left[-\frac{\hbar^2}{2m} \nabla^2 + V_{ext}(r) \right] \psi(r) + \frac{1}{2} \int dr dr' \psi^\dagger(r) \psi^\dagger(r') V(r-r') \psi(r') \psi(r) \quad (5.4)$$

where $V(r-r')$ describes an arbitrary two-body interaction potential and m denotes the mass of particles.

For a weakly interacting dilute alkali condensate, the two-body interaction potential $V(r-r')$ reduces to the effective potential characterized by a single parameter, the s-wave scattering length a :

$$V(r-r') = g\delta(r-r') \quad (5.5)$$

where $g = \frac{4\pi\hbar^2 a}{m}$.

Now, nonlinear Schrodinger equation for the condensate wavefunction $\Phi(x)$ is derived in the mean-field description:

$$\left(-\frac{\hbar^2}{2m} \nabla^2 + V_{ext}(r) + g\Phi^2(x) \right) \Phi(x) = \mu\Phi(x) \quad (5.6)$$

where μ is the chemical potential. The equation 5.6 is called ‘‘Gross-Pitaevskii equation’’ [69, 70] which is one of the main tools for investigating ultracold Bose condensed atoms trapped in a nonuniform potential. The generalization of Bogoliubov’s mean-field description to time-dependent configurations is given by the Heisenberg equation

$$i\hbar \frac{\partial}{\partial t} \Phi(x, t) = [\Phi, \hat{H}] \quad (5.7)$$

giving the equation for the condensate wavefunction $\Psi(x, t)$.

For more comprehensive discussions on the description of Bose condensed atoms, I refer the reader to many excellent books, for example by Pethick and Smith [152] and Pitaevskii and Stringari [159].

5.2 Decoherence in Interacting Bose Gases

Decoherence can be defined as the loss of information from the system that we are considering into the environment. The major sources of decoherence are either the interaction of the system with the environment or the intrinsic quantum and/or thermal fluctuations in the system. In the system of cold atomic gases, the information we are interested in is the phase of the condensate. By definition described in previous section, the condensate has phase coherence over the whole system. However, the system of condensates inevitably undergoes decoherence process due to quantum and thermal fluctuations associated with atom-atom interactions. Of particular interest is the loss of phase coherence with time (so-called *phase diffusion*) and the loss of spatial coherence along the condensate (*phase fluctuation*).

Phase diffusion

For two separated Bose-Einstein condensates, a state of well-defined relative phase (so called *phase coherent state*), $|\phi\rangle$, is a superposition state of many relative *number states*, $|N_1, N_2\rangle$ (or $|k, N - k\rangle$), where N_1 and N_2 are the occupation of each well for $N = N_1 + N_2$ atoms. Initially ($t = 0$), a phase coherent state takes the form of:

$$|\phi(t = 0)\rangle = \frac{1}{2^{N/2}} \sum_{k=0}^N \sqrt{{}_N C_k} e^{i\phi k} |k, N - k\rangle \quad (5.8)$$

Because of atom-atom interactions in the condensates, the energy of number states, $E(N_1, N_2)$, have a quadratic dependence on the atom numbers N_1 and N_2 :

$$E(N_1, N_2) = \frac{d\mu}{dk} \Big|_{k=N/2} (k - N/2)^2 \text{ where } k = \frac{N + (N_1 - N_2)}{2} \quad (5.9)$$

where μ is the chemical potential of condensates. As a result, the different relative number states have different phase evolution rates [35, 96] leading to a spread of evolution rates, causing “*phase diffusion*” or “*decoherence*” of the relative phase with time. A phase coherent state at time t is given by:

$$|\phi(t)\rangle = \frac{1}{2^{N/2}} \sum_{k=0}^N \sqrt{{}_N C_k} e^{i\phi k} e^{-iR(k-N/2)^2 t} |k, N - k\rangle \quad (5.10)$$

The phase diffusion rate, R , is proportional to the derivative of the chemical potential of condensates, $\mu(N_i)$ ($i = 1, 2$), with respect to the atom number and the standard deviation of the relative atom number, ΔN_r [35, 122, 202, 96, 117, 97]:

$$R = (2\pi/h)(d\mu/dN_i)_{N_i=N/2}\Delta N_r \quad (5.11)$$

A typical decoherence time $1/R$ in a condensate is less than 50 ms. A number squeezed state with sub-Poissonian number fluctuations ($\Delta N_r = \sqrt{N}/s$), where $s > 1$ is the squeezing factor, will exhibit a reduced phase diffusion rate relative to a phase coherent state with $\Delta N_r = \sqrt{N}$. Now, the question is how to prepare a number squeezed state in condensates. Indeed, it turned out that atom-atom interactions tends to localize atoms during splitting process leading to number squeezing as we shall discuss in the next chapter 6.

In contrast to normal diffusion processes, the phase uncertainty, $\Delta\phi$, increases here linearly. The phase uncertainty evolves with time as follows:

$$\Delta\phi(t)^2 = \Delta\phi_0^2 + (Rt)^2 \quad (5.12)$$

where $\Delta\phi_0 \simeq (s/\Delta N_r)$ is the initial phase uncertainty. Interestingly, the term “phase diffusion” is not really appropriate because the phase diffusion has a time dependence of $\propto t$, not $\propto \sqrt{t}$.

Phase fluctuation

So far, we have seen that a Bose-Einstein condensate should have a phase coherence over a long-range length scale which is equal to the size of the condensate. This long-range coherence in a condensate is generally valid in three-dimensional systems, but not in one- or two-dimensional systems where phase fluctuations play the important role.

Phase fluctuations cause the condensate to break up into several quasi-condensates with random phase, i.e. long range coherence is lost. This usually happens in elongated geometries when the temperature is sufficiently high to excite such modes [155, 51], or in interacting one-dimensional condensates even at zero temperature due to quantum fluctuations [23].

A typical elongated trap geometry, for example realized by an atom chip, has an aspect ratio of ~ 200 [179, 174, 101], sufficient to induce phase fluctuations in a quasi-condensate along the axial direction [155] already at very low temperatures (or in the 1D case, even at zero temperature). When the temperature of a condensate is

above the characteristic temperature,

$$T^* = \frac{15N(\hbar\omega_z)^2}{32\mu} \quad (5.13)$$

where μ is the chemical potential, N total atom number, ω_z axial trap frequency, and \hbar the Planck's constant divided by 2π [155], then thermal excitations of low energy axial modes lead to longitudinal phase fluctuations. For temperatures above T^* , the coherence length L^* of a phase-fluctuating condensate is shorter than the length L of the condensate $L^*/L = T^*/T$ [155].

When Bose condensates are used for atom interferometry, spatial phase fluctuations have two major consequences. First, they speed up phase diffusion, since $\Delta N/N$ refers now to the atom number in a single quasi-condensate. Second, they make the atom interferometer much more sensitive to random relative displacements of the split condensates, which have to be smaller than the coherence length, which, for condensates with phase fluctuations, can be much smaller than the size of the condensate.

5.3 Measurement of the Relative Phase between Two Condensates

Bose-Einstein condensates have phase coherence over the whole atomic cloud unless phase diffusion and phase fluctuations emerge and destroy it. Of particular interest has been the investigation of phase coherence properties in various systems such as the Josephson junction in a double-well potential, optical lattices, and elongated one-dimensional system.

In related efforts, access to a phase-coherent condensate has brought a new family of interferometry technique in atom optics, so-called confined atom interferometry. Until our work reported in chapter 7, the only method to read out the relative phase has been the “ballistic expansion” method. In this scheme, two spatially separated condensates with the well-defined relative phase are released after some hold time from their confining potential, and finally the phase shift is obtained by imaging and analyzing the interference pattern formed in the overlapped atomic cloud. To date, the relative phase has been reliably measured after ballistic expansion of two separated condensates to decrease the atomic density [177]; therefore atom-atom interactions are negligible during phase read-out. Nevertheless, the ballistic expansion method lacks

the simplicity and robustness of in-trap recombination. In addition, the condensates cannot be recycled after phase read-out because of the destructive expansion of the condensates.

In this section, we demonstrate three different phase read-out methods; (1) ballistic expansion method (2) phase sensitive in-trap recombination method and (3) optical read-out method (summarized in figure 5-2). Recent developments including the method (2) and (3) suggest that the confined atom interferometer can circumvent the deleterious effects of atom-atom interactions during phase read-out.

(1) Ballistic expansion method

In this method, the relative phase between the two separated condensates is determined by the spatial phase of their matter wave interference pattern formed after ballistic expansion as described in figure 5-1. The ballistic expansion reduces the atomic density so that the effects atom-atom interactions are neglected when two condensate are overlapped. For a ballistic expansion time $t \gg 1/\omega_r$ where ω_r is the trap frequency along the axis connecting two condensates, each condensate had a quadratic phase profile [46],

$$\psi_{\pm}(\vec{r}, t) = \sqrt{n_{\pm}(\vec{r}, t)} \exp(i \frac{m}{2\hbar t} |\vec{r} \pm \vec{d}/2|^2 + \phi_{\pm}) \quad (5.14)$$

where \pm indicates the left or right condensate, n_{\pm} the condensate density, m atomic mass, \vec{d} the vector connecting two condensates, and ϕ_{\pm} the condensate phase. The overlapped interference pattern now becomes,

$$n(\vec{r}, t) = |\psi_+ + \psi_-|^2 = [n_+ + n_- + 2\sqrt{n_+n_-} \cos(\frac{md}{\hbar t}x + \phi_r)] \quad (5.15)$$

Here, the relative phase ($\phi_+ - \phi_-$) can be extracted from the spatial phase shift $\phi_r = \phi_+ - \phi_-$ in the modulated pattern of eq. 5.15. In the experiment, one can fit an integrated cross section of the matter wave interference pattern with sinusoidally-modulated Gaussian curve (see figure 5-1),

$$I(x) = \alpha \exp(-(x - x_0)^2/\sigma^2) [1 + \beta \cos(\frac{2\pi}{\lambda}(x - x_0) + \phi_r)]. \quad (5.16)$$

obtaining the relative phase, ϕ_r , of two condensates. Note that fringe spacing, $\lambda = \frac{\hbar t}{md}$, is proportional to the expansion time and the inverse of the separation between two condensates.

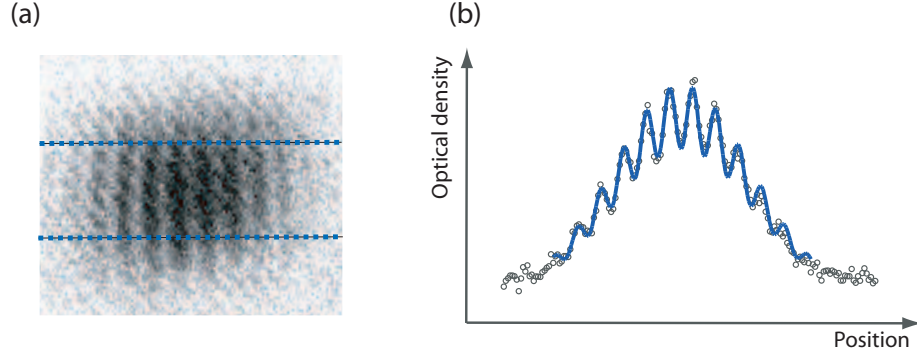


Figure 5-1: Matter-wave interference and relative phase read-out. (a) Absorption image of an overlapped condensate released from double-well potential is taken after 10 ms time-of-flight. The optical density profile (open circle in (b)), obtained by integrating the the optical signal between two dashed lines, is fitted to a sinusoidally-modulated Gaussian curve (blue curve in (b)) as shows in section 5.3 from which the relative phase is measured.

(2) Phase sensitive in-trap recombination method

In contrast to the ballistic expansion of atom clouds, in-trap recombination of two condensates is inherently simple and robust, and moreover it allows one to store the condensates in a confined potential during the measurement process. This is one definite advantage of a confined atom interferometer without precedent in optics. The challenge, however, is how to extract the relative phase after connecting two originally separated condensates. It was pointed out that the recombination process may produce the excited mode with exponential growth rate, leading to an unstable measurement in phase [60]. Recently, however, we demonstrated that in-trap recombination leads to heating of the atomic cloud. The heating is phase-sensitive and can be used as a robust phase read-out of the atom interferometer. This method potentially gives us an opportunity to recycle condensates after resetting the temperature through evaporating cooling. Experimental details shall be discussed in chapter 7.1.

(3) Optical read-out method

Both phase read-out methods we have seen above rely on the merger of two separated condensates with or without ballistic expansion. This requires coherent control of external (motional) state in order not to perturb the phase. Recently, a new phase-readout method based on stimulated light scattering was proposed [158], and demonstrated experimentally [166]. Two counter-propagating laser beams outcouple

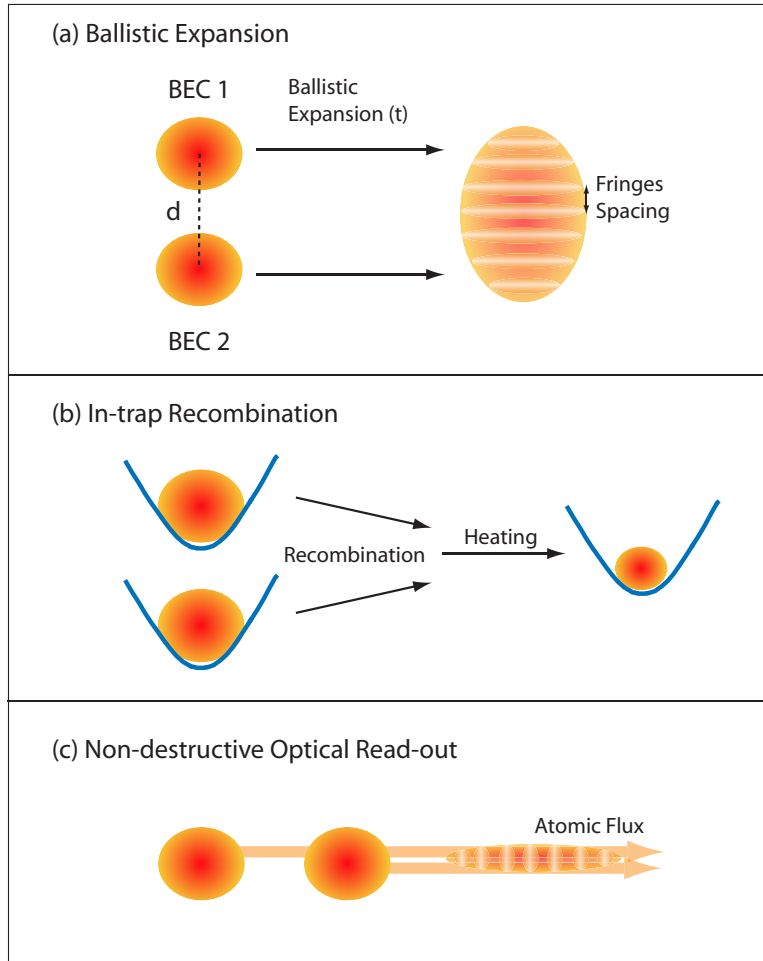


Figure 5-2: Schematics for measuring the relative phase of two separated condensates are shown: (a) ballistic expansion method, (b) in-trap recombination method, and (c) non-destructive optical read-out method. Additional details are discussed in the text.

a small fraction of atoms from the two spatially separated condensates leading to an interference between outcoupled atomic clouds. By monitoring the rate of outcoupled atoms or the number of scattered photons, the relative phase between two original condensates can be determined. In this process, the phase measurement establishes the relative phase between two (originally) independent condensates. Note that this method is nondestructive similar to the in-trap recombination method.

5.4 Tools for the Study of Coherence Properties of a Bose gas

For the study of coherence properties in Bose gases including phase diffusion [177, 174, 101], phase fluctuations [80, 163, 99], and non-equilibrium dynamics in one-dimensional system [83, 23], interferometric measurements provide a very robust and precise way to extract the physical quantities that we want to measure. For all these purposes, it is imperative that the relative phase between two Bose condensates is not perturbed by the splitting process itself. Recently, the coherent control of external (or motional) [177, 174, 101] and internal [21] quantum states ² in a Bose condensate has been demonstrated. Here, we focus on the external dynamics assuming that internal quantum states (usually hyperfine state in cold atom experiments) are conserved. By deforming a single trapping potential into double wells, the wavepacket of a condensate is spatially delocalized into two wells adiabatically; we call this process “*coherent splitting*”. For the coherent splitting, there are two important time scales, namely the oscillation period in a trap τ_{trap} and the collapse time $\tau_{collapse}$. The time scale τ at which the splitting ends up should be adiabatic with respect to the external dynamics (i.e. $\tau \gg \tau_{trap}$), but non-adiabatic the internal time scale related to collapse-revival process (i.e. $\tau \ll \tau_{collapse}$). In a typical BEC experiment, $\tau_{collapse}$ is on the order of 5~50 ms.

The coherent splitting in a confined interferometer has been firstly demonstrated by Shin *et al.* in an optical double-well potential [177], and then by Schumm *et al.* in a magnetic trap combined with oscillating radio frequency field [174].

Coherent splitter using an adiabatic RF-induced potential

Adiabatic RF-induced potential was first proposed in order to trap neutral atoms in a two-dimensional geometry [208]. Combining static magnetic trapping field with oscillating radio frequency (RF) near fields, the original magnetic potential adiabatically evolves into the effective dressed potential as described in figure 5-3 (a)-(c). Here, an RF field couples internal atomic state with different magnetic moments characterized by the quantum number m_F ³. In a dressed state basis, the effective potential $V_{eff}(r)$

²Note that coherent control of internal states (in state-dependent fashion) is a crucial ingredient to realize quantum entanglement in combination with controlled collisions.

³Adiabatic RF-induced splitting sometimes can be considered as “anti-evaporation”. Whereas the evaporation process removes atoms with higher kinetic energy in an untrapped internal state by adiabatically coupling two different internal state, RF-induced splitting adiabatically keeps atoms in trapped internal state. In evaporation, the RF resonance is near the outer turning point; in

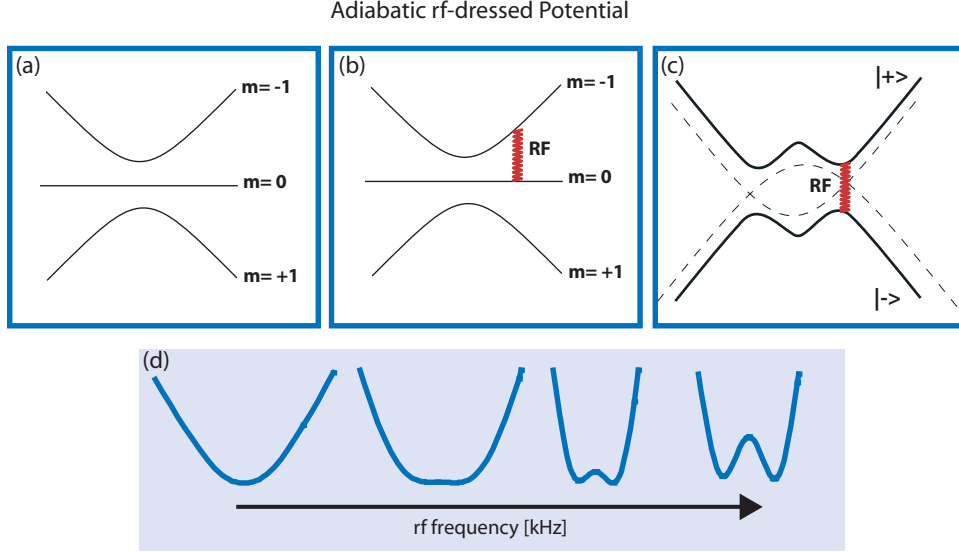


Figure 5-3: Schematic for an adiabatic RF-induced splitter used in MIT experiments. Three different spin states are shown in (a). In the presence of oscillating radio frequency fields (b), the effective potential becomes double wells in a dressed state basis (c). (d) By adjusting the RF frequency, a single well is smoothly transformed into double wells allowing for coherent splitting of a condensate. Note that coherent splitting can also be possible by varying RF amplitude at a fixed RF frequency [174].

at position r is determined by

$$V_{eff}(r) = m_F \sqrt{[\mu_B g_F B_{d.c}(r) - \hbar \omega_{RF}]^2 + [\mu_B g_F B_{RF\perp}(r)/2]^2} \quad (5.17)$$

where g_F is the Lande g -factor, μ_B the Bohr magneton, $B_{d.c}$ the magnitude of the static magnetic field, $B_{RF\perp}$ the magnitude of the component of the RF field perpendicular to the direction of static field, and ω_{RF} the RF frequency.

Recently, the adiabatic rf-induced potential has been implemented into an atom chip realizing coherent splitting of condensates [174]. By turning on the RF field adiabatically, the single trapping potential smoothly transforms into double wells. Here, the conditions for adiabatic switch-on of the RF field are given by Landau-Zener theory.

The wires on the atom chip carry both d.c current and oscillating current. Depending on the relative geometry between the static trapping potential and the RF field, the direction of splitting can be arbitrarily controlled as described in figure 5-4 (a) [84].

RF-induced splitting, it is near the inner turning point.

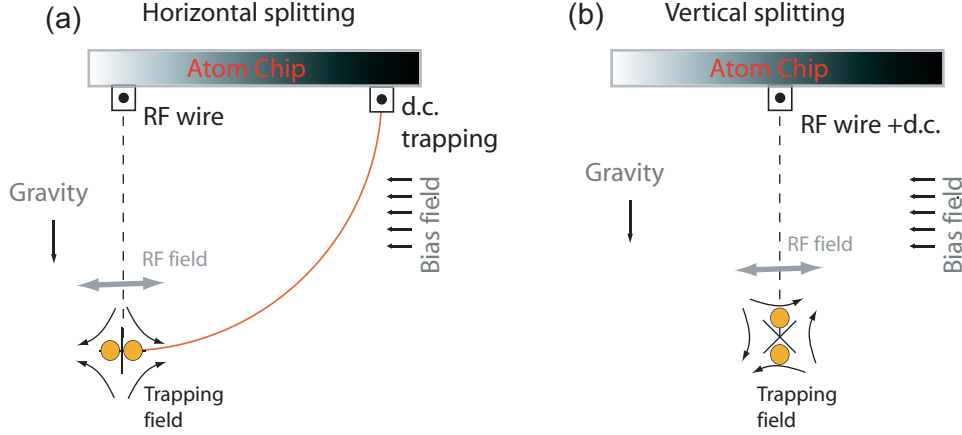


Figure 5-4: The spatial orientation of the double-well potential is determined by the relative orientation of the static magnetic field and the oscillating magnetic RF field. Potential minima form where both the static and the oscillating fields are parallel as described in (a) and (b). The red circle in (a) represents the position of the trapping potential where a double-well potential is formed in the horizontal direction.

The adiabatic RF-induced splitting has several advantages [119] over the conventional two-wire scheme [179] which requires two independent wires generating quadrupole trap. During the merging and splitting process in the two-wire scheme, the trapping potential becomes very weak. Confinement is no longer parabolic, but caused only by higher-order multipoles (usually hexapole) leading to a significant weak confinement. This often induces unwanted atom loss during splitting, and therefore makes the splitting region unstable. The adiabatic RF-induced splitting, however keeps the confinement tight during splitting or merging and does not suffer from the atom loss. In addition, the RF-induced splitting is less sensitive to magnetic bias fields and realizes high trap-frequencies far from a surface.

Figure 5-4 demonstrates the coherent beam splitter implemented at MIT (see chapter 6 for experimental details).

Towards precision measurement with Bose-Einstein condensates.

So far, we have discussed the phase coherence between two separated condensates. This property allows us to build a new type of atom interferometer with BECs. In atomic physics, precision measurements are usually performed at low atomic densities because of collisional shifts and dephasing. Since the atom-atom interaction energy results in so-called clock shifts [63] which are proportional to the high density, most precision measurements with neutral atoms are performed with free-falling atoms in

atomic beams [118, 73] or in fountain geometries [151]. Major efforts are currently directed towards atom interferometry using confined geometries, such as atom traps or waveguides, often realized by using atom chips [59, 45]. These geometries are promising in terms of compactness and portability, and also offer the prospect of extending interrogation times beyond the typical 0.5 s achievable in the atomic fountains [151]. In spite of these advantages, confined atom interferometer has a few intrinsic limitations; e.g. phase diffusion [35, 122, 202, 96, 117, 97] and spatial phase fluctuations (see section 5.2). In the following chapter, we shall show that a chip-based atom interferometer can be operated even in the presence of both phase diffusion and phase fluctuations.

Chapter 6

Long Phase Coherence Time via Number Squeezing and Phase Fluctuations of BECs in a Double-well Potential

This chapter describes the experimental studies of phase coherence and the decoherence dynamics of Bose-Einstein condensates in a double-well potential. The experiments were reported in two publications:

- G.-B. Jo, Y. Shin, S. Will, T. A. Pasquini, M. Saba, W. Ketterle, D. E. Pritchard, M. Vengalattore, and M. Prentiss

Long phase coherence time and number squeezing of two Bose-Einstein condensates on an atom chip

Physical Review Letters **98**, 030407 (2007) Included in appendix H.

- G.-B. Jo, J.-H. Choi, C.A. Christensen, Y.-R. Lee, T.A. Pasquini, W. Ketterle, and D.E. Pritchard

Matter-wave Interferometry with Phase Fluctuating Bose-Einstein Condensates

Physical Review Letters **99**, 240406 (2007) Included in appendix E.

In this chapter, we discuss the phase coherence of a Bose-Einstein condensate trapped in an elongated atom-chip trap. Two main questions are addressed in section 6.1 and 6.2 respectively:

- (1) How long can the *phase coherence* between separated condensates be maintained

and how can one enhance the phase coherence time?

(2) What is the effect of spatial *phase fluctuations* on atom interferometry?

6.1 Long Phase Coherence Time and Number Squeezing

The distinguished property of Bose-Einstein condensates (BECs) is their *phase coherence*. High-contrast interference between condensates [11] clearly revealed this property. Observations of many interesting phenomena, including Josephson oscillations [36, 5], number squeezing [142], and the transition from superfluid to Mott insulator [66] rely on phase coherence between two spatially separated condensates.

As we have seen in the previous chapter 5, an RF beam splitter allows us to study and/or exploit the phase coherence in condensates in many different ways. Here, our system consists of a double-well potential on an atom chip with adjustable barrier between two wells. This tunable barrier in a double-well system allows for the preparation of coherent state of condensates, the realization of Josephson junction, the study of decoherence dynamics, and the development of confined atom interferometry. Furthermore, the geometry of the magnetic trap generated by an atom chip introduces low-dimensional effects including phase fluctuations as follows.

- Highly nonequilibrium system :

In contrast to equilibrium properties of a Bose condensate, the relaxation dynamics from nonequilibrium states is not well-understood [90]. One reason is that it is relatively difficult to prepare such a nonequilibrium state in a coherent manner. For the split-condensate system built in MIT experiments [99], a phase coherent state is highly out of equilibrium, and the condensates inevitably suffer from both quantum and thermal decoherence over time. In particular, the relaxation process is of interest and importance in low-dimensional systems in which quantum decoherence effects are more prominent [99, 83, 85].

- Bosonic Josephson Junction (BJJ) :

The Josephson effects, predicted by Brian D. Josephson in 1962 [104], occur when two macroscopic quantum states are weakly connected. First experimental realization was made in the system of two superconductors coupled via an insulating thin film and later the effects were observed in superfluid helium-3 and helium-4. Recently, the Josephson effects was also studied in Bose-Einstein

condensates [36, 2]. Bose-Einstein condensates in a double-well potential with tunable barrier becomes available allowing for unprecedented quantitative investigation of the Josephson effects.

- Low-dimensional physics :

As we have discussed in the section 5.2, the effect of phase fluctuations associated with quantum and thermal fluctuations becomes important in elongated quasi-1D condensates realized on an atom chip. The coherent dynamics in degenerate quasi-1D Bose atoms can be investigated in an interferometric way using coherent the RF splitter.

- Towards chip-based atom interferometry :

A coherent beam splitter is one of the essential parts for confined atom interferometry. In general, a good confined atom interferometer requires the following conditions: (1) high atomic density leading to large signal-to-noise ratio, (2) long phase coherence time for high sensitivity, (3) efficient and reliable phase read-out, and (4) uniform phase along the condensate. Bose-Einstein condensates, a very bright source of atoms, have been considered to be used in a confined atom interferometer because of their phase coherence and high atomic density (condition (1)). In this chapter, we experimentally demonstrate that a chip-based atom interferometer installed at MIT is promising to maintain phase coherence over a sufficiently long time (condition (2)). The robustness of the system against phase fluctuations is also described in section 6.2 (condition (4)). For phase read-out methods, conventional and recently developed methods are described in section 5.3 and chapter 7. All recent developments including MIT experiments suggest that it is possible to operate confined atom interferometer with Bose condensates at high atomic density.

6.1.1 Splitting Process in a Double-well Potential: a Bosonic Josephson Junction

Splitting of the condensate results in two separated condensates which cannot be suitably described by the Gross-Pitaevskii equation (GPE) [69, 70] which describes atoms only in a single-mode. This can be resolved by taking an approximate form of the bosonic field operator in the two-mode basis which naturally consists of the ground [symmetric, figure 6-1 (a)] and the first excited state [antisymmetric, figure 6-1 (b)] in a double-well system. In this section, I will derive a relevant Josephson Hamiltonian

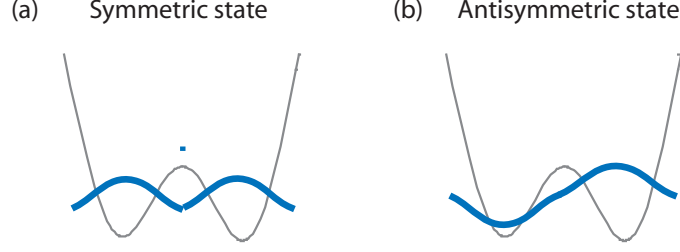


Figure 6-1: Schematic illustration of the ground and the first excited state in a double-well potential. The symmetric ground state (a) and the antisymmetric excited state (b) are shown.

describing the splitting of the condensates in the two-mode approximation.

Two-mode approximation and a Josephson Hamiltonian

The relevant Hamiltonian describing weakly interacting bose condensed atoms in a double-well potential is given by

$$\hat{H} = \int d^3r \left[-\frac{\hbar^2}{2m} \Psi^\dagger(r) \nabla^2 \Psi(r) + U(r) \Psi^\dagger(r) \Psi(r) + \frac{g}{2} \Psi^\dagger(r) \Psi^\dagger(r) \Psi(r) \Psi(r) \right] \quad (6.1)$$

where $\Psi(r)$ is a bosonic field operator, $U(r)$ the external potential describing a double-well, and $g = 4\pi a \hbar^2 / m$ the interaction strength with the s-wave scattering length a and atomic mass m . In two-mode approximation, $\Psi(r)$ becomes the superposition of the ground state ψ_g and the excited state ψ_e with appropriate creation (or annihilation) operators:

$$\Psi(r) = \hat{a}_g \psi_g + \hat{a}_e \psi_e \quad (6.2)$$

Here, \hat{a}_g^\dagger (\hat{a}_e^\dagger) is the creation operator for a particle in the ground state (excited state). Now, the observable quantities such as the atom number and the relative phase can be conveniently described by changing the basis as follows:

$$\hat{a}_L = \frac{1}{\sqrt{2}}(\hat{a}_g + \hat{a}_e) \text{ and } \hat{a}_R = \frac{1}{\sqrt{2}}(\hat{a}_g - \hat{a}_e) \quad (6.3)$$

In this new basis, the relevant quantum state become ψ_R (ψ_L) denoting the wavefunction of localized atoms in the right (left) well. More intuitive form can be obtained by inserting equations 6.2 and 6.3 into equation 6.1. Neglecting two-particle tunneling

process ¹, the two-mode Hamiltonian takes a form of

$$\hat{H} = \frac{e_c}{2}\hat{n}^2 - e_j\hat{\alpha} \quad (6.4)$$

where

$$\hat{n} = \frac{\hat{a}_R^\dagger\hat{a}_R - \hat{a}_L^\dagger\hat{a}_L}{2}, \quad \hat{\alpha} = \frac{\hat{a}_L^\dagger\hat{a}_R + \hat{a}_R^\dagger\hat{a}_L}{2} \quad (6.5)$$

Here, two conjugate operators \hat{n} and $\hat{\alpha}$ are the atom number difference (or relative atom number) and the tunneling operator related to the relative phase respectively. The coefficient $e_c = 4g \int dr |\psi_g|^2 |\psi_e|^2$ describes the local interaction within each well and e_j tunneling energy of particles. In the splitting process, e_j is a function of time. The equation 6.4, sometimes known as Bose-Hubbard Hamiltonian, captures essential physics of many phenomena including ac/dc-Josephson effect and self-trapping.

What is the ground-state wavefunction of the Hamiltonian 6.4? In the limiting case of large tunneling energy $e_j \gg e_c$, the ground state wavefunction takes the form of $\frac{\psi_R + \psi_L}{\sqrt{2}}$ containing the well-defined relative phase between two wells. On the other hand, the ground state becomes a Fock state minimizing the atom number difference when the local interaction e_c is dominant.

The equation 6.4 derived from the two-mode approximation describes relevant dynamical properties of Bose Josephson junction as a function of two relevant wavefunctions ψ_g and ψ_e . Two conjugate observables, however, the atom number difference ΔN and the relative phase ϕ , can be calculated only when ψ_g and ψ_e are exactly known. For a sufficiently low temperature, the many-body Schrödinger equation reduces to Gross-Pitaevskii equation (GPE) and two wavefunctions ψ_g and ψ_e can be derived. Now, a Josephson Hamiltonian in terms of ΔN and ϕ is given by

$$\hat{H}_{Josephson} = \frac{E_c}{2}N_r^2 - E_j \cos(\phi) \simeq \frac{E_c}{2}N_r^2 + E_j\phi^2 \quad (6.6)$$

where $N_r = N_L - N_R$ is the atom number difference of atoms in the two condensates ². Here, N_r and ϕ are conjugate variables satisfying $[N_r, \phi] = i$. Indeed, the charging energy E_c is given by $E_c = \frac{d\mu}{dN}$ where μ is the chemical potential. Note that the equation 6.6 is equivalent to the Hamiltonian of a harmonic oscillator with a characteristic frequency of $\omega = \sqrt{E_c E_j}$ when N_r and ϕ correspond to position and momentum variables.

¹Two-particle tunneling process term is proportional to $(\hat{a}_L^\dagger\hat{a}_R + \hat{a}_R^\dagger\hat{a}_L)^2$.

²Here, we assume that $\hbar = m = 1$ for convenience.

Description of the splitting process: Rabi, Josephson, and Fock regime

To describe the splitting process of the condensates, it is useful to study the property of the ground state of the Josephson Hamiltonian 6.6. First, comparing the equation 6.6 with a harmonic oscillator, the relative number fluctuation is simply given by $\Delta N_r = (\frac{E_j}{E_c})^{1/4}$ strongly depending on the ratio of the charging and tunneling energies. Note that this expression is not suitable in Rabi regime. In Rabi regime, the two-particle tunneling process we have neglected in the expression 6.4 is not negligible. In this case, the tunneling energy E_j must be renormalized to obey Poissonian distribution.

For our purpose, it is convenient to divide three different regimes as follows (see figure 6-2):

- Rabi regime: $E_c/E_j \ll 1/N^2$ and $\Delta N_r \approx \sqrt{N}$
- Josephson regime: $1/N^2 \ll E_c/E_j \ll 1$ and $1 \ll \Delta N_r \ll \sqrt{N}$
- Fock regime: $1 \ll E_c/E_j$ and $\Delta N_r \ll 1$

The ground states in these regimes have different statistics in the atom number and the relative phase. In Rabi regime, the relative atom number fluctuates with $\Delta N_r \approx \sqrt{N}$, obeying Poissonian distribution. The system corresponds to the non-interacting limit in this regime, and the relative phase is well-defined. In the Josephson regime, the distribution of atom number is sub-Poissonian leading to a number-squeezed state ($1 \ll \Delta N_r \ll \sqrt{N}$). The relative phase can be well-defined in this regime although there is a small amount of quantum noise in the phase. In a Bose condensate, the uncertainty in the phase is negligible as the atom number, N , is large enough. In contrast to other regimes, the ground state in the Fock regime have only a well-defined atom number, not a relative phase. The uncertainty in the phase diverges infinitely.

The description of three different regimes in the Josephson junction may guide us to obtain a simplified description of the splitting process. The tunneling energy $E_j(t)$ changes from infinity to zero within the time scale of τ_s when a condensate splits into two parts. By noting that two time scales $\omega(t) = \sqrt{E_c E_j}$ and τ_s exist in the system, we can distinguish two steps of the splitting process (see figure 6-2). When $\omega(t) > 1/\tau_s$ (step 1 in figure 6-2), the system of the double-well potential evolves adiabatically so that the ground state of the equation 6.6 should describe the actual state of the system in a good approximation. If adiabatic condition is no longer valid at t^* (therefore $\omega(t) < 1/\tau_s$), the rest of the splitting is approximated to “instantaneous splitting” (step 2 in figure 6-2). In other word, one assumes that the

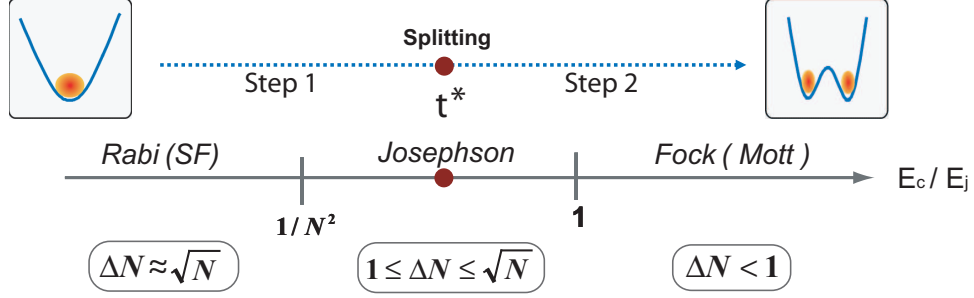


Figure 6-2: Three different regimes in the description of the dynamic splitting of condensate: Rabi, Josephson, and Fock regimes.

tunneling energy E_j becomes zero at t^* . Therefore, the final state when the splitting ends is determined by the ground state of the system at the moment t^* . Note that slow (or adiabatic) splitting results in the Fock state in which $\Delta N_r = 0$ whereas the fast splitting³ the final state lies in the Rabi regime.

The condition $\omega(t^*) = 1/\tau_s$ implies that the uncertainty in the relative atom number after the splitting process is given by

$$\Delta N_r = \sqrt{\frac{1}{E_c \tau_s}} \Big|_{t=t^*} \quad \text{where } E_c = \frac{d\mu}{dN} \quad (6.7)$$

This result implies that one can prepare a number-squeezed state in a double-well potential via the dynamic splitting. The main knob is the speed of the splitting process, τ_s , which will determine the critical time t^* (see figure 6-2). In a harmonic trap, a squeezing factor ξ becomes:

$$\xi = \frac{\sqrt{N}}{\Delta N_r} = \sqrt{\frac{2}{5} \mu \tau_s} \quad (6.8)$$

As we have seen in the previous chapter 5, Bose condensates suffer from intrinsic phase diffusion leading to the potential problem with atom interferometry. In the following section 6.1.2, we will discuss how we prepare a number-squeezed state through the dynamic splitting and the effect of number squeezing on the phase diffusion. In the MIT experiment [101], this simple model gives a squeezing factor of ~ 13 with $\tau_s = 75$ ms and $\mu = \hbar \times 6$ kHz.

³We shall see the condition for “fast splitting” in the next paragraph: $\tau_s \ll 1/\mu$.

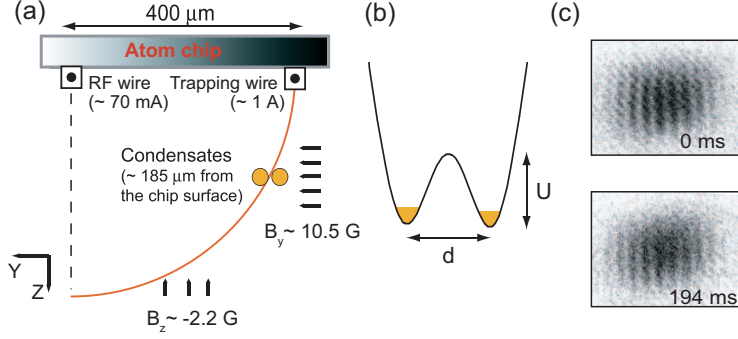


Figure 6-3: (a) Schematic of the atom chip interferometer is shown. (b) Double-well potential. The separation d between the two wells and the barrier height U were controlled by adjusting the frequency or amplitude of the RF field. (c) Matter wave interference. For various hold times after splitting, absorption images of condensates released from the double-well potential were taken after 10 ms time-of-flight. The field of view is $260 \times 200 \mu\text{m}$.

6.1.2 Preparation of a Number-squeezed State on an Atom Chip

So far, we have discussed the possibility of preparing a number-squeezed state through splitting process. The result (see equation 6.8) may encourage us to operate an atom interferometer with high atomic density source even in the presence of deleterious phase diffusion. Indeed the repulsive atom-atom interactions make it energetically favorable for the two condensates to split with equal numbers in a double-well potential, whereas number fluctuations, such as in a coherent state, cost energy [131, 33]. The relation 6.8 implies this process; the higher the atomic density (or chemical potential) is, the less the relative atom number fluctuates. Interaction-induced squeezing reduces the phase diffusion caused by the same interactions [35, 122, 202, 96, 117, 97, 131, 33]

Coherent splitting and matter-wave interference

Bose-Einstein condensates of $\sim 4 \times 10^5$ ^{23}Na atoms in the $|F = 1, m_F = -1\rangle$ state were transported into the science chamber and subsequently transferred into a magnetic trap generated by atom chip wires and external bias field [179]. A double-well potential in the horizontal plane was formed using adiabatic RF-induced splitting as described in figure. 6-3 (a) [208, 174] and in section 5.4.

Atoms were confined radially by the combined magnetic potential of a current-carrying wire and external bias field as described in figure 6-3. Axial confinement in

x direction was provided by a pair of endcap wires (not shown) [179]. By dressing the atoms with an oscillating radio frequency (RF) field from a second wire, the single minimum in the magnetic trapping potential was deformed into a double-well [174]. If the trapping position lies on the circle containing the trapping wire and centered on the RF wire, the splitting occurs in the horizontal plane. Condensates were placed $185 \mu\text{m}$ away from the chip surface. For the single well, the radial (axial) trap frequency was $f_r = 2.1 \text{ kHz}$ ($f_z = 9 \text{ Hz}$) and the Larmor frequency at the trap center was $\approx 190 \text{ kHz}$ ($B_x \approx 0.27 \text{ G}$). Splitting was performed over $\tau_s = 75 \text{ ms}$ by linearly ramping the frequency of the RF field from 143 kHz to 225 kHz . Gravity points in the $+z$ direction. Typical double-well potential is shown in figure. 6-3 (b). The separation d between the two wells and the barrier height U were controlled by adjusting the frequency or amplitude of the RF field. Typically, the separation of the two wells was $d \sim 8.7 \mu\text{m}$, the height of the trap barrier was $U \sim h \times 30 \text{ kHz}$, and the chemical potential of the condensates, measured from the trap bottom, was $\mu \sim h \times 6 \text{ kHz}$ (see figure 6-3(b)).

The lifetime of the atoms at the splitting position was $\sim 1.8 \text{ s}$, significantly longer than in our previously demonstrated two-wire splitting method [81, 41, 179].

Atoms were held in the double-well potential for varying hold times, released by turning off the trapping potential within $30 \mu\text{s}$ at a known phase of the RF field, overlapped, and interfered in time-of-flight (see figure 6-3 (c)). The relative phase of the two condensates was measured as the spatial phase of the interference pattern [177, 179] as described in chapter 5.

When the trapping potential was switched off, we observed strong correlation between the population distribution of the spin components and the phase of the RF field at the moment of release, probably since the strength of the RF field ($\sim 0.35\text{G}$) was comparable to the local static field ($\sim 0.27\text{G}$) [13]. The trapping potential was switched off at a value of the RF phase chosen to release atoms predominantly in the $|F = 1, m_F = -1\rangle$ state.

Atom interferometry in a double-well potential

Phase evolution : An atom interferometer requires two independent condensates without any weak link which may lock the phase [177, 179]. To demonstrate this independence, we monitored the relative phase over short intervals right after and after up to 190 ms delay time. During each of these intervals, the phase evolved linearly with time at $\sim 2\pi \times 200 \text{ Hz}$, the signature of independent condensates (figure 6-4). The non-vanishing phase evolution rates are attributed to small asymmetries in the

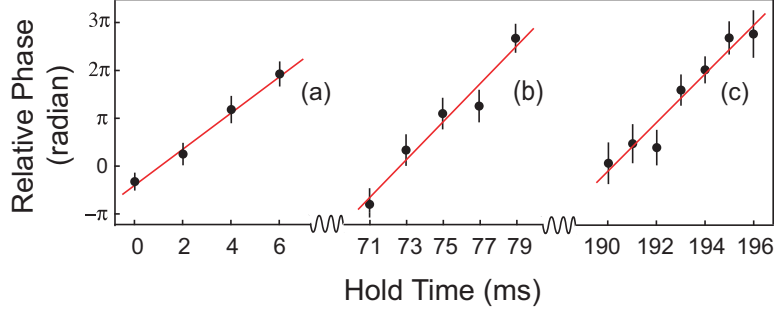


Figure 6-4: Phase evolution of the relative phase during three different time intervals. The evolution rate of the relative phase are determined from the linear fit to be (a) 191 Hz, (b) 198 Hz, and (c) 255 Hz. The data points represent the average of ten measurements for (a) and (b), and fifteen for (c).

two trapping potentials, which lead to slightly different chemical potential after the splitting process. The time variation of this rate is attributed to axial motion of the two separated condensates. Note that the observed drift of the phase evolution rate of ~ 60 Hz is only 1% of the condensates' chemical potential. In principle, the phase drift could be zeroed by a compensation field, but this has not been attempted.

Phase imprinting and read-out To rule out the possibility that any weak link existed during the 200 ms time evolution and reset the relative phase, we demonstrated that an applied phase shift could be read out 200 ms after its appliance (figure 6-5). This proves that two independently evolving condensates have preserved phase coherence up to 200 ms, a factor of 10 longer than the phase diffusion time, $\tau_c = 1/R \simeq 20$ ms, for our parameters.

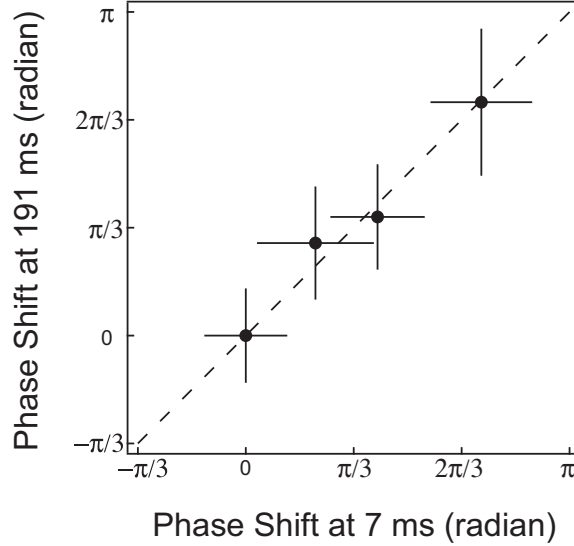


Figure 6-5: Applying various phase shifts to the condensates at 2 ms after splitting, the shifts of the relative phase were measured at 7 ms and 191 ms, showing strong correlation. The dotted line denotes the ideal case of perfect phase coherence. Phase shifts were applied by pulsing an additional magnetic field in the z direction for $50 \mu\text{s}$ with variable amplitude.

Quantitative analysis of phase coherence: Rayleigh test

What is the experimental criterion for phase coherence between two condensates after some hold time? Most conveniently, one can measure the relative phases from the interference patterns formed after some ballistic expansion, and obtain the distribution of phases for different experimental runs [177, 174] which is typically characterized by the standard deviation. For the quantitative study of phase coherence, however, the standard deviation of the phase does not provide the best characterization because the phase is measured modulo 2π (so-called circular data). In the limit of a large data set, a completely random distribution has a phase variance of $\sim (3\pi/5)^2$. Already for smaller variances, the overlap of the tails of the Gaussian distribution can cause ambiguities.

To measure correlations in circular data appropriately, we perform a *Rayleigh test* [58] on the measured relative phases as described in figure 6-6. Here, we represent each measurement of the relative phase as a phasor with unit length and compare the length of the sum of N measured phasors with the expectation value of \sqrt{N} for N random phasors. The larger the difference, the smaller is the probability that the data set is compatible with a random phase distribution. This probability of

Rayleigh Test

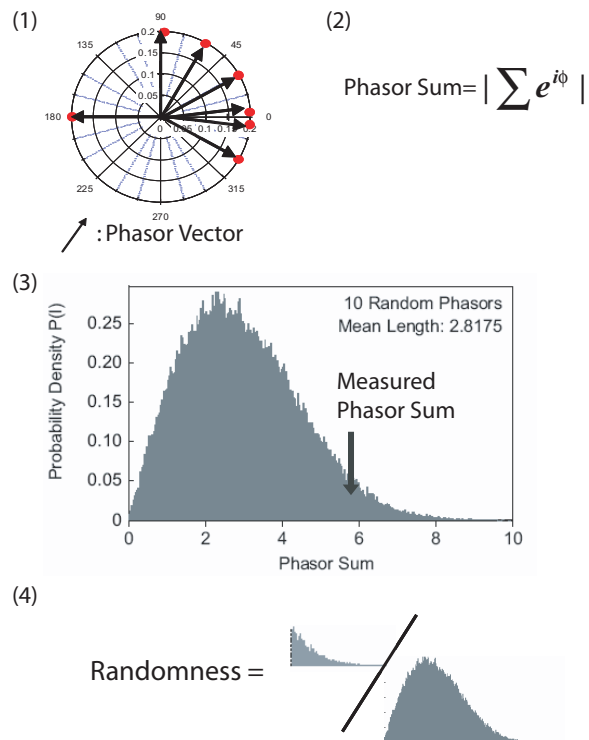


Figure 6-6: Quantitative study of phase coherence. In a circular data (1), the *Rayleigh test* compares the phasor sum of the data (2) with the distribution of phasor sums for random data (3) and returns the randomness (4), the probability that uncorrelated measurements would produce a phasor sum larger than the measurement.

uncorrelated phases is called *randomness* [58]. Uncorrelated data have an expected value of randomness near 0.5, while strongly correlated data would have a small value, e.g. ten data points drawn from a distribution with variance $(\pi/5)^2$ have a probability of only 10^{-4} to be compatible with uncorrelated phases. If a series of phase measurements has a randomness value of 0.01 (0.1), the relative phase is non-random with a probability of 99% (90%).

6.1.3 Phase Diffusion and Number Squeezing

To study phase diffusion in our system, we analyze the distribution of ten measurements of the relative phase at various times after splitting, as shown in figure 6-7. The data show a well-defined phase (with probability $> 90\%$) for times shorter than ~ 200 ms. In contrast, the simulation for a coherent state in our experimental conditions, shown as a blue dotted line, predicts the same scatter of phase measurements already after ~ 20 ms. Fitting a phase diffusion model to the data points with randomness probability > 0.1 , gives a phase diffusion time of 200 ms. The solid line is a fit which includes the initial variance $\Delta\phi_0^2$:

$$\Delta\phi(t)^2 = \Delta\phi_0^2 + (Rt)^2 \quad (6.9)$$

The variance of the initial state, $\Delta\phi_0^2 = (0.28\pi)^2$ is dominated by technical noise including fitting errors and non-ideal trap switch off. The contribution due to initial number fluctuations, $\Delta\phi_0^2 \simeq (s/\sqrt{N})^2$, is $\sim (7.1 \times 10^{-4}\pi)^2$ for a coherent state ($s=1$), and remains small unless the squeezing leads to number fluctuations on the order of a single atom, $s \sim \sqrt{N}$. The fitted value for the phase diffusion rate of $R = 5 \text{ s}^{-1}$ includes technical shot-to-shot variations in the relative atom number of two condensates after splitting and thermal fluctuation. Therefore, the inferred squeezing factor $s=10$ represents a lower bound. It implies that our relative atom number fluctuations were smaller than $\pm 0.03\%$ corresponding to ± 50 atoms.

Locally the interference pattern of two pure condensates should always have 100% contrast, where contrast is defined as the density amplitude of the interference fringes over the mean density. Since in our experiment the contrast is derived from interference pattern integrated along the line-of-sight, it decreased gradually with time and exhibited fluctuations most likely due to asymmetric axial motion (figure 6-7(b)). Except for small regions near 110 and 300 ms hold time, the contrast was above 10%, sufficient for accurate determination of the phase. The small windows with poor contrast have a large probability for random phases.

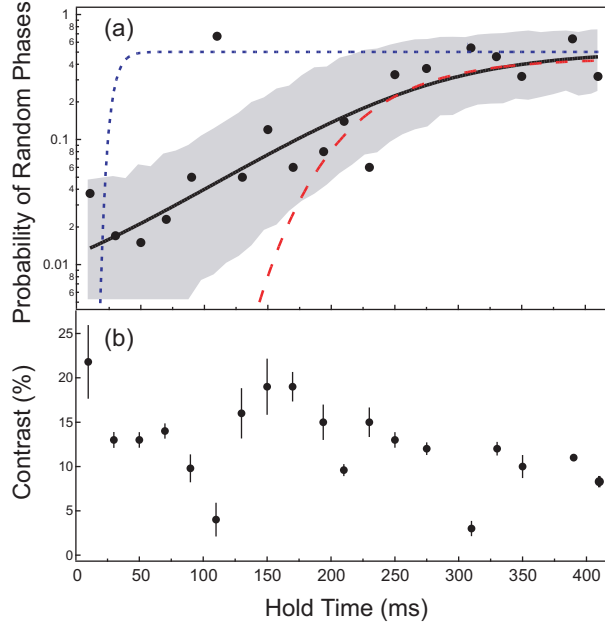


Figure 6-7: (a) The randomness probability of ten measurements of the relative phase is displayed up to 400 ms after splitting. The blue dotted curve (red dashed curve) shows a simulation for a phase-coherent state (number squeezed state with $s = 10$), which have negligible initial phase uncertainty. The solid line includes an initial phase uncertainty of 0.28π (see text). The shaded region represents the window where ten data points from the sample with the given phase uncertainty would fall with 50% probability. (b) Contrast of the interference pattern. Since the endcap wires generate a field gradient $\frac{\partial B_z}{\partial x}$ as well as a field curvature $\frac{\partial^2 B_x}{\partial x^2}$ at the position of the condensates, the two wells are not parallel to the trapping wire and consequently have slightly different axial trapping potential. This difference induces relative axial motion of the two condensates, which periodically reduces the contrast.

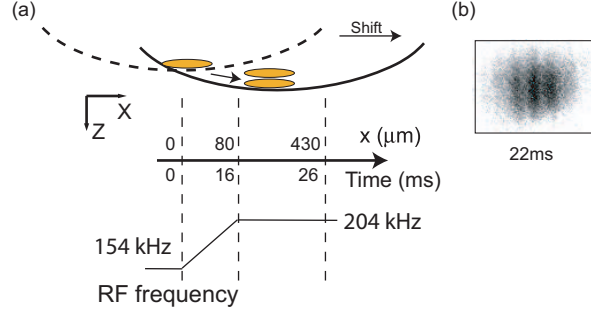


Figure 6-8: a) A single trapped condensate at rest was accelerated by shifting the trap center by $\sim 430 \mu\text{m}$ in the axial direction ($t = 0$ ms). The frequency of the RF field was linearly ramped from 154 kHz to 204 kHz during 16 ms after launch, splitting the condensates and separating them by $5 - 6 \mu\text{m}$. (b) Phase measurements were done for up to 26 ms after the launch. The probability for random phases was determined for data sets of ten measurements. Until 16 ms, this probability was extremely low (less than 10^{-12}) and the relative phase was constant, implying that the two condensates were still connected. For $t > 16$ ms, the relative phase evolved (similar to figure 6-4), and the probability for a random phase distribution was smaller than 10%. This demonstrates that phase coherence was preserved after full splitting. The figure shows the interference pattern for $t = 22$ ms. The field of view is $260 \times 200 \mu\text{m}$.

6.1.4 Conclusion and Remarks

So far, we showed that we can operate a BEC interferometer at high atomic density, with mean-field energies exceeding $h \times 6$ kHz. Using a radio frequency (RF) induced beam splitter [208, 41, 174], we demonstrate that condensates can be split reproducibly, so that even after 200 ms, or more than one thousand cycles of the mean-field evolution, the two condensates still have a controlled phase. The observed coherence time of 200 ms is ten times longer than the phase diffusion time for a coherent state. This work is a major advance in the coherence time of confined atom interferometers, which have operated at interrogation times below ~ 50 ms [177, 174, 62] due to technical limitations. This work also advances the preparation of number squeezed states to much higher atom numbers [101, 172]. Previous experiments in optical lattices [142, 66, 55] and in an optical trap [40] were limited to very small populations ($\sim 1 - 1000$ atoms). In addition, the fact that the clouds could be prepared on an atom chip with dc and RF electric currents, but without any laser beams, is promising for future applications.

Rotational sensitive interferometry: “Sagnac effect”

The work presented so far, and also all previous work on interferometry of confined or guided atoms, featured geometries without any enclosed area between the two paths of the interferometer. An enclosed area is necessary for rotational sensitivity [169, 118, 73] and requires moving atoms. As described in figure 6-8, we were able to extend the coherent beam splitter to condensates moving on an atom chip. The observed coherence time (10 ms) and propagation distance after splitting ($\sim 350 \mu\text{m}$) were only limited by the chip geometry. This corresponds to an enclosed area of $\sim 1500 \mu\text{m}^2$, and a response factor $\frac{4\pi m A}{h} \sim 7.9 \times 10^{-5} \text{rad}/\Omega_e$ for rotation sensing, where m is the probe particle mass and Ω_e the earth rotation rate [20].

Atom loss and Number squeezing

In the experiment, the condensates after coherent splitting exhibit losses with the lifetime of 1.8 s. These stochastic atom losses introduce the relative atom number uncertainty ΔN_{loss} during the hold :

$$\Delta N_{loss} \approx \sqrt{N_0 \frac{\Delta t}{\tau_{loss}}} \quad (6.10)$$

where $N_0 \sim 4 \times 10^5$ is the total number of atoms right after splitting, $\Delta t \simeq 200 \text{ ms}$ denotes hold time, and $\tau_{loss}^{-1} \sim (1.8 \text{ s})^{-1}$ is an initial atom loss rate. According to the relation 6.10, the atom number fluctuation due to atom losses becomes $\Delta N_{loss} \approx 200$ atoms. This estimation is inconsistent with our estimation of relative atom number fluctuations of 50 atoms in the experiment.

The discrepancy in the atom number fluctuations may be resolved in two ways. First, the stochastic nature of the atom losses spontaneously suppresses the relative atom number fluctuations [93]. The dependance of the atom loss rate on the atomic density tends to reduce the relative atom number; therefore suppresses the atom number fluctuation. For the losses via three-body collisions, it has been shown that the atom losses induce atom number squeezing by a factor of ~ 2 [93]. Second, the lifetime of the condensates after splitting may be longer than $\sim 1.8 \text{ s}$ since the atom loss rate is proportional to n^2 where n is the atomic density. In the experiment, the lifetime of $\sim 1.8 \text{ s}$ was measured at the splitting position without RF fields.

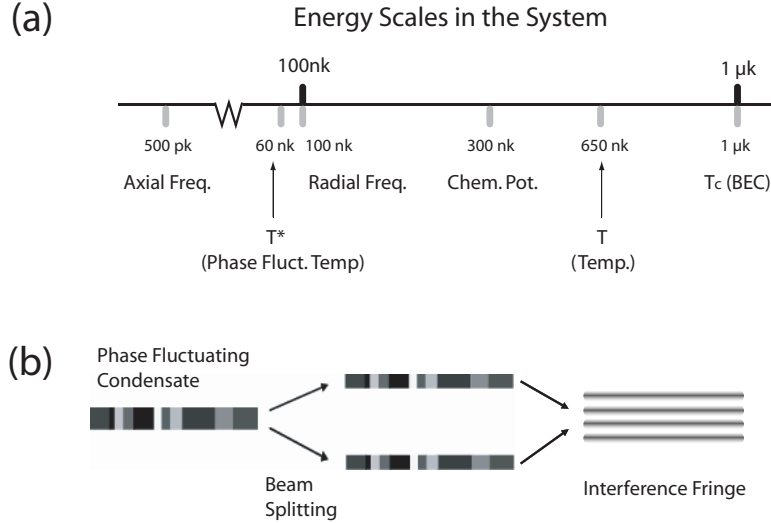


Figure 6-9: Phase fluctuations in an elongated condensate. (a) Relevant energy scale is described in an elongated condensate of the MIT experiment. The characteristic temperature T^* for phase fluctuations and the typical temperature T of the condensate are shown. (b) In the splitting process, the effect of the phase fluctuations are common-mode to both condensates. Therefore, the interference pattern formed in the overlapped atomic cloud after ballistic expansion must be straight even in the presence of the phase fluctuations. However, the relative motion of the condensates associated with asymmetries in the double well potential may cause the degradation the contrast in the interference fringe.

6.2 Matter-wave Interferometry with Phase Fluctuating Bose-Einstein Condensates

6.2.1 Phase Fluctuations in an Elongated Bose-Einstein Condensate

The phase coherence in elongated Bose-Einstein condensates (BECs) suffers from spatial phase fluctuations even well below the BEC transition temperature. In this section, I briefly demonstrate that atom interferometers using such condensates are robust against phase fluctuations, i.e. the relative phase of the split condensate is reproducible despite axial phase fluctuations. For comprehensive discussion on the experimental details, I refer to Ref. [99].

Previous experiments [179, 174, 101] including the one in the previous section 6.1.2 on atom interferometry have operated in a regime, where phase fluctuations are predicted to be present. As described in figure 6-9 (a), the characteristic temperature

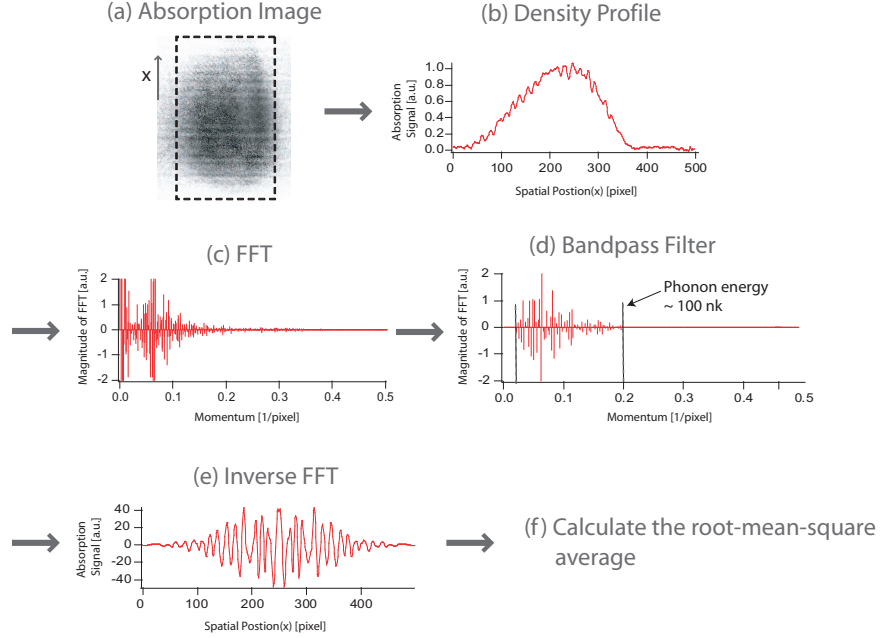


Figure 6-10: Measurement of phase fluctuations in a single condensate. (a) Absorption image of the expanded atomic cloud after 7 ms time-of-flight was taken. For quantitative analysis of the spatial phase fluctuations in a condensate, the density profile in (b) obtained from an absorption image is Fourier transformed as in (c). After filtering out high and low momentum components as in (d), the profile is transformed back (e) and its root-mean-square average is determined (f). The high momentum limit of 0.2 pixel^{-1} in (d) corresponds to the phonon energy of 100 nK which is equal to the characteristic energy determined by the radial trap frequency. Note that the phonons with low energy less than 100 nK mainly contributes to the phase fluctuations in the elongated trap.

T^* for phase fluctuations (see equation 5.13) is much lower than the temperature, T , of the system. However, their presence has not been observed because the interferometer was read out by integrating the interference fringes along the axial direction. Other experiments characterized phase fluctuations by interferometric techniques [80] and Bragg spectroscopy [163], but didn't study the effect of phase fluctuations on an atom interferometer.

In this section, we demonstrate the axial phase fluctuations spatially resolved and characterize their effect on the atom interferometer. We show explicitly, that atom interferometry can be performed in the presence of phase fluctuations. This has been expected [23], since for sufficiently short times after splitting, those fluctuations are identical for both condensates and therefore don't affect the measurement of the relative phase (see figure 6-9 (b)). For the same reason, atom interferometry is possible

with thermal clouds of atoms [73]. However, already at short times, phase fluctuations degrade the contrast and can limit the performance of the atom interferometer. This degradation is not due to the quantum effect of the increased relative number fluctuations in each quasi-condensate because of the high degree of number squeezing, but is rather caused by asymmetries in the double well potential leading to relative motion of the condensates.

6.2.2 Effect of Phase Fluctuations on Atom Interferometry

Quantifying phase fluctuations

To study the effect of phase fluctuations, we first characterized the amount of phase fluctuations in the condensate before splitting by observing density modulations of the expanded atomic cloud after 7 ms time-of-flight (figure 6-10 (a)). In trap, the mean-field interaction energy suppresses density fluctuations, but ballistic expansion converts phase fluctuations into density modulations [51] since the initial velocity field is proportional to the gradient of the phase. The number of observed density striations of around ten is consistent with the ratio of the measured temperature of $\sim 650 \pm 100$ nK and the calculated value of $T^* \simeq 60$ nK. Since the barrier height is comparable to the temperature, we assume that both condensates interact with the same heat bath. However, we don't expect any difference to the case of two separated thermal clouds. The longitudinal phase fluctuations were quantified by measuring the root-mean-square average of the density fluctuations as described in figure 6-10.

The amount of phase fluctuations was controlled by changing the atom number and the temperature with rf-evaporation. The rf field generated by the rf wire [figure 5-4 (b)] was swept down from ~ 20 kHz above the Larmor frequency at the trap center to a variable final value, leading to a variable chemical potential and temperature of the condensate (figure 6-11 inset)⁴. The variation of the spatial phase fluctuations with chemical potential is shown in figure 6-11 (a).

Effect of phase fluctuation on the reproducibility of the relative phase

The effect of phase fluctuation on an atom interferometry was characterized by measuring the reproducibility of the relative phase of split condensates as described in figure 6-11 (b). To this end, we split the condensates coherently and observe the reproducibility of ten interference fringes (“randomness”) obtained by recombining

⁴In the final stage of the evaporation, the ratio of trap depth to temperature was rather small (≈ 2), possibly due to heating from the atom chip potential.

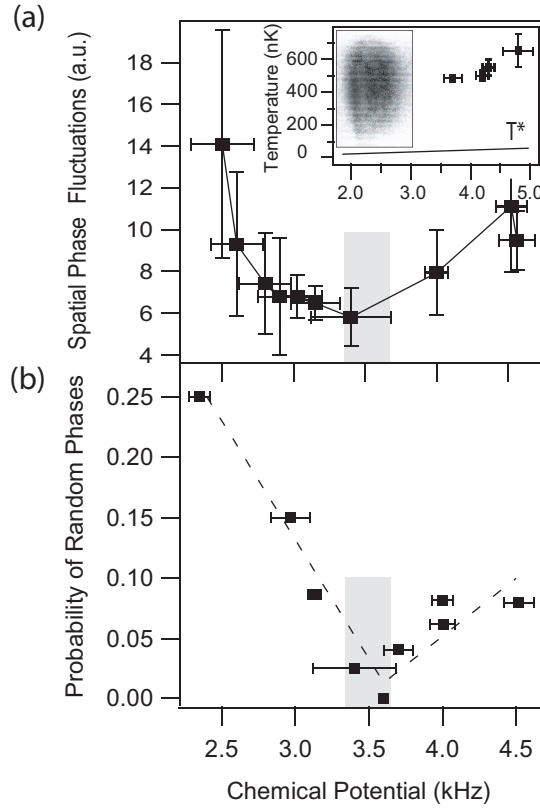


Figure 6-11: (a) Spatial phase fluctuations in a single condensate. The phase fluctuations were characterized by observing the density modulations in an absorption image of the expanded cloud after 8 ms time-of-flight (see inset) and calculating the rms fluctuations as described in reference [51]. The chemical potential (or atom number) was controlled by additional rf-evaporative cooling. The temperature of the condensate is shown in the inset graph. For chemical potentials less than 3.5 kHz, we could not measure the temperature of a condensate due to the lack of discernable thermal atoms. The observed phase fluctuations do not decrease monotonically, but show a minimum at the chemical potential of ~ 3.5 kHz, probably because the effect of the lower temperature was more than offset by the loss in the atom number. In the inset graph, T^* displays the characteristic temperature for the onset of the phase fluctuations. (b) Effect of spatial phase fluctuations on the reproducibility of the relative phase right after splitting. The probability of random phases was measured with variable longitudinal phase fluctuations immediately after splitting (0 ms hold time). The phase was determined by analyzing the central $\sim 40\%$ of the axial length of the interference pattern.

the condensates during ballistic expansion. For values of the chemical potential larger than 3.0 kHz, the randomness is less than 0.1 which implies a reproducible phase with 90% confidence.

Comparing (a) and (b) in figure 6-11, one clearly recognizes the degradation of reproducibility of the relative phase with increasing spatial phase fluctuations. We cannot rule out that the condensate had some weak collective excitations after preparation. However, the amount of the excitation should not depend on the final temperature. Therefore, we attribute the temperature dependence of the fringe contrast to phase fluctuations.

Chapter 7

Development of Atom Optics Elements

This chapter focuses on the experiments reported in two publications:

- G.-B. Jo, J.-H. Choi, C.A. Christensen, T.A. Pasquini, Y.-R. Lee, W. Ketterle, and D.E. Pritchard
Phase Sensitive Recombination of Two Bose-Einstein condensates on an atom chip
Physical Review Letters **98**, 180401 (2007) Included in appendix F
- Caleb A. Christensen, Sebastian Will, Michele Saba, Gyu-Boong Jo, Yong-Il Shin, Wolfgang Ketterle, and David Pritchard
Trapping of Ultracold atoms in a hollow-core photonic crystal fiber
Phys. Rev. A **78**, 033429 (2008) Included in appendix G

7.1 Phase Sensitive Recombination of Two Bose-Einstein Condensates

Coherent splitting of a Bose-Einstein condensate and resulting long phase coherence time have allowed us to study merger dynamics of two separated condensates. Encouraged by the long phase coherence time for the time up to 200 ms (see chapter 6), we tried to coherently split a condensate and reversely recombine two separated condensates in a trap. Many discussions of confined atom interferometers, inspired by optical fiber interferometers, propose a read-out by merging the two separated clouds as we tried [79, 185, 137]. These discussions usually assume non-interacting atoms [79, 10]

and don't address the deleterious effects of atomic interactions, including dephasing, collisional shifts, and phase diffusion [35, 122, 202, 96, 117, 97]. A recent study showed that the recombination process is much more sensitive to atomic interactions than the splitting process since merging clouds with the opposite phase involves excited modes of the recombined potential and can lead to exponential growth of unstable modes [186]. To circumvent these problems, previous realizations of confined atom interferometry usually used ballistic expansion of the two spatially independent condensates, which decreases the atomic density before overlap [177, 179, 174, 101] or worked at very low atom densities and pushed the clouds into each other with photon recoil [62]. While this avoids the deleterious effects of atom-atom interactions during the recombination, it lacks the inherent simplicity and robustness of in-trap recombination.

In this section, I briefly introduce a new phase read-out method using in-trap recombination of two separated condensates. It turns out that in-trap recombination leads to heating of the atomic cloud which is phase-dependent. Our result demonstrated that it can be used as a robust and sensitive read-out of the atom interferometer. The resulting oscillations of the condensate atom number are dramatic (typically $\sim 25\%$ contrast), occur over a wide range of recombination rates, and permit high signal to noise ratios since they simply require a measurement of the total number of condensate atoms in the trap.

Phase-sensitive recombination of two condensates

The recombination of two condensates was implemented using a radio frequency induced double well potential as described in figure 6-3. By changing the RF frequency, two separated condensates with well-defined relative phase were prepared and then the double well potential was deformed into a single well as described in figure 7-1 (a).

The phase-sensitive excitations after recombination lead to an increase in temperature based on our working assumption that the phase-sensitive excitation of the cloud decays quickly, on the order of ~ 1 ms in our system, and leads to an increase in temperature on the order of $\hbar\omega/k_B \simeq 100$ nK for the case of $\Delta\phi = \pi$, and less for other values of $\Delta\phi$ where ω is the radial trap frequency and $\Delta\phi$ denotes the relative phase.

The increase in temperature of a merged cloud can be monitored by measuring the central atom density during ballistic expansion. Phase-sensitive collective excitations, in addition to mechanical excitations from the splitting and merging processes, heat

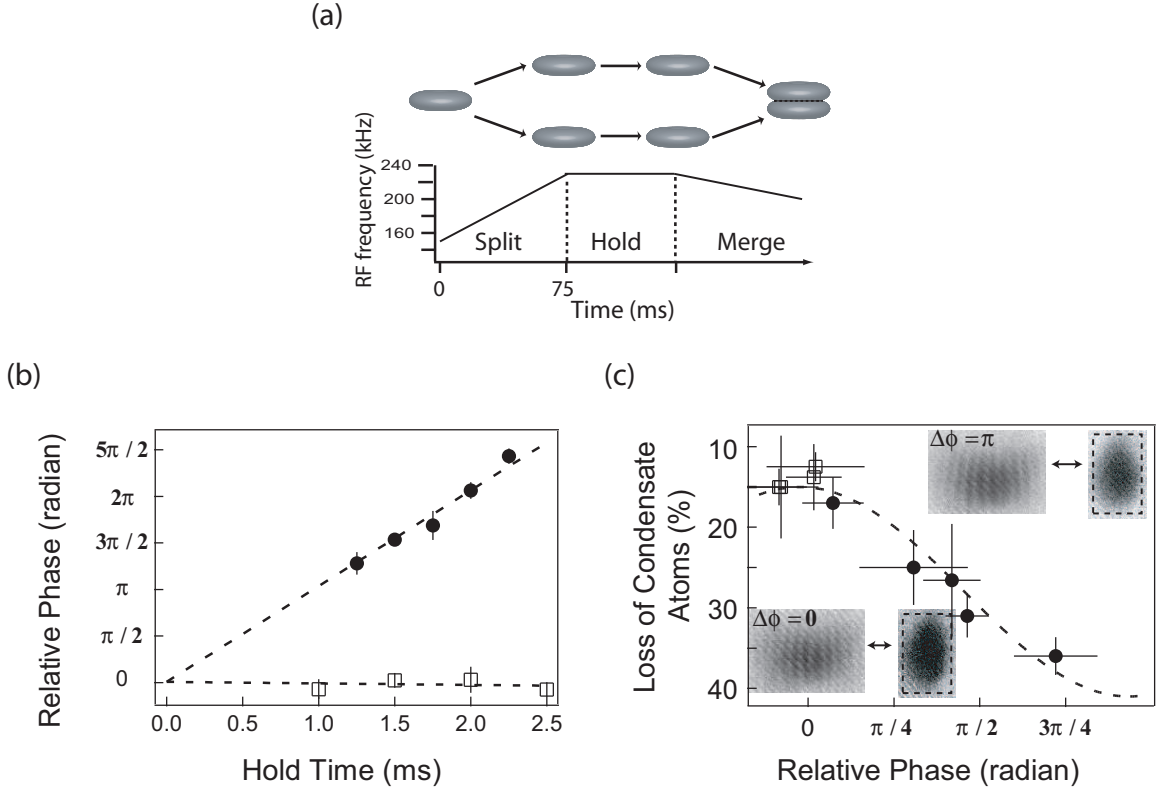


Figure 7-1: Phase-sensitive recombination of two separate condensates. (a) The phase-coherent condensates were prepared using a radio frequency induced double well potential on an atom chip [101]. The splitting was done within 75 ms by ramping up the rf frequency from 140 kHz to 225 kHz. During the hold time, the relative phase of two independent condensates evolved with time at ~ 500 Hz. After a variable time, the double well potential was deformed into a single well and the two trapped condensates were merged by decreasing the rf frequency by 33 kHz over a variable “recombination time”. The condensates started to spill over the barrier after $\leq 10\%$ of the recombination time or ~ 3 kHz decrease of the rf frequency. (b) The relative phase of two split condensates was monitored for various hold time after splitting by suddenly releasing the two condensates and observing interference fringes. For the independent condensates (solid circle), the evolution rate of the relative phase were determined from the linear fit to be ~ 500 Hz. For the weakly coupled condensates (open square), the relative phase did not evolve. At 0 ms hold time, the relative phase was set to zero for both cases. (c) For the same range of delay times as in (b), the condensate atom loss after in-trap recombination was determined. The relative phase (x-axis) was obtained from interference patterns as in (b). The merging time was 5 ms. The matter-wave interference patterns (after 9 ms time-of-flight) and absorption images of merged clouds (after 8 ms time-of-flight) show the correlation between phase shift and absorption signal (see inset). The field of view is $260 \times 200 \mu\text{m}$ and $160 \times 240 \mu\text{m}$ for matter-wave interferences and merged clouds respectively.

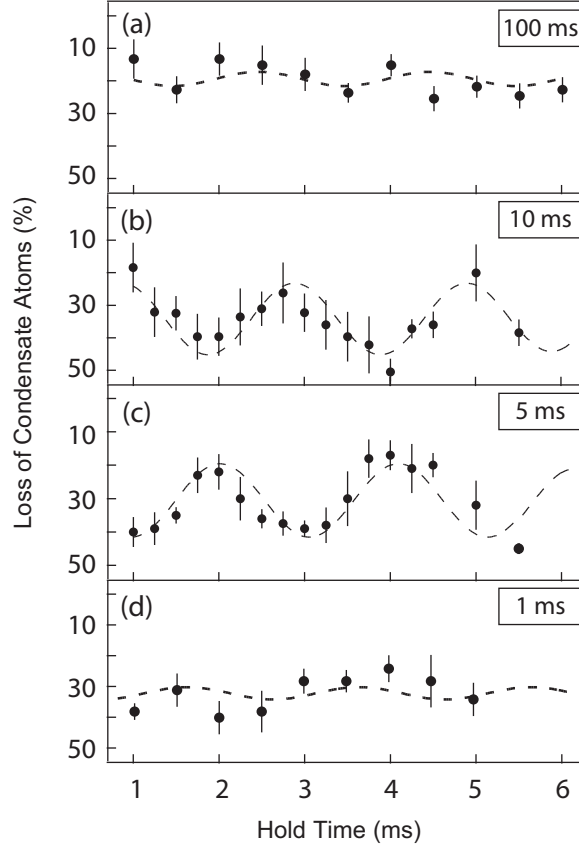


Figure 7-2: The condensate atom loss was monitored during a variable hold time for the two split condensates whose relative phase evolved at ~ 500 Hz. The merging was done for different values of the recombination time: 100 ms (a), 10 ms (b), 5 ms (c), and 1 ms (d). The dotted lines are sinusoidal curves fitted with fixed frequency ~ 500 Hz. The reproducible phase shift for the 5 ms and 10 ms data occurred during the recombination process. The data points represent the average of 6 measurements.

the cloud and lower the condensate fraction and, therefore, reduce the central density. In the experiment, the split condensates were held in the double well potential for varying hold times, merged into a single potential, and released by turning off the trapping potential.

After 8 ms time-of-flight, we measured the number of atoms in a fixed area which is comparable to the size of (expanded) Thomas-Fermi radius [dotted box in figure 7-1(c)]. While the total atom number was conserved, the number within the fixed area decreased, indicating that the temperature had increased. The fractional loss of condensate atoms was obtained as the ratio of atom number after recombination to the atom number before splitting.

To confirm that this oscillatory heating was associated with the relative phase

of the split condensates, we measured the relative phase as the spatial phase of the interference pattern when the split condensates were suddenly released and interfered during ballistic expansion [figure 7-1 (b)] [177]. Figure 7-1 (b) and (c) show the strong correlation between the relative phase and the heating of atom clouds. As the relative phase increased from 0 to π , the atom loss after recombination increased [figure 7-1(c)]; π -relative phase (0-relative phase) difference leads to maximum (minimum) loss of condensate atoms.

The use of phase-sensitive recombination as a read-out for an atom interferometer is demonstrated in figure 7-2. The separated condensates accumulate relative phase for an evolution time of up to 6 ms which is read out after in-trap recombination. The phase-sensitive recombination signal showed high contrast over a wide range of recombination times (figure 7-2). The observed largest amplitudes of condensate atom loss correspond to a change in temperature on the order of ~ 100 nK, in agreement with the estimate in the introduction. This is testimony to the insensitivity of the energy of phase-dependent excitations against changes in the exact recombination parameters, and is promising for further applications of chip-based atom interferometry.

7.2 Trapping of Ultracold Atoms in a Hollow-core Photonic Crystal Fiber

In this section, I briefly describe a proof-of-principle experiment showing the possibility of trapping of ultracold atoms in a hollow-core photonic crystal fiber. This project was originally initiated by Michele Saba in BEC III. The hollow-core fiber was implemented into the atom chip setup described in figure 2-1. For more experimental details, I refer to Ref. [39].

Ultracold atoms in waveguides are being used for studying quantum optics [191], performing atom interferometry [196, 101], and implementing schemes for quantum-information science [192]. Of particular interest is the ability of waveguides and microtraps to strongly confine atoms, providing high optical densities, strong interactions with light, and mechanisms for transporting atoms for further experiments. Recently major efforts has been directed toward trapping of ultracold atoms in the hollow-core optical fibers because of its intrinsic feature: simultaneously confining both a small number of ultracold atoms and photons inside the small volume of the hollow-core.

In particular, recently developed hollow-core photonic crystal fibers (model: Blaze Photonics HC-1060-02) which propagate a single Gaussian mode light (1064 nm wavelength) confined to a hollow core allow us to overcome the uncontrolled guiding of atoms in the conventional hollow core fibers used in the previous experiments [162, 94, 135]. Here, we have succeeded in trapping of ultracold atoms in the hollow-core photonic crystal fiber. This preliminary experiment has shown that the ensemble of cold atoms can be loaded into the hollow core fiber with tight confinement.

In the experiment, the Bose-Einstein condensates trapped in the red-detuned optical dipole trap (ODT) is positioned 1 mm away from the end of a fiber (see figure 7-3). The atoms trapped in the ODT is transferred into the core of the fiber by coupling the red-detuned light into the fiber from the other side of the fiber [hereafter called the hollow-core trap(HCT)]. By adjusting the intensities of two lights, the atom can be loaded into the fiber or be retrieved controllably as described in figure 7-4. The number of atoms after retrieval is about 5% of the 10^6 atoms initially prepared in the ODT.

This system, consisting of tightly confined ultracold atoms in the core of the fiber, would open a new area of nonlinear quantum optics if a small number of photons are introduced in the same region. To date, few-photon nonlinear optics has been only

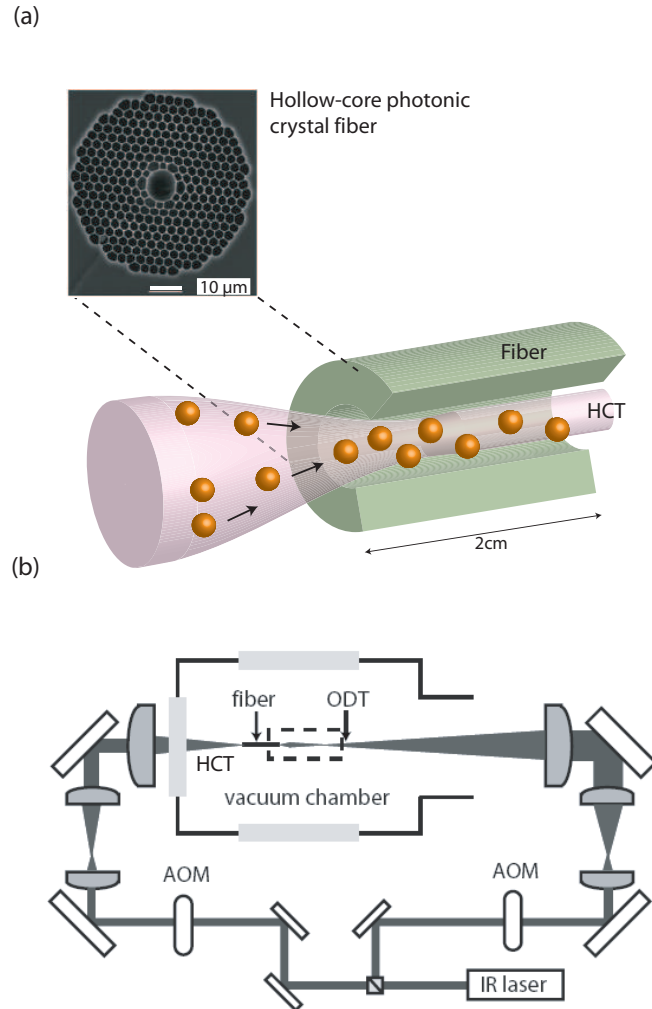


Figure 7-3: Schematic illustrations for trapping of atoms in a hollow-core fiber. (a) The atoms are transferred from a free-space ODT into a trap formed by a red-detuned Gaussian light mode confined to the core of the fiber (HCT). The fiber used in the experiment is 2 cm long. (b) Diagram of the optics setup. The light for the ODT and the HCT is produced by a 1064 nm Spectra-Physics J201-BL-106C diode pumped solid state multimode laser. Intensities are controlled by using acousto-optical modulators. The beams are frequency shifted such that they have 50 MHz relative detuning in order to prevent static interference fringes in regions where the traps overlap.

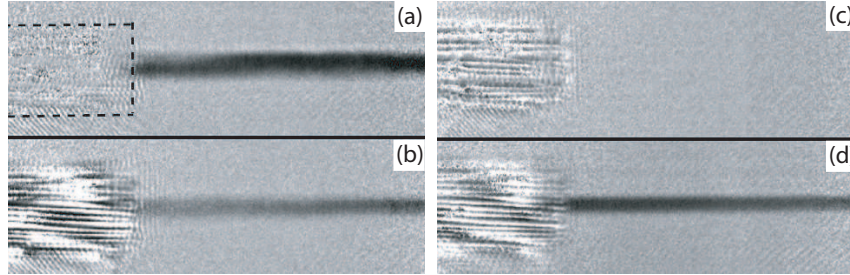


Figure 7-4: Images of atoms in the ODT during the experiment. (a) Atoms are held in the ODT near the fiber, with no light coupled into the fiber. The dashed line indicates the position of the 100 μm thick fiber. (b) Light is coupled to the fiber, and as the ODT intensity is ramped down, atoms are depleted from the ODT until (c) no atoms remain outside the fiber when the ODT power reaches zero. (d) After ramping the ODT back up, atoms that were trapped in the HCT return to the ODT.

possible in the system of the cavity in which atoms strongly interact with photons. This enhancement between atoms and photons would be also feasible in the hollow-core fiber system. For example, the recent seminal work has demonstrated the optical switching with cold atoms in the hollow core fiber [15].

Chapter 8

Conclusion and Outlook

Transition to strongly interacting physics in BEC III

This thesis contains two different experimental studies of bosonic and fermionic gases. Over 6 years after producing the first Bose-Einstein condensate in the BEC III lab (June 2001), major efforts had been directed toward understanding the properties of condensates and demonstrating atom interferometry with Bose condensed atoms. To this end, a series of proof-of-principle experiments had been successfully demonstrated as summarized in the Ph.d. theses [113, 89, 147] of former members of Ketterle/Pritchard group. These highly productive results benefit from the concept of “Science Chamber” in our lab. In summer 2007, the apparatus was upgraded to generate a degenerate Bose-Fermi mixture of ^{23}Na and ^6Li . Adding fermions opened new opportunities to explore quantum magnetism in a repulsive Fermi gas and heteronuclear molecules consisting of bosonic ^{23}Na and fermionic ^6Li atoms. Also, from this point, we broadened the scope of research direction toward the understanding of the strongly interacting regime in a gas of ultracold atoms. My Ph.D. research described in this thesis is an example showing how the field of ultracold dilute gases evolves into the area of strongly correlated physics.

8.1 The future in BEC III

At the moment when I was writing this thesis, the major efforts were directed toward two projects simultaneously in the science chamber: (1) the study of itinerant ferromagnetism in a Fermi Gas of ultracold atoms and (2) the production of fermionic heteronuclear molecules. For itinerant ferromagnetism, the study can be extended into a low-dimensional system with or without optical lattices. In a lattice system,

there are many fundamental questions relevant to magnetism, waiting to be answered by experiments with cold atoms [123]. Also, the simulation of a model Hamiltonian in a repulsive Fermi gas such as the Stoner model would contribute to the realization of the quantum simulator in atomic physics. The production of fermionic heteronuclear molecules would also open a new era to study the properties of the dipolar atomic gas. In addition, the flexibility of the science chamber will allow us to explore systems consisting of fermi atoms, fermionic heteronuclear molecules, or Bose-Fermi mixtures.

I am leaving the science chamber lab in capable hands and I hope that the science chamber will continue to contribute to the field of cold atom physics. Given the advances and successes we have already accomplished in the science chamber, I believe the future is bright.

Appendix A

Properties of ^{23}Na and ^6Li .

This appendix contains summarizes properties of ^{23}Na and ^6Li .

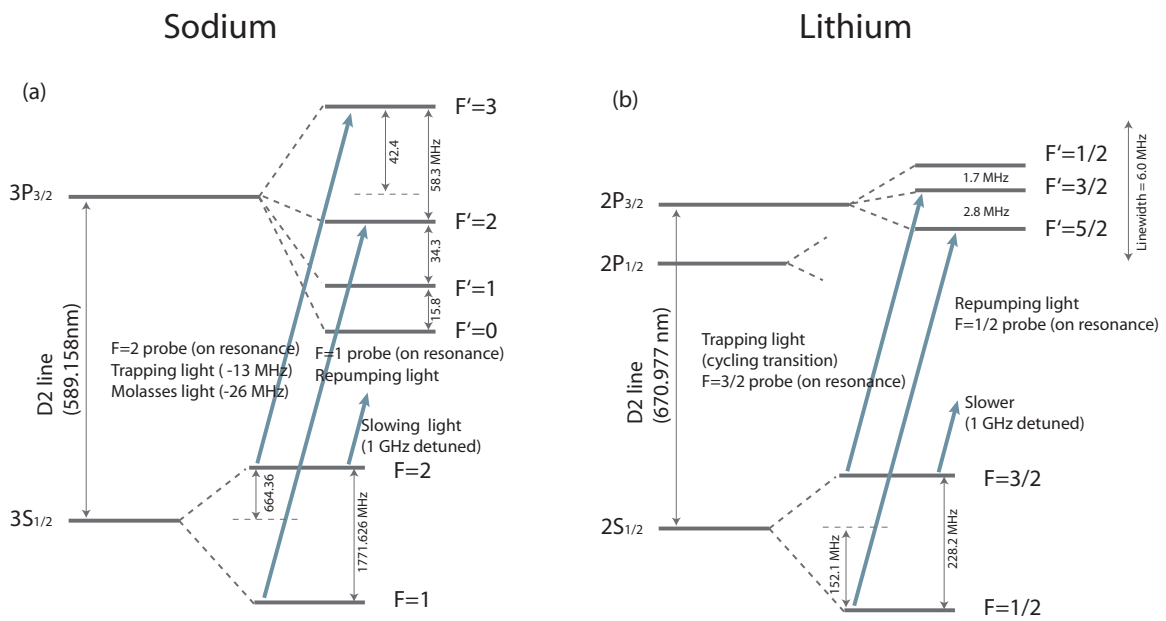


Figure A-1: Sodium and lithium D_2 transition hyperfine structure, with frequency splittings between the hyperfine energy levels. The frequency of the light used for trapping, repumping, slower, and imaging is shown.

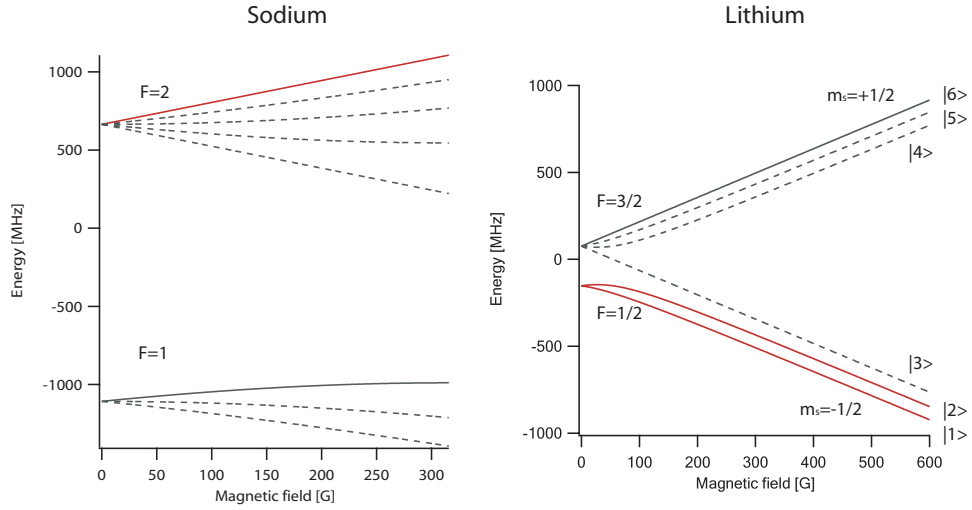


Figure A-2: ^{23}Na and ^6Li hyperfine structure in an external magnetic field. For ^{23}Na with a nuclear spin $I = 3/2$, there are $(2S + 1)(2I + 1) = 8$ hyperfine states. For ^6Li with $I = 1$, six hyperfine states are available. A $F=1$ and $F=2$ sodium condensate is produced in the hyperfine state $|F = 1, m_F = -1\rangle$ (black solid line) and $|F = 2, m_F = 2\rangle$ (red solid line) respectively. Sympathetic cooling with a $F=2$ condensate is performed in the stretched state $|F = 3/2, m_F = 3/2\rangle$ (labeled as |6>, black solid line) for lithium atoms. A repulsive two-component Fermi gas of lithium atoms is prepared in the two lowest hyperfine states $|F = 1/2, m_F = -1/2\rangle$ and $|F = 1/2, m_F = 1/2\rangle$ (labeled as |1> and |2> respectively) near the Feshbach resonance located at 834 G.

Appendix B

Designs for the Apparatus

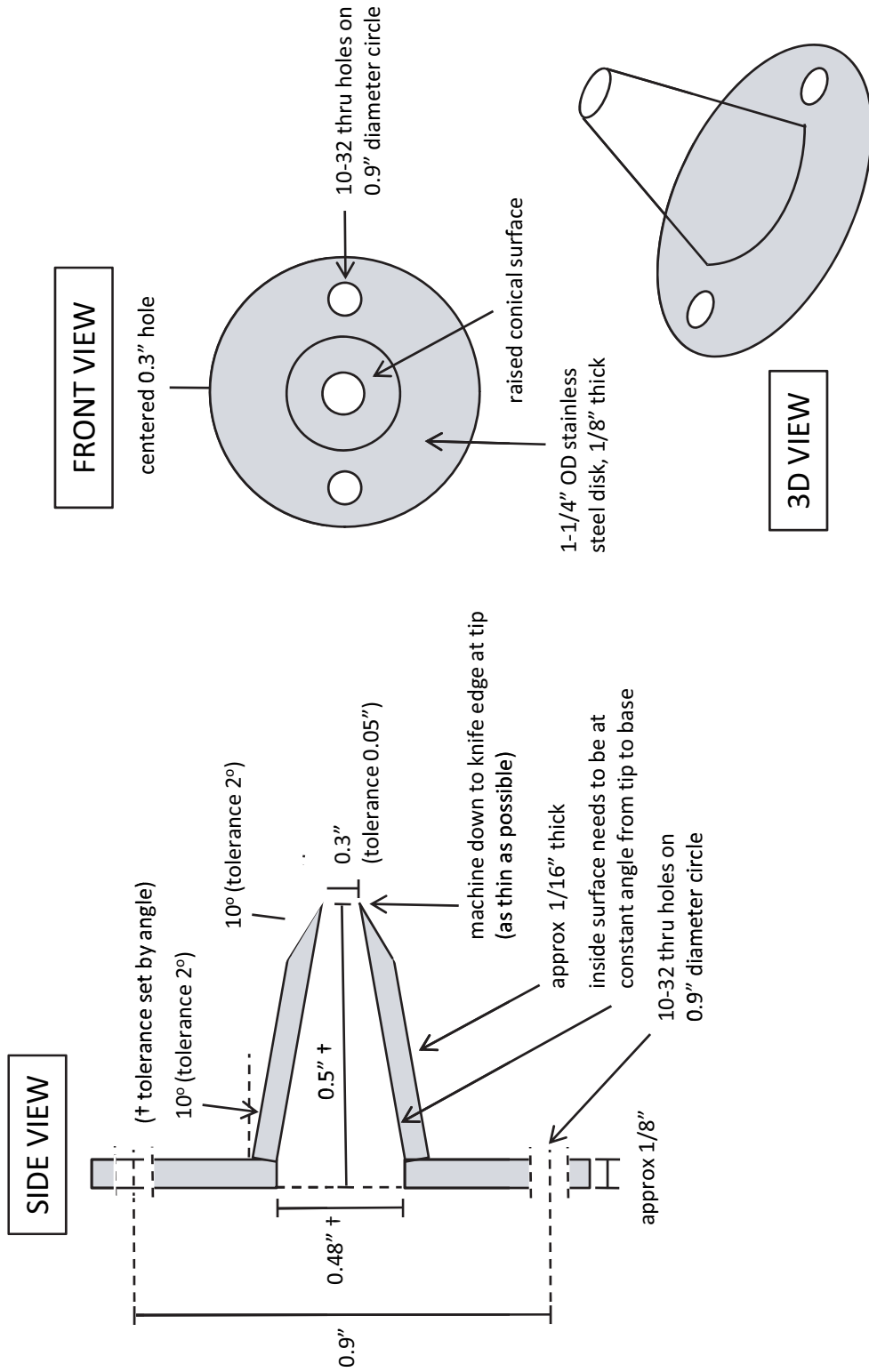
This appendix contains designs for the apparatus.

- Atomic beam skimmer
- Oven nozzle design
- Mount design for an atom chip experiment
- Design for a new science chamber
- Design for a re-entrant port

(a) Atomic Beam Skimmer

: material: non-magnetic 304 stainless steel

(Image courtesy : Tout Wang)

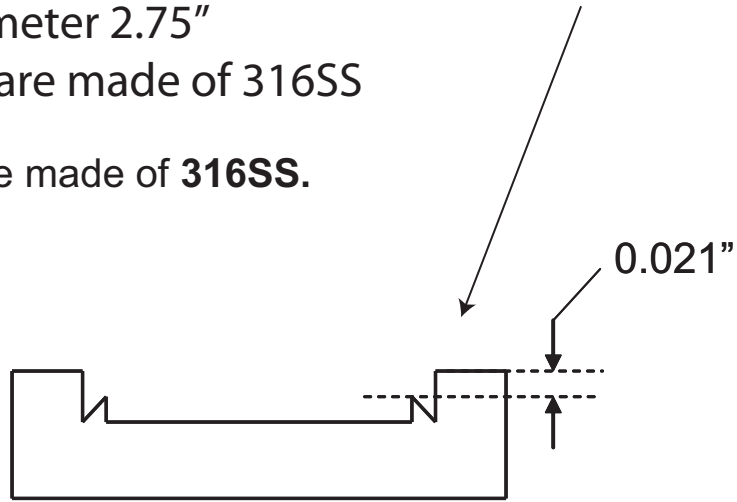


(b) Oven Nozzle Design

* All CF flanges are for Ni gaskets (with less indentation), nominal diameter 2.75"

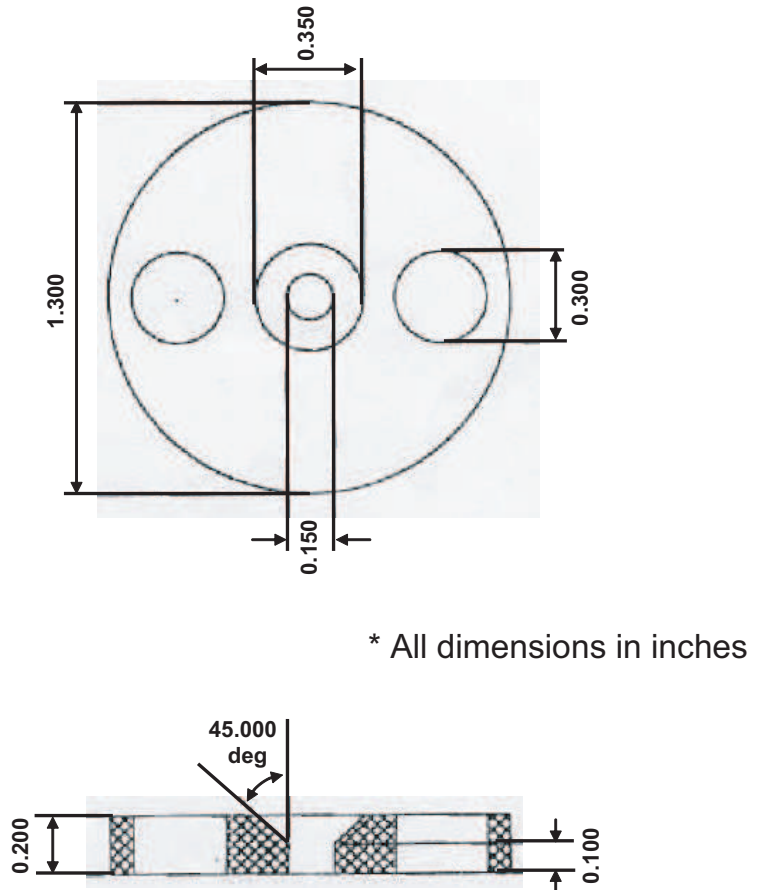
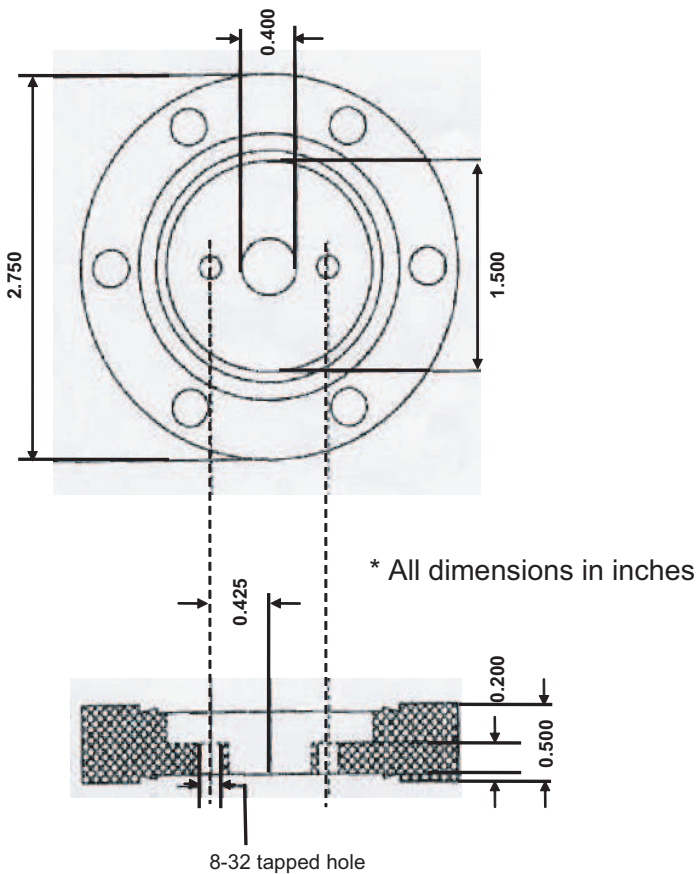
* All the parts are made of 316SS

** All the parts are made of **316SS**.



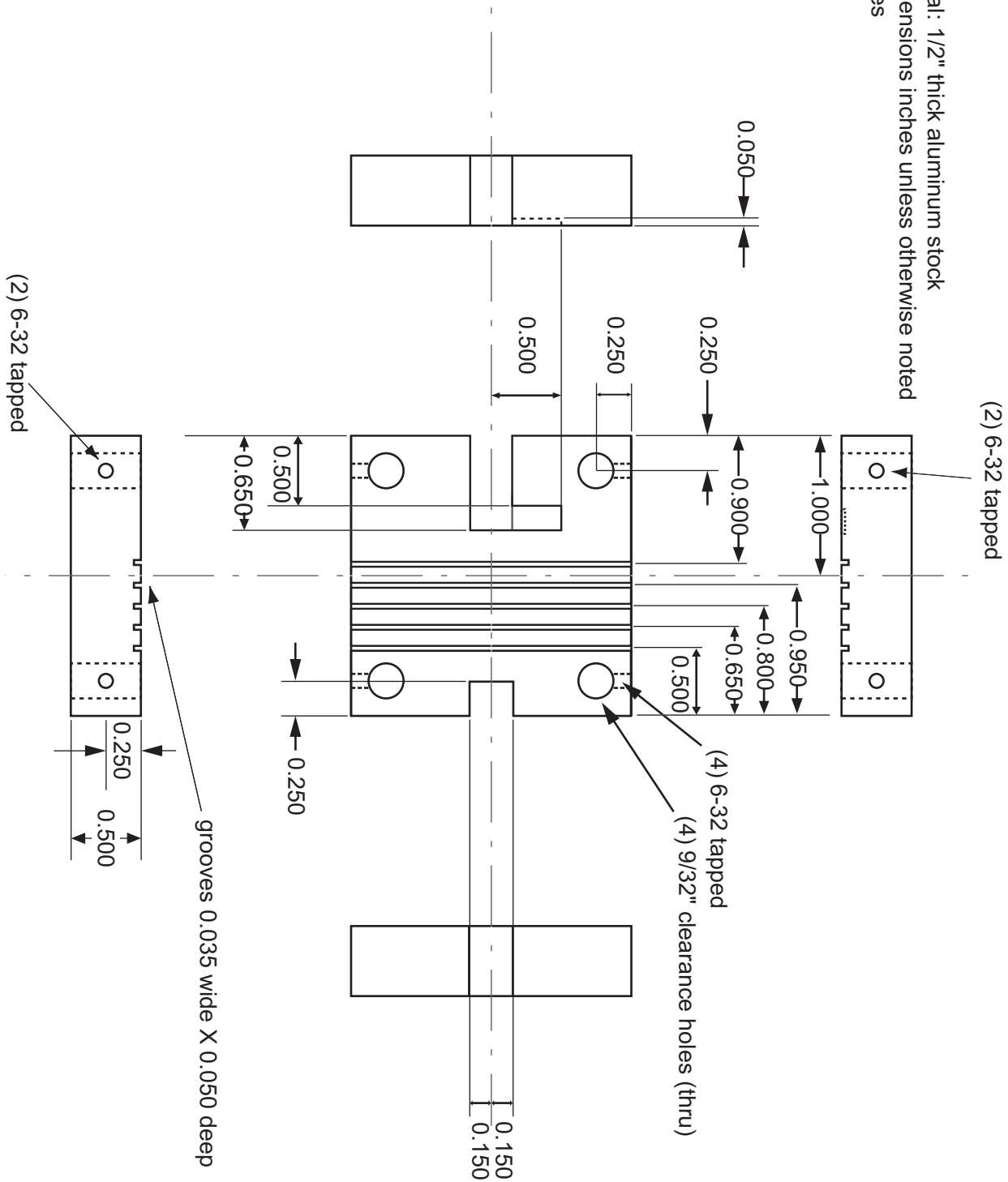
Oven nozzle A

Oven nozzle B

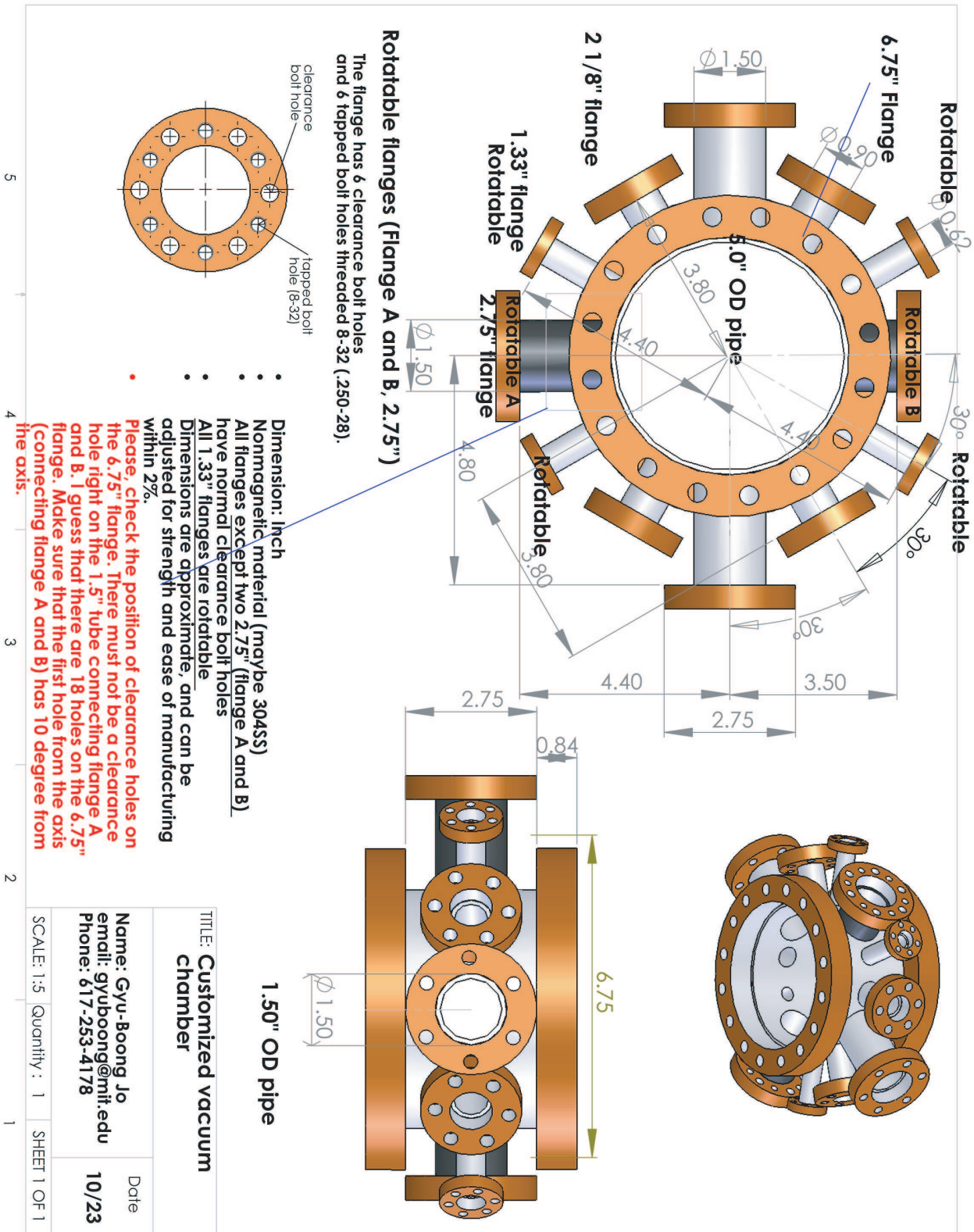


(c) Mount Design for an Atom Chip Experiment built in 2005

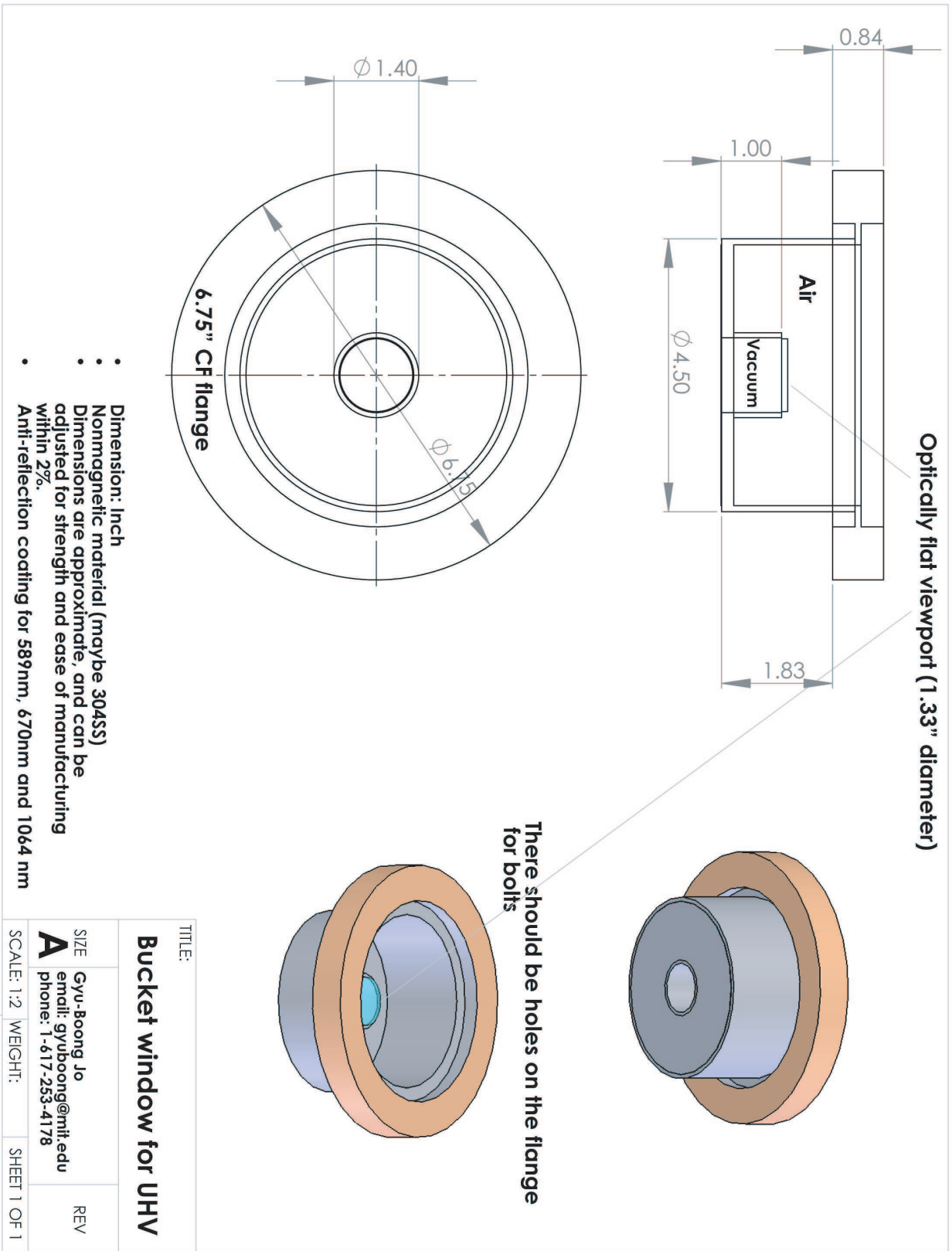
Material: 1/2" thick aluminum stock
 All dimensions inches unless otherwise noted
 2 pieces



(d) Design for a New Science Chamber



(e) Design for a re-entrant Port



Appendix C

Itinerant ferromagnetism in a Fermi gas of ultracold atoms

This appendix contains a reprint of Ref. [102]: Gyu-Boong Jo, Ye-Ryoung Lee, Jae-Hoon Choi, Caleb A. Christensen, Tony H. Kim, Joseph H. Thywissen, David E. Pritchard, and Wolfgang Ketterle *Itinerant Ferromagnetism in a Fermi Gas of Ultracold Atoms*, Science **325**, 1521-1524 (2009).

ble spectra could easily push this effect to higher frequencies that are beneficial for a variety of practical applications (30).

References and Notes

- D. Schurig, J. B. Pendry, D. R. Smith, *Opt. Express* **15**, 14772 (2007).
- A. V. Kildishev, W. Cai, U. K. Chettiar, V. M. Shalaev, *N. J. Phys.* **10**, 115029 (2008).
- J. B. Pendry, D. Schurig, D. R. Smith, *Science* **312**, 1780 (2006).
- Z. Liu, H. Lee, Y. Xiong, C. Sun, X. Zhang, *Science* **315**, 1686 (2007).
- H.-T. Chen *et al.*, *Appl. Phys. Lett.* **93**, 091117 (2008).
- J. N. Gollub, J. Y. Chin, T. J. Cui, D. R. Smith, *Opt. Express* **17**, 2122 (2009).
- H.-T. Chen *et al.*, *Nature Photon.* **2**, 295 (2008).
- I. Gil *et al.*, *Electron. Lett.* **40**, 1347 (2004).
- M. M. Qazilbash *et al.*, *Appl. Phys. Lett.* **92**, 241906 (2008).
- W. J. Padilla, A. J. Taylor, C. Highstrete, L. Mark, R. D. Averitt, *Phys. Rev. Lett.* **96**, 107401 (2006).
- A. Degiron, J. J. Mock, D. R. Smith, *Opt. Express* **15**, 1115 (2007).
- T. Driscoll *et al.*, *Appl. Phys. Lett.* **93**, 024101 (2008).
- I. V. Shadrivov, N. A. Zharova, A. A. Zharov, Y. S. Kivshar, *Phys. Rev. E Stat. Nonlin. Soft Matter Phys.* **70**, 046615 (2004).
- T. Driscoll *et al.*, *Appl. Phys. Lett.* **91**, 062511 (2007).
- M. Di Ventra, Y. V. Pershin, L. O. Chua, *Proc. IEEE* **97**, 1371 (2009).
- Materials and methods are available as supporting material on Science Online.
- A. Zylbersztein, N. F. Mott, *Phys. Rev. B Solid State* **11**, 4383 (1975).
- B.-G. Chae, H.-T. Kim, D.-H. Youn, K.-Y. Kang, *Physica B* **369**, 76 (2005).
- S. Lysenko *et al.*, *Appl. Surf. Sci.* **252**, 5512 (2006).
- M. M. Qazilbash *et al.*, *Science* **318**, 1750 (2007).
- T. Driscoll, H. T. Kim, B. G. Chae, M. Di Ventra, D. N. Basov, *Appl. Phys. Lett.* **95**, 043503 (2009).
- R. Lopez, L. A. Boatner, T. E. Haynes, R. F. Haglund Jr., L. C. Feldman, *Appl. Phys. Lett.* **85**, 1410 (2004).
- G. V. Eleftheriades, O. Siddiqui, A. K. Iyer, *Microwave Wireless Compon. Lett. IEEE* **13**, 51 (2003).
- J. D. Baena *et al.*, *Microwave Theory Tech. IEEE Trans.* **53**, 1451 (2005).
- S. Tretyakov, <http://arxiv.org/abs/cond-mat/0612247> (2006).
- J. J. Yang *et al.*, *Nat. Nanotechnol.* **3**, 429 (2008).
- Y. Muraoka, Z. Hiroi, *Appl. Phys. Lett.* **80**, 583 (2002).
- H.-T. Kim *et al.*, *N. J. Phys.* **6**, 52 (2004).
- I. Shadrivov, *SPIE Newsroom* doi:10.1117/2.1200811.1390 (2008).
- V. M. Shalaev, *Nature Photon.* **1**, 41 (2007).
- This work is supported by the U.S. Department of Energy (DOE), the Air Force Office of Scientific Research (AFOSR), and ETRI. Work at UCSD on VO₂ was supported by DOE–Basic Energy Sciences and the metamaterials work was supported by AFOSR and ETRI. M.D. acknowledges partial support from NSF. H.K. acknowledges research support from a project of the Ministry of Knowledge Economy in Korea.

Supporting Online Material

www.sciencemag.org/cgi/content/full/1176580/DC1
Materials and Methods
Fig. S1
Table S1
References

20 May 2008; accepted 4 August 2009

Published online 20 August 2009;

10.1126/science.1176580

Include this information when citing this paper.

Itinerant Ferromagnetism in a Fermi Gas of Ultracold Atoms

Gyu-Boong Jo,^{1*} Ye-Ryoung Lee,¹ Jae-Hoon Choi,¹ Caleb A. Christensen,¹ Tony H. Kim,¹ Joseph H. Thywissen,² David E. Pritchard,¹ Wolfgang Ketterle¹

Can a gas of spin-up and spin-down fermions become ferromagnetic because of repulsive interactions? We addressed this question, for which there is not yet a definitive theoretical answer, in an experiment with an ultracold two-component Fermi gas. The observation of nonmonotonic behavior of lifetime, kinetic energy, and size for increasing repulsive interactions provides strong evidence for a phase transition to a ferromagnetic state. Our observations imply that itinerant ferromagnetism of delocalized fermions is possible without lattice and band structure, and our data validate the most basic model for ferromagnetism introduced by Stoner.

Magnetism is a macroscopic phenomenon with its origin deeply rooted in quantum mechanics. In condensed-matter physics, there are two paradigms for magnetism: localized spins interacting via tunneling and delocalized spins interacting via an exchange energy. The latter gives rise to itinerant ferromagnetism, which is responsible for the properties of transition metals such as cobalt, iron, and nickel. Both kinds of magnetism involve strong correlations and/or strong interactions and are not yet completely understood. For localized spins, the interplay of magnetism with d-wave superfluidity and the properties of frustrated spin materials are topics of current research. For itinerant ferromagnetism (1–7), phase transition theories are still qualitative.

We implemented the Stoner model, a textbook Hamiltonian for itinerant ferromagnetism (8), by using a two-component gas of free fer-

mions with short-range repulsive interactions, which can capture the essence of the screened Coulomb interaction in electron gases (8). However, there is no proof so far that this simple model for ferromagnetism is consistent when the strong interactions are treated beyond mean-field approaches. It is known that this model fails in one dimension, where the ground state is singlet for arbitrary interactions, or for two particles in any dimension (3). In our work, cold atoms were used to perform a quantum simulation of this model Hamiltonian in three dimensions, and we showed experimentally that this Hamiltonian leads to a ferromagnetic phase transition (2). This model was also realized in helium-3 (9), but the liquid turn into a solid phase and not into a ferromagnetic phase at high pressure. It has also been applied to neutrons in neutron stars (10).

To date, magnetism in ultracold gases has been studied only for spinor (11, 12) and dipolar (13) Bose-Einstein condensates (BECs). In these cases, magnetism is driven by weak spin-dependent interactions, which nevertheless determine the structure of the condensate because of a bosonic enhancement factor. In contrast, here we describe the simulation of quantum magnetism in a strongly interacting Fermi gas.

An important recent development in cold atom science has been the realization of superfluidity and the BEC–Bardeen-Cooper-Schrieffer (BCS) crossover in strongly interacting, two-component Fermi gases near a Feshbach resonance (14). These phenomena occur for attractive interactions for negative scattering length and for bound molecules (corresponding to a positive scattering length for two unpaired atoms). Very little attention has been given to the region of atoms with strongly repulsive interactions. One reason is that this region is an excited branch, which is unstable against near-resonant three-body recombination into weakly bound molecules. Nevertheless, many theoretical papers have proposed a two-component Fermi gas near a Feshbach resonance as a model system for itinerant ferromagnetism (15–22), assuming that the decay into molecules can be sufficiently suppressed. Another open question is the possibility of a fundamental limit for repulsive interactions. Such a limit due to unitarity or many-body physics may be lower than the value required for the transition to a ferromagnetic state. We show that this is not the case and that there is a window of metastability where the onset of ferromagnetism can be observed.

A simple mean-field model captures many qualitative features of the expected phase transition but is not adequate for a quantitative description of the strongly interacting regime. The total energy of a two-component Fermi gas of average density n (per spin component) in a volume V is given by $E_F 2Vn \left\{ \frac{3}{10} [(1 + \eta)^{5/3} + (1 - \eta)^{5/3}] + \frac{2}{3\pi} k_F a (1 + \eta)(1 - \eta) \right\}$, where E_F is the Fermi energy of a gas, k_F is the Fermi wave vector of a gas, a is the scattering length characterizing short-range interactions between the two components, and $\eta = \Delta n/n = (n_1 - n_2)/(n_1 + n_2)$ is the magnetization of the Fermi gas. The local magnetization of the Fermi gas is nonzero when the gas separates into two volumes, where the densities n_1 and n_2 of the two spin states differ

¹Massachusetts Institute of Technology—Harvard Center for Ultracold Atoms, Research Laboratory of Electronics, Department of Physics, Massachusetts Institute of Technology, Cambridge, MA 02139, USA. ²Department of Physics, University of Toronto, Toronto, Ontario M5S1A7, Canada.

*To whom correspondence should be addressed. E-mail: gyuboong@mit.edu

by $2\Delta n$. We studied an ensemble in which the number of atoms in each spin state is conserved. This is equivalent to a free electron gas at zero external magnetic field where the total magnetization is zero. The interaction term represents any short-range spin-independent potential. When the gas is fully polarized, it avoids the repulsive interaction but increases its kinetic energy by a factor of $2^{2/3}$. The phase transition occurs when the minimum in energy is at nonzero magnetization (Fig. 1A) at $k_F a = \pi/2$. This onset was previously discussed in the context of phase separation in a two-component Fermi gas (15–18). Figure 1B shows several consequences of the phase transition for a system at constant pressure. First, for increasing repulsive interactions, the gas expands, lowering its density and Fermi energy; kinetic energy is therefore reduced. When the gas enters the ferromagnetic phase, kinetic energy increases rapidly because of the larger local density per spin state. Furthermore, the volume has a maximum value at the phase transition. This can be understood by noting that pressure in our model is $(2/3)E_{\text{kin}}/V + E_{\text{int}}/V$, where E_{kin} is kinetic energy and E_{int} is interaction energy. At the phase transition, the system increases its kinetic energy and reduces its interaction energy, thus reducing the pressure. This maximum in pressure at constant volume turns into a maximum in volume for a system held at constant pressure or in a trapping potential. We have observed three predictions of this model: (i) the onset of local magnetization through the suppression of inelastic collisions, (ii) the minimum in kinetic energy, and (iii) the maximum in the size of the cloud. These qualitative features are generic for the ferromagnetic phase transition and should also be present in more-advanced models (19).

We start with an atom cloud consisting of an equal mixture of ^6Li atoms in the lowest two hyperfine states, held at 590 G in an optical dipole trap with additional magnetic confinement (23). The number of atoms per spin state is approximately 6.5×10^5 , which corresponds to a Fermi temperature T_F of ~ 1.4 μK . The effective temperature T could be varied between $T/T_F = 0.1$ and $T/T_F = 0.6$ and was determined immediately after the field ramp by fitting the spatial distribution of the cloud with a finite temperature Thomas-Fermi profile. We define k_F^0 as the Fermi wave vector of the noninteracting gas calculated at the trap center. Applying the procedure discussed in (24) to repulsive interactions, we estimate that the real temperature is approximately 20% larger than the effective one. The effective temperature did not depend on $k_F^0 a$ for $k_F^0 a < 6$. At higher temperatures, additional shot-to-shot noise was caused by large fluctuations in the atom number. From the starting point at 590 G, the magnetic field was increased toward the Feshbach resonance at 834 G, thus providing adjustable repulsive interactions. Because of the limited lifetime of the strongly interacting gas, it was necessary to ap-

ply the fastest possible field ramp, limited to 4.5 ms by eddy currents. The ramp time is approximately equal to the inverse of the axial trap frequency (23) and therefore only marginally adiabatic. Depending on the magnetic field during observation, either atoms or molecules were detected by absorption imaging as described in fig. S1 (25).

The emergence of local spin polarization can be observed by the suppression of (either elastic or inelastic) collisions, because the Pauli exclusion principle forbids collisions in a fully polarized cloud. We monitored inelastic three-body collisions, which convert atoms into molecules. The rate (per atom) is proportional to $f(a,T)n_1n_2$ or $f(a,T)n^2(1-\eta^2)$ and is therefore a measure of the magnetization η . For $k_F a \ll 1$, the rate coefficient $f(a,T)$ is proportional to $a^6 \max(T, T_F)$ (26). This rate can be observed by monitoring the initial drop in the number of atoms during the first 2 ms after the field ramp. We avoided longer observation times, because the increasing molecule fraction could modify the properties of the sample.

A sharp peak appears in the atom loss rate around $k_F^0 a \approx 2.5$ at $T/T_F = 0.12$ (Fig. 2), indicating a transition in the sample to a state with local magnetization. The gradual decrease is consistent with the inhomogeneous density of the cloud, where the transition occurs first in the center. The large suppression of the loss rate indicates a large local magnetization of the cloud.

The kinetic energy of the cloud was determined by suddenly switching off the optical trap and the Feshbach fields immediately after the field ramp and then imaging state $|1\rangle$ atoms at zero field using the cycling transition after a ballistic expansion time of $\Delta t = 4.6$ ms. The kinetic energy was obtained from the Gaussian radial width σ_x as $E_{\text{kin}} = [(3m\sigma_x^2)/(2\Delta t^2)]$ where m is the mass of the ^6Li atom. A minimum of the kinetic energy at $k_F^0 a \approx 2.2$ for the coldest temperature $T/T_F = 0.12$ nearly coincided with

the onset of local polarization (Fig. 3). The peak in the atom loss rate occurs slightly later than the minimum of kinetic energy, probably because $f(a,T)$ increases with a (22). Because the temperature did not change around $k_F^0 a \approx 2.2$, the increase in kinetic energy is not caused by heating but by a sudden change in the properties of the gas, which is consistent with the onset of ferromagnetism. The observed increase in kinetic energy is approximately 20% at $T/T_F = 0.12$, smaller than the value $(2^{2/3} - 1) = 0.59$ predicted for a fully polarized gas. This discrepancy could be due to the absence of polarization or partial polarization in the wings of the cloud. Also, it is possible that the measured kinetic energy of the strongly interacting gas before the phase transition includes some interaction energy if the Feshbach fields are not suddenly switched off. For the current switch-off time of ~ 100 μs , this should be only a 5% effect, but the magnetic field decay may be slower because of eddy currents.

Finally, Fig. 4 shows our observation of a maximum cloud size at the phase transition, in agreement with the prediction of the model. The cloud size may not have fully equilibrated, because our ramp time was only marginally adiabatic, but this alone cannot explain the observed maximum.

The suppression of the atom loss rate, the minimum in kinetic energy, and the maximum in cloud size show a strong temperature dependence between $T/T_F = 0.12$ and 0.22. The properties of a normal Fermi gas approaching the unitarity limit with $k_F^0 a \gg 1$ should be insensitive to temperature variations in this range; therefore, the observed temperature dependence provides further evidence for a transition to a new phase.

At higher temperature (e.g., $T/T_F = 0.39$ as shown in Fig. 3), the observed nonmonotonic behavior becomes less pronounced and shifts to larger values of $k_F^0 a$ for $3 \leq k_F^0 a \leq 6$. For all three observed properties (Figs. 2 to 4), a nonmonotonic behavior is no longer observed at $T/T_F = 0.55$ (27). One interpretation is that at this temperature and

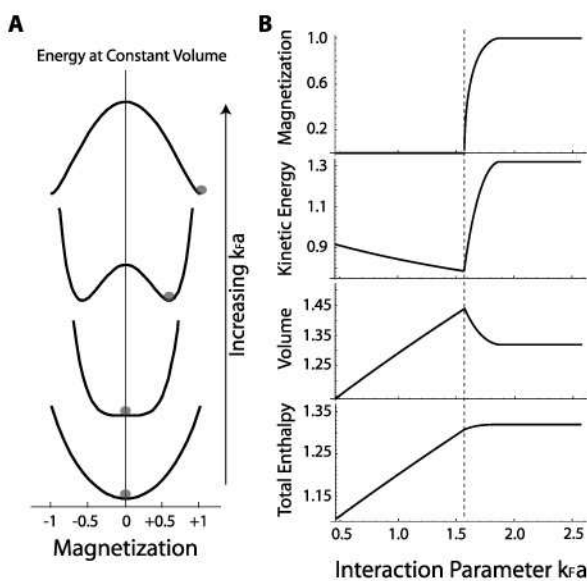


Fig. 1. Ferromagnetic phase transition at $T = 0$, according to the mean-field model described in the text. The onset of itinerant ferromagnetism occurs when the energy as a function of magnetization flips from a U shape to a W shape (A). (B) Enthalpy, volume, and kinetic energy, normalized to their values for the ideal Fermi gas, and magnetization as a function of the interaction parameter $k_F a$. k_F is defined by the density of the gas. The dotted line marks the phase transition.

above, there is no longer a phase transition. In a mean-field approximation, a ferromagnetic phase would appear at all temperatures but for increasing values of $k_F^0 a$. Our observations may imply that the interaction energy saturates around $k_F^0 a \approx 5$.

The spin-polarized ferromagnetic state should not suffer from inelastic collisions. However, typical lifetimes were 10 to 20 ms, which were probably related to a small domain size and three-body recombination at domain walls.

Fig. 2. Atom loss rate as a probe for local spin polarization, for different temperatures. $T/T_F = 0.55$ (triangles, dashed curve), $T/T_F = 0.22$ (open circles, dotted curve), and $T/T_F = 0.12$ (solid circles, solid black curve). The curves are guides to the eye, based on the assumption of a loss rate that saturates for increasing a in the normal state. The shaded area around the phase transition at $T/T_F = 0.12$ highlights the same region as in Figs. 3 and 4.

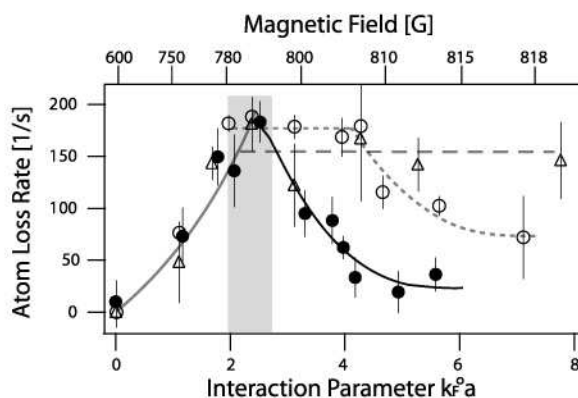
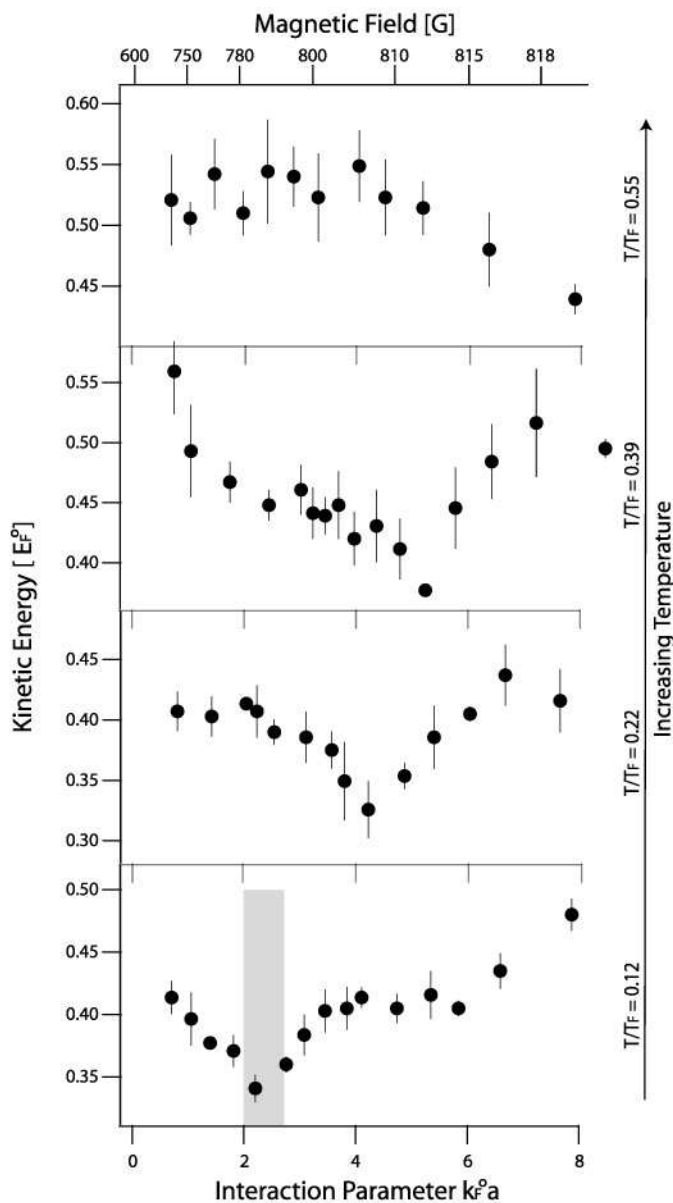


Fig. 3. Kinetic energy of a repulsively interacting Fermi gas determined for different interaction parameters $k_F^0 a$ and temperatures. The measured kinetic energy is normalized by the Fermi energy E_F^0 of the noninteracting Fermi gas at $T = 0$, calculated at the trap center with the same number of atoms per spin state. Each data point represents the average of three or four measurements.



We were unsuccessful in imaging ferromagnetic domains using differential in situ phase-contrast imaging (28). A signal-to-noise level of ~ 10 suggests that there were at least 100 domains in a volume given by our spatial resolution of $\sim 3 \mu\text{m}$ and by the radial size of the cloud. This implies that the maximum volume of the spin domains is $\sim 5 \mu\text{m}^3$, containing ~ 50 spin-polarized atoms. We suspect that the short lifetime prevented the domains from growing to a larger size and eventually adopting the equilibrium texture of the ground state, which has been predicted to have the spins pointing radially outward, like a hedgehog (20, 22). All our measurements are sensitive only to local spin polarization and are independent of domain structure and texture.

The only difference between our experiment and the ideal Stoner model is a molecular admixture of 25% (Fig. 4). The molecular fraction was constant for $k_F^0 a > 1.8$ for all temperatures and therefore cannot be responsible for the sudden change of behavior of the gas at $k_F^0 a \approx 2.2$ at the coldest temperature $T/T_F = 0.12$. This prediction was confirmed by repeating the kinetic energy measurements with a molecular admixture of 60%. The minimum in the kinetic energy occurred at the same value of $k_F^0 a$ within experimental accuracy.

For a comparison of the observed phase transition at $k_F^0 a \approx 2.2$ to the theoretical predictions, the ideal gas k_F^0 has to be replaced by the value for the interacting gas, which is smaller by $\sim 15\%$ because of the expansion of the cloud (Fig. 4), resulting in a critical value for $k_F a \approx 1.9 \pm 0.2$. At $T/T_F = 0.12$, the finite temperature correction in the critical value for $k_F a$ is predicted to be less than 5% (19). The observed value for $k_F a$ is larger than both the mean-field prediction of $\pi/2$ and the second-order prediction of 1.054 at zero temperature (19). Depending on the theoretical approach, the phase transition has been predicted to be first or second order. This could not be discerned in our experiment because of the inhomogeneous density of the cloud.

It has been speculated (19) that earlier experiments on the measurement of the interaction energy (29) and radio frequency spectroscopy of Fermi gases (30) showed evidence for the transition to a ferromagnetic state at or below $k_F a = 1$. This interpretation seems to be ruled out by our experiment.

Our work demonstrates a remarkable asymmetry between positive and negative scattering length. Early work (15) predicted that for $k_F |a| = \pi/2$, both an attractive and a repulsive Fermi gas become mechanically unstable (against collapse and phase separation, respectively). In an attractive Fermi gas, however, the mechanical instability does not occur [due to pairing (31)], in contrast to our observations in a repulsive Fermi gas. This suggests that the maximum total repulsive energy [in units of $3/5(2Vn)E_F$] is larger than the maximum attractive energy $|\beta|$ of 0.59 (32) that is realized for infinite a (23).

The interpretation of our results in terms of a phase transition to itinerant ferromagnetism is based on the agreement with the prediction of simplified models [Fig. 1, (15–22)]. Future

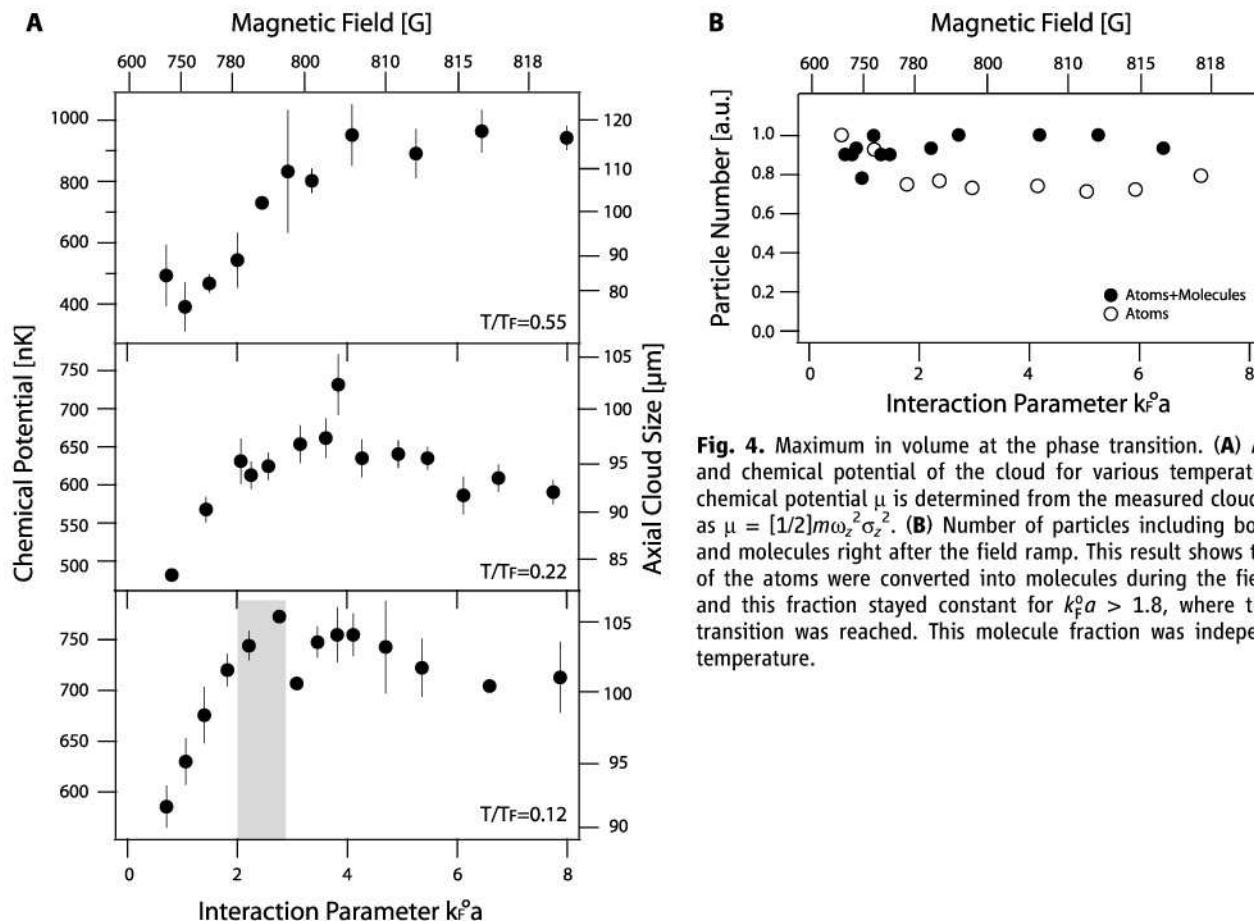


Fig. 4. Maximum in volume at the phase transition. **(A)** Axial size and chemical potential of the cloud for various temperatures. The chemical potential μ is determined from the measured cloud size, σ_z , as $\mu = [1/2]m\omega_z^2\sigma_z^2$. **(B)** Number of particles including both atoms and molecules right after the field ramp. This result shows that 25% of the atoms were converted into molecules during the field ramp, and this fraction stayed constant for $k_F^2 a > 1.8$, where the phase transition was reached. This molecule fraction was independent of temperature.

work should address how the observed signatures are modified by strong interactions and correlations. Additional insight can be obtained by varying the magnetic field ramp time over a wide range and studying the relaxation toward an equilibrium state (33).

Heisenberg and Bloch's explanation for ferromagnetism was based on exchange energy; that is, the Pauli principle and spin-independent repulsive interactions between the electrons. However, it was unknown what other "ingredients" were needed for itinerant ferromagnetism. It was not until 1995 (6, 7) that a rigorous proof was given that, in certain lattices, spin-independent Coulomb interactions can give rise to ferromagnetism in itinerant electron systems. Our finding suggests that Heisenberg's idea does not require a lattice and band structure but already applies to a free gas with short-range interactions. Our experiment can be regarded as quantum simulation of a Hamiltonian for which even the existence of a phase transition was unproven. This underlines the potential of cold atom experiments as quantum simulators for many-body physics.

References and Notes

1. F. Bloch, *Z. Phys.* **57**, 545 (1929).
2. E. Stoner, *Philos. Mag.* **15**, 1018 (1933).
3. E. Lieb, D. Mattis, *Phys. Rev.* **125**, 164 (1962).
4. P. W. Brouwer, Y. Oreg, B. I. Halperin, *Phys. Rev. B* **60**, R13977 (1999).

5. D. Vollhardt, N. Blumer, K. Held, M. Kollar, *Metallic Ferromagnetism—An Electronic Correlation Phenomenon*, vol. 580 of *Lecture Notes in Physics* (Springer, Heidelberg, Germany, 2001).
6. H. Tasaki, *Phys. Rev. Lett.* **75**, 4678 (1995).
7. A. Tanaka, H. Tasaki, *Phys. Rev. Lett.* **98**, 116402 (2007).
8. D. W. Snoke, *Solid State Physics: Essential Concepts* (Addison-Wesley, San Francisco, CA, 2008).
9. D. Vollhardt, *Rev. Mod. Phys.* **56**, 99 (1984).
10. J. Pfarr, *Z. Phys.* **251**, 152 (1972).
11. J. Stenger *et al.*, *Nature* **396**, 345 (1998).
12. L. E. Sadler, J. M. Higbie, S. R. Leslie, M. Vengalattore, D. M. Stamper-Kurn, *Nature* **443**, 312 (2006).
13. T. Lahaye *et al.*, *Nature* **448**, 672 (2007).
14. M. Inguscio, W. Ketterle, C. Salomon, *Ultra-cold Fermi Gases, Proceedings of the International School of Physics Enrico Fermi, Course CLXIV* (IOS Press, Amsterdam, 2008).
15. M. Houbiers *et al.*, *Phys. Rev. A* **56**, 4864 (1997).
16. L. Salasnich, B. Pozzi, A. Parola, L. Reatto, *J. Phys. At. Mol. Opt. Phys.* **33**, 3943 (2000).
17. M. Amoruso, I. Meccoli, A. Minguzzi, M. Tosi, *Eur. Phys. J. D* **8**, 361 (2000).
18. T. Sogo, H. Yabu, *Phys. Rev. A* **66**, 043611 (2002).
19. R. A. Duine, A. H. MacDonald, *Phys. Rev. Lett.* **95**, 230403 (2005).
20. I. Berdnikov, P. Coleman, S. H. Simon, *Phys. Rev. B* **79**, 224403 (2009).
21. S. Zhang, H. Hung, C. Wu, preprint available at <http://arxiv.org/abs/0805.3031v4> (2008).
22. L. J. LeBlanc, J. H. Thywissen, A. A. Burkov, A. Paramekanti, *Phys. Rev. A* **80**, 013607 (2009).
23. Materials and methods are available as supporting material on Science Online.
24. J. Kinast *et al.*, *Science* **307**, 1296 (2005).
25. M. W. Zwierlein *et al.*, *Phys. Rev. Lett.* **91**, 250401 (2003).
26. J. P. D'Incao, B. D. Esry, *Phys. Rev. Lett.* **94**, 213201 (2005).

27. The interpretation of the loss rate is complicated because $f(a,T)$ is unknown for $k_F a \geq 1$. The three-body rate $f(a,T)$ is expected to be unitarity saturated for $k_F a \gg 1$ (34). The lines in Fig. 2 indicate that the observed loss rate is consistent with unitarity saturation and a sudden drop at the phase transition, which occurs at large values of $k_F a$ at higher temperature.
28. Y. Shin, M. W. Zwierlein, C. H. Schunck, A. Schirotzek, W. Ketterle, *Phys. Rev. Lett.* **97**, 030401 (2006).
29. T. Bourdel *et al.*, *Phys. Rev. Lett.* **91**, 020402 (2003).
30. S. Gupta *et al.*, *Science* **300**, 1723 (2003).
31. P. Nozières, S. Schmitt-Rink, *J. Low Temp. Phys.* **59**, 195 (1985).
32. J. Carlson, S. Reddy, *Phys. Rev. Lett.* **95**, 060401 (2005).
33. M. Babadi, D. Pekker, R. Sensarma, A. Georges, E. Demler, preprint available at <http://arxiv.org/abs/0908.3483> (2009).
34. T. Weber, J. Herbig, M. Mark, H.-C. Nägerl, R. Grimm, *Phys. Rev. Lett.* **91**, 123201 (2003).
35. Supported by NSF and the Office of Naval Research, through the Multidisciplinary University Research Initiative program, and under Army Research Office grant no. W911NF-07-1-0493 with funds from the Defense Advanced Research Projects Agency Optical Lattice Emulator program. G.-B.J. and Y.-R.L. acknowledge additional support from the Samsung Foundation. We thank E. Demler, W. Hofstetter, A. Paramekanti, L. J. LeBlanc, and G. J. Conduit for useful discussions; T. Wang for experimental assistance; and A. Keshet for development of the computer control system.

Supporting Online Material

www.sciencemag.org/cgi/content/full/325/5947/1521/DC1
 Materials and Methods
 SOM Text
 Fig. S1
 References

1 June 2009; accepted 21 July 2009
 10.1126/science.1177112

on October 1, 2009

Downloaded from

Supporting online materials for

Itinerant Ferromagnetism in a Fermi Gas of Ultracold Atoms

Gyu-Boong Jo^{1*}, Ye-Ryoung Lee¹, Jae-Hoon Choi¹, Caleb A. Christensen¹, Tony H. Kim¹, Joseph H. Thywissen², David E. Pritchard¹, and Wolfgang Ketterle¹

¹MIT-Harvard Center for Ultracold Atoms, Research Laboratory of Electronics, Department of Physics, Massachusetts Institute of Technology, Cambridge, MA 02139, USA

²Department of Physics, University of Toronto, Toronto, Ontario M5S1A7, Canada

*To whom correspondence should be addressed; E-mail: gyuboong@mit.edu

Materials and Methods

Preparation of the ultracold ⁶Li cloud The first step is the production of a spin-polarized Fermi gas in the $|F = 3/2, m_F = 3/2\rangle$ state by sympathetic cooling with bosonic ²³Na atoms in a magnetic trap as described in ref (SI). The ⁶Li cloud was then loaded into a deep optical dipole trap with a maximum power of 3W and radial trap frequency of ~ 3.0 kHz, followed by an RF transfer into the lowest hyperfine state $|F = 1/2, m_F = 1/2\rangle$. Additional axial confinement was provided by magnetic fields. An equal mixture of $|1\rangle$ and $|2\rangle$ spin states (corresponding to the $|F = 1/2, m_F = 1/2\rangle$ and $|F = 1/2, m_F = -1/2\rangle$ states at low magnetic field) was prepared by a Landau-Zener RF sweep at a magnetic field of 590 G, followed by 1 s for decoherence and further evaporative cooling at 300 G. Finally, the optical trapping potential was adiabatically reduced over 600 ms, and the field increased back to 590 G. The trap had

a depth of $7.1 \mu\text{K}$ and was nearly cigar shaped with frequencies $\nu_x = \nu_y \simeq 300 \text{ Hz}$ and $\nu_z \simeq 70 \text{ Hz}$.

Supporting online text

Estimation of the maximum total repulsive energy Full phase separation at zero temperature requires a total repulsive energy of $(2^{2/3} - 1) = 0.59$ in units of $3/5(2Vn)E_F$. At finite temperature T , one has to add TS where $S = (2Vn)k_B \ln 2$ is the entropy difference between the two phases. Our tentative observation of a ferromagnetic phase at $T = 0.39T_F$ implies a repulsive energy of ~ 1.04 assuming full phase separation, larger than the maximum attraction energy of 0.59 .

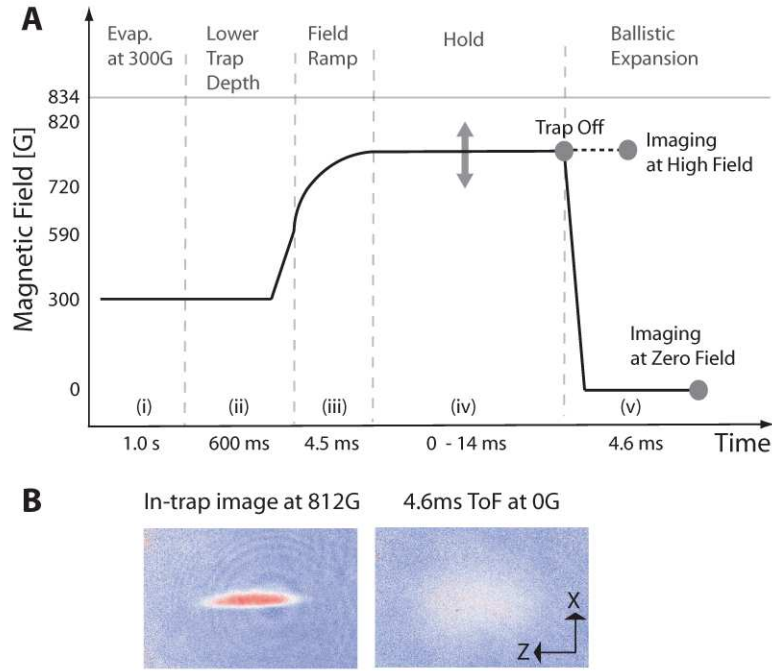


Fig. S1: (A) The schematic shows the time sequence of the experiment. The sample was exposed to the magnetic field of interest for 0 - 14 ms and analyzed in-situ for loss measurement or after 4.6 ms time-of-flight for the measurement of kinetic energy and the axial size of the cloud. The Feshbach fields were suddenly switched off at a rate of $1\text{G}/\mu\text{s}$, preventing the conversion of interaction energy into kinetic energy during the expansion. (B) This absorption image shows the $|1\rangle$ component of the cloud trapped at 812 G (left), and after 4.6 ms ballistic expansion imaged at zero field (right). The field of view is $840\mu\text{m}\times 550\mu\text{m}$. The magnetic field ramp was limited by eddy currents to 4.5 ms. Spectroscopic measurements of the magnetic field showed that the field was trailing behind the current which was controlled with a time constant faster than 1 ms.

References and Notes

S1. Z. Hadzibabic, *et al.*, *Phys. Rev. Lett.* **91**, 160401 (2003).

Response to comment by Tin-Lun Ho on “Itinerant Ferromagnetism in a Strongly Interacting Fermi Gas of Ultracold Atoms”, *Science* **325**, 1521 (2009)

Gyu-Boong Jo¹, Ye-Ryoung Lee¹, Jae-Hoon Choi¹, Caleb A. Christensen¹, Tony H. Kim¹, Joseph H. Thywissen², David E. Pritchard¹, and Wolfgang Ketterle¹

¹MIT-Harvard Center for Ultracold Atoms, Research Laboratory of Electronics, Department of Physics, Massachusetts Institute of Technology, Cambridge, MA 02139, USA

²Department of Physics, University of Toronto, Toronto, Ontario M5S1A7, Canada

Ho claims in his comment that our experiment is direct evidence that itinerant ferromagnetism does not exist in ultracold Fermi gases. This claim is incorrect and based on an invalid estimate of relaxation times and an erroneous interpretation of the detectability of ferromagnetic domains. We point out that the experimental evidence is consistent with the existence of ferromagnetism, but further experiments are needed to distinguish a ferromagnetic ground state from a non-magnetic ground state with ferromagnetic correlations.

In our recent paper (*1*), we showed for a Fermi gas of lithium-6 atoms that the lifetime, kinetic energy, and cloud size vary non-monotonously for increasing repulsive interactions, and that this behavior is consistent with predictions of a phase transition to a ferromagnetic state based on mean-field models. However, we were not able to observe ferromagnetic domains due to finite imaging resolution and line of sight integration, which suggests that the size of domains were smaller than $2\mu\text{m}$.

We explicitly state in our paper that all our measurements are sensitive only to local spin polarization and are independent of domain structure. This implies that further experimental evidences are required to distinguish between equilibrium domains and short-range fluctuating domains. In our conclusion, we explicitly point out that our interpretation in terms of a phase transition to itinerant ferromagnetism is based on the qualitative agreement with the prediction

of simple models (2). We also stated that strong interactions and correlations, for which no detailed theoretical treatment exists, could possibly modify our findings.

The possible importance of correlations is reiterated by Ho. However, no theoretical treatment is provided in his comment. Instead, he refers to theoretical studies in lattices, but it is not clear how they can be applied to the continuum case studied in our paper. Recent work (3) shows, within a phenomenological model, that correlations can lead to similar experimental signatures as we have observed. However, the model does not quantitatively agree with our data, and has some qualitative discrepancies as well; for example the extrema of lifetime, kinetic energy and cloud size don't occur at the same value of the parameter $k_F a$, where k_F is the Fermi momentum and a the s-wave scattering length, in contrast to our observations. It would be interesting to see if further development of the alternative theories could lead to quantitative agreement with experiments. Note that a ferromagnetic phase transition has been predicted by theories including mean-field and correlations in second order (4, 5), but it remains to be seen if correlations are adequately treated.

Ho argues that our non-observation of spin domains clearly shows their absence and therefore the existence of a non-magnetic state. He states that even if the formation of domains favors small sizes, there should be occasionally a domain which is large enough to be detected. However, Ho makes no predictions about the statistics of occurrence of large domains, and how they could be detected in the presence of statistical and systematic noise sources. We note that our non-observation of domains was based on visual inspections of several images which didn't show any discernable textures. We presented these results in our paper using weak language (for example, "a signal-to-noise ratio ... suggests" and "we suspect...") and gave estimates without any error bars. Ho's suggestion of looking for the rare event of a large domain conflicts with interference fringes, speckle and other imaging artifacts which, at some level, are present in all experimental images. To exclude the existence of such domains, one needs a prediction about their probability of occurrence, and a careful analysis of all experimental limitations.

Recent work (6), posted prior to Ho's comment, makes predictions about the size distribution of domains and their growth rate after a rapid quench across a critical value of $k_F a$. These authors conclude that the expected pattern size of $\sim 2k_F^{-1}$ is much smaller than the experimental imaging resolution and provide a theoretical explanation for the non-observation of domains.

Finally, Ho claims that large domains should form on a time scale \hbar/E_F , where \hbar is Planck's constant divided by 2π and E_F the Fermi energy, which is fast compared to the hold time in our experiment. This estimate is incorrect. It should apply only to the local response, i.e. screening of interactions and local correlations, but not to the formation of domains, which should show a slowing down near the quantum critical point. The time of domain formation must depend on their size l , so there is a second dimensionless parameter $k_F l$ in the problem. This is directly confirmed in the calculations of Ref. (6) which predict that the time scale for domain formation strongly depends on the domain size and how far the system is quenched beyond the critical point.

In conclusion, we strongly disagree with Ho that our experiment has shown that Fermi gases with strong repulsive interactions are non-magnetic. Ho's claim ignores the dependence of the time scale for domain formation on their size. So far, the experimental evidence is consistent with a phase transition to a ferromagnetic state, but it cannot rule out a non-magnetic state with strong ferromagnetic correlations, partly due to the fact that no detailed theoretical predictions exist for such a state.

We thank Eugene Demler for valuable discussions.

References and Notes

1. G.-B. Jo, *et al.*, *Science* **325**, 1521 (2009).
2. See references (15)-(22) of the original paper (1).
3. H. Zhai, Preprint available at <http://arxiv.org/abs/0909.4917> (2009).
4. R. A. Duine, A. H. MacDonald, *Phys. Rev. Lett.* **95**, 230403 (2005).
5. G. J. Conduit, B. D. Simons, Preprint available at <http://arxiv.org/abs/0907.3725> (2009).
6. M. Babadi, D. Pekker, R. Sensarma, A. Georges, E. Demler, Preprint available at <http://arxiv.org/abs/0908.3483> (2009).

Appendix D

Long Phase Coherence Time and Number Squeezing of two Bose-Einstein Condensates on an Atom Chip

This appendix contains a reprint of Ref. [101]: G.-B. Jo, Y. Shin, S. Will, T. A. Pasquini, M. Saba, W. Ketterle, D. E. Pritchard, M. Vengalattore, and M. Prentiss, *Long Phase Coherence Time and Number Squeezing of two Bose-Einstein Condensates on an Atom Chip*, Phys. Rev. Lett. **98**, 030407 (2007).

Long Phase Coherence Time and Number Squeezing of Two Bose-Einstein Condensates on an Atom Chip

G.-B. Jo, Y. Shin, S. Will, T. A. Pasquini, M. Saba, W. Ketterle, and D. E. Pritchard*

MIT-Harvard Center for Ultracold Atoms, Research Laboratory of Electronics, Department of Physics, Massachusetts Institute of Technology, Cambridge, Massachusetts 02139, USA

M. Vengalattore and M. Prentiss

MIT-Harvard Center for Ultracold Atoms, Jefferson Laboratory, Physics Department, Harvard University, Cambridge, Massachusetts 02138, USA

(Received 26 August 2006; published 19 January 2007)

We measure the relative phase of two Bose-Einstein condensates confined in a radio frequency induced double-well potential on an atom chip. We observe phase coherence between the separated condensates for times up to ~ 200 ms after splitting, a factor of 10 longer than the phase diffusion time expected for a coherent state for our experimental conditions. The enhanced coherence time is attributed to number squeezing of the initial state by a factor of 10. In addition, we demonstrate a rotationally sensitive (Sagnac) geometry for a guided atom interferometer by propagating the split condensates.

DOI: [10.1103/PhysRevLett.98.030407](https://doi.org/10.1103/PhysRevLett.98.030407)

PACS numbers: 03.75.Dg, 03.75.Lm, 39.20.+q

Precision measurements in atomic physics are usually done at low atomic densities to avoid collisional shifts and dephasing. This applies to both atomic clocks and atom interferometers. At high density, the atomic interaction energy results in so-called clock shifts [1], and leads to phase diffusion in Bose-Einstein condensates (BECs) [2–7]. Most precision measurements with neutral atoms are performed with free-falling atoms in atomic beams [8,9] or in fountain geometries [10]. Major efforts are currently directed towards atom interferometry using confined geometries, such as atom traps or waveguides, often realized by using atom chips [11]. These geometries are promising in terms of compactness and portability, and also offer the prospect of extending interrogation times beyond the typical 0.5 s achievable in the atomic fountains [10].

However, given the deleterious effects of high atomic density, those devices were thought to be able to operate only at low density and therefore at small flux, seriously limiting the achievable signal-to-noise ratio and sensitivity. Here we show that we can operate BEC interferometer at high density, with mean field energies exceeding $h \times 6$ kHz, where h is Planck's constant. Using a radio frequency (rf) induced beam splitter [12–14], we demonstrate that condensates can be split reproducibly, so that even after 200 ms, or more than 1000 cycles of the mean field evolution, the two condensates still have a controlled phase. The observed coherence time of 200 ms is 10 times longer than the phase diffusion time for a coherent state. Therefore, repulsive interactions during the beam splitting process [15] have created a nonclassical squeezed state with relative number fluctuations 10 times smaller than for a Poissonian distribution.

Our work is a major advance in the coherence time of confined atom interferometers, which have operated at interrogation times below ~ 50 ms [13,16,17] due to tech-

nical limitations. Our work also advances the preparation of number squeezed states to much higher atom numbers. Previous experiments in optical lattices [18,19] and in an optical trap [20] were limited to very small populations (~ 1 –1000 atoms). In addition, the fact that the clouds could be prepared on an atom chip with dc and rf electric currents, but without any laser beams, is promising for future applications. Finally, operating the rf-induced beam splitter on propagating condensates, we realized an on-chip Sagnac interferometer.

For two separated Bose-Einstein condensates, a state of well-defined relative phase (phase-coherent state), $|\phi\rangle$, is a superposition state of many relative number states, $|N_r = N_1 - N_2\rangle$, where N_1 and N_2 are the occupation of each well for $N = N_1 + N_2$ atoms. Because of atom-atom interactions in the condensates, the energy of number states, $E(N_1, N_2)$, have quadratic dependence on the atom numbers N_1 and N_2 so that the different relative number states have different phase evolution rates [2,5]. A superposition state will therefore have a spread of evolution rates, causing “phase diffusion” or “decoherence” of the relative phase with time. In contrast to normal diffusion processes, the phase uncertainty, $\Delta\phi$, increases here linearly. The phase diffusion rate, R , is proportional to the derivative of the chemical potential of condensates, $\mu(N_i)$ ($i = 1, 2$), with respect to the atom number and the standard deviation of the relative atom number, ΔN_r : $R = (2\pi/h)(d\mu/dN_i)_{N_i=N/2}\Delta N_r$ [2–7]. A number squeezed state with sub-Poissonian number fluctuations ($\Delta N_r = \sqrt{N}/s$), where $s > 1$ is the squeezing factor, will exhibit a reduced phase diffusion rate relative to a phase-coherent state with $\Delta N_r = \sqrt{N}$.

Bose-Einstein condensates of $\sim 4 \times 10^5$ ^{23}Na atoms in the $|F = 1, m_F = -1\rangle$ state were transferred into a mag-

netic trap generated by the trapping wire on an atom chip and external bias field [21]. A double-well potential in the horizontal plane was formed using adiabatic rf-induced splitting as described in Fig. 1(a) [12–14]. Typically, the separation of the two wells was $d \sim 8.7 \mu\text{m}$, the height of the trap barrier was $U \sim h \times 30 \text{ kHz}$, and the chemical potential of the condensates, measured from the trap bottom, was $\mu \sim h \times 6 \text{ kHz}$ [Fig. 1(b)]. The lifetime of the atoms at the splitting position was $\sim 1.8 \text{ s}$, significantly longer than in our previously demonstrated two-wire splitting method [21,22]. rf-induced splitting has several advantages over two-wire schemes: no loss channel (open port) during splitting, less sensitivity to magnetic bias fields, and realization of high trap frequencies far from a surface [23]. Atoms were held in the double well for varying hold times, released by turning off the trapping potential within $30 \mu\text{s}$ at a known phase of the rf field [24], overlapped, and interfered in time of flight [Fig. 1(c)]. The relative phase of the two condensates was measured as the spatial phase of the interference pattern [16,21].

An atom interferometer requires two independent condensates without any weak link which may lock the phase [16,21]. To demonstrate this independence, we monitored the relative phase over short intervals right after and after up to 190 ms delay time. During each of these intervals, the

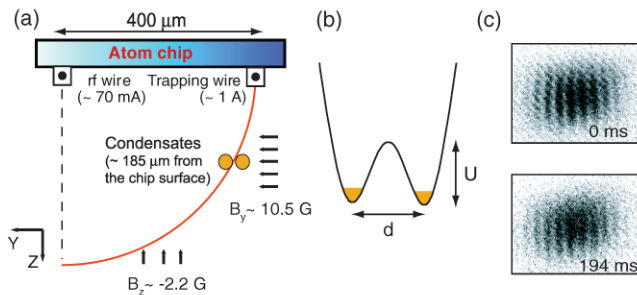


FIG. 1 (color online). Schematic of the atom chip interferometer. (a) Atoms were confined radially by the combined magnetic potential of a current-carrying wire and external bias field. Axial confinement in the x direction was provided by a pair of end cap wires (not shown) [21]. By dressing the atoms with an oscillating rf field from a second wire, the single minimum in the magnetic trapping potential was deformed into a double well [13]. If the trapping position lies on the circle containing the trapping wire and centered on the rf wire, the splitting occurs in the horizontal plane. Condensates were placed $185 \mu\text{m}$ away from the chip surface. For the single well, the radial (axial) trap frequency was $f_r = 2.1 \text{ kHz}$ ($f_z = 9 \text{ Hz}$) and the Larmor frequency at the trap center was $\approx 190 \text{ kHz}$ ($B_x \approx 0.27 \text{ G}$). Splitting was performed over 75 ms by linearly ramping the frequency of the rf field from 143 to 225 kHz . Gravity points in the $+z$ direction. (b) Double-well potential. The separation d between the two wells and the barrier height U were controlled by adjusting the frequency or amplitude of the rf field. (c) Matter wave interference. For various hold times after splitting, absorption images of condensates released from the double-well potential were taken after 10 ms time of flight. The field of view is $260 \times 200 \mu\text{m}$.

phase evolved linearly with time at $\sim 2\pi \times 200 \text{ Hz}$, the signature of independent condensates (Fig. 2). The non-vanishing phase evolution rates are attributed to small asymmetries in the two trapping potentials, which lead to slightly different chemical potential after the splitting process. The time variation of this rate is attributed to axial motion of the two separated condensates. Note that the observed drift of the phase evolution rate of $\sim 60 \text{ Hz}$ is only 1% of the condensates' chemical potential. In principle, the phase drift could be zeroed by a compensation field, but this has not been attempted.

To rule out the possibility that any weak link existed during the 200 ms time evolution and reset the relative phase, we demonstrated that an applied phase shift could be read out 200 ms after its appliance (Fig. 3). This proves that two independently evolving condensates have preserved phase coherence up to 200 ms , a factor of 10 longer than the phase diffusion time, $\tau_c = 1/R \approx 20 \text{ ms}$, for our parameters.

For the quantitative study of phase fluctuations, the standard deviation of the phase does not provide the best characterization because the phase is measured modulo 2π . In the limit of a large data set, a completely random distribution has a phase variance of $\sim (3\pi/5)^2$. Already for smaller variances, the overlap of the tails of the Gaussian distribution can cause ambiguities. As a more appropriate measure of correlation, we represent each measurement of the relative phase as a phasor with unit length and compare the length of the sum of N measured phasors with the expectation value of \sqrt{N} for N random phasors. The larger the difference, the smaller is the probability that the data set is compatible with a random phase distribution. This probability of uncorrelated phases is called randomness [26]. Uncorrelated data have an expected value of randomness near 0.5 , while strongly correlated data would have a small value, e.g., ten data points drawn from a distribution with variance $(\pi/5)^2$ have a probability of only 10^{-4} to be compatible with uncorrelated phases.

To study phase diffusion in our system, we analyze the distribution of ten measurements of the relative phase at

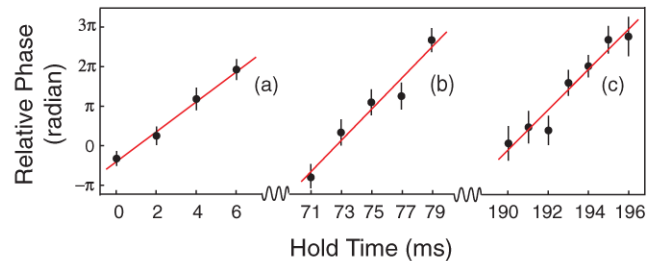


FIG. 2 (color online). Phase evolution of the relative phase during three different time intervals. The evolution rate of the relative phase are determined from the linear fit to be (a) 191 , (b) 198 , and (c) 255 Hz . The data points represent the average of ten measurements for (a) and (b), and 15 for (c).

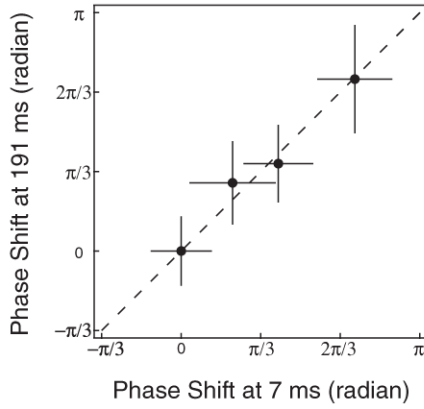


FIG. 3. Long phase coherence of two separated condensates. Applying various phase shifts to the condensates at 2 ms after splitting, the shifts of the relative phase were measured at 7 and 191 ms, showing strong correlation. The dotted line denotes the ideal case of perfect phase coherence. Phase shifts were applied by pulsing an additional magnetic field in the z direction for $50 \mu\text{s}$ with variable amplitude.

various times after splitting, as shown in Fig. 4. The data show a well-defined phase (with probability $>90\%$) for times shorter than ~ 200 ms. In contrast, the simulation for a coherent state in our experimental conditions, shown as a blue dotted line, predicts the same scatter of phase measurements already after ~ 20 ms. Fitting a phase diffusion model to the data points with randomness probability >0.1 , gives a phase diffusion time of 200 ms. The solid line is a fit which includes the initial variance $\Delta\phi_0^2$:

$$\Delta\phi(t)^2 = \Delta\phi_0^2 + (Rt)^2. \quad (1)$$

The variance of the initial state, $\Delta\phi_0^2 = (0.28\pi)^2$ is dominated by technical noise including fitting errors and non-ideal trap switch off. The contribution due to initial number fluctuations, $\Delta\phi_0^2 \approx (s/\Delta N_r)^2$, is $\sim (7.1 \times 10^{-4}\pi)^2$ for a coherent state ($s = 1$), and remains small unless the squeezing leads to number fluctuations on the order of a single atom, $s \sim \sqrt{N}$. The fitted value for the phase diffusion rate of $R = 5 \text{ s}^{-1}$ includes technical shot-to-shot variations in the relative atom number of two condensates after splitting and thermal fluctuation. Therefore, the inferred squeezing factor $s = 10$ represents a lower bound. It implies that our relative atom number fluctuations were smaller than $\pm 0.03\%$ corresponding to ± 50 atoms.

Locally the interference pattern of two pure condensates should always have 100% contrast, where contrast is defined as the density amplitude of the interference fringes over the mean density. Since in our experiment the contrast is derived from interference pattern integrated along the line of sight, it decreased gradually with time and exhibited fluctuations most likely due to asymmetric axial motion [Fig. 4(b)]. Except for small regions near 110 and 300 ms hold time, the contrast was above 10%, sufficient for accurate determination of the phase. The small windows

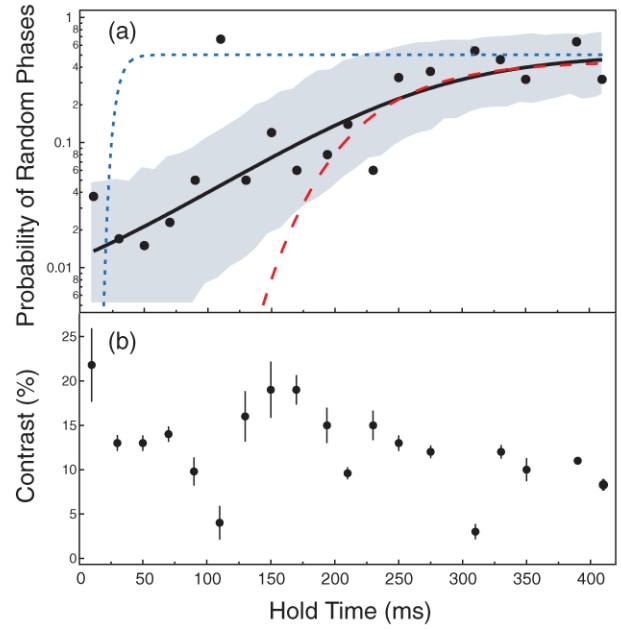


FIG. 4 (color online). Phase diffusion and number squeezing. (a) The randomness probability of ten measurements of the relative phase is displayed up to 400 ms after splitting. The blue dotted curve (red dashed curve) shows a simulation for a phase-coherent state (number squeezed state with $s = 10$), which have negligible initial phase uncertainty. The solid line includes an initial phase uncertainty of 0.28π (see text). The shaded region represents the window where ten data points from the sample with the given phase uncertainty would fall with 50% probability. (b) Contrast of the interference pattern. Since the end cap wires generate a field gradient $\frac{\partial B_z}{\partial x}$ as well as a field curvature $\frac{\partial^2 B_z}{\partial x^2}$ at the position of the condensates, the two wells are not parallel to the trapping wire and consequently have slightly different axial trapping potential. This difference induces relative axial motion of the two condensates, which periodically reduces the contrast.

with poor contrast have a large probability for random phases.

The observed long phase coherence time implies that the initial state is number squeezed. The probable origin of number squeezing during the splitting is repulsive atom-atom interactions [15]. The interactions make it energetically favorable for the two condensates to split with equal numbers in a symmetric double-well potential, whereas number fluctuations, such as in a coherent state, cost energy. Describing splitting dynamics by the Josephson Hamiltonian shows how the interplay of tunneling and interactions leads to an increase of squeezing as the barrier is increased [15,27]. Assuming that the squeezing can no longer increase when the Josephson frequency becomes slower than the inverse splitting time, we estimate a squeezing factor of ~ 13 for our experimental conditions [27]. For our elongated condensates, phase fluctuations are present for temperature above ~ 100 nK which is $\sim 1/10$ of the BEC transition temperature [28]. Since we cannot

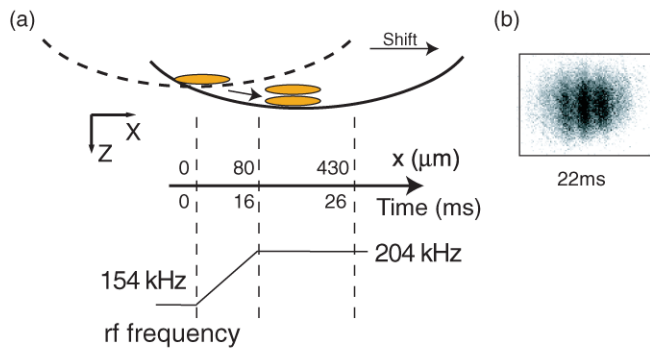


FIG. 5 (color online). Confined atom interferometry with enclosed area. (a) A single trapped condensate at rest was accelerated by shifting the trap center by $\sim 430 \mu\text{m}$ in the axial direction ($t = 0$ ms). The frequency of the rf field was linearly ramped from 154 to 204 kHz during 16 ms after launch, splitting the condensates and separating them by $5\text{--}6 \mu\text{m}$. (b) Phase measurements were done for up to 26 ms after the launch. The probability for random phases was determined for data sets of ten measurements. Until 16 ms, this probability was extremely low (less than 10^{-12}) and the relative phase was constant, implying that the two condensates were still connected. For $t > 16$ ms, the relative phase evolved (similar to Fig. 2), and the probability for a random phase distribution was smaller than 10%. This demonstrates that phase coherence was preserved after full splitting. The figure shows the interference pattern for $t = 22$ ms. The field of view is $260 \times 200 \mu\text{m}$.

measure the temperature of an almost pure condensate in time of flight, it is not clear whether the interfering condensates had correlated phase fluctuations or not.

The work presented so far, and also all previous work on interferometry of confined or guided atoms, featured geometries without any enclosed area between the two paths of the interferometer. An enclosed area is necessary for rotational sensitivity [8,9,29] and requires moving atoms. As described in Fig. 5, we were able to extend the coherent beam splitter to condensates moving on an atom chip. The observed coherence time (10 ms) and propagation distance after splitting ($\sim 350 \mu\text{m}$) were only limited by the chip geometry. This corresponds to an enclosed area of $\sim 1500 \mu\text{m}^2$, and a response factor $\frac{4\pi m A}{h} \sim 7.9 \times 10^{-5} \text{ rad}/\Omega_e$ for rotation sensing, where m is the probe particle mass and Ω_e the earth rotation rate [30].

In conclusion, the present work demonstrates a long phase coherence time of ~ 200 ms between two spatially separated condensates on an atom chip, rivaling the interrogation times in fountain-type interferometers [10]. Number squeezing by a factor ≥ 10 occurs during the preparation of the split state, providing a well-defined phase beyond the phase diffusion limit for a coherent state. Thus, interaction-induced squeezing reduces the phase diffusion caused by the same interactions [15]. These results show that it is both possible and promising to use

condensates at high density for interferometry on an atom chip.

This work was funded by DARPA, NSF, ONR, and NASA. G.-B. Jo and S. Will acknowledge additional support from Samsung Foundation and the Studienstiftung des deutschen Volkes, respectively. We thank C. Christensen for experimental assistance.

*Electronic address: http://cua.mit.edu/ketterle_group/

- [1] K. Gibble and S. Chu, Phys. Rev. Lett. **70**, 1771 (1993).
- [2] Y. Castin and J. Dalibard, Phys. Rev. A **55**, 4330 (1997).
- [3] M. Lewenstein and L. You, Phys. Rev. Lett. **77**, 3489 (1996).
- [4] E. M. Wright, D. F. Walls, and J. C. Garrison, Phys. Rev. Lett. **77**, 2158 (1996).
- [5] J. Javanainen and M. Wilkens, Phys. Rev. Lett. **78**, 4675 (1997).
- [6] A. J. Leggett and F. Sols, Phys. Rev. Lett. **81**, 1344 (1998).
- [7] J. Javanainen and M. Wilkens, Phys. Rev. Lett. **81**, 1345 (1998).
- [8] A. Lenef *et al.*, Phys. Rev. Lett. **78**, 760 (1997).
- [9] T. L. Gustavson, P. Bouyer, and M. A. Kasevich, Phys. Rev. Lett. **78**, 2046 (1997).
- [10] A. Peters, K. Chung, and S. Chu, Nature (London) **400**, 849 (1999).
- [11] R. Folman *et al.*, Adv. At. Mol. Opt. Phys. **48**, 263 (2002).
- [12] O. Zobay and B. M. Garraway, Phys. Rev. Lett. **86**, 1195 (2001).
- [13] T. Schumm *et al.*, Nature Phys. **1**, 57 (2005).
- [14] Y. Colombe *et al.*, Europhys. Lett. **67**, 593 (2004).
- [15] C. Menotti *et al.*, Phys. Rev. A **63**, 023601 (2001).
- [16] Y. Shin *et al.*, Phys. Rev. Lett. **92**, 050405 (2004).
- [17] O. Garcia *et al.*, Phys. Rev. A **74**, 031601(R) (2006).
- [18] C. Orzel *et al.*, Science **291**, 2386 (2001).
- [19] M. Greiner *et al.*, Nature (London) **415**, 39 (2002).
- [20] C.-S. Chuu *et al.*, Phys. Rev. Lett. **95**, 260403 (2005).
- [21] Y. Shin *et al.*, Phys. Rev. A **72**, 021604(R) (2005).
- [22] E. A. Hinds, C. J. Vale, and M. G. Boshier, Phys. Rev. Lett. **86**, 1462 (2001).
- [23] I. Lesanovsky *et al.*, Phys. Rev. A **73**, 033619 (2006).
- [24] We observed strong correlation between the population distribution of the spin components and the phase of the rf field at the moment of release, probably since the strength of the rf field (~ 0.35 G) was comparable to the local static field (~ 0.27 G) [25]. The trapping potential was switched off at a value of the rf phase chosen to release atoms predominantly in the $|F = 1, m_F = -1\rangle$ state.
- [25] S. Autler and C. Townes, Phys. Rev. **100**, 703 (1955).
- [26] N. Fisher, *Statistical Analysis of Circular Data* (Cambridge University Press, New York, 1993).
- [27] A. A. Burkov, M. D. Lukin, and Eugene Demler cond-mat/0701058.
- [28] D. S. Petrov, G. V. Shlyapnikov, and J. T. M. Walraven, Phys. Rev. Lett. **87**, 050404 (2001).
- [29] M. Sagnac, C. R. Acad. Sci. **157**, 708 (1913).
- [30] P. Berman, *Atom Interferometry* (Academic, New York, 1997).

Appendix E

Matter-Wave Interferometry with Phase Fluctuating Bose-Einstein Condensates

This appendix contains a reprint of Ref. [99]: G.-B. Jo, J.-H. Choi, C. A. Christensen, Y.-R. Lee, T. A. Pasquini, W. Ketterle, and D. E. Pritchard, *Itinerant Ferromagnetism*, Phys. Rev. Lett. **99**, 240406 (2007).

Matter-Wave Interferometry with Phase Fluctuating Bose-Einstein Condensates

G.-B. Jo, J.-H. Choi, C. A. Christensen, Y.-R. Lee, T. A. Pasquini, W. Ketterle, and D. E. Pritchard*

*MIT-Harvard Center for Ultracold Atoms, Research Laboratory of Electronics, Department of Physics,
Massachusetts Institute of Technology, Cambridge, Massachusetts 02139, USA*

(Received 26 June 2007; published 14 December 2007)

Elongated Bose-Einstein condensates (BECs) exhibit strong spatial phase fluctuations even well below the BEC transition temperature. We demonstrate that atom interferometers using such condensates are robust against phase fluctuations; i.e., the relative phase of the split condensate is reproducible despite axial phase fluctuations. However, larger phase fluctuations limit the coherence time, especially in the presence of some asymmetries in the two wells of the interferometer.

DOI: [10.1103/PhysRevLett.99.240406](https://doi.org/10.1103/PhysRevLett.99.240406)

PACS numbers: 03.75.Dg, 03.75.Lm, 39.20.+q

A noninteracting zero temperature Bose-Einstein condensate is the matter-wave analogue to the optical laser, and therefore the ideal atom source for atom interferometry. Finite temperature and atomic interactions profoundly change the coherence properties of a condensate and introduce phase fluctuations and phase diffusion. Those phenomena are of fundamental interest [1–6], but also of practical importance because they may limit the performance of atom interferometers [7–9]. This applies, in particular, to magnetic microtraps and waveguides (e.g., atom chips) [10] since tight confinement and elongated geometry enhances phase diffusion and phase fluctuations.

Phase *diffusion* is a quantum effect associated with the coherent splitting of the condensate. Number fluctuations lead to density fluctuations, which, due to interactions, cause fluctuations of the energy and cause diffusion of the relative phase proportional to the chemical potential times $\Delta N/N$, the amount of fluctuations in the relative atom number. In our previous work [11,12], we showed that such phase diffusion could be dramatically reduced by number squeezing, increasing the coherence time. In this paper, we characterize and discuss the role of spatial phase *fluctuations* in an atom interferometer.

Phase *fluctuations* cause the condensate to break up into several quasicondensates with random phase; i.e., long range coherence is lost. This usually happens in elongated geometries when the temperature is sufficiently high to excite such modes [1,2], or in interacting one-dimensional condensates even at zero temperature due to quantum fluctuations [13]. Spatial phase fluctuations have two major consequences for atom interferometry. First, they speed up phase diffusion, since $\Delta N/N$ refers now to the atom number in a single quasicondensate. Second, they make the atom interferometer much more sensitive to random relative displacements of the split condensates, which have to be smaller than the coherence length, which, for condensates with phase fluctuations, can be much smaller than the size of the condensate.

A typical elongated trap geometry, realized by an atom chip, has an aspect ratio of ~ 200 [8,11,14], sufficient to induce phase fluctuations in a quasicondensate along the

axial direction [1] already at very low temperatures (or in the 1D case, even at zero temperature). When the temperature of a condensate is above the characteristic temperature, $T^* = 15N(\hbar\omega_z)^2/32\mu$, where μ is the chemical potential, N total atom number, ω_z axial trap frequency, and \hbar the Planck's constant divided by 2π [1], then thermal excitations of low energy axial modes lead to longitudinal phase fluctuations. For temperatures above T^* , the coherence length L^* of a phase-fluctuating condensate is shorter than the length L of the condensate $L^*/L = T^*/T$ [1].

Previous experiments [8,11,14] on atom interferometry have operated in a regime where phase fluctuations are predicted to be present. However, their presence has not been observed because the interferometer was read out by integrating the interference fringes along the axial direction. Other experiments characterized phase fluctuations by interferometric techniques [15] and Bragg spectroscopy [16], but did not study the effect of phase fluctuations on an atom interferometer.

In this Letter we observe the axial phase fluctuations spatially resolved and characterize their effect on the coherence time of the atom interferometer. We show explicitly that atom interferometry can be performed in the presence of phase fluctuations. This has been expected [13], since for sufficiently short times after splitting, those fluctuations are identical for both condensates and therefore do not affect the measurement of the relative phase. For the same reason, atom interferometry is possible with thermal clouds of atoms [17]. However, already at short times, phase fluctuations degrade the contrast and can limit the coherence time. As we discuss below, we believe that this degradation is not due to the quantum effect of the increased relative number fluctuations in each quasicondensate because of the high degree of number squeezing, but is rather caused by asymmetries in the double-well potential leading to relative motion of the condensates.

Bose-Einstein condensates of $\sim 4 \times 10^5$ ^{23}Na atoms in the $|F=1, m_F=-1\rangle$ state were transferred into a magnetic trap generated by the trapping wire on an atom chip and external bias field [14]. Using adiabatic rf-induced splitting [8,18], a double-well potential in the vertical plane (paral-

lel to the gravity direction) was formed as illustrated in Fig. 1(a) [19]. Gravity was compensated by a magnetic field gradient from the trapping wire. Typically, the separation of the two wells was $d \sim 6 \mu\text{m}$, the height of the trap barrier was $U \sim h \times 10 \text{ kHz}$, and the difference of the trap bottom between two wells $\sim h \times 300 \text{ Hz}$. The trapping frequencies were $\sim 2 \text{ kHz}$ (radial) and $\sim 10 \text{ Hz}$ (axial). The absorption imaging light for data acquisition was resonant with the $|F=2\rangle \rightarrow |F'=3\rangle$ cycling transition for the trapped atoms and was aligned perpendicular to the condensate axis [side imaging in Fig. 1(c)]. The atoms were optically pumped into the $|F=2\rangle$ hyperfine level with a pulse resonant with the $|F=1\rangle \rightarrow |F'=2\rangle$ transition.

First, we characterized the presence of phase fluctuations in the condensate before splitting by observing density modulations of the expanded atomic cloud after 7 ms time of flight (Fig. 2 inset). In trap, the mean-field interaction energy suppresses density fluctuations, but ballistic expansion converts phase fluctuations into density modulations [2] since the initial velocity field is proportional to the gradient of the phase. The number of observed density striations of around ten is consistent with the ratio of the measured temperature of $\sim 650 \pm 100 \text{ nK}$ and the calculated value of $T^* \approx 60 \text{ nK}$. Since the barrier height is comparable to the temperature, we assume that both condensates interact with the same heat bath. However, we do not expect any difference to the case of two separated thermal clouds.

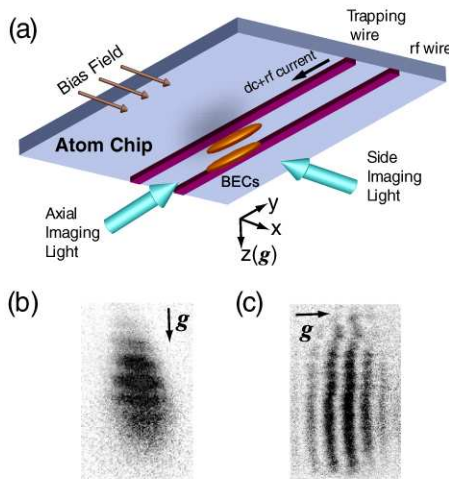


FIG. 1 (color online). Geometry of the atom chip interferometer. (a) Atoms were confined radially by the combined magnetic potential of a current-carrying wire and an external bias field. A pair of end cap wires (not shown) provided axial confinement. The single well was deformed into a vertical double well within 15 ms by adding rf current into the trapping wire dressing the atoms with oscillating rf fields. Absorption image was taken by a probe beam directed along the condensate axis [(b), axial imaging] and perpendicular to the condensate axis [(c), side imaging]. All data in this Letter were obtained using side imaging. The fields of view are $160 \times 260 \mu\text{m}$ and $180 \times 100 \mu\text{m}$ for axial and side imaging, respectively.

The longitudinal phase fluctuations were quantified by measuring the root-mean-square average of the density fluctuations as described in Fig. 2 [20]. The amount of phase fluctuations was controlled by changing the atom number and the temperature with rf-evaporation. The rf field generated by the rf wire [Fig. 1(a)] was swept down from $\sim 20 \text{ kHz}$ above the Larmor frequency at the trap center to a variable final value, leading to a variable chemical potential and temperature of the condensate (Fig. 2 inset) [21]. The variation of the spatial phase fluctuations with chemical potential is shown in Fig. 2.

Having firmly established the presence of phase fluctuations, we can now demonstrate the robustness of an atom interferometer against longitudinal phase fluctuations. For this, we split the condensates and observe the reproducibility of ten interference fringes obtained by recombining the condensates during ballistic expansion. The regular, almost straight interference fringes (Figs. 1 and 3) show that the spatial phase fluctuations are common mode and do not affect the relative phase in a major way.

However, when we increase the amount of phase fluctuations, we observe an increasing blurring or waviness of the interference fringes (Fig. 3). The number of wiggles of the waviness is comparable to the modulation pattern observed in the ballistic expansion of single condensates (Fig. 2). Of course, without any technical imperfection in

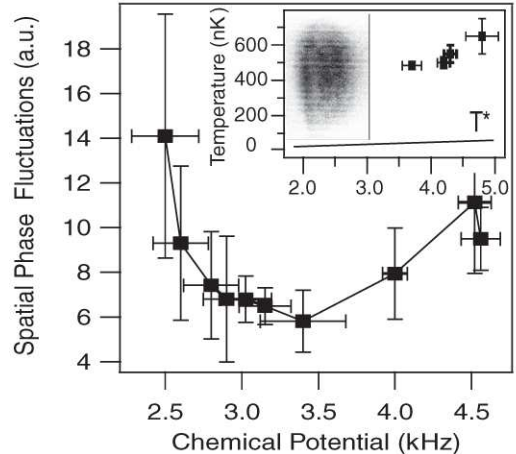


FIG. 2. Spatial phase fluctuations in a single condensate. The phase fluctuations were characterized by observing the density modulations in an absorption image of the expanded cloud after 8 ms time-of-flight (see inset) and calculating the rms fluctuations as described in Ref. [2]. The chemical potential (or atom number) was controlled by additional rf-evaporative cooling. The temperature of the condensate is shown in the inset graph. For chemical potentials less than 3.5 kHz, we could not measure the temperature of a condensate due to the lack of discernible thermal atoms. The observed phase fluctuations do not decrease monotonically, but show a minimum at the chemical potential of $\sim 3.5 \text{ kHz}$, probably because the effect of the lower temperature was more than offset by the loss in the atom number. In the inset graph, T^* displays the characteristic temperature for the onset of the phase fluctuations.

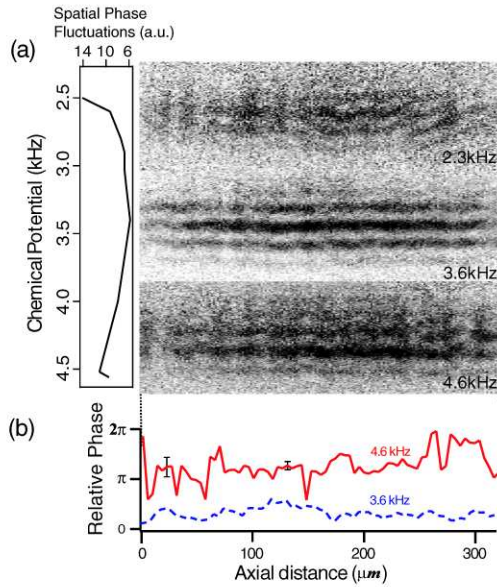


FIG. 3 (color online). Effect of spatial phase fluctuation on the waviness of interference fringes. (a) Interference fringes obtained right after splitting a condensate. For large spatial phase fluctuation (e.g., 4.6 kHz), the fringe pattern shows more significant wiggles than for smaller phase fluctuations (e.g., 3.6 kHz). (b) From the fringes for 3.6 kHz (dashed line) and 4.6 kHz (solid line) chemical potentials, relative phases are obtained along the axial direction. In both cases, the overall relative phase can be well determined by averaging along the axial coordinate, but considerable axial variations of the relative phase were observed in the regime of large longitudinal phase fluctuations (solid line). The error bars indicate the statistical uncertainty in the phase determination.

the splitting process, phase fluctuations would be common mode and not lead to any observable effects right after the splitting. For the smallest amount of spatial phase fluctuations, the relative phase is almost constant along the axial direction [dashed line in Fig. 3(b)]. The effect of larger phase fluctuations is displayed by the solid line. However, an average relative phase can still be determined.

To quantify the reproducibility of the relative phase, we determine the probability of the ten measurements of the relative phase being random (called randomness) [11] (Fig. 4). For values of the chemical potential larger than 3.0 kHz, the randomness is less than 0.1 which implies a reproducible phase with 90% confidence. However, by comparing Figs. 2 and 4, one clearly recognizes the degradation of reproducibility of the relative phase with increasing spatial phase fluctuations. We cannot rule out that the condensate had some weak collective excitations after preparation. However, the amount of the excitation should not depend on the final temperature. Therefore, we attribute the temperature dependence of the fringe contrast to phase fluctuations.

By introducing a variable hold time after the splitting, we can examine how spatial phase fluctuations limit the coherence time of a matter-wave interferometer. Figure 5

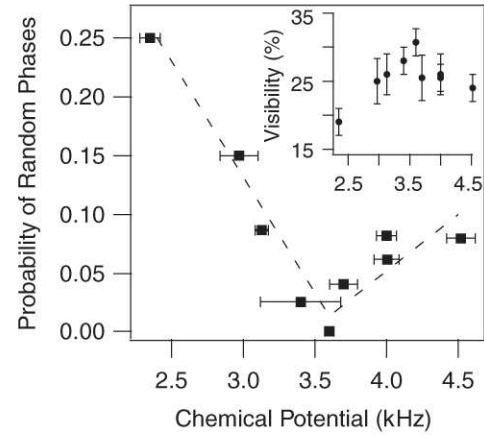


FIG. 4. Effect of spatial phase fluctuations on the reproducibility of the relative phase right after splitting. The probability of random phases was measured with variable longitudinal phase fluctuations immediately after splitting (0 ms hold time). The phase was determined by analyzing the central $\sim 40\%$ of the axial length of the interference pattern. In the inset graph, the visibility of the integrated interference fringe over the central $\sim 40\%$ is shown.

shows the increase of randomness with hold time. For the smallest amount of phase fluctuations (chemical potential ~ 3.4 kHz, black squares in Fig. 5), the phase coherence time is ~ 23 ms. As the spatial phase fluctuations increase (solid circles and open squares in Fig. 5), the phase coherence time becomes shorter [22]. It should be noted that in the absence of spatial phase fluctuations, for a condensate with zero temperature, the rate of phase diffusion decreases with chemical potential, proportional to $\sim \mu^{-1/4}$ [3,4], which is also valid at finite temperature [3]. Our observed increase of decoherence with increasing chemical potential is therefore attributed to the increase of spatial phase fluctuations. The increasing waviness of the interference fringes show that the decoherence is caused by randomization of the relative phase along the axial direction [Fig. 5(b)].

By which mechanism do the spatial phase fluctuations affect the interferometer signal? For our experimental parameters, the rate of phase diffusion (assuming Poissonian number fluctuations after the splitting) is ~ 20 ms [3,4]. For our value of T/T^* , the condensate fragments into ~ 10 quasicondensates which should decrease the coherence time by a factor of $\sqrt{10}$ to about 7 ms. Our observation of much longer coherence times implies strong squeezing of the relative number fluctuations, as already observed in Ref. [11]. In Ref. [11] we inferred a reduction of the number fluctuations below shot noise by a factor of 10. However, having now established the presence of strong phase fluctuations, we should reinterpret our previous result. Those data were taken at a value of T/T^* of about 7, which implies that the number fluctuations for each quasicondensate was squeezed by a factor of ~ 25 . Our current experiments were carried out in a rotated geometry (in

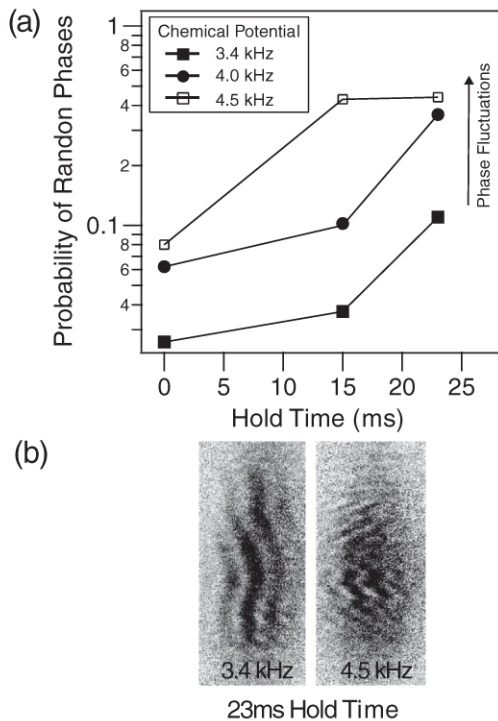


FIG. 5. Effect of longitudinal phase fluctuations on the coherence time between the split condensates. (a) The probability for a random phase for ten measurements of the relative phase is shown for three different amounts of the longitudinal phase fluctuations. (b) For condensates in the regime of large longitudinal phase fluctuations (~ 4.5 kHz), interference fringes show more wavy patterns, which led to the increased randomness of the measured relative phase.

order to be able to observe along a radial direction), but the value of $T/T^* \sim 10$ is similar. If we assume that the squeezing factor is the same, then we should have observed phase coherence times comparable to the 200 ms observed previously [11].

We therefore conclude that the shorter coherence times observed in this Letter are not limited by the fundamental quantum phase diffusion of quasicondensates because of strong number squeezing, but rather reflect the interplay of spatial phase fluctuations and some relative motion of the two condensates. This is probably due to some asymmetries in the current trapping potential [23] and/or technical noise. The loss of coherence due to phase fluctuations starts already during the splitting process (Figs. 3 and 4), and increases with hold time.

The main conclusions of this Letter are that matter-wave interferometers are robust against spatial phase fluctuations, especially when strong number squeezing mitigates the fragmentation into smaller quasicondensates (which show faster phase diffusion than a single condensate) resulting in coherence times of up to 200 ms [11]. However, spatial phase fluctuations make the interferome-

ter much more sensitive to residual relative motion of the two split condensates and therefore require a highly symmetric double-well potential.

This work was funded by DARPA, NSF, and ONR. G.-B. Jo and Y.-R. Lee acknowledge additional support from the Samsung foundation. We thank H. Kim for experimental assistance and Y. Shin for critical reading of the manuscript. We also thank E. Demler for stimulating discussions.

*http://cua.mit.edu/ketterle_group/

- [1] D. S. Petrov, G. V. Shlyapnikov, and J. T. M. Walraven, *Phys. Rev. Lett.* **87**, 050404 (2001).
- [2] S. Dettmer *et al.*, *Phys. Rev. Lett.* **87**, 160406 (2001).
- [3] M. Lewenstein and L. You, *Phys. Rev. Lett.* **77**, 3489 (1996).
- [4] Y. Castin and J. Dalibard, *Phys. Rev. A* **55**, 4330 (1997).
- [5] D. S. Petrov, M. Holzmann, and G. V. Shlyapnikov, *Phys. Rev. Lett.* **84**, 2551 (2000).
- [6] D. S. Petrov, G. V. Shlyapnikov, and J. T. M. Walraven, *Phys. Rev. Lett.* **85**, 3745 (2000).
- [7] Y. Shin *et al.*, *Phys. Rev. Lett.* **92**, 050405 (2004).
- [8] T. Schumm *et al.*, *Nature Phys.* **1**, 57 (2005).
- [9] S. Hofferberth *et al.*, *Nature (London)* **449**, 324 (2007).
- [10] J. Fortagh and C. Zimmermann, *Rev. Mod. Phys.* **79**, 235 (2007).
- [11] G.-B. Jo *et al.*, *Phys. Rev. Lett.* **98**, 030407 (2007).
- [12] G.-B. Jo *et al.*, *Phys. Rev. Lett.* **98**, 180401 (2007).
- [13] R. Bistritzer and E. Altman, *Proc. Natl. Acad. Sci. U.S.A.* **104**, 9955 (2007).
- [14] Y. Shin *et al.*, *Phys. Rev. A* **72**, 021604(R) (2005).
- [15] D. Hellweg *et al.*, *Phys. Rev. Lett.* **91**, 010406 (2003).
- [16] S. Richard *et al.*, *Phys. Rev. Lett.* **91**, 010405 (2003).
- [17] T. Gustavson, P. Bouyer, and M. Kasevich, *Phys. Rev. Lett.* **78**, 2046 (1997).
- [18] O. Zobay and B. M. Garraway, *Phys. Rev. Lett.* **86**, 1195 (2001).
- [19] S. Hofferberth *et al.*, *Nature Phys.* **2**, 710 (2006).
- [20] For quantitative analysis of the spatial phase fluctuations, the density profile obtained from an absorption image is Fourier transformed. After filtering out high and low momentum components, the profile is transformed back and its root-mean-square average is determined (Fig. 2).
- [21] In the final stage of the evaporation, the ratio of trap depth to temperature was rather small (≈ 2), possibly due to heating from the atom chip potential.
- [22] We did not study the temporal evolution for chemical potentials smaller than 3.4 kHz due to the large fluctuations in the evaporation process.
- [23] In our trap geometry, the two condensates in vertically separated potential wells feel different magnetic fields from a pair of end cap wires. The slightly asymmetric axial confinement leads to some quadrupolar relative motion of the two separated condensates. For the determination of the relative phase, we select the central region where the fringes were parallel to the axial direction.

Appendix F

Phase-Sensitive Recombination of Two Bose-Einstein Condensates on an Atom Chip

This appendix contains a reprint of Ref. [100]: G.-B. Jo, J.-H. Choi, C.A. Christensen, T.A. Pasquini, Y.-R. Lee, W. Ketterle, and D.E. Pritchard, *Phase-Sensitive Recombination of Two Bose-Einstein Condensates on an Atom Chip*, Phys. Rev. Lett. **98**, 180401 (2007).



Phase-Sensitive Recombination of Two Bose-Einstein Condensates on an Atom Chip

G.-B. Jo, J.-H. Choi, C. A. Christensen, T. A. Pasquini, Y.-R. Lee, W. Ketterle, and D. E. Pritchard*

*MIT-Harvard Center for Ultracold Atoms, Research Laboratory of Electronics, Department of Physics,
Massachusetts Institute of Technology, Cambridge, Massachusetts 02139, USA*

(Received 28 February 2007; published 30 April 2007)

The recombination of two split Bose-Einstein condensates on an atom chip is shown to result in heating which depends on the relative phase of the two condensates. This heating reduces the number of condensate atoms between 10% and 40% and provides a robust way to read out the phase of an atom interferometer without the need for ballistic expansion. The heating may be caused by the dissipation of dark solitons created during the merging of the condensates.

DOI: [10.1103/PhysRevLett.98.180401](https://doi.org/10.1103/PhysRevLett.98.180401)

PACS numbers: 03.75.Dg, 03.75.Lm, 39.20.+q

Most experiments in atom interferometry use freely propagating atom clouds [1–3]. Alternative geometries are confined-atom interferometers where atoms [3] are guided or confined in trapping potentials [4], often realized by using atom chips [5]. These geometries are promising in terms of compactness and portability, and also offer the prospect of extending interrogation times beyond the typical 0.5 s achievable in the atomic fountains. Such interferometers can be used to study atom-surface interactions [6] and Josephson phenomena [7].

Many discussions of confined-atom interferometers propose a readout by merging the two separated clouds [8–10]. These discussions usually assume noninteracting atoms [8,11] and do not address the deleterious effects of atomic interactions, including dephasing, collisional shifts, and phase diffusion [12–17]. A recent study showed that the recombination process is much more sensitive to atomic interactions than the splitting process since merging clouds with the opposite phase involves excited modes of the recombined potential and can lead to exponential growth of unstable modes [18]. To circumvent these problems, previous realizations of confined-atom interferometry used ballistic expansion of the two spatially independent condensates, which decreases the atomic density before overlap [4,19–21] or worked at very low atom densities and pushed the clouds into each other with photon recoil [22,23]. While this avoids the deleterious effects of atom-atom interactions during the recombination, it lacks the inherent simplicity and robustness of in-trap recombination. Furthermore, in-trap recombination, combined with dispersive, *in situ*, imaging [24], could make it possible to recycle the condensate for the next measurement cycle after resetting the temperature through evaporating cooling. The detection optics for *in situ* imaging may even be integrated onto the atom chip [25]. Moreover, a trapped sample at high optical density can be read out with subshot noise precision using cavity-enhanced atom detection [26].

In this Letter, we show that in-trap recombination leads indeed to heating of the atomic cloud. However, this heating is phase dependent and can be used as a robust and sensitive readout of the atom interferometer. The resulting

oscillations of the condensate atom number are dramatic (typically $\sim 25\%$ contrast), occur over a wide range of recombination rates, and permit high signal to noise ratios since they simply require a measurement of the total number of condensate atoms in the trap.

The implications of phase-sensitive recombination extend beyond atom interferometry. Recombination with uncontrolled phase was used to replenish a continuous Bose-Einstein condensate (BEC) [27] or to create vortices [28]. An extreme case of the merge process, where two condensates are suddenly connected, has been studied by optically imprinting a dark soliton into a single trapped condensate [29,30]. Here we use methods of atom interferometry to prepare two condensates with well-defined relative phase and study the merging process for variable recombination times.

Two special cases of the merging process can be exactly described (Fig. 1). Two noninteracting separated condensates with the same phase should adiabatically evolve into the ground state of the combined potential, whereas a π -relative phase should result in the lowest lying antisymmetric state with excitation energy $N\hbar\omega$, where N is the total number of atoms in a trap and ω is the transverse frequency of the trapping potential. The other limiting case is a merging process where a thin membrane separates two interacting condensates until the potentials are merged, and then is suddenly removed. For the 0-relative phase, the merged condensate is in its Thomas-Fermi ground state. For a π -relative phase, however, the merged condensate contains a dark soliton. Although the wave function differs from the ground state only in a thin layer, the total energy of this excited state is proportional to $N\hbar\omega$, as the lowest antisymmetric state in the noninteracting case [31].

Our working assumption is that the phase-sensitive excitation of the cloud decays quickly, on the order of ~ 1 ms in our system, and leads to an increase in temperature on the order of $\hbar\omega/k_B \approx 100$ nK for the case of $\Delta\phi = \pi$, and less for other values of $\Delta\phi$, where k_B is the Boltzmann constant. The parameters of our experiment were intermediate between limiting cases of suddenness or adiabaticity, and we found a window of recombination times for

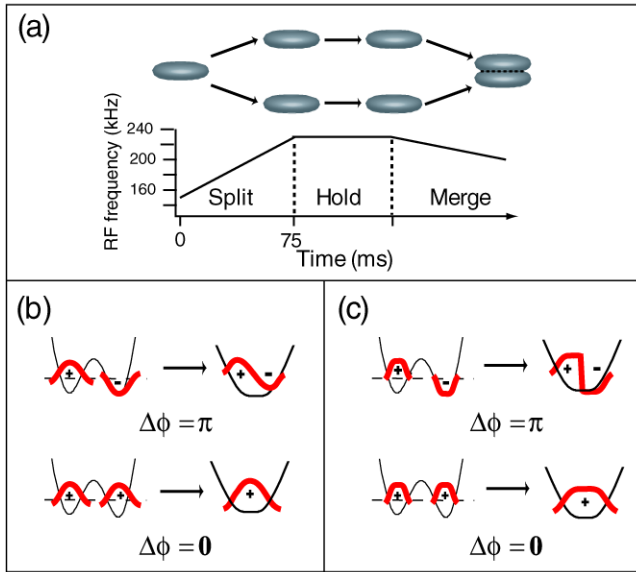


FIG. 1 (color online). Schematic of the in-trap recombination with a well-defined relative phase. (a) The phase-coherent condensates were prepared using a radio frequency induced double-well potential on an atom chip [21]. The splitting was done within 75 ms by ramping up the rf frequency from 140 to 225 kHz. During the hold time, the relative phase of two independent condensates evolved with time at ~ 500 Hz. After a variable time, the double-well potential was deformed into a single well and the two trapped condensates were merged by decreasing the rf frequency by 33 kHz over a variable “recombination time.” The condensates started to spill over the barrier after $\leq 10\%$ of the recombination time or ~ 3 kHz decrease of the rf frequency. (b),(c) The merged matter-wave functions are shown for the cases of an adiabatic merger of noninteracting condensates and for a sudden merger of interacting condensates.

the phase-sensitive readout to which none of these descriptions apply.

Bose-Einstein condensates of $\sim 4 \times 10^5$ ^{23}Na atoms in the $|F = 1, m_F = -1\rangle$ state were transferred into a magnetic trap generated by the trapping wire on an atom chip and an external bias field [19]. The cloud had a condensate fraction $\approx 90\%$ and the temperature was $\sim 1/2$ of the BEC transition temperature, well above 0.1 when axial phase fluctuations are excited. Using adiabatic rf-induced splitting [20,32], a double-well potential in the horizontal plane was formed. Typically, the separation of the two wells was $d \sim 6 \mu\text{m}$, the height of the trap barrier was $U \sim h \times 10 \text{ kHz}$, and the chemical potential of the condensates, measured from the trap bottom, was $\mu \sim h \times 6 \text{ kHz}$, where h is Planck’s constant. In the experiment, the coherence time of two separated condensates was at least ~ 50 ms [21]. The recombination of two split condensates was realized by reducing the rf frequency as described in Fig. 1(a), which decreases the trap barrier height. The merging occurred slowly compared to the time scale determined by the radial trap frequency (~ 1 kHz) to minimize mechanical excitation.

To monitor the energy increase after recombination, we measured the central atom density during ballistic expansion. Phase-sensitive collective excitations, in addition to mechanical excitations from the splitting and merging processes, heat the cloud and lower the condensate fraction and, therefore, reduce the central density. In the experiment, the split condensates were held in the double-well potential for varying hold times, merged into a single potential, and released by turning off the trapping potential within $30 \mu\text{s}$. After 8 ms time of flight, we measured the number of atoms in a fixed area which is comparable to the size of (expanded) Thomas-Fermi radius [dotted box in Fig. 2(c)]. While the total atom number was conserved, the number within the fixed area decreased, indicating that the temperature had increased. The fractional loss of condensate atoms was obtained as the ratio of atom number after recombination to the atom number before splitting.

The fractional loss of condensate atoms was reproducible for a given hold time, and observed to oscillate between 15% and 35% as a function of hold time at a rate of 500 Hz (Figs. 2 and 3). The observed oscillations are sinusoidal, although the nonlinear interactions can give rise to nonsinusoidal variations [16]. To confirm that this oscillatory heating was associated with the relative phase of the split condensates, we measured the relative phase as the spatial phase of the interference pattern when the split condensates were suddenly released and interfered during ballistic expansion [Fig. 2(a)] [4]. The strong correlation between the two measurements [Fig. 2(b)] is the central result of this Letter. As the relative phase increased from 0 to π , the atom loss after recombination increased [Fig. 2(b)]; the π -relative phase (0-relative phase) difference leads to maximum (minimum) loss of condensate atoms.

The use of phase-sensitive recombination as a readout for an atom interferometer is demonstrated in Fig. 3. The separated condensates accumulate relative phase for an evolution time of up to 6 ms which is read out after in-trap recombination. The phase-sensitive recombination signal showed high contrast over a wide range of recombination times [Figs. 3 and 4(a)]. The observed largest amplitudes of condensate atom loss correspond to a change in temperature on the order of ~ 100 nK, in agreement with the estimate in the introduction. This is testimony to the insensitivity of the energy of phase-dependent excitations against changes in the exact recombination parameters, and is promising for further applications of chip-based atom interferometry.

The dependence of the condensate atom loss on the recombination time allows us to speculate about different excitations caused by the merging process. The 1 ms recombination time shows little contrast [Fig. 3(d)]. This time scale is comparable to the period of radial oscillations, and one would expect breakdown of adiabaticity and excitation of collective excitations independent of the relative phase. Significant loss ($\sim 30\%$) was observed for all relative phases and masked or suppressed any phase-sensitive signal. The loss of contrast for the long recombination

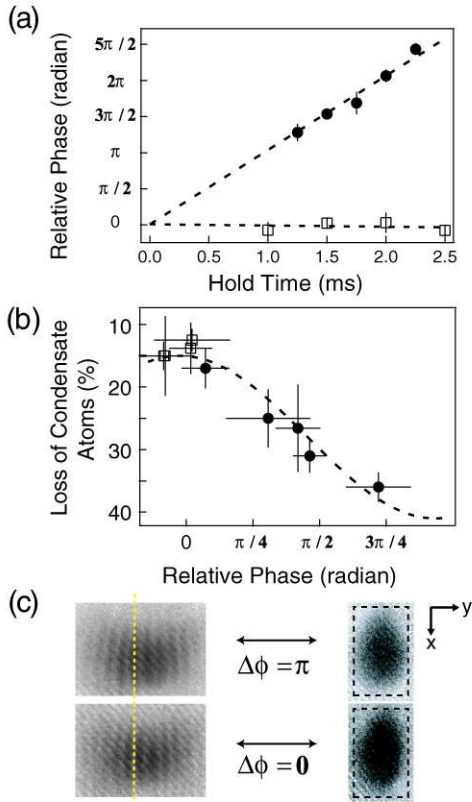


FIG. 2 (color online). Phase-sensitive recombination of two separate condensates. (a) The relative phase of two split condensates was monitored for various hold time after splitting by suddenly releasing the two condensates and observing interference fringes. For the independent condensates (solid circle), the evolution rate of the relative phase was determined from the linear fit to be ~ 500 Hz. For the weakly coupled condensates (open square), the relative phase did not evolve. At 0 ms hold time, the relative phase was set to zero for both cases. (b) For the same range of delay times as in (a), the condensate atom loss after in-trap recombination was determined. The relative phase (x axis) was obtained from interference patterns as in (a). The merging time was 5 ms. (c) The matter-wave interference patterns (after 9 ms time of flight) and absorption images of merged clouds (after 8 ms time of flight) show the correlation between phase shift and absorption signal. The field of view is $260 \times 200 \mu\text{m}$ and $160 \times 240 \mu\text{m}$ for matter-wave interferences and merged clouds, respectively.

times could be caused by relaxation of the phase-sensitive collective excitation during the merging process when the condensates are connected only by a region of low density, and solitonlike excitations have lower energy. An alternative explanation is the evolution of the relative phase (at ~ 500 Hz) during the effective recombination time. In a simple picture assuming a thin membrane being slowly pulled out between the condensates, a phase evolution during this time would create local solitons with phases varying between 0 and π . This could wash out the phase-sensitive signal to an average value. Since the data for 100 ms recombination time show low loss [comparable to the zero relative phase loss for faster recombination

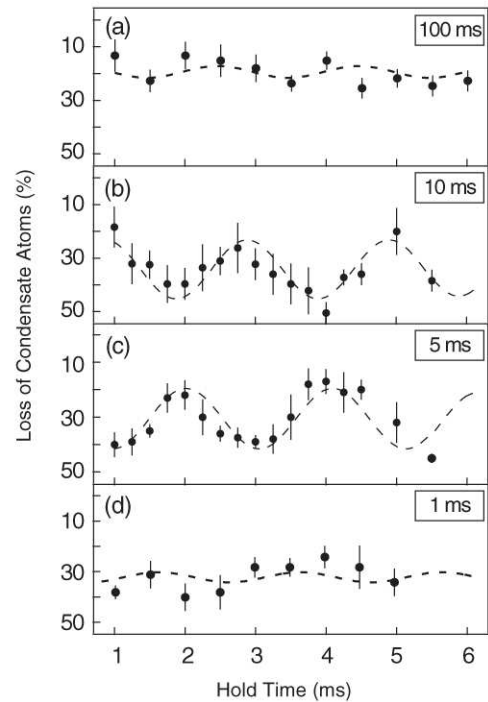


FIG. 3. Oscillations of condensate atom loss after recombination reflecting the coherent phase evolution. The condensate atom loss was monitored during a variable hold time for the two split condensates whose relative phase evolved at ~ 500 Hz. The merging was done for different values of the recombination time: 100 (a), 10 (b), 5 (c), and 1 ms (d). The dotted lines are sinusoidal curves fitted with fixed frequency ~ 500 Hz. The reproducible phase shift for the 5 and 10 ms data occurred during the recombination process. The data points represent the average of 6 measurements.

times, Fig. 3(d)], we favor the first explanation. Furthermore, it is not clear during what fraction of the ramp time of the rf frequency (called the recombination time) the effective merging of the condensates and the creation of a phase-sensitive collective excitation occurs. The time between when the barrier equals the chemical potential and when the barrier reaches $\sim 70\%$ of the chemical potential is 10% of the recombination time. Another open question is what the rate of phase evolution is at the moment of the merger. It is plausible that during splitting, the condensates have the same chemical potential, and that the observed difference is created only when the condensates are further separated by ramping up the barrier. This would imply that during recombination, the situation reverses, the chemical potential difference is reduced and reaches near zero when the condensates merge. In any case, our work raises intriguing questions for further experimental and theoretical studies: What kind of phase-sensitive excitations are created during a merger process? How and when do they dissipate, and what would happen when two condensates with different chemical potentials are merged?

The present work demonstrates that interactions between atoms and collective excitations are not necessarily deleterious to direct recombination of separated trapped

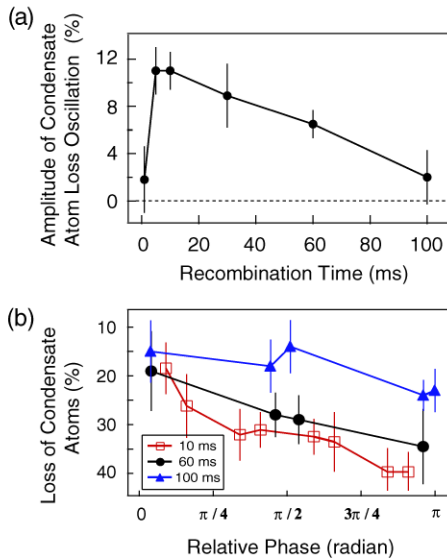


FIG. 4 (color online). Recombination time and atom loss. (a) The amplitude of atom loss oscillations was determined for various recombination times. (b) Assuming that minimum atom loss occurs at 0-relative phase of the two condensates, relative phases were obtained from the fitted atom loss oscillations in Fig. 3.

condensates that have acquired a relative phase in atom interferometry. In contrast, the phase-sensitive generation of collective excitations is used to monitor the relative phase. This complements our previous work where atomic interactions were shown to enhance the coherence time by preparing a number squeezed state with the help of atomic interactions during the beam splitting process [21]. So the merger between condensed matter and atomic physics goes both ways. In recent years, atomic physics has developed powerful tools to study many-body physics [33], and, as we have shown here, many-body physics provides methods and tools to atom optics.

This work was funded by DARPA, NSF, and ONR. G.-B. Jo and Y.-R. Lee acknowledge additional support from the Samsung Foundation. We would like to acknowledge Y. Shin for useful discussions, and M. Vengalattore and M. Prentiss for atom chip fabrication.

*Electronic address: http://cua.mit.edu/ketterle_group/

- [1] D. W. Keith, C. R. Ekstrom, Q. A. Turchette, and D. E. Pritchard, *Phys. Rev. Lett.* **66**, 2693 (1991).
- [2] M. Kasevich and S. Chu, *Phys. Rev. Lett.* **67**, 181 (1991).
- [3] P. Berman, *Atom Interferometry* (Academic, New York, 1997).
- [4] Y. Shin, M. Saba, T. A. Pasquini, W. Ketterle, D. E. Pritchard, and A. E. Leanhardt, *Phys. Rev. Lett.* **92**, 050405 (2004).
- [5] J. Fortagh and C. Zimmermann, *Rev. Mod. Phys.* **79**, 235 (2007).
- [6] J. D. Perreault and A. D. Cronin, *Phys. Rev. Lett.* **95**, 133201 (2005).
- [7] M. Albiez, R. Gati, J. Fölling, S. Hunsmann, M. Cristiani, and M. K. Oberthaler, *Phys. Rev. Lett.* **95**, 010402 (2005).
- [8] W. Hänsel, J. Reichel, P. Hommelhoff, and T. W. Hänsch, *Phys. Rev. A* **64**, 063607 (2001).
- [9] J. A. Stickney and A. A. Zozulya, *Phys. Rev. A* **66**, 053601 (2002).
- [10] A. Negretti and C. Henkel, *J. Phys. B* **37**, L385 (2004).
- [11] E. Andersson, T. Calarco, R. Folman, M. Andersson, B. Hessmo, and J. Schmiedmayer, *Phys. Rev. Lett.* **88**, 100401 (2002).
- [12] Y. Castin and J. Dalibard, *Phys. Rev. A* **55**, 4330 (1997).
- [13] M. Lewenstein and L. You, *Phys. Rev. Lett.* **77**, 3489 (1996).
- [14] E. M. Wright, D. F. Walls, and J. C. Garrison, *Phys. Rev. Lett.* **77**, 2158 (1996).
- [15] J. Javanainen and M. Wilkens, *Phys. Rev. Lett.* **78**, 4675 (1997).
- [16] A. J. Leggett and F. Sols, *Phys. Rev. Lett.* **81**, 1344 (1998).
- [17] J. Javanainen and M. Wilkens, *Phys. Rev. Lett.* **81**, 1345 (1998).
- [18] J. A. Stickney and A. A. Zozulya, *Phys. Rev. A* **68**, 013611 (2003).
- [19] Y. Shin, C. Sanner, G.-B. Jo, T. A. Pasquini, M. Saba, W. Ketterle, D. E. Pritchard, M. Vengalattore, and M. Prentiss, *Phys. Rev. A* **72**, 021604 (2005).
- [20] T. Schumm, S. Hofferberth, L. Andersson, S. Wildermuth, S. Groth, I. Bar-Joseph, J. Schmiedmayer, and P. Krüger, *Nature Phys.* **1**, 57 (2005).
- [21] G.-B. Jo, Y. Shin, S. Will, T. A. Pasquini, M. Saba, W. Ketterle, D. E. Pritchard, M. Vengalattore, and M. Prentiss, *Phys. Rev. Lett.* **98**, 030407 (2007).
- [22] O. Garcia, B. Deissler, K. J. Hughes, J. M. Reeves, and C. A. Sackett, *Phys. Rev. A* **74**, 031601(R) (2006).
- [23] E. Su, S. Wu, and M. Prentiss, physics/0701018.
- [24] M. R. Andrews, M.-O. Mewes, N. J. van Druten, D. S. Durfee, D. M. Kurn, and W. Ketterle, *Science* **273**, 84 (1996).
- [25] T. Steinmetz, A. Balocchi, Y. Colombe, D. Hunger, T. Hänsch, R. Warburton, and J. Reichel, physics/0606231.
- [26] I. Teper, Y.-J. Lin, and V. Vuletic, *Phys. Rev. Lett.* **97**, 023002 (2006).
- [27] A. P. Chikkatur, Y. Shin, A. E. Leanhardt, D. Kielpinski, E. Tsikata, T. L. Gustavson, D. E. Pritchard, and W. Ketterle, *Science* **296**, 2193 (2002).
- [28] D. R. Scherer, C. N. Weiler, T. W. Neely, and B. P. Anderson, cond-mat/0610187.
- [29] S. Burger, K. Bongs, S. Dettmer, W. Ertmer, K. Sengstock, A. Sanpera, G. V. Shlyapnikov, and M. Lewenstein, *Phys. Rev. Lett.* **83**, 5198 (1999).
- [30] J. Denschlag, J. E. Simsarian, D. L. Feder, C. W. Clark, L. A. Collins, J. Cubizolles, L. Deng, E. W. Hagley, K. Helmerson, and W. P. Reinhardt *et al.*, *Science* **287**, 97 (2000).
- [31] In a layer on the order of the healing length ξ , the soliton has a kinetic energy per atom proportional to $(1/\xi)^2$. With the Thomas-Fermi radius proportional to $\hbar/(\omega\xi)$, the number of atoms covered by the soliton is proportional to $N\omega\xi^2$, and the total energy to $N\hbar\omega$. If the condensates were merged along their long axis, the soliton energy would be smaller by the aspect ratio, that is, ~ 200 .
- [32] O. Zobay and B. M. Garraway, *Phys. Rev. Lett.* **86**, 1195 (2001).
- [33] J. R. Anglin and W. Ketterle, *Nature (London)* **416**, 211 (2002).

Appendix G

Trapping of Ultracold Atoms in a Hollow-core Photonic Crystal Fiber

This appendix contains a reprint of Ref. [39]: C.A. Christensen, S. Will, M. Saba, G.-B. Jo, Y. Shin, W. Ketterle, and D.E. Pritchard, *Trapping of Ultracold Atoms in a Hollow-core Photonic Crystal Fiber*, Phys. Rev. A. **78**, 033429 (2008).

Trapping of ultracold atoms in a hollow-core photonic crystal fiber

Caleb A. Christensen,¹ Sebastian Will,² Michele Saba,³ Gyu-Boong Jo,¹ Yong-II Shin,¹
Wolfgang Ketterle,¹ and David Pritchard¹

¹MIT-Harvard Center for Ultracold Atoms, Research Laboratory of Electronics, Department of Physics,
Massachusetts Institute of Technology, Cambridge, Massachusetts 02139, USA

²Institut für Physik, Johannes Gutenberg-Universität, 55099 Mainz, Germany

³Dipartimento di Fisica, Università di Cagliari, Cagliari, Italy

(Received 29 July 2008; published 25 September 2008)

Ultracold sodium atoms have been trapped inside a hollow-core optical fiber. The atoms are transferred from a free-space optical dipole trap into a trap formed by a red-detuned Gaussian light mode confined to the core of the fiber. We show that at least 5% of the atoms held initially in the free-space trap can be loaded into the core of the fiber and retrieved outside.

DOI: [10.1103/PhysRevA.78.033429](https://doi.org/10.1103/PhysRevA.78.033429)

PACS number(s): 37.10.Gh, 03.75.Be, 42.70.Qs

I. INTRODUCTION

Ultracold atoms in waveguides are being used for studying quantum optics [1], performing atom interferometry [2–5], and implementing schemes for quantum-information science [6]. Of particular interest is the ability of waveguides and microtraps to strongly confine atoms, providing high optical densities, strong interactions with light, and mechanisms for transporting atoms for further experiments.

Hollow-core optical fibers can guide and confine both atoms and light. Previous experiments have reported guiding atoms in optical dipole traps (ODTs) formed by light guided in hollow fibers [7–10]; these experiments used capillaries which guide light in multiple modes in the cladding or core. Such fibers are susceptible to speckle or inhomogeneous fields causing uncontrolled guiding, heating, or loss due to local absence of confinement. Recently developed alternatives are photonic crystal fibers which propagate a single Gaussian mode confined to a hollow core [11,12]. If ultracold atoms are efficiently loaded into such a mode using red-detuned light, the atoms might be held for long times or controllably transported along the fiber. The first experiments have succeeded in trapping ultracold atoms [13] or guiding thermal [14] or laser-cooled atoms [15] through hollow-core photonic band gap fibers.

This paper presents results [13] on the transfer of trapped ultracold sodium atoms into a hollow-core fiber, and the retrieval of a significant fraction (at least 5%) back in the external trap.

II. EXPERIMENTAL PROCEDURE

We produce sodium Bose-Einstein condensates (BECs) using laser cooling and rf evaporation in a dc Ioffe-Pritchard magnetic trap, then load the BEC into a red-detuned ODT formed by a focused laser. The ODT focus can be moved by translating the focusing optics outside the vacuum chamber [16]. This procedure typically delivers a condensate of 10^6 atoms to a separate vacuum chamber holding a fiber. The ODT is positioned 1 mm from the end of a hollow-core photonic crystal fiber (2 cm long, Blaze Photonics HC-1060-02) which supports a red-detuned Gaussian mode in the core,

hereafter called the hollow-core trap (HCT). The fiber has a $10\ \mu\text{m}$ hollow core that atoms can enter. By adjusting the intensities of the two traps, the atoms can be controllably transferred between them.

The light for the ODT and the HCT is produced by a 1064 nm Spectra-Physics J201-BL-106C diode pumped solid state multimode laser. Intensities are controlled by using acousto-optical modulators. The beams are frequency shifted such that they have 50 MHz relative detuning in order to prevent static interference fringes in regions where the traps overlap. The laser is coupled to the core mode by focusing the beam onto the fiber tip from outside the vacuum chamber (Fig. 1). Using a retractable mirror, the light exiting the other end of the fiber can be observed to determine how well the core mode is coupled, as well as how much light has coupled into other modes that can propagate in the cladding or on the surface of the fiber.

Because the 1064 nm trapping light is far detuned from the 589 nm ^{23}Na D_2 line, the light scattering rate, which scales as $1/\delta^2$, is less than 10^{-3} Hz. Therefore radiation pressure, heating, and trap loss associated with scattering are negligible in the experiment. In the far-detuned limit where $\delta \gg \Omega_R, \Gamma$, the potential is given by

$$U(r) = \frac{\hbar[\Omega_R(r)]^2}{4} \left(\frac{1}{\omega_L - \omega_0} + \frac{1}{\omega_L + \omega_0} \right) \\ = \frac{\hbar\Gamma^2 I(r)}{8I_{\text{sat}}} \left(\frac{1}{\delta} + \frac{1}{2\omega_0 + \delta} \right), \quad (1)$$

where $[\Omega_R(r)]^2$ is the squared Rabi frequency, proportional to the position-dependent beam intensity $I(r)$, $\delta = \omega_L - \omega_0$ is the laser detuning in rad/s, and Γ is the natural linewidth. For the sodium D_2 line, the saturation intensity $I_{\text{sat}} = 6\ \text{mW}/\text{cm}^2$ and $\Gamma = 2\pi \times 10\ \text{MHz}$. Note that the counter-rotating term accounts for 25% of the potential.

The focus of the ODT has a waist $w_0 = 20\ \mu\text{m}$, approximated by a Gaussian profile of

$$I(\rho, z) = \frac{2P}{\pi w(z)^2} e^{-2\rho^2/w(z)^2} \quad (2)$$

where ρ is the radial coordinate, z is the axial distance from the focal plane, $w(z)$ is the beam radius

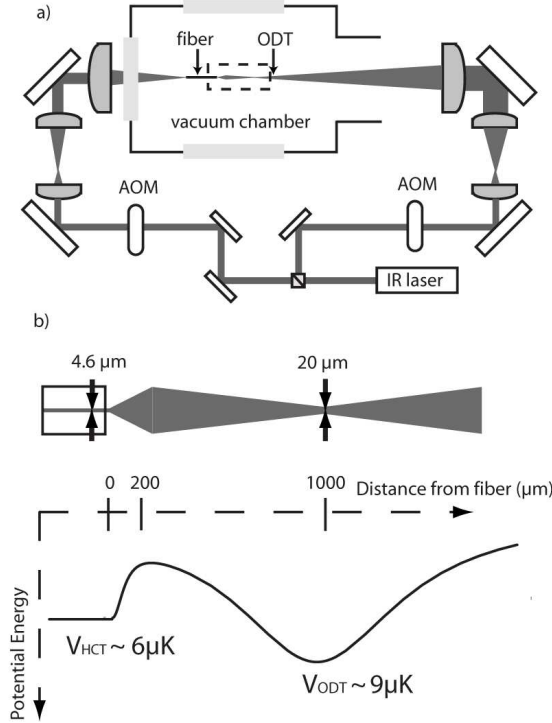


FIG. 1. (a) Diagram of the optics setup. Note that both beams used for trapping are first-order-diffracted beams from acousto-optic modulators. (b) Closeup of the region near the fiber where the atoms are held and transferred. The combined potential of the traps with 150 mW in the ODT and 5 mW in the HCT is sketched.

$w(z) = w_0 \sqrt{1 + (\lambda z / \pi w_0^2)^2}$, and P is the beam power. The HCT mode is approximately Gaussian in the radial direction with a waist of $4.6 \mu\text{m}$. Assuming only the core mode is excited, the mode is axially constant along the fiber and diverges at the fiber tip according to the Gaussian formula, with the appropriate P and w_0 .

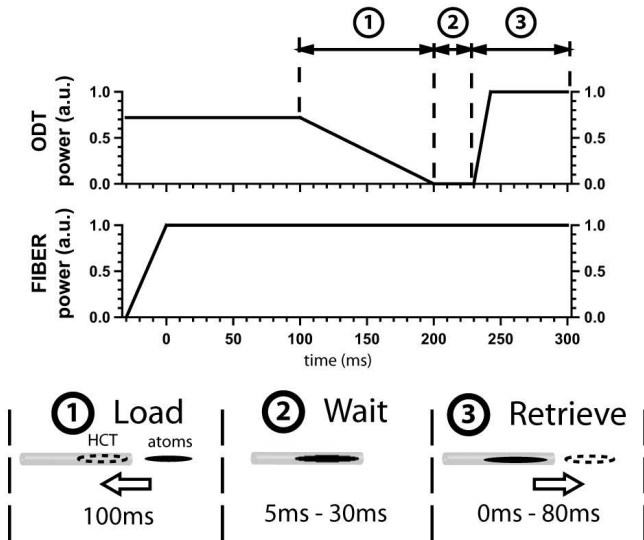


FIG. 2. Time line for transferring atoms by ramping laser power. The fiber light is ramped up while the atoms are in the ODT, and the ODT is ramped down to transfer to the HCT (1), turned off for holding (2), and ramped up to retrieve the atoms (3).

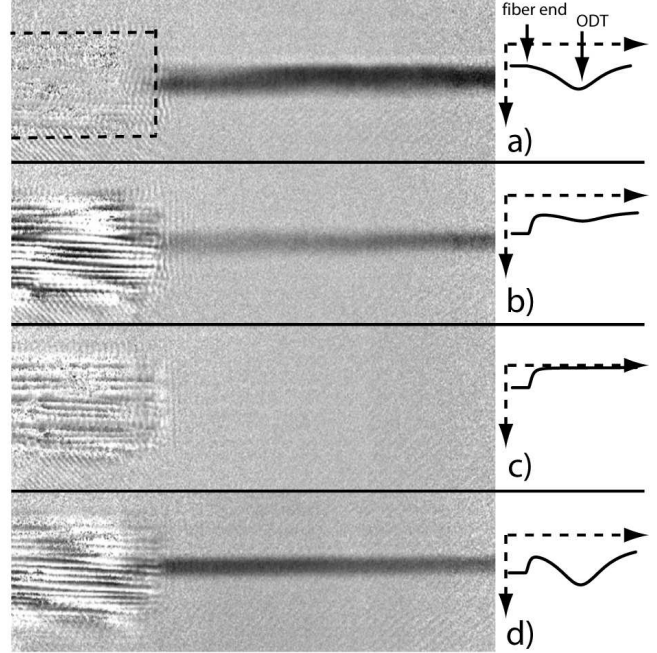


FIG. 3. Images of atoms in the ODT during the experiment. Also shown are sketches of the corresponding combined potential of the HCT and ODT. (a) Atoms are held in the ODT near the fiber, with no light coupled into the fiber. The dashed line indicates the position of the $100 \mu\text{m}$ thick fiber. (b) Light is coupled to the fiber, and as the ODT intensity is ramped down, atoms are depleted from the ODT until (c) no atoms remain outside the fiber when the ODT power reaches zero. (d) After ramping the ODT back up, atoms that were trapped in the HCT return to the ODT.

The calculated depths of the ODT and HCT are 5.8×10^{-2} and $1.2 \mu\text{K}/\text{mW}$, respectively [Fig. 1(b)]. The maximum power in the ODT is 150 mW. Potentials are qualitatively consistent with our observations if we assume a maximum power of 5 mW in the core mode of the fiber. Bench tests suggested that three times more power could couple through the fiber, but we believe that the extra power was in surface or cladding modes and did not contribute to the core intensity.

The ODT is positioned in front of the fiber, and the laser intensities in the two traps are ramped to perform the transfer (Fig. 2). As the ODT depth is reduced (step 1 in the figure), atoms are pulled out of the trap and are accelerated into the potential well of the HCT. The ODT is turned off completely while the atoms are held within the HCT (step 2). After some hold time the ODT is ramped up and atoms transfer back to the ODT (step 3).

Absorption images are obtained during the loading and retrieving process to measure the atom number in the ODT (Fig. 3). From the final ODT number we determine the overall efficiency of the process.

III. RESULTS

Based on the analysis of absorption images we measure 5×10^4 atoms in the ODT after retrieval, corresponding to about 5% of the 10^6 atoms initially delivered at the start of

the experiment. The successful transfer of atoms into the HCT and their retrieval is the main result of this paper.

Images recorded while the ODT power is ramped down reveal that the number of atoms is gradually reduced until the ODT power reaches zero [see Figs. 3(b) and 3(c)]. Once the ODT power drops to zero, any remaining atoms either fall into the HCT potential well, or are lost from either trap.

The atoms are then held in the trap for up to 30 ms, several hundred radial trapping periods. After this time, the ODT intensity is ramped back up, and the atom number outside the fiber increases over 80 ms [Fig. 3(d)] until a maximum is reached. In varying the hold time, the retrieved number changed by at most 30%, indicating a lifetime longer than 50 ms. Longer hold times were not explored in the current setup. To rule out alternate trapping mechanisms, we performed some experimental runs under identical parameters except with no light in the HCT, and found that no atoms are recovered, indicating that the atoms indeed are loaded into and retrieved from the HCT.

The initial and final cloud sizes were similar, implying similar temperatures before and after the transfer. This temperature may be estimated at a few microkelvins by assuming evaporation continually occurs in the finite-depth optical trap, leading to temperatures at a fraction of the trap depth.

IV. DISCUSSION

Our experimental scheme for transferring atoms between the two traps was guided by the concept of adiabatic transfer in a double-well potential, where the atoms always occupy the deeper well. Our results are consistent with this picture. We do not know whether the transfer of atoms involves tunneling, spilling over the barrier, or sloshing. This reflects that the potential between the two traps is likely to be affected by spurious modes traveling along the fiber surface or in the cladding and interfering with the light in the core. In fact, we frequently observed light coupled into the cladding leading to distortions in the mode after the fiber. Without proper alignment, the cladding modes prevented atoms from being loaded into the fiber or trapped atoms in local maxima outside the fiber. The successful transfer was possible only with great care in coupling to minimize light in the cladding modes. In the future, a coupling lens inside the vacuum

could replace the final lens (which was 10 cm away from the fiber), resulting in more controlled and stable coupling of light. We do not try to describe the exact dynamics of the transfer without better knowledge of the potential between the two wells.

Observation of the atoms inside the fiber would reveal the dynamics of the loading and trapping process. Although the fiber is transparent to resonant light, absorption imaging from the side was not possible due to severe scattering and refraction. However, resonant light could be propagated along the core mode to provide information on the integrated density of atoms inside the fiber.

We were unable to observe atoms being guided completely through the fiber, probably because of low atom density and the lack of an appropriate trap in which to collect them after the fiber. It may turn out to be difficult to control the light intensity along the fiber core sufficiently to avoid undesirable accelerations of the atoms, to localize them inside the fiber, or to propagate them through the fiber in a controlled way. In this case, it may be advantageous to use the fiber mode for strong transverse confinement but add magnetic confinement for the axial direction. This could be accomplished with a quadrupole trap, where, by changing the balance of currents in anti-Helmholtz coils, the axial minimum could be swept across the fiber to controllably propagate the atomic cloud. With this setup, one could obtain detailed information on atom lifetime at different positions within the fiber. Originally, we had the intention to take more quantitative data with such an improved setup, but the priorities of the laboratory changed. Therefore, we have presented our qualitative results in this paper.

In conclusion, we have shown that optical dipole traps are well suited to load ultracold atoms into a hollow-core photonic crystal fiber. The reported retrieval efficiency of 5% is a lower bound for the transfer efficiency, and can probably be substantially increased with an improved setup.

ACKNOWLEDGMENTS

This work was funded by DARPA, NSF, and ONR. G.-B.J. and S.W. acknowledge additional support from Samsung Foundation and the Studienstiftung des Deutschen Volkes, respectively.

-
- [1] I. Teper, Y.-J. Lin, and V. Vuletic, *Phys. Rev. Lett.* **97**, 023002 (2006).
 [2] G.-B. Jo, J.-H. Choi, C. A. Christensen, T. A. Pasquini, Y.-R. Lee, W. Ketterle, and D. E. Pritchard, *Phys. Rev. Lett.* **98**, 180401 (2007).
 [3] S. Wu, E. Su, and M. Prentiss, *Phys. Rev. Lett.* **99**, 173201 (2007).
 [4] E. Andersson, T. Calarco, R. Folman, M. Andersson, B. Hessmo, and J. Schmiedmayer, *Phys. Rev. Lett.* **88**, 100401 (2002).
 [5] Y.-J. Wang, D. Z. Anderson, V. M. Bright, E. A. Cornell, Q. Diot, T. Kishimoto, M. Prentiss, R. A. Saravanan, S. R. Segal, and S. Wu, *Phys. Rev. Lett.* **94**, 090405 (2005).
 [6] P. Treutlein, T. W. Hänsch, J. Reichel, A. Negretti, M. A. Cirone, and T. Calarco, *Phys. Rev. A* **74**, 022312 (2006).
 [7] M. J. Renn, D. Montgomery, O. Vdovin, D. Z. Anderson, C. E. Wieman, and E. A. Cornell, *Phys. Rev. Lett.* **75**, 3253 (1995).
 [8] H. Ito, T. Nakata, K. Sakaki, M. Ohtsu, K. I. Lee, and W. Jhe, *Phys. Rev. Lett.* **76**, 4500 (1996).
 [9] R. G. Dall, M. D. Hoogerland, K. G. H. Baldwin, and S. J. Buckman, *J. Opt. B: Quantum Semiclassical Opt.* **1**, 396 (1999).
 [10] D. Müller, E. A. Cornell, D. Z. Anderson, and E. R. I. Abraham, *Phys. Rev. A* **61**, 033411 (2000).

- [11] R. F. Cregan, B. J. Mangan, J. C. Knight, T. A. Birks, P. S. J. Russell, P. J. Roberts, and D. C. Allan, *Science* **285**, 1537 (1999).
- [12] P. Roberts *et al.*, *Opt. Express* **13**, 236 (2005).
- [13] S. Will, diploma thesis, Universitat Mainz, 2006.
- [14] T. Takekoshi and R. J. Knize, *Phys. Rev. Lett.* **98**, 210404 (2007).
- [15] M. Bajcsy, S. Hofferberth, V. Balic, T. Peyronel, M. Hafezi, A. S. Zibrov, V. Vuletic, and M. Lukin (unpublished).
- [16] T. L. Gustavson, A. P. Chikkatur, A. E. Leanhardt, A. Gorlitz, S. Gupta, D. E. Pritchard, and W. Ketterle, *Phys. Rev. Lett.* **88**, 020401 (2001).

Appendix H

Interference of Bose-Einstein condensates split with an atom chip

This appendix contains a reprint of Ref. [179]: Y. Shin, C. Sanner, G.-B. Jo, T. A. Pasquini, M. Saba, W. Ketterle, and D. E. Pritchard, *Interference of Bose-Einstein condensates split with an atom chip*, Phys. Rev. A **72**, 021604(R) (2005).

Interference of Bose-Einstein condensates split with an atom chip

Y. Shin, C. Sanner, G.-B. Jo, T. A. Pasquini, M. Saba, W. Ketterle, and D. E. Pritchard*
 MIT-Harvard Center for Ultracold Atoms, Research Laboratory of Electronics, Department of Physics,
 Massachusetts Institute of Technology, Cambridge, Massachusetts 02139, USA

M. Vengalattore and M. Prentiss
 MIT-Harvard Center for Ultracold Atoms, Jefferson Laboratory, Physics Department, Harvard University,
 Cambridge, Massachusetts 02138, USA

(Received 10 June 2005; published 11 August 2005)

We have used a microfabricated atom chip to split a single Bose-Einstein condensate of sodium atoms into two spatially separated condensates. Dynamical splitting was achieved by deforming the trap along the tightly confining direction into a purely magnetic double-well potential. We observed the matter wave interference pattern formed upon releasing the condensates from the microtraps. The intrinsic features of the quartic potential at the merge point, such as zero trap frequency and extremely high field-sensitivity, caused random variations of the relative phase between the two split condensates. Moreover, the perturbation from the abrupt change of the trapping potential during the splitting was observed to induce vortices.

DOI: [10.1103/PhysRevA.72.021604](https://doi.org/10.1103/PhysRevA.72.021604)

PACS number(s): 03.75.Dg, 03.75.Kk, 39.20.+q

Coherent manipulation of matter waves is the ultimate goal of atom optics, and diverse atom optical elements have been developed such as mirrors, beamsplitters, gratings, and waveguides. An atom chip integrates these elements on a microfabricated device allowing precise and stable alignment [1–3]. Recently, this atom chip technology has been combined with Bose-Einstein condensed atoms [4,5], and opened the prospect for chip-based atom interferometers with Bose-Einstein condensates. Despite various technical problems [6–10], there have been advances toward that goal, such as excitationless propagation in a waveguide [6] and demonstration of a Michelson interferometer involving splitting along the axis of a single waveguide [11].

Coherent splitting of matter waves into spatially separate atomic wave packets with a well-defined relative phase is a prerequisite for further applications such as atom interferometry and quantum information processing, and it has been a major experimental challenge. The methods envisioned for coherent splitting on atom chips can be divided in two classes. One is splitting in momentum space and subsequently generating a spatial separation, using scattering of atoms from a periodic optical potential [11,12]. The other is dynamical splitting by directly deforming a single wave packet into two spatially separated wave packets, which can be considered as cutting off the link between two wave packets, i.e., stopping tunneling through the barrier separating two wave packets. Splitting in momentum space has led to remarkably clean interferometric measurements when the atoms were allowed to propagate freely after splitting, but it has been pointed out that momentum splitting of confined atoms (e.g., inside a waveguide) is problematic due to spatially dependent phase shifts induced by atom-atom interactions during separation [11,13]. Dynamical splitting in real space instead is perfectly compatible with

keeping atoms confined, a feature beneficial to the versatility of interferometers. There has been a theoretical debate concerning the adiabatic condition for coherent dynamical splitting [14–17]. In our recent experiment with an optical double-well potential, we demonstrated that it is possible to dynamically split a condensate into two parts in a coherent way [18].

In this work, we studied the dynamical splitting of condensates in a purely magnetic double-well potential on an atom chip. We developed an atom chip to generate a symmetric double-well potential and succeeded in observing the matter wave interference of two split condensates, from which the coherence of the splitting process was investigated. We found that the mechanical perturbations during splitting are violent enough to generate vortices in condensates. We discuss the adiabatic condition of the splitting process.

A magnetic double-well potential was realized with an atom chip using a two-wire scheme [19]. The experimental setup of the atom chip is shown in Fig. 1. When two chip wires have currents, I_C , in the $-y$ direction and the external magnetic field, B_x , is applied in the $+x$ direction, two lines of local minima in the magnetic field are generated above the chip surface. Each local minimum has a quadruple field configuration in the xz plane, and with an additional nonzero magnetic field in the axial direction (y -direction), two Ioffe-Pritchard magnetic traps can be formed. The relative magnitude of B_x to the field from I_C determines the direction of separation and the distance of the two traps. The atom chip was set to face downward and the two traps are vertically (horizontally) separated when $B_x < B_{x0}$ ($B_x > B_{x0}$). $B_{x0} = \mu_0 I_C / \pi d$ is the critical field magnitude for merging two magnetic harmonic potentials to form a single quartic potential, where d is the distance between the two chip wires and μ_0 is the permeability of the vacuum. The merge point is located at the middle of the two wires and $d/2$ away from the chip surface. In our experiment, $d = 300 \mu\text{m}$; thus, the splitting happened

*URL: http://cua.mit.edu/ketterle_group/

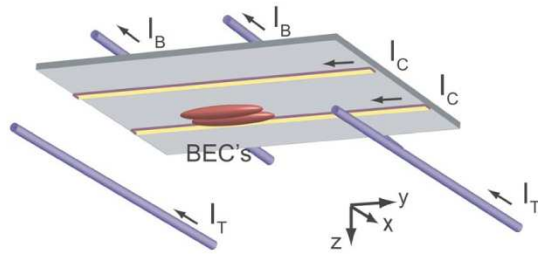


FIG. 1. (Color online) Schematic diagram of the atom chip. A magnetic double-well potential was created by two chip wires with a current I_C in conjunction with an external magnetic field. The distance between the two chip wires was $300\ \mu\text{m}$. A pair of external wires with I_B provided the axial confinement along the y direction, and another pair of external wires with I_T were used for reducing the antisymmetry effect. (For details, see text.) Gravity was in the $+z$ direction.

more than $200\ \mu\text{m}$ away from the chip wires to avoid deleterious surface effects [6–10]. The chip wires of $12\ \mu\text{m}$ height and $50\ \mu\text{m}$ width were electroplated with Au on a thermally oxidized Si substrate with a $2\text{-}\mu\text{m}$ -thick Au evaporated film. The chip was glued on an Al block for heat dissipation [20] and the current capacity was 5 A in a continuous mode.

The axial trapping potential was carefully designed to ensure that condensates split perpendicular to the axial direction and stay in the same axial position. The two wells have opposite responses to B_z : positive B_z makes the left (right) well move upward (downward). If B_z changes along the axial direction, the two wells are no longer parallel and the gravitational force would cause an axial displacement of the two split condensates. When endcap wires are placed only on the chip surface as in our previous work [21], a nonzero field gradient $\partial B_z/\partial y$ inevitably accompanies a field curvature $\partial^2 B_y/\partial y^2$ for the axial confinement, i.e., B_z changes from positive to negative along the axial direction. In order to provide the axial confinement and at the same time minimize $\partial B_z/\partial y$, we placed two pairs of external wires 1.5 mm above and 4 mm below the chip surface. This three-dimensional design of axial confinement was necessary for obtaining the interference signal of two split condensates. Moreover, maintaining the geometric symmetry of two wells will be crucial for longer coherence time after splitting [18].

The splitting process was demonstrated with the experimental procedures described in Fig. 2. Bose-Einstein condensates of $|F=1, m_F=-1\rangle$ ^{23}Na atoms were transferred and loaded in a magnetic trap generated by the atom chip [6,21,22]. Experimental parameters were $I_C=1.8\ \text{A}$, $B_{x0}=24\ \text{G}$, $B_y=1\ \text{G}$, and the axial trap frequency $f_y=13\ \text{Hz}$. Condensates were first loaded in the bottom well, $500\ \mu\text{m}$ away from the chip surface, brought up to $30\ \mu\text{m}$ below the merge point in 1 s, and held there for 2 s to damp out excitations. The long-living axial dipole excitation induced in the transfer phase was damped by applying a repulsive potential wall at the one end of the condensates with a blue-detuned

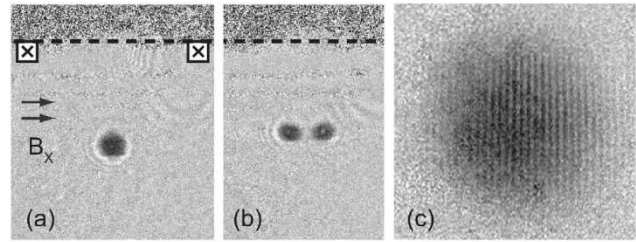


FIG. 2. Splitting of condensates. (a) Condensates were initially loaded and prepared in the bottom well and (b) split into two parts by increasing the external magnetic field, B_x . For clarity, two condensates were split by $80\ \mu\text{m}$. The dash line indicates the chip surface position. The currents in the chip wires flow into the page and B_x is parallel to the wire separation. Two condensates were released from the magnetic double-well potential and the matter wave interference pattern of two condensates formed after time-of-flight. (c) Typical absorption image of interference fringes taken after 22 ms time-of-flight. The fringe spacing was $14.8\ \mu\text{m}$, corresponding to a condensate separation of $25.8\ \mu\text{m}$.

laser beam ($532\ \text{nm}$)¹. The whole procedure was carried out with a radio-frequency (rf) shield and, just before splitting, condensates contained over 8.0×10^5 atoms without a discernible thermal population. Splitting was done by ramping $\Delta B_x = B_x - B_{x0}$ linearly from $-140\ \text{mG}$ to $100 \pm 20\ \text{mG}$ in 200 ms. The separation between two condensates was controlled by the final value of B_x . The magnetic trap was then quickly turned off within $20\ \mu\text{s}$, a duration much shorter than the inverse of any trap frequency, preventing random perturbations. High-contrast matter wave interference fringes were observed after releasing the condensates and letting them expand in time-of-flight (Fig. 2), indicating that the splitting procedure was smooth enough to produce two condensates having uniform phases along their long axial axis perpendicular to the splitting direction. In order to study the coherence of the splitting, the relative phase of the two split condensates was determined from the spatial phase of the matter wave interference pattern.

The relative phase of two split condensates turned out to be unpredictable when they were fully separated (Fig. 3). The separation of two condensates was determined from the spacing, λ_s , of the interference fringes, using the formula $d = ht/m\lambda_s$ where h is Planck's constant, m is atomic mass, and t is time-of-flight. The typical fringe spacing was $\lambda \approx 15\ \mu\text{m}$ with $t=22\ \text{ms}$, corresponding to $d \approx 26\ \mu\text{m}$. Given the precise knowledge of the fabricated wires, the full trap parameters can be calculated. Assuming that the condensates followed trap centers in the motional ground state, it was found that when the barrier height was over 1.5 kHz, the

¹In a perfectly symmetric double-well potential, two condensates would oscillate in phase after splitting. Furthermore, this could be used for developing a rotation-sensitive atom interferometer with a guiding potential. However, the axial trap frequencies for the two wells were found to be different by 12% due to the imperfect fabrication of wires.

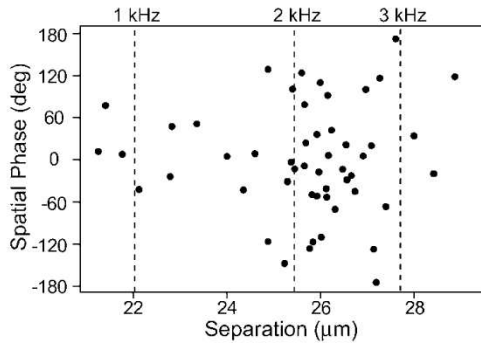


FIG. 3. Spatial phase of interference fringes. The separation of two condensates was determined from the spacing of interference fringes. Fifty repetitions of the same experiment are plotted, where the experimental control value for the external magnetic field, B_x , was fixed when the atoms were released. Three dash lines indicate the separations of two wells with the barrier height of 1 kHz, 2 kHz, and 3 kHz, respectively.

relative phase started to be random.² Since the chemical potential of the condensates, $\mu = 1.4 \pm 0.2$ kHz, was very close to this barrier height, the condensates just started to lose their coupling at this point.

Surprisingly, a phase singularity was observed in the interference patterns with high visibility. The fork shape of interference fringes represents a phase winding around a vortex core [23]. This vortex interference pattern appeared more frequently with faster splitting and further separation. An external perturbation can lead to internal excitations in condensates. Splitting might be considered as slicing condensates in two parts. The fact that the observed “forks” (Fig. 4) always open towards the top implies that the slicing always occurred in the same direction and created either vortices with positive charge on the left side or with negative charge on the right side. A possible vortex formation mechanism is topological imprinting when the zero point of the magnetic field crosses through condensates resulting in a doubly quantized vortex in spin-1 condensates [21,22]. However, since we have never observed the interference pattern of a doubly quantized vortex, we think that this scenario is unlikely.

We now discuss how the trapping potential changes during the splitting process (Fig. 5). When condensates split into two wells, the trap frequency, f_x , in the splitting direction vanishes and the separation of two wells abruptly increases to $15 \mu\text{m}$ with a small magnetic field change of $\delta B_x \approx 10$ mG. For a single particle in a harmonic potential, the quantity $\alpha \equiv (1/f_x^2)(\partial f_x / \partial B_x)(dB_x/dt)$ accounts for the transition probability from the ground state to the first excited state and parametrizes the external adiabaticity of the process, neglecting the collective excitations of a condensate. $\alpha \ll 1$ should be maintained to keep condensates staying in the motional ground state. With $dB_x/dt = 1.2$ G/s, $\alpha < 1$ at $f_x > 150$ Hz, but obviously, α diverges to infinity near the merge point and its definition no longer holds. Since the

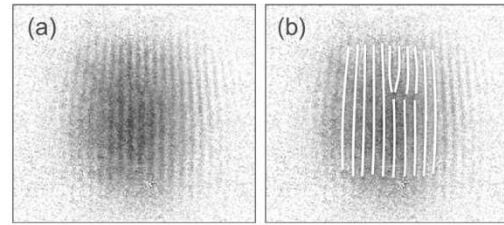


FIG. 4. Vortex interference. (a) An absorption image showing the vortex interference pattern of a vortex state. The probability of vortex generation was $\sim 8\%$ for the experimental parameters of Fig. 3, where data points with vortices were not included. Vortex interference patterns appeared more frequently with faster splitting and further separation. (b) Same as (a), but with lines indicating regions with constant phase.

energy level spacing diminishes, the adiabatic condition in the quartic potential around the merge point becomes more stringent. The abrupt change of trapping potential will induce mechanical perturbations of condensates. Subsequent dissipation or coupling into internal excitation modes [24] would make the relative phase of two split condensates unpredictable. The observed phase singularity definitely shows the breakdown of adiabaticity.

One possible alternative to avoid passing through the merge point is starting with two weakly linked condensates in a double-well potential where the barrier height is lower than the chemical potential of condensates and controlling the coupling between two condensates with a small change of the barrier height. This method was used to reduce the motional perturbation in our previous work [18]. However,

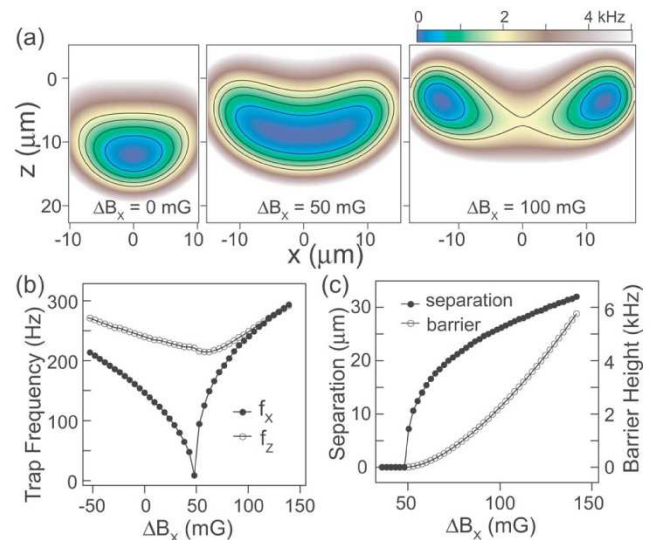


FIG. 5. (Color online) Trapping potential during splitting. (a) Radial cross sections of trapping potential including gravity for $\Delta B_x = 0, 50,$ and 100 mG, where ΔB_x is the field deviation from the critical field magnitude B_{x0} which is the field magnitude for forming a single quartic trap. The origin of coordinates is the merge point without gravity. Contour lines correspond to 0.5, 1, 1.5, and 2 kHz above the bottom of the trap. (b) Trap frequencies in each direction. (c) Separation of two trap centers and barrier height between two wells.

²When the separation was less than $20 \mu\text{m}$ and two condensates were linked, the uncertainty of the spatial phase of fringes was less than 60° .

since the sensitivity of the trapping potential to the magnetic field is extremely high when the trap centers are close to the merge point, it was technically difficult to have a stable double-well potential with a small barrier height. The lifetime of condensates measured around the merge point was >5 s away from the merge point ($\Delta B_x < -50$ mG or $\Delta B_x > 150$ mG) and <100 ms near the merge point ($0 < \Delta B_x < 100$ mG).³ With a barrier height of 0.5 kHz in our experiment, the sensitivity of the barrier height and the condensate separation to B_x is 0.04 kHz/mG and $0.3 \mu\text{m/mG}$, respectively. $\delta B_x = 1$ mG corresponds to $\delta I_C = 7.5 \times 10^{-5}$ A. Extreme current stabilization and shielding of ambient magnetic field fluctuations may be necessary for controlling a phase-coherent splitting process. Another alternative for preparing a coherent state of two spatially separated condensates is first preparing two condensates in the ground states in

³For positions with $\Delta B_x > 0$ (“after” splitting), the condensates were moved to the left well without passing through the merge point.

each well and then establishing a well-defined relative phase with an optical method [25]. This scheme is currently under investigation.

In conclusion, we have demonstrated the interference of two Bose-Einstein condensates released from an atom chip. The condensates were created by dynamical splitting of a single condensate and could be kept confined in a magnetic double-well potential, separated by an arbitrary distance. We studied the coherence of the dynamical splitting process by measuring the relative phase of two split condensates and identified technical limitations, intrinsic to the magnetic field geometry, that prevented coherent splitting with a predictable phase. This study is a promising step in the route towards atom chip interferometers and might serve as a guide for the design of future microfabricated atom optics devices.

This work was funded by ARO, NSF, ONR, DARPA, and NASA. C.S. acknowledges additional support from the Studienstiftung des deutschen Volkes, G.-B.J. from the Samsung Lee Kun Hee Scholarship Foundation, and M.S. from the Swiss National Science Foundation.

-
- [1] D. Müller, D. Z. Anderson, R. J. Grow, P. D. D. Schwindt, and E. A. Cornell, *Phys. Rev. Lett.* **83**, 5194 (1999).
- [2] N. H. Dekker, C. S. Lee, V. Lorent, J. H. Thywissen, S. P. Smith, M. Drndić, R. M. Westervelt, and M. Prentiss, *Phys. Rev. Lett.* **84**, 1124 (2000).
- [3] R. Folman, P. Krüger, D. Cassettari, B. Hessmo, T. Maier, and J. Schmiedmayer, *Phys. Rev. Lett.* **84**, 4749 (2000).
- [4] H. Ott, J. Fortágh, G. Schlotterbeck, A. Grossmann, and C. Zimmermann, *Phys. Rev. Lett.* **87**, 230401 (2001).
- [5] W. Hänsel, P. Hommelhoff, T. W. Hänsch, and J. Reichel, *Nature (London)* **413**, 498 (2001).
- [6] A. E. Leanhardt, A. P. Chikkatur, D. Kielpinski, Y. Shin, T. L. Gustavson, W. Ketterle, and D. E. Pritchard, *Phys. Rev. Lett.* **89**, 040401 (2002).
- [7] J. Fortágh, H. Ott, S. Kraft, A. Günther, and C. Zimmermann, *Phys. Rev. A* **66**, 041604(R) (2002).
- [8] A. E. Leanhardt, Y. Shin, A. P. Chikkatur, D. Kielpinski, W. Ketterle, and D. E. Pritchard, *Phys. Rev. Lett.* **90**, 100404 (2003).
- [9] M. P. A. Jones, C. J. Vale, D. Sahagun, B. V. Hall, and E. A. Hinds, *Phys. Rev. Lett.* **91**, 080401 (2003).
- [10] J. Estève, C. Aussibal, T. Schumm, C. Figl, D. Maily, I. Bouchoule, C. I. Westbrook, and A. Aspect, *Phys. Rev. A* **70**, 043629 (2004).
- [11] Y.-J. Wang, D. Z. Anderson, V. M. Bright, E. A. Cornell, Q. Diot, T. Kishimoto, M. Prentiss, R. A. Saravanan, S. R. Segal, and S. Wu, *Phys. Rev. Lett.* **94**, 090405 (2005).
- [12] P. J. Martin, B. G. Oldaker, A. H. Miklich, and D. E. Pritchard, *Phys. Rev. Lett.* **60**, 515 (1988).
- [13] M. Olshanii and V. Dunjko, e-print cond-mat/0505358.
- [14] J. Javanainen and M. Wilkens, *Phys. Rev. Lett.* **78**, 4675 (1997).
- [15] A. J. Leggett and F. Sols, *Phys. Rev. Lett.* **81**, 1344 (1998).
- [16] C. Menotti, J. R. Anglin, J. I. Cirac, and P. Zoller, *Phys. Rev. A* **63**, 023601 (2001).
- [17] L. Pezzé, A. Smerzi, G. P. Berman, A. R. Bishop, and L. A. Collins, e-print cond-mat/0411567.
- [18] Y. Shin, M. Saba, T. A. Pasquini, W. Ketterle, D. E. Pritchard, and A. E. Leanhardt, *Phys. Rev. Lett.* **92**, 050405 (2004).
- [19] E. A. Hinds, C. J. Vale, and M. G. Boshier, *Phys. Rev. Lett.* **86**, 1462 (2001).
- [20] S. Groth, P. Krüger, S. Wildermuth, R. Folman, T. Fernholz, J. Schmiedmayer, M. Mahalu, and I. Bar-Joseph, *Appl. Phys. Lett.* **85**, 2980 (2004).
- [21] Y. Shin, M. Saba, M. Vengalattore, T. A. Pasquini, C. Sanner, A. E. Leanhardt, M. Prentiss, D. E. Pritchard, and W. Ketterle, *Phys. Rev. Lett.* **93**, 160406 (2004).
- [22] A. E. Leanhardt, A. Görlitz, A. P. Chikkatur, D. Kielpinski, Y. Shin, D. E. Pritchard, and W. Ketterle, *Phys. Rev. Lett.* **89**, 190403 (2002).
- [23] S. Inouye, S. Gupta, T. Rosenband, A. P. Chikkatur, A. Görlitz, T. L. Gustavson, A. E. Leanhardt, D. E. Pritchard, and W. Ketterle, *Phys. Rev. Lett.* **87**, 080402 (2001).
- [24] H. Ott, J. Fortágh, S. Kraft, A. Günther, D. Komma, and C. Zimmermann, *Phys. Rev. Lett.* **91**, 040402 (2003).
- [25] M. Saba, T. A. Pasquini, C. Sanner, Y. Shin, W. Ketterle, and D. E. Pritchard, *Science* **307**, 1945 (2005).

Bibliography

- [1] A.A. Abrikosov and I.M. Khalatnikov. *Sov. Phys. JETP*, 6:888, 1958.
- [2] Michael Albiez, Rudolf Gati, Jonas Fölling, Stefan Hunsmann, Matteo Cristiani, and Markus K. Oberthaler. Direct observation of tunneling and nonlinear self-trapping in a single bosonic josephson junction. *Physical Review Letters*, 95(1):010402, 2005.
- [3] J. F. Allen and A. D. Misener. Flow of liquid helium II. *Nature*, 141:75, 1938.
- [4] M. Amoruso, I. Meccoli, A. Minguzzi, and M.P. Tosi. Density profiles and collective excitations of a trapped two-component fermi vapour. *Eur. Phys. J. D*, 8:361, 2000.
- [5] B.P. Anderson and M.A. Kasevich. Macroscopic quantum interference from atomic tunnel arrays. *Science*, 282(2):1686, October 1998.
- [6] M. H. Anderson, J. R. Ensher, M. R. Matthews, C. E. Wieman, and E. A. Cornell. Observation of Bose-Einstein condensation in a dilute atomic vapor. *Science*, 269:198–201, 1995.
- [7] P. W. Anderson and W. F. Brinkman. Anisotropic superfluidity in ^3he : A possible interpretation of its stability as a spin-fluctuation effect. *Phys. Rev. Lett.*, 30(22):1108–1111, May 1973.
- [8] P. W. Anderson and W. F. Brinkman. *The Physics of Liquid and Solid Helium, Part II*. Wiley, New York, 1978.
- [9] P.W. Anderson. *Basic Notion of Condensed matter physics*. Westview Press, Oxford, 1997.
- [10] Erika Andersson, Tommaso Calarco, Ron Folman, Mauritz Andersson, Björn Hessmo, and Jörg Schmiedmayer. Multimode interferometer for guided matter waves. *Phys. Rev. Lett.*, 88(10):100401, Feb 2002.

- [11] M.R. Andrews, C.G. Townsend, H.-J. Miesner, D.s. Durfee, D.M. Kurn, and W. Ketterle. Observation of interference between two Bose condensates. *Science*, 275:637, January 1997.
- [12] E. Arimondo, W. D. Phillips, and F. Strumia (editors). *Laser Manipulation of Atoms and Ions, Proceedings of the International School of Physics Enrico Fermi, Course CXVIII*. North-Holland, Amsterdam, 1992.
- [13] S.H. Autler and C.H. Townes. Stark effect in rapidly varying fields. *Phys. Rev.*, 100(2):703, October 1955.
- [14] Mehrtash Babadi, David Pekker, Rajdeep Sensarma, Antoine Georges, and Eugene Demler. Non-equilibrium dynamics of interacting fermi systems in quench experiments. *preprint available in arXiv.org*, 2009.
- [15] M. Bajcsy, S. Hofferberth, V. Balic, T. Peyronel, M. Hafezi, A. S. Zibrov, V. Vuletic, and M. D. Lukin. Efficient all-optical switching using slow light within a hollow fiber. *Phys. Rev. Lett.*, 102(20):203902, May 2009.
- [16] W. S. Bakr, J. I. Gillen, A. Peng, S. Fölling, and M. Greiner. Quantum gas microscope detecting single atoms in a hubbard regime optical lattice. *Nature*, 462:74, 2009.
- [17] J. Bardeen, L. N. Cooper, and J. R. Schrieffer. Theory of superconductivity. *Phys. Rev.*, 108(5):1175–1204, Dec 1957.
- [18] M. Bartenstein, A. Altmeyer, S. Riedl, S. Jochim, C. Chin, J. Hecker Denschlag, and R. Grimm. Crossover from a molecular Bose-Einstein condensate to a degenerate Fermi gas. *Phys. Rev. Lett.*, 92:120401, 2004.
- [19] Ilya Berdnikov, P. Coleman, and Steven H. Simon. Itinerant ferromagnetism in an atom trap. *Phys. Rev. B*, 79(22):224403, 2009.
- [20] P. Berman. *Atom Interferometry*. Academic Press, New York, 1997.
- [21] P. Böhi, M.F. Riedel, J. Hoffrogge, J. Reichel, and P. Hänsch, T.W. and Treutlein. Coherent manipulation of Bose-Einstein condensates with state-dependent microwave potentials on an atom chip. *Nat. Phys.*, 5:592, 2009.
- [22] Juliette Billy and et. al. Direct observation of anderson localization of matter waves in a controlled disorder. *Nature*, 453:891, 2008.

- [23] R. Bistritzer and E. Altman. Intrinsic dephasing in one-dimensional ultracold atom interferometers. *PNAS*, 104(24):9955–9959, 2007.
- [24] F. Bloch. Bemerkung zur elektronentheorie des ferromagnetismus und der elektrischen leitfhigkeit. *Z.Phys.*, 57:545, 1929.
- [25] Immanuel Bloch, Jean Dalibard, and Wilhelm Zwerger. Many-body physics with ultracold gases. *Reviews of Modern Physics*, 80(3):885, 2008.
- [26] N. N. Bogoliubov. On the theory of superfluidity. *J. Phys. (USSR)*, 11:23, 1947.
- [27] Niels Bohr. *PhD thesis*. PhD thesis, Copenhagen, 1911.
- [28] S. N. Bose. Plancks Gesetz und Lichtquantenhypothese. *Z. Phys.*, 26:178, 1924.
- [29] T. Bourdel, J. Cubizolles, L. Khaykovich, K. M. F. Magalhes, S. J. J. M. F. Kokkelmans, G. V. Shlyapnikov, and C. Salomon. Measurement of the interaction energy near a Feshbach resonance in a ^6Li Fermi gas. *Phys. Rev. Lett.*, 91:020402, 2003.
- [30] T. Bourdel, L. Khaykovich, J. Cubizolles, J. Zhang, F. Chevy, M. Teichmann, L. Tarruell, S. J. J. M. F. Kokkelmans, and C. Salomon. Experimental study of the BEC-BCS crossover region in lithium 6. *Phys. Rev. Lett.*, 93:050401, 2004.
- [31] I. Brodie and J.J. Muray. *The physics of Micro/Nano-Fabrication*. Plenum Press, New York, 1992.
- [32] P. W. Brouwer, Yuval Oreg, and B. I. Halperin. Mesoscopic fluctuations of the ground-state spin of a small metal particle. *Phys. Rev. B*, 60(20):R13977–R13980, Nov 1999.
- [33] A. A. Burkov, M. D. Lukin, and Eugene Demler. Decoherence dynamics in low-dimensional cold atom interferometers. *Physical Review Letters*, 98(20):200404, 2007.
- [34] J. Carlson and Sanjay Reddy. Asymmetric two-component fermion systems in strong coupling. *Phys. Rev. Lett.*, 95(6):060401, Aug 2005.
- [35] Y. Castin and J. Dalibard. Relative phase of two Bose-Einstein condensates. *Phys. Rev. A*, 55(6):4330, June 1997.

- [36] F. S. Cataliotti, S. Burger, C. Fort, P. Maddaloni, F. Minardi, A. Trombettoni, A. Smerzi, and M. Inguscio. Josephson Junction Arrays with Bose-Einstein Condensates. *Science*, 293(5531):843–846, 2001.
- [37] Ananth P. Chikkatur. *Colliding and Moving Bose-Einstein Condensates: Studies of superfluidity and optical tweezers for condensate transport*. PhD thesis, Massachusetts Institute of Technology, 2002.
- [38] Cheng Chin, Rudolf Grimm, Paul Julienne, and Eite Tiesinga. Feshbach resonances in ultracold gases. *Preprint available in arXiv.org*, 2008.
- [39] Caleb A. Christensen, Sebastian Will, Michele Saba, Gyu-Boong Jo, Yong-Il Shin, Wolfgang Ketterle, and David Pritchard. Trapping of ultracold atoms in a hollow-core photonic crystal fiber. *Phys. Rev. A*, 78(3):033429, Sep 2008.
- [40] C.-S. Chuu, F. Schreck, T.P. Meyrath, J.L. Hanssen, G.N. Price, and M.G. Raizen. Direct observation of sub-poissonian number statistics in a degenerate Bose gas. *Phys. Rev. Lett.*, 95(4):260403, December 2005.
- [41] Y. Colombe, E. Knyazchyan, O. Morizot, B. Mercier, V. Lorent, and H. Perrin. Ultracold atoms confined in rf-induced two-dimensional trapping potentials. *Europhys. Lett.*, 67(4):593, August 2004.
- [42] G. J. Conduit and Ehud Altman. Effect of three-body loss on itinerant ferromagnetism in an atomic fermi gas, 2009.
- [43] G. J. Conduit, A. G. Green, and B. D. Simons. Inhomogeneous phase formation on the border of itinerant ferromagnetism. *Phys. Rev. Lett.*, 103(20):207201, Nov 2009.
- [44] G. J. Conduit and B. D. Simons. Repulsive atomic gas in a harmonic trap on the border of itinerant ferromagnetism. *Phys. Rev. Lett.*, 103(20):200403, Nov 2009.
- [45] Alexander D. Cronin, Jörg Schmiedmayer, and David E. Pritchard. Optics and interferometry with atoms and molecules. *Rev. Mod. Phys.*, 81(3):1051–1129, Jul 2009.
- [46] Franco Dalfovo, Stefano Giorgini, Lev P. Pitaevskii, and Sandro Stringari. Theory of Bose-Einstein condensation in trapped gases. *Rev. Mod. Phys.*, 71(3):463–512, Apr 1999.

- [47] K. B. Davis, M.-O. Mewes, M. R. Andrews, N. J. van Druten, D. S. Durfee, D. M. Kurn, and W. Ketterle. Bose-Einstein condensation in a gas of sodium atoms. *Phys. Rev. Lett.*, 75:3969–3973, 1995.
- [48] J. P. D’Incao and B. D. Esry. Scattering length scaling laws for ultracold three-body collisions. *Phys. Rev. Lett.*, 94(21):213201, Jun 2005.
- [49] D.C.Mattis. *The theory of magnetism*. Springer-Verlag, Berlin, 1981.
- [50] C. DeDominicis and P. C. Martin. Energy of interacting fermi systems. *Phys. Rev.*, 105(4):1417–1419, Feb 1957.
- [51] S. Dettmer, D. Hellweg, P. Ryytty, J. J. Arlt, W. Ertmer, K. Sengstock, D. S. Petrov, G. V. Shlyapnikov, H. Kreutzmann, L. Santos, and M. Lewenstein. Observation of phase fluctuations in elongated Bose-Einstein condensates. *Phys. Rev. Lett.*, 87(16):160406, Oct 2001.
- [52] R. A. Duine and A. H. MacDonald. Itinerant ferromagnetism in an ultracold atom fermi gas. *Phys. Rev. Lett.*, 95(23):230403, Nov 2005.
- [53] A. Einstein. Quantentheorie des einatomigen idealen Gases. *Sitzungsberichte der preussischen Akademie der Wissenschaften*, Bericht 22:261–267, 1924.
- [54] A. Einstein. Zur Quantentheorie des idealen Gases. *Sitzungsberichte der preussischen Akademie der Wissenschaften*, Bericht 3:18–25, 1925.
- [55] J. Esteve, C. Gross, A. Weller, S. Giovanazzi, and M. K. Oberthaler. Squeezing and entanglement in a Bose-Einstein condensate. *Nature*, 455:1216, 2008.
- [56] A. L. Fetter and J. D. Walecka. *Quantum Theory of Many-Particle Systems*. McGraw-Hill, New York, 1971. reprint appeared as Dover Edition in Dover Publications, Inc., Mineola, N.Y. (2003).
- [57] Richard P. Feynman. Simulating physics with computers. *International Journal of Theoretical Physics*, 21:467, 1982.
- [58] N.I. Fisher. *Statistical analysis of circular data*. Cambridge University Press, New York, 1993.
- [59] F. Folman, P. Krüger, J. Schmiedmayer, J. Denschlag, and C. Henkel. Microscopic atom optics:from wires to an atom chip. *Advances in atomic, molecular, and optical physics*, 48(2):263, August 2002.

- [60] Jozsef Fortagh and Claus Zimmermann. Magnetic microtraps for ultracold atoms. *Reviews of Modern Physics*, 79(1):235, 2007.
- [61] D. G. Fried, T. C. Killian, L. Willmann, D. Landhuis, S. C. Moss, D. Kleppner, and T. J. Greytak. Bose-Einstein condensation of atomic hydrogen. *Phys. Rev. Lett.*, 81:3811–3814, 1998.
- [62] O. Garcia, B. Deissler, K.J. Hughes, J.M. Reeves, and C.A. Sackett. A condensate interferometer with long coherence time and large arm separation. *cond-mat/0603772*, 58(2):1450, March 2006.
- [63] K. Gibble and S. Chu. Laser-cooled cs frequency standard and a measurement of the frequency shift due to ultracold collisions. *Phys. Rev. Lett.*, 70(4):1771, March 1993.
- [64] J. I. Gillen, W. S. Bakr, A. Peng, P. Unterwaditzer, S. Fölling, and M. Greiner. Two-dimensional quantum gas in a hybrid surface trap. *Phys. Rev. A*, 80(2):021602, Aug 2009.
- [65] Stefano Giorgini, Lev P.Pitaevskii, and Sandro Stringari. Theory of ultracold atomic fermi gases. *Reviews of Modern Physics*, 80(4):1215, 2008.
- [66] M. Greiner, O. Mandel, T. Esslinger, T.W. Hänsch, and I. Bloch. Quantum phase transition from a superfluid to a mott insulator in a gas of ultracold atoms. *Nature*, 415(2):39, January 2002.
- [67] M. Greiner, C. A. Regal, and D. S. Jin. Emergence of a molecular Bose-Einstein condensate from a Fermi gas. *Nature*, 426:537, 2003.
- [68] Dennis S. Greywall. Specific heat of normal liquid ${}^3\text{he}$. *Phys. Rev. B*, 27(5):2747–2766, Mar 1983.
- [69] E. P. Gross. Structure of a quantized vortex in boson systems. *Il Nuovo Cimento (1955-1965)*, 20:454, 1961.
- [70] E. P. Gross. Vortex lines in an imperfect Bose gas. *Sov.Phys.-JETP*, 13:451, 1961.
- [71] A. Günther, S. Kraft, M. Kemmler, D. Koelle, R. Kleiner, C. Zimmermann, and J. Fortágh. Diffraction of a Bose-Einstein condensate from a magnetic lattice on a microchip. *Phys. Rev. Lett.*, 95(17):170405, Oct 2005.

- [72] S. Gupta, Z. Hadzibabic, M. W. Zwierlein, C. A. Stan, K. Dieckmann, C. H. Schunck, E. G. M. van Kempen, B. J. Verhaar, and W. Ketterle. Radio-Frequency Spectroscopy of Ultracold Fermions. *Science*, 300(5626):1723–1726, 2003.
- [73] T.L. Gustavson, P. Bouyer, and M.A. Kasevich. Precision rotation measurements with an atom interferometer gyroscope. *Phys. Rev. Lett.*, 78(11):2046, March 1997.
- [74] T.L. Gustavson, A.P. Chikkatur, A.E. Leanhardt, A. Görlitz, S. Gupta, D.E. Pritchard, and W. Ketterle. Transport of Bose-Einstein condensates with optical tweezers. *Phys. Rev. Lett.*, 88(2):020401, January 2001.
- [75] Martin C. Gutzwiller. Effect of correlation on the ferromagnetism of transition metals. *Phys. Rev. Lett.*, 10(5):159–162, Mar 1963.
- [76] Martin C. Gutzwiller. Correlation of electrons in a narrow s band. *Phys. Rev.*, 137(6A):A1726–A1735, Mar 1965.
- [77] Z. Hadzibabic. *Studies of a Quantum Degenerate Fermionic Lithium Gas*. PhD thesis, Massachusetts Institute of Technology, 2003.
- [78] Z. Hadzibabic, S. Gupta, C. A. Stan, C. H. Schunck, M. W. Zwierlein, K. Dieckmann, and W. Ketterle. Fiftyfold improvement in the number of quantum degenerate fermionic atoms. *Phys. Rev. Lett.*, 91(16):160401, Oct 2003.
- [79] W. Hänsel, J. Reichel, P. Hommelhoff, and T. W. Hänsch. Trapped-atom interferometer in a magnetic microtrap. *Phys. Rev. A*, 64(6):063607, Nov 2001.
- [80] D. Hellweg, L. Cacciapuoti, M. Kottke, T. Schulte, K. Sengstock, W. Ertmer, and J. J. Arlt. Measurement of the spatial correlation function of phase fluctuating Bose-Einstein condensates. *Phys. Rev. Lett.*, 91(1):010406, Jul 2003.
- [81] E.A. Hinds, C.J. Vale, and M.G. Boshier. Two-wire waveguide and interferometer for cold atoms. *Phys. Rev. Lett.*, 86(8):1462, February 2001.
- [82] J. E. Hirsch. Two-dimensional hubbard model: Numerical simulation study. *Phys. Rev. B*, 31(7):4403–4419, Apr 1985.
- [83] S. Hofferberth, I. Lesanovsky, B. Fischer, T. Schumm, and J. Schmiedmayer. Non-equilibrium coherence dynamics in one-dimensional Bose gases. *Nature*, 449(324), 2007.

- [84] S. Hofferberth, I. Lesanovsky, B. Fischer, J. Verdu, and J. Schmiedmayer. Radiofrequency-dressed-state potentials for neutral atoms. *Nature Phys.*, 2:710, 2006.
- [85] S. Hofferberth, I. Lesanovsky, T. Schumm, A. Imambekov, V. Gritsev, E. Demler, and J. Schmiedmayer. Probing quantum and thermal noise in an interacting many-body system. *Nat.Phys*, 4:489, 2008.
- [86] M. Houbiers, R. Ferwerda, H. T. C. Stoof, W. I. McAlexander, C. A. Sackett, and R. G. Hulet. Superfluid state of atomic *6*Li in a magnetic trap. *Phys. Rev. A*, 56(6):4864–4878, Dec 1997.
- [87] K. Huang. *Statistical Mechanics*. Wiley, New York, 1987.
- [88] Kerson Huang and C. N. Yang. Quantum-mechanical many-body problem with hard-sphere interaction. *Phys. Rev.*, 105(3):767–775, Feb 1957.
- [89] Yong il Shin. *Experiments with Bose-Einstein Condensates in a Double-well Potential*. PhD thesis, Massachusetts Institute of Technology, 2006.
- [90] A. Imambekov, V. Gritsev, and E. Demler. Fundamental noise in matter interferometers. Proceedings of the International School of Physics Enrico Fermi, Course CLXIV, page 591. IOS Press, Amsterdam, 2008.
- [91] M. Inguscio, W. Ketterle, and C. Salomon. *Ultracold Fermi Gases, Proceedings of the International School of Physics "Enrico Fermi", Course CLXIV*. IOS Press, Amsterdam, 2008.
- [92] M. Inguscio, S. Stringari, and C. E. Wieman (editors). *Bose-Einstein condensation in atomic gases, Proceedings of the International School of Physics Enrico Fermi, Course CXL*. IOS Press, Amsterdam, 1999.
- [93] A. Itah, H. Veksler, O. Lahav, A. Blumkin, C. Moreno, C. Gordon, and J. Steinhauer. Direct observation of number squeezing in an optical lattice, 2009.
- [94] H. Ito, T. Nakata, K. Sakaki, M. Ohtsu, K. I. Lee, and W. Jhe. Laser spectroscopy of atoms guided by evanescent waves in micron-sized hollow optical fibers. *Phys. Rev. Lett.*, 76(24):4500–4503, Jun 1996.
- [95] D. Jaksch, C. Bruder, J. I. Cirac, C. W. Gardiner, and P. Zoller. Cold bosonic atoms in optical lattices. *Phys. Rev. Lett.*, 81:3108–3111, 1998.

- [96] J. Javanainen and M. Wilkens. Phase and phase diffusion of a split Bose-Einstein condensate. *Phys. Rev. Lett.*, 78(25):4675, 1997.
- [97] J. Javanainen and M. Wilkens. Reply. *Phys. Rev. Lett.*, 81(6):1345, August 1998.
- [98] J. Hubbard. Theory of the fermion liquid. *Proceedings of the Royal Society of London Series A*, 276(1365):238, 1963.
- [99] G.-B. Jo, J.-H. Choi, C. A. Christensen, Y.-R. Lee, T. A. Pasquini, W. Ketterle, and D. E. Pritchard. Matter-wave interferometry with phase fluctuating Bose-Einstein condensates. *Phys. Rev. Lett.*, 99(24):240406, Dec 2007.
- [100] G.-B. Jo, J.-H. Choi, C. A. Christensen, T. A. Pasquini, Y.-R. Lee, W. Ketterle, and D. E. Pritchard. Phase-sensitive recombination of two Bose-Einstein condensates on an atom chip. *Phys. Rev. Lett.*, 98(18):180401, 2007.
- [101] G.-B. Jo, Y. Shin, S. Will, T. A. Pasquini, M. Saba, W. Ketterle, D. E. Pritchard, M. Vengalattore, and M. Prentiss. Long phase coherence time and number squeezing of two Bose-Einstein condensates on an atom chip. *Phys. Rev. Lett.*, 98(3):030407, 2007.
- [102] Gyu-Boong Jo, Ye-Ryoung Lee, Jae-Hoon Choi, Caleb A. Christensen, Tony H. Kim, Joseph H. Thywissen, David E. Pritchard, and Wolfgang Ketterle. Itinerant Ferromagnetism in a Fermi Gas of Ultracold Atoms. *Science*, 325(5947):1521–1524, 2009.
- [103] Robert Jordens, Niels Strohmaier, Kenneth Gunter, Henning Moritz, and Tilman Esslinger. A mott insulator of fermionic atoms in an optical lattice. *Nature*, 455:204, 2008.
- [104] B. D. Josephson. 'original paper predicting josephson effect'. *Phys. Lett.*, 1:251, 1962.
- [105] J. Kanamori. Electron correlation and ferromagnetism of transition metals. *Prog. Theor. Phys*, 30:275, 1963.
- [106] P. Kapitza. Viscosity of liquid helium below the λ -point. *Nature*, 141:74, 1938.
- [107] J. Kinast, A. Turlapov, J.E. Thomas, Q. Chen, J. Stajic, and K. Levin. Heat capacity of a strongly interacting fermi gas. *Science*, 307(5713):1296, 2005.

- [108] Thorsten Köhler, Krzysztof Góral, and Paul S. Julienne. Production of cold molecules via magnetically tunable feshbach resonances. *Rev. Mod. Phys.*, 78(4):1311–1361, Dec 2006.
- [109] L.-P. Levy. *Magnetism and Superconductivity*. Springer, Heidelberg, 2000.
- [110] Th Lahaye, T. Koch, B. Frohlich, M. Fattori, J. Metz, A. Griesmaier, S. Giovanazzi, and T. Pfau. *Nature*, 448:672, 2007.
- [111] A. Layzer and D. Fay. *Int. J. Magn.*, 1:135, 1971.
- [112] A. E. Leanhardt, Y. Shin, D. Kielpinski, D. E. Pritchard, and W. Ketterle. Coreless vortex formation in a spinor Bose-Einstein condensate. *Phys. Rev. Lett.*, 90(14):140403, Apr 2003.
- [113] Aaron E. Leanhardt. *Microtraps and Waveguides for Bose-Einstein Condensates*. PhD thesis, Massachusetts Institute of Technology, 2003.
- [114] L. J. LeBlanc, J. H. Thywissen, A. A. Burkov, and A. Paramekanti. Repulsive fermi gas in a harmonic trap: Ferromagnetism and spin textures. *Phys. Rev. A*, 80(1):013607, 2009.
- [115] Patrick A. Lee, Naoto Nagaosa, and Xiao-Gang Wen. Doping a mott insulator: Physics of high-temperature superconductivity. *Rev. Mod. Phys.*, 78(1):17–85, Jan 2006.
- [116] T. D. Lee and C. N. Yang. Many-body problem in quantum mechanics and quantum statistical mechanics. *Phys. Rev.*, 105(3):1119–1120, Feb 1957.
- [117] A.J. Leggett and F. Sols. Comment on “phase and phase diffusion of split Bose-Einstein condensate”. *Phys. Rev. Lett.*, 81(6):1344, August 1998.
- [118] A. Lenef, T.D. Hammond, E.T. Smith, M.S. Chapman, R.A. Rubenstein, and D.E. Pritchard. Rotation sensing with an atom interferometer. *Phys. Rev. Lett.*, 78(5):760, February 1997.
- [119] I. Lesanovsky, T. Schumm, S. Hofferberth, M. Andersson, P. Krüer, and J. Schmiedmayer. Adiabatic radio-frequency potentials for the coherent manipulation of matter waves. *Phys. Rev. A*, 73:033619, March 2006.
- [120] Benjamin Lev. Fabrication of micro-magnetic traps for cold neutral atoms. *Quantum Inf. Comput*, 3(3):450, 2003.

- [121] K. Levin and O. T. Valls. Phenomenological theories of liquid ^3He . *Physics Reports*, 98(1):1 – 56, 1983.
- [122] M. Lewenstein and L. You. Quantum phase diffusion of a Bose-Einstein condensate. *Phys. Rev. Lett.*, 77(12):3489, October 1996.
- [123] Maciej Lewenstein, Anna Sanpera, Veronica Ahufinger, Bogdan Damski, Aditi Sen, and Ujjwal Sen. Ultracold atomic gases in optical lattices: mimicking condensed matter physics and beyond. *Advances in Physics*, 56:243, 2007.
- [124] Elliott Lieb and Daniel Mattis. Theory of ferromagnetism and the ordering of electronic energy levels. *Phys. Rev.*, 125(1):164–172, Jan 1962.
- [125] Elliott H. Lieb. Two theorems on the hubbard model. *Phys. Rev. Lett.*, 62(10):1201–1204, Mar 1989.
- [126] Elliott H. Lieb, Robert Seiringer, and Jan Philip Solovej. Ground-state energy of the low-density fermi gas. *Phys. Rev. A*, 71(5):053605, May 2005.
- [127] Elliott H. Lieb and F. Y. Wu. Absence of mott transition in an exact solution of the short-range, one-band model in one dimension. *Phys. Rev. Lett.*, 20(25):1445–1448, Jun 1968.
- [128] Hilbert v. Löhneysen, Achim Rosch, Matthias Vojta, and Peter Wölfle. Fermi-liquid instabilities at magnetic quantum phase transitions. *Rev. Mod. Phys.*, 79(3):1015–1075, Aug 2007.
- [129] F. London. The λ -phenomenon of liquid helium and the Bose-Einstein degeneracy. *Nature*, 141:643, 1938.
- [130] F. London. On the Bose-Einstein condensation. *Phys. Rev.*, 54:947, 1938.
- [131] C. Menotti, J.R. Anglin, J.I. Cirac, and P. Zoller. Dynamic splitting of a Bose-Einstein condensate. *Phys. Rev. A*, 63:023601, January 2001.
- [132] A. J. Moerdijk, B. J. Verhaar, and A. Axelsson. Resonances in ultracold collisions of ^6Li , ^7Li , and ^{23}Na . *Phys. Rev. A*, 51(6):4852–4861, Jun 1995.
- [133] Franz Mohling. Very low-temperature fermi gas. *Phys. Rev.*, 122(4):1062–1090, May 1961.
- [134] M.P.Marder. *Condensed matter physics*. Wiley-Interscience, New York, 2000.

- [135] Dirk Müller, Eric A. Cornell, Dana Z. Anderson, and Eric R. I. Abraham. Guiding laser-cooled atoms in hollow-core fibers. *Phys. Rev. A*, 61(3):033411, Feb 2000.
- [136] Yosuke Nagaoka. Ferromagnetism in a narrow, almost half-filled s band. *Phys. Rev.*, 147(1):392–405, Jul 1966.
- [137] Antonio Negretti and Carsten Henkel. Enhanced phase sensitivity and soliton formation in an integrated bec interferometer. *J. Phys. B: At. Mol. Opt. Phys.*, 37(23):L385–L390, 2004.
- [138] P. Nozières and S. Schmitt-Rink. Thermodynamic measurements in a strongly interacting fermi gas. *J. Low Temp. Phys.*, 59(195):1, 1985.
- [139] Maxim Olshanii and Ludovic Pricoupenko. Rigorous approach to the problem of ultraviolet divergencies in dilute Bose gases. *Phys. Rev. Lett.*, 88(1):010402, Dec 2001.
- [140] K. Onnes. Investigations into the properties of substances at low temperatures, which have led, amongst other things, to the preparation of liquid helium. Nobel lecture, December 13 in Nobel Lectures, Physics 1901-1921, Elsevier Publishing Company, Amsterdam, 1967.
- [141] G. Ortiz, M. Harris, and P. Ballone. Zero temperature phases of the electron gas. *Phys. Rev. Lett.*, 82(26):5317–5320, Jun 1999.
- [142] C. Orzel, A.K. Tuchman, M.L. Fenselau, M. Yasuda, and M.A. Kasevich. Squeezed states in a Bose-Einstein condensate. *Science*, 291(8):2386, March 2001.
- [143] D. D. Osheroff, R. C. Richardson, and D. M. Lee. Evidence for a new phase of solid $he3$. *Phys. Rev. Lett.*, 28(14):885–888, Apr 1972.
- [144] G. B. Partridge, K. E. Strecker, R. I. Kamar, M. W. Jack, and R. G. Hulet. Molecular probe of pairing in the BEC-BCS crossover. *Phys. Rev. Lett.*, 95:020404, 2005.
- [145] T. A. Pasquini, M. Saba, G.-B. Jo, Y. Shin, W. Ketterle, D. E. Pritchard, T. A. Savas, and N. Mulders. Low velocity quantum reflection of Bose-Einstein condensates. *Phys. Rev. Lett.*, 97(9):093201, 2006.

- [146] T. A. Pasquini, Y. Shin, C. Sanner, M. Saba, A. Schirotzek, D. E. Pritchard, and W. Ketterle. Quantum reflection from a solid surface at normal incidence. *Phys. Rev. Lett.*, 93(22):223201, Nov 2004.
- [147] Thomas A. Pasquini. *Quantum Reflection of Bose-Einstein Condensates*. PhD thesis, Massachusetts Institute of Technology, 2007.
- [148] R.K. Pathria. *Statistical Mechanics*. Butterworth-Heinemann, Oxford, 1996.
- [149] O. Penrose and L. Onsager. Bose-Einstein condensation and liquid helium. *Phys. Rev.*, 104:576, 1956.
- [150] Michael E. Peskin and Daniel V. Schroeder. *An introduction to quantum field theory*. Westview Press, New York, 1995.
- [151] A. Peters, K.Y. Chung, and S. Chu. Measurement of gravitational acceleration by dropping atoms. *Nature*, 400(2):849, August 1999.
- [152] C.J. Pethick and H. Smith. *Bose-Einstein condensation in dilute gases*. Cambridge University Press, New York, 2008.
- [153] D. S. Petrov. Three-body problem in fermi gases with short-range interparticle interaction. *Phys. Rev. A*, 67(1):010703, Jan 2003.
- [154] D. S. Petrov, C. Salomon, and G. V. Shlyapnikov. Weakly bound dimers of fermionic atoms. *Phys. Rev. Lett.*, 93(9):090404, Aug 2004.
- [155] D. S. Petrov, G. V. Shlyapnikov, and J. T. M. Walraven. Phase-fluctuating 3d Bose-Einstein condensates in elongated traps. *Phys. Rev. Lett.*, 87(5):050404, Jul 2001.
- [156] J. Pfarr. Magnetic properties of neutron matter. *Z.Phys.*, 251:152, 1972.
- [157] David Pines and Philippe Nozieres. *The Theory of Quantum Liquids*. W.A. Benjamin Inc., New York, 1966.
- [158] L. Pitaevskii and S. Stringari. Interference of Bose-Einstein condensates in momentum space. *Phys. Rev. Lett.*, 83(21):4237–4240, Nov 1999.
- [159] Lev Pitaevskii and Sandro Stringari. *Bose-Einstein Condensation*. Oxford University Press, New York, 2003.

- [160] Ludovic Pricoupenko and Yvan Castin. One particle in a box: The simplest model for a fermi gas in the unitary limit. *Phys. Rev. A*, 69(5):051601, May 2004.
- [161] T.P. Purdy and D.M. Stamper-Kurn. Integrating cavity quantum electrodynamics and ultracold-atom chips with on-chip dielectric mirrors and temperature stabilization. *Applied Physics B: Lasers and Optics*, 90:401, 2008.
- [162] M. J. Renn, D. Montgomery, O. Vdovin, D. Z. Anderson, C. E. Wieman, and E. A. Cornell. Laser-guided atoms in hollow-core optical fibers. *Phys. Rev. Lett.*, 75(18):3253–3256, Oct 1995.
- [163] S. Richard, F. Gerbier, J. H. Thywissen, M. Hugbart, P. Bouyer, and A. Aspect. Momentum spectroscopy of 1d phase fluctuations in Bose-Einstein condensates. *Phys. Rev. Lett.*, 91(1):010405, Jul 2003.
- [164] Giacomo Roati and et.al. Anderson localization of a non-interacting Bose-Einstein condensate. *Nature*, 453:895, 2008.
- [165] A. Robert, O. Sirjean, A. Browaeys, J. Poupard, S. Nowak, D. Boiron, C. I. Westbrook, and A. Aspect. A Bose-Einstein condensate of metastable atoms. *Science*, 292:461–464, 2001.
- [166] M. Saba, T. A. Pasquini, C. Sanner, Y. Shin, W. Ketterle, and D. E. Pritchard. Light Scattering to Determine the Relative Phase of Two Bose-Einstein Condensates. *Science*, 307(5717):1945–1948, 2005.
- [167] Subir Sachdev. *Quantum Phase Transitions*. Cambridge University Press, New York, 1999.
- [168] L. E. Sadler, J. M. Higbie, S. R. Leslie, M. Vengalattore, and D. M. Stamper-Kurn. Spontaneous symmetry breaking in a quenched ferromagnetic spinor Bose-Einstein condensate. *Nature*, 443:312–315, 2006.
- [169] M. Sagnac. Stark effect in rapidly varying fields. *C.R.Acad. Sci*, 157(2):708, October 1913.
- [170] L. Salasnich, B. Pozzi, A. Parola, and L. Reatto. Thermodynamic measurements in a strongly interacting fermi gas. *J. Phys. B: At. Mol. Opt. Phys.*, 33:3943, 2000.

- [171] F. Pereira Dos Santos, J. Léonard, J. Wang, C. J. Barrelet, F. Perales, E. Rasel, C. S. Unnikrishnan, M. Leduc, and C. Cohen-Tannoudji. Bose-Einstein condensation of metastable helium. *Phys. Rev. Lett.*, 86:3459–3462, 2001.
- [172] Monika H. Schleier-Smith, Ian D. Leroux, and Vladan Vuletic. Reduced-quantum-uncertainty states of an ensemble of two-level atoms, 2008.
- [173] U. Schneider, L. Hackermuller, S. Will, Th. Best, I. Bloch, T. A. Costi, R. W. Helmes, D. Rasch, and A. Rosch. Metallic and Insulating Phases of Repulsively Interacting Fermions in a 3D Optical Lattice. *Science*, 322(5907):1520–1525, 2008.
- [174] T. Schumm, S. Hofferberth, L.M. Andersson, S. Wildermuth, S. Groth, I. Bar-Joseph, J. Schmiedmayer, and P. Krüger. Matter-wave interferometry in a double well on an atom chip. *Nature physics*, 1:57, October 2005.
- [175] C.H. Schunck, Y. Shin, A. Schirotzek, and W. Ketterle. *Nature*, 454:739, 2008.
- [176] Y. Shin, G.-B. Jo, M. Saba, T. A. Pasquini, W. Ketterle, and D. E. Pritchard. Optical weak link between two spatially separated Bose-Einstein condensates. *Phys. Rev. Lett.*, 95(17):170402, Oct 2005.
- [177] Y. Shin, M. Saba, T.A. Pasquini, W. Ketterle, D.E. Pritchard, and A.E. Leanhardt. Atom interferometry with Bose-Einstein condensates in a double-well potential. *Phys. Rev. Lett.*, 92(5):050405, February 2004.
- [178] Y. Shin, M. Saba, M. Vengalattore, T. A. Pasquini, C. Sanner, A. E. Leanhardt, M. Prentiss, D. E. Pritchard, and W. Ketterle. Dynamical instability of a doubly quantized vortex in a Bose-Einstein condensate. *Phys. Rev. Lett.*, 93(16):160406, Oct 2004.
- [179] Y. Shin, C. Sanner, G.-B. Jo, T.A. Pasquini, M. Saba, W. Ketterle, D.E. Pritchard, M. Vengalattore, and M. Prentiss. Interference of Bose-Einstein condensates split with an atom chip. *Phys. Rev. A*, 72:021604, August 2005.
- [180] Y. Shin, M. W. Zwierlein, C. H. Schunck, A. Schirotzek, and W. Ketterle. Observation of phase separation in a strongly interacting imbalanced fermi gas. *Phy. Rev. Lett.*, 97(3):030401, 2006.
- [181] David W. Snoke. *Solid state physics:Essential concepts*. Addison-Wesley, San Francisco, 2008.

- [182] T. Sogo and H. Yabu. Collective ferromagnetism in two-component fermi-degenerate gas trapped in a finite potential. *Phys. Rev. A*, 66(4):043611, Oct 2002.
- [183] C. A. Stan. *Experiments with Interacting Bose and Fermi Gases*. PhD thesis, Massachusetts Institute of Technology, 2005.
- [184] J. Stenger, S. Inouye, D. M. Stamper-Kurn, H.-J. Miesner, A. P. Chikkatur, and W. Ketterle. Spin domains in ground-state Bose-Einstein condensates. *Nature*, 396:345, 1998.
- [185] James A. Stickney and Alex A. Zozulya. Wave-function recombination instability in cold-atom interferometers. *Phys. Rev. A*, 66(5):053601, Nov 2002.
- [186] James A. Stickney and Alex A. Zozulya. Influence of nonadiabaticity and nonlinearity on the operation of cold-atom beam splitters. *Phys. Rev. A*, 68(1):013611, Jul 2003.
- [187] E.C Stoner. Stoner’s instability. *Phil. Mag.*, 15:1018, Oct 1933.
- [188] Akinori Tanaka and Hal Tasaki. Metallic ferromagnetism in the hubbard model: A rigorous example. *Phys. Rev. Lett.*, 98(11):116402, 2007.
- [189] Hal Tasaki. Ferromagnetism in the hubbard models with degenerate single-electron ground states. *Phys. Rev. Lett.*, 69(10):1608–1611, Sep 1992.
- [190] Hal Tasaki. Ferromagnetism in hubbard models. *Phys. Rev. Lett.*, 75(25):4678–4681, Dec 1995.
- [191] Igor Teper, Yu-Ju Lin, and Vladan Vuletić. Resonator-aided single-atom detection on a microfabricated chip. *Phys. Rev. Lett.*, 97(2):023002, Jul 2006.
- [192] Philipp Treutlein, Theodor W. Hänsch, Jakob Reichel, Antonio Negretti, Markus A. Cirone, and Tommaso Calarco. Microwave potentials and optimal control for robust quantum gates on an atom chip. *Phys. Rev. A*, 74(2):022312, Aug 2006.
- [193] D. Vollhardt. *Rev. Mod. Phys.*, 56(1):99, Jan 1984.
- [194] D. Vollhardt, N. Blumer, K. Held, and M. Kollar. *Metallic Ferromagnetism - An Electronic Correlation Phenomenon*. Springer, Heidelberg, 2001, 2001. Lecture Notes in Physics, Vol. 580.

- [195] Lei Wang, Xi Dai, Shu Chen, and X. C. Xie. Magnetism of cold fermionic atoms on the p band of an optical lattice. *Phys. Rev. A*, 78(2):023603, Aug 2008.
- [196] Ying-Ju Wang, Dana Z. Anderson, Victor M. Bright, Eric A. Cornell, Quentin Diot, Tetsuo Kishimoto, Mara Prentiss, R. A. Saravanan, Stephen R. Segal, and Saijun Wu. Atom michelson interferometer on a chip using a Bose-Einstein condensate. *Phys. Rev. Lett.*, 94(9):090405, Mar 2005.
- [197] Tino Weber, Jens Herbig, Michael Mark, Hanns-Christoph Nägerl, and Rudolf Grimm. Three-body recombination at large scattering lengths in an ultracold atomic gas. *Phys. Rev. Lett.*, 91(12):123201, Sep 2003.
- [198] Robert M. White. *Quantum Theory of Magnetism*. Springer, Heidelberg, 2007.
- [199] E. Wigner. On the interaction of electrons in metals. *Phys. Rev.*, 46(11):1002–1011, Dec 1934.
- [200] W.H. Wing. Magnetic properties of neutron matter. *Prog. Quantum Electron.*, 8:181, 1984.
- [201] W.J.Heisenberg. Theory of the fermion liquid. *Z.Phys.*, 49:619, 1928.
- [202] E.M. Wright, D.F. Walls, and J.C. Garrison. Collapses and revivals of Bose-Einstein condensates formed in samll atomic samples. *Phys. Rev. Lett.*, 77(11):2158, September 1996.
- [203] Fa Yueh Wu and Eugene Feenberg. Theory of the fermion liquid. *Phys. Rev.*, 128(2):943–955, Oct 1962.
- [204] C. N. Yang. Concept of off-diagonal long-range order and the quantum phases of liquid he and of superconductors. *Rev. Mod. Phys.*, 34(4):694–704, Oct 1962.
- [205] Hui Zhai. Correlated versus ferromagnetic state in repulsively interacting two-component fermi gases. *Phys. Rev. A*, 80(5):051605, Nov 2009.
- [206] S. Zhang, H. Hung, and C. Wu. Proposed realization of itinerant ferromagnetism in optical lattices, 2008.
- [207] Shizhong Zhang, Hsiang-Hsuan Hung, and Congjun Wu. Proposed realization of itinerant ferromagnetism in optical lattices, 2008.
- [208] O. Zobay and B.M. Garraway. Two-dimensional atom trapping in field-induced adiabatic potential. *Phys. Rev. Lett.*, 86(7):1195, February 2001.

- [209] F. H. Zong, C. Lin, and D. M. Ceperley. Spin polarization of the low-density three-dimensional electron gas. *Phys. Rev. E*, 66(3):036703, Sep 2002.
- [210] M. W. Zwierlein, J. R. Abo-Shaeer, A. Schirotzek, C. H. Schunck, and W. Ketterle. Vortices and superfluidity in a strongly interacting Fermi gas. *Nature*, 435:1047–1051, 2005.
- [211] M. W. Zwierlein, C. A. Stan, C. H. Schunck, S. M. F. Raupach, S. Gupta, Z. Hadzibabic, and W. Ketterle. Observation of Bose-Einstein condensation of molecules. *Phys. Rev. Lett.*, 91(25):250401, Dec 2003.
- [212] M. W. Zwierlein, C. A. Stan, C. H. Schunck, S. M. F. Raupach, A. J. Kerman, and W. Ketterle. Condensation of pairs of fermionic atoms near a Feshbach resonance. *Phys. Rev. Lett.*, 92:120403, 2004.
- [213] M.W. Zwierlein. *High-Temperature Superfluidity in an Ultracold Fermi Gas*. PhD thesis, Massachusetts Institute of Technology, 2006.